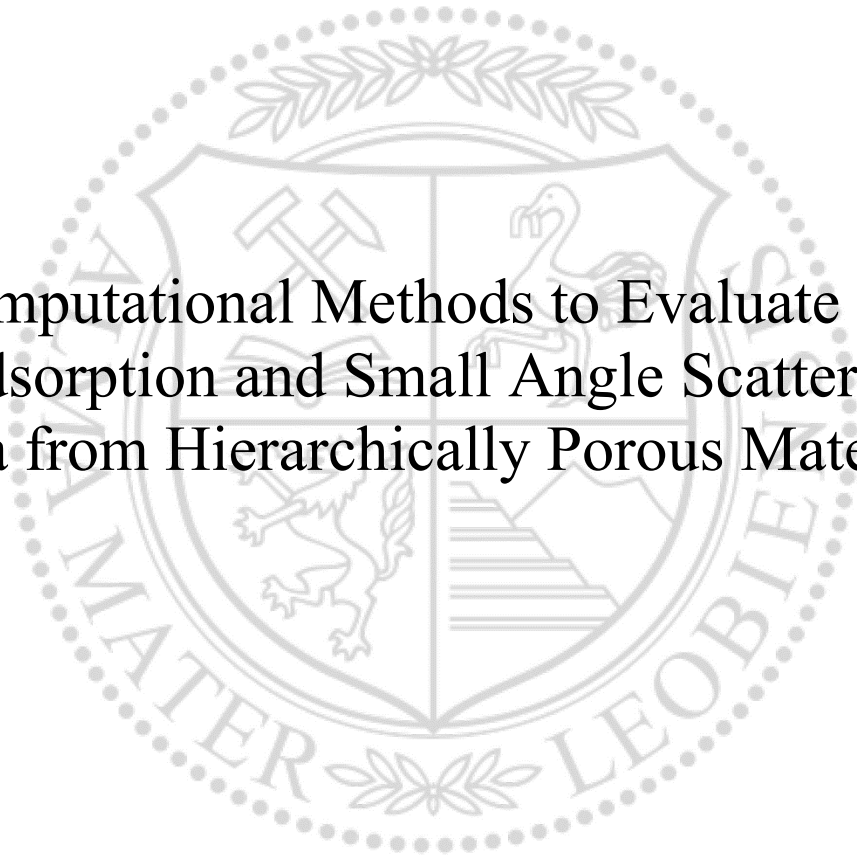




Institute of Physics

Doctoral Thesis



Computational Methods to Evaluate Gas
Adsorption and Small Angle Scattering
Data from Hierarchically Porous Materials

Lukas Ludescher, Dipl.Ing.

June 2020

EIDESSTATTLICHE ERKLÄRUNG

Ich erkläre an Eides statt, dass ich diese Arbeit selbständig verfasst, andere als die angegebenen Quellen und Hilfsmittel nicht benutzt, und mich auch sonst keiner unerlaubten Hilfsmittel bedient habe.

Ich erkläre, dass ich die Richtlinien des Senats der Montanuniversität Leoben zu "Gute wissenschaftliche Praxis" gelesen, verstanden und befolgt habe.

Weiters erkläre ich, dass die elektronische und gedruckte Version der eingereichten wissenschaftlichen Abschlussarbeit formal und inhaltlich identisch sind.

Datum 30.06.2020

Unterschrift Verfasser/in
Lukas, Ludescher

Acknowledgements

I want to devote my thanks to the many people who helped and encouraged me during my doctoral studies.

First and foremost, my doctoral advisor Oskar Paris. I am very grateful for the freedom and trust I received during my PHD while walking along different avenues and approaches of physics. I am especially thankful for his openness and ideas and the many hours gifted full with nurturing discussions. He actively cared in fostering and challenging my knowledge and my quality of work with his unweaving confidence; I could not have wished for a better companion- and mentorship.

Further, I'd like to thank my lab and the DIANA-project colleagues:

Roland Morak for his help, assistance and input in all experiments conducted in this thesis, as well the time spent on several, seemingly endless hours together spent in beamtimes.

Florian Putz, who performed the synthesis of the materials investigated and who tirelessly worked on ensuring high sample quality and the many hours shared in beamtimes.

Also, Stephan Braxmeier who ensured fully functioning and convenient to use equipment for the experiments conducted at beamtimes at the FRM II at the MLZ Garching, Munich. Here I would also extend my thanks to Christian Balzer, who was always ready to discuss theory and share valuable experimental data.

A general thanks is warmly extended to the 'seniors' of the DIANA project, Nicola Hüsing from the Paris-Lodron University, Salzburg, and Gudrun Reichenauer, CAE Bavaria, who, with Oskar Paris, guided all of us and contributed substantially to the realization of the project.

I would also like to thank Gennady Gor, who enabled me to perform theoretical considerations by hosting me for three months at his group at the NJIT, New Jersey, USA, and his considerable contribution to my understanding of theoretical concepts involving adsorption and adsorption induced deformation.

Furthermore, Paul Zaslansky, who was never short in expressing his encouragement and his infectious excitement for his field of study, as well as the meticulously sliced and prepared human root dentin samples.

A special thanks is also extended to all the colleagues working at the Institute of Physics at the Montanuniversität Leoben by making even some of the most tedious working days enjoyable in several coffee breaks and always being ready to give scientific input in any topic that arose during my PHD.

Also, to Heide Kirchberger, who carefully and patiently fixed any administrative error I have performed, especially during the beginning of my PHD, and ensured that we were always on time, regardless on how many plates she had spinning.

Last, but definitely not least, I thank my family, who greatly supported me during my doctoral studies and had endless patience and support during stressful times, but also their genuine excitement and support during all the good times.

Abstract

The objective of this thesis was the determination and description of adsorption induced deformation in different monolithic hierarchically nanoporous materials. These included two synthetic materials, monolithic hierarchically nanoporous silica and carbon, and one biological material in human root dentin.

The mesoscopic structure of the silica material is highly similar to SBA-15, which was used to study adsorption induced deformation with in-situ adsorption small angle x-ray scattering (SAXS) in earlier works, and is equally suited as a model material to investigate adsorption and adsorption induced deformation. The silica monoliths are built up from a disordered network of struts, which are about 1 μm in length and 400 nm in diameter. Every strut exhibits 2-D hexagonally ordered, cylindrical mesopores with a diameter of 6 – 7 nm and lattice constant of ~ 10 nm. Depending on the materials thermal history, different amount of accessible micropores with a characteristic size of < 2 nm are embedded in the silica mesopore walls. The monolithic character enables to measure macroscopic deformation using in-situ adsorption dilatometry. In connection with in-situ small angle neutron scattering (SANS), the deformation induced by adsorption of water in three silica materials exhibiting different amounts of micropores was determined. The small angle neutron scattering and dilatometry strain isotherms were successfully modelled using a macroscopic, thermodynamic model of adsorption induced deformation from literature. So-called 'apparent-deformations', which occur in in-situ adsorption SAXS data of a monolithic, hierarchically porous materials, determined from the difference between water strain isotherms obtained with SAXS and SANS on the same silica material, were determined and successfully modelled using a simple, hierarchical pore model. During the investigation of apparent strains, subtle effects pertaining to the process of adsorption and the compressive or tensile nature of apparent strains were observed, hinting at a unique process of water adsorption in silica materials.

In-situ n-pentane and water adsorption SANS and dilatometry experiments on monolithic, hierarchically nanoporous carbon materials were conducted. These carbon materials exhibit the macroscopic strut-network structure of monolithic silica materials, but on the mesoscopic level they are exactly the inverse of the silica materials mesopore structure, where 2-D hexagonally ordered carbon nanowires with a diameter of about 6 – 7 nm and a lattice constant of ~ 10 nm. To interpret the strain isotherms acquired on three different carbons with different amount of micropores, a model of adsorption in concave mesopore spaces was adapted. This model was able to qualitatively describe nitrogen and n-pentane adsorption isotherms. N-pentane strain isotherms of all carbon sample were interpreted and even partially quantified using the results of the adsorption model.

Finally, in-situ water-absorption SAXS data were measured on human root dentin. Using correlation length, swelling of collagen situated between crystalline mineral platelets was observed. Additionally, hints of filling of structures in human root dentin according to their hierarchical level of structures were found.

Zusammenfassung

Das Ziel dieser Arbeit war die Bestimmung und Beschreibung der adsorptions-induzierten Deformation unterschiedlicher Materialien. Diese umfassten zwei synthetische Materialien, einmal monolithisches, hierarchisch-nanoporöses Silica und monolithischer, hierarchisch-nanoporöser Kohlenstoff, und ein biologisches Material in humanem Wurzeldentin.

Die Mesostruktur der untersuchten Silikamaterialien entspricht in etwa SBA-15 und stellt somit ebenso ein Modellmaterial dar an dem Adsorption und adsorptions-induzierte Deformation schon in früheren Arbeiten untersucht wurden. Ein Silica-Monolith ist aus einem ungeordneten Netzwerk von sogenannten ‚Struts‘, mit Durchmesser ~ 400 nm und ~ 1 μ m Länge, aufgebaut, die parallele, 2-D hexagonal angeordnete, zylindrische Mesoporen mit einem Durchmesser von $\sim 6 - 7$ nm und einem Gitterparameter von ~ 10 nm enthalten. In den Mesoporenwänden sind, je nach thermischer Geschichte, Mikroporen mit charakteristischen Längen von < 2 nm eingebettet. Der monolithische Charakter lässt jedoch auch die Untersuchung der makroskopischen Deformation mit in-situ adsorptions Dilatometrie zu, die von unseren Partnern am Zentrum für Angewandte Energie-Forschung (ZAE) Bayern durchgeführt wurde. Im Zusammenhang mit in-situ Wasser-adsorptions SANS-Messungen, erhält man dadurch ein vollständiges Bild der Verformung dieser Materialien, Diese wurde in dieser Arbeit erfolgreich für zwei Silicamaterialien erfolgreich unter Anwendung eines thermodynamischen Modells, entwickelt von Christian Balzer (ZAE, Bayern), für in-situ Wasser-Adsorption modelliert. So-genannte ‚scheinbare Verformungen‘, welche in in-situ Adsorption SAXS Messungen auftreten, wurden an einer kalzinierten Silica-Probe aus der Differenz in gemessener Dehnung zwischen SANS und SAXS Messungen bestimmt und erfolgreich mit einem simplen, hierarchischen Modell bestimmt. Im Rahmen dieser Untersuchungen wurden weitere interessante Zusammenhänge zwischen Adsorption und in-situ SAXS gefunden. So war es unter anderem möglich eine Abschätzung der Adsorptionsisotherme aus Streudaten zu gewinnen. Ähnliche SANS Experimente zur Bestimmung der adsorptionsinduzierten Deformation in monolithischen, hierarchisch nanoporösen Kohlenstoffen wurden unter Adsorption von n-Pentan und Wasser durchgeführt und von in-situ Adsorption-Dilatometrie Messungen, durchgeführt von Christian Balzer (ZAE, Bayern) komplettiert. Die untersuchten Kohlenstoffe sind auf der mesoskopisch-hierarchischen Ebene das strukturelle Negativ der Silica-materialien und enthalten daher im Vergleich keine zylindrischen Mesoporen sondern 2-D hexagonal angeordnete Kohlenstoffnanofasern mit einem Durchmesser von $6 - 7$ nm und einem Gitterparameter von ~ 10 nm. Auf der makroporösen Ebene entsprechen sich die Strukturen der Kohlenstoff und Silikamaterialien hingegen wieder. Um die gemessenen adsorption-induzierten Verformungen interpretieren zu können, wurde ein Modell zur Sorption in in den konkaven Mesoporen angewandt. Mit diesem Modell konnte zumindest qualitativ die n-Pentan und Stickstoff Adsorptionsisotherme beschrieben werden. Unter Anwendung dieses Modells konnten in-situ n-Pentan Adsorption SANS- und Dilatometriedaten interpretiert und in einigen Bereichen der Strainisothermen sogar quantifiziert werden. Schlussendlich wurden in-situ Wasserabsorption SAXS-Messungen an humanem

Wurzeldentin durchgeführt. Aus der Korrelationslänge konnte Deformation des Kollagens zwischen den kristallinen Mineralplättchen festgestellt werden. Zusätzlich gab es Hinweise auf die sequentielle Füllung der Probe gemäß dem hierarchischen Level der Strukturen mit Wasser.

Table of Contents

1	Introduction	1
2	Materials	5
2.1	Nanoporous Silica Materials	5
2.2	Nanoporous Carbon Materials	7
2.3	Biological Materials: Human Root Dentin.....	8
3	Theoretical Basics	11
3.1	Small Angle Scattering.....	11
3.1.1	Basics of Small Angle Scattering	11
3.1.2	Structural Model of Mineralized Biological Tissue	16
3.1.3	Hierarchical Model of Macro-, Meso- and Microporous Silica.....	17
3.1.4	Filling Fractions obtained from the hierarchical Pore-Model.....	20
3.1.5	Determination of Integrated Peak Intensities from ordered Mesopores	22
3.1.6	The Debye Scattering Formula for 3D and 2D	24
3.1.7	Apparent Deformation	25
3.2	Theoretical Basics on Macroscopic Thermodynamic Modelling of Physisorption	27
3.2.1	Short Introduction to Adsorption.....	27
3.2.2	Specific Pore Volumina.....	28
3.2.3	Modelling of Sorption in Cylindrical Mesopores by Gibbs free energy	32
3.2.4	Variational Approach to Physisorption in Complex Pore Geometries	37
3.2.5	Equivalence between the Grand Potential and the Gibbs free energy description	40
3.2.6	Disjoining Pressure.....	42
3.3	Adsorption Induced Deformation.....	45
3.3.1	Origin of Surface Stress: Bangham Effect.....	45
3.3.2	Thermodynamic Model of Adsorption Induced Deformation	47
3.3.3	Adsorption Induced Stress on Carbon Nanowires	50
3.3.4	Adsorption Induced Deformation of Slit Pores in the Mesopore regime	54
4	Experimental Techniques and Procedures.....	57
4.1	Ex-Situ Small Angle X-Ray Scattering.....	57
4.2	In-Situ Small Angle X-Ray Scattering – Human Root Dentin	58
4.2.1	Vapor Dosing	58
4.2.2	In-Situ water absorption SAXS measurements in Human Root Dentin.....	60
4.3	In-situ water and n-pentane adsorption SANS on Carbon	61

4.3.1	Vapor Dosing	62
4.3.2	SANS.....	63
4.4	In-situ water adsorption SANS on Silica	64
5	Modelling of strains and apparent strains in hierarchical Silica.....	66
5.1	In-situ small-angle neutron scattering investigation of adsorption-induced deformation in silica with hierarchical porosity	66
5.1.1	Experimental Results and Modelling	66
5.1.2	Discussion of Results	71
5.2	Hierarchically Nanoporous Silica: Adsorption Isotherm and Adsorption-Induced Deformation from Small-Angle X-ray Scattering.....	75
5.2.1	Experimental Results:.....	75
5.2.2	Theoretical Modelling.....	77
5.2.3	Discussion.....	87
6	Adsorption and Adsorption induced deformation in hierarchical carbons with concave pores	90
6.1	Capillary Bridge Formation between Hexagonally Ordered Carbon Nanorods	90
6.1.1	Characterization.....	90
6.1.2	Computational Details and Results	95
6.1.3	Simplified Capillary Bridge model.....	99
6.1.4	Discussion.....	103
6.2	Adsorption induced deformation in monolithic, hierarchically nanoporous carbon with concave mesoporosity	105
6.2.1	Experimental Results.....	105
6.2.2	Discussion.....	120
7	Human Root Dentin	123
7.1	Experimental Results.....	123
7.2	Discussion.....	132
8	Summary & Outlook	135
9	References	140

1 Introduction

Porous materials are prevalent in the modern world, as their unique properties, such as high specific adsorption surface or their specific strength and ductility find applications ranging from aviation¹, gas adsorption and storage², water cleansing³, energy storage⁴, actuators, sensors and even biomedical applications⁵ in state of the art drug delivery systems. The relevance of porous materials is far reaching, as especially in agriculture sufficient water content of soil is a necessity to grow crops in a world of soon-to-be 8 billion people. Even further, with the first clear signs of Global Warming, technologies involving energy storage and carbon capture might be a vital component to combat Climate Change. Study of porous materials is consequently not only relevant for high-tech applications, but also of interest for the general population.

First experiments using porous materials were probably already conducted in antiquity as clay was used as a drying and bleaching agent. First systematic research was conducted in 1773 by Scheele who observed the adsorption of air in coal by a volumetric method which in principle remains state-of-the-art to-date. Further, to understand the properties of soil useful in farming, investigations on the density of dry earth and mud were conducted⁶. These observations back then were more or less purely experimental, as proper theoretical formalisms were not yet developed. Description of adsorption was not properly achieved for a long time although further research into this topic was conducted until Gibbs released his groundbreaking works on thermodynamics⁷. Around this time Lord Kelvin and subsequently Helmholtz first connected surface tension of a meniscus with the pressure difference between the fluid and vapor phase, essentially describing condensation. Within this theoretical framework it was now possible to relate the amount adsorbed by a surface to thermodynamic potentials. Of particular note is the work by Irving Langmuir, who worked as staff scientist at General Electric in the early twentieth century and observed the adsorption of atomic hydrogen on tungsten coils in early incandescent light bulbs. This process was investigated by him in more detail and led to the discovery of the famous Langmuir isotherm equation⁸. This relatively simple isotherm describes the adsorption of monolayers on smooth surfaces, which he was later rewarded a Nobel Prize for. Further developments such as the Brunauer-Emmett-Teller isotherm for multilayer sorption⁹ built on this seminal work, but further big strides in the theoretical description of adsorption in nanoporous materials which would relate the detailed pore shape to adsorption characteristics were not yet achieved. This was later developed in parallel in the East and West during Cold War times, where works by Derjaguin¹⁰ and Broekhoff and de-Boer^{11,12} successfully allowed a coherent thermodynamic description of a sorption isotherm relating pore size and shape to the shape of the isotherm. Although only cylindrical mesopores were considered, this seminal work allowed for a more complete description of sorption physics and allowed to characterize certain porous media, such as Vycor glass, with high precision. The next step in characterization of porous media was taken when first non-local density functional methods (NLDFT)¹³ were developed in the early nineties of the last century, where for the first time a Kernel for adsorption of nitrogen in carbon slit pores was calculated and compared to Grand Canonical Monte Carlo (GCMC) simulations. In contrast to macroscopic thermodynamic methods, such as the Derjaguin-Broekhoff-deBoer (DBdB) method, where the adsorbed fluid was assumed to be of uniform density, density functional theories allowed for a variation in adsorbed fluid density. By calculating adsorption isotherms of a certain combination of vapor and adsorbing substrate, Kernels¹⁴ can be defined which are then

used to fit experimentally determined sorption isotherms with so far unparalleled accuracy. Around this time, first synthetic nanoporous materials with highly ordered and well defined mesopores, such as MCM-41¹⁵, were developed. These materials allowed the further development of characterization techniques where NLDFT was expanded by calculating kernels for other adsorbates and materials. But these methods had the distinct drawback that they only assumed completely flat meso- and micropore walls, which is not representative for real pore geometries. Hence, the Quenched Solid Density Functional theory (QSDFT) was developed by Ravikovitch and Neimark¹⁶, where the completely flat pore wall is substituted with a transition area, which both substrate and adsorbed liquid can occupy simultaneously. This transition area between substrate and pore is meant to represent rough and corrugated interfaces and further enhances the precision of characterization of nanopores.

Research on the mechanical properties of porous materials reaches close to a century back in time, where first studies of influence of ambient humidity on building materials was performed by McBain and Ferguson¹⁷. Although this work focussed on swelling of building materials it inspired further investigations. Subsequent works describing adsorption induced deformation by Bangham¹⁸ related the expansion of coal upon adsorption to an effective decrease in the surface energy of the solid, relaxing stress in the material leading to expansion. This was a first quantitative description of adsorption induced deformation due to change in the materials surface energy which led to its name - 'Bangham effect'. The methods employed in these historical studies are reliant on the measurement of deformation of a macroscopic sample via dilatometry, which in itself only gives indirect results of nanoscale processes leading to deformation. Bangham's law was challenged once adsorption induced deformation in coal and porous glasses was measured with more refined dilatometric techniques^{19,20}, where pronounced contraction of the materials upon adsorption was found^{21,22}. As the Bangham effect only predicted expansion upon adsorption, the contraction was related to the formation of liquid bridges between opposing pore walls^{21,22}. Unfortunately, interest in adsorption induced deformation decreased around the 1950s, as the existing experimental techniques, materials and computational resources didn't allow for a more detailed understanding of adsorption induced deformation and scientific progress stalled until the end of the twentieth century.

First works on the adsorption induced deformation using scattering and diffraction methods were performed in the nineties of the last century, where the deformation of a thin silicon layer with etched, cylindrical, parallel nanopores under pentane adsorption was measured by tracking the coherence peak of crystalline silica^{23,24}. Scattering methods themselves are usually only applicable for highly ordered materials, which severely limited the usecases of this method. Again, the breakthrough in the mesoscopic study of adsorption induced deformation was achieved when synthetic materials with highly ordered mesoporosity were first investigated with Small-Angle X-ray scattering. Originally, the ordered porosity was desired to study oil-retention and flow in mesopores, but soon they found increasing interest in other scientific fields. After an initial study on adsorption induced deformation via Nitrogen adsorption in MCM-41 was performed in the early 2000's²⁵, systematic measurements of adsorption induced deformation conducted by the group of Paris et al^{26,27} were performed in the end of the 2000's. These measurements proved to be highly valuable as they allowed to develop and test thermodynamic models of adsorption induced deformation²⁸⁻³¹. The popular solvation pressure approach was developed earlier by Ravikovitch et al¹⁶, but only came to full fruition around a decade later as a first coherent description of adsorption induced

deformation in cylindrical mesopores from macroscopic thermodynamics, namely by application of Derjaguin-Breokhoff-deBoer theory, was achieved by Balzer et al^{32,33}. A reason for this considerable step forwards was a combination of experimental techniques, in-situ sorption dilatometry and Small angle Scattering (SAS), on monolithic hierarchically nanoporous silica materials^{34,35}, which allowed to test adsorption induced deformation on a mesoscopic and macroscopic scale simultaneously³⁶.

Balzer et al³⁶ compared both, in-situ n-pentane adsorption SAXS and dilatometry, strain isotherms collected on a monolithic silica sample and found that the maximum strain, which occurred once all meso- and micropores were filled, was a factor of two larger in dilatometry than in SAXS. This was in contrast to a later study from Morak et al³⁷ on a similar material where they were able to show in a combined in-situ sorption dilatometry and Small Angle Neutron Scattering (SANS) study, where zero length density water was used, that the maximum adsorption induced strain should coincide between both techniques. In their work it was implied that earlier experimental works on adsorption induced deformation^{26,27}, where in-situ physisorption Small Angle X-Ray Scattering (SAXS) was applied, did contain so-called apparent strains which lead to a systematic deviation in measured strains from real strains in the material. The concept of apparent strains was first introduced in the context of deformation induced by vapor adsorption in cylindrical mesopores in SBA-15 by Prass et al³⁸. Their work explored apparent strains due to n-pentane, perfluoropentane and water adsorption, but was limited to effects occurring in the relative pressure interval associated with capillary condensation in the materials mesopores. The distribution of mesopore diameters lead to different pressures of capillary condensation, with the sudden change in scattering length density contrast of mesopores due to filling leading to apparent strains. In contrast, the results from Morak et al³⁷ indicated that apparent strains exist over the whole range of relative pressures covered in in-situ adsorption SAXS experiments, but no model to correct for these effects in SAXS was introduced. So far, the only way to measure quantitative strain isotherms in mesoporous materials is via in-situ adsorption SANS with a zero-length scattering density vapor.

Progress in the research of adsorption induced deformation was not only limited to silica materials, as synthesis of monolithic, hierarchically nanoporous carbon materials was also achieved^{39,40}. Similar nanoporous carbon materials have found particular interest in recent years as they are used in novel energy storage concepts in batteries and supercapacitors⁴⁰. Koczwara et al³⁹ detected pore swelling in a supercapacitor electrode made from monolithic, hierarchically nanoporous carbon in an in-situ SAXS experiment as a function of applied voltage. The strain isotherms obtained through SAXS closely matched strain isotherms obtained with in-situ dilatometry on the same material, which proves that pore swelling is indeed present in charging and depletion cycles in supercapacitors. In contrast to adsorption induced deformation investigated in silica where physisorption is the driving force of deformation, local rearrangement of ions due to applied voltage to the electrode causes deformation.

Synthetic, well ordered porous materials are good model materials to study sorption and adsorption induced deformation and allow for advanced engineering attempts⁴¹. Further advances can also be made if biological materials are studied in this respect^{42,43}. In contrast to most engineering materials which are overwhelmingly pure or alloyed metals which need to be extracted from earth and processed for use in a specific application, biological materials achieve similar mechanical parameters using biology and some mineral phases⁴⁴. Their properties are hence not purely related to phases present, but

also to their hierarchical arrangement, which is quite prominent in materials such as bone or root dentin⁴⁵. But if one seeks to understand the properties of biological materials in their entirety, it is crucial to investigate the role of water as it plays a dominant role in the full realization of the properties achievable by biological materials^{46,47}.

Although the original intent of this work was to utilize synchrotron SAXS to investigate adsorption induced deformation of hierarchical, nanoporous silica materials, its scope soon shifted and widened to research on adsorption in biological materials, scattering theory in in-situ adsorption SAXS and adsorption in nanoporous carbon materials. In this regard, the combination of experimental work and computational modelling proved to be fruitful, when several experimental techniques and latest advances in the characterization and modelling of nanoporous materials were combined. During the course of this thesis several questions concerning adsorption and adsorption induced deformation arose:

- What is the origin of so-called apparent strain in in-situ adsorption small angle x-ray scattering?
- In how far influences the curvature of a substrate the measured adsorption, especially in concave pore spaces?
- How do materials exhibiting concave pore spaces deform upon adsorption? Is the understanding of adsorption in such materials sufficient to interpret their strain isotherms?
- How does dehydration and rehydration influence the structure of biological matter such as root dentin?

The range of topics encountered, from quite subtle effects concerning the influence of small angle x-ray versus neutron neutron scattering in adsorption, to deformation of concave pore spaces to biological materials, shows the breadth of the physics of adsorption. This thesis is also a testament to the fact that adsorption induced deformation and apparent deformation contribute to the understanding of it's underlying processes, namely adsorption, can elucidate the physics of adsorption. Consequently, several groups and scientists were involved as cooperation partners in answering these and similar questions. Synthesis of synthetic silica and carbon materials was performed by Florian Putz under guidance from his doctoral advisor Nicola Hüsing, Paris-Lodron University Salzburg. Measurement of adsorption- and dilatometric strain isotherms used in this thesis was performed by Christian Balzer and Stefan Braxmeier from Gudrun Reichenauer's group, ZAE Würzburg, Bayern. Modelling of adsorption strain isotherms on silica was developed by Christian Balzer in cooperation with Alexander Neimark, Rutgers University, and Gennady Gor, New Jersey Institute of Technology. Gennady Gor was also kind enough to host me for three months to develop and apply theoretical models of adsorption in carbon materials in 2017. Root dentin samples investigated in this thesis were provided by Paul Zaslansky, Julius Wolf Institute, Charité Berlin. Finally, in-situ adsorption small angle x-ray and neutron scattering measurements were performed in close cooperation with Roland Morak from the Montanuniversität Leoben.

2 Materials

Porous materials have at least been investigated since the 18. century⁶, where the density of dry and wet earth, essentially mud, was characterized and mathematically described. Ever since, the study of porous materials has advanced significantly, due to their special characteristics. They have high specific surface areas, dependent on the size of the accessible pores inside, and can exhibit relatively good stiffness at a low macroscopic density. This clearly defines their applications in industry, ranging from light weight constructions in fields such as aviation⁴⁸ where reliability is key, chemical applications such as catalysis⁴⁹ or energy storage⁵⁰ or even in medical applications⁵¹.

The pores in a material applied in the uses mentioned range considerably in size, from fractions of nanometers to several microns. They are usually classified by size according to the International Union of Pure and Applied Chemistry (IUPAC)⁵², with micropores being smaller than 2 nm, mesopores in-between 2 and 50 nm and macropores being any void space with a characteristic size of larger than 50 nm. Porous materials today are usually synthesized to have characteristic sizes in a range appropriate for the given application. Although initially forgotten, highly ordered meso- and microporous materials have been synthesized since the late sixties⁵³ and were rediscovered and also independently developed in the 90s of the last century¹⁵. These materials possess advantageous properties such as tuning of the pore sizes, high accessibility and the possibility for functionalization of the pore walls⁵⁴, but were only synthesised as a loose powder of individual meso- and microporous grains. In the 2000s pioneering works from Nicola Hüsing's group^{34,55} and Nakanishi et al⁵⁶ achieved synthesis of monolithic, hierarchically nanoporous materials with highly ordered meso- and disordered micropores. Two types of these synthetic materials, one silicon and one carbon based, and a biological material in root dentin⁴⁵ are of interest in this work and are now presented.

2.1 Nanoporous Silica Materials

The hierarchically structured porous silica material was synthesized by Florian Putz³⁵ from the group of Dr. Nicola Hüsing (Paris-Lodron University, Salzburg).

The macroscopic samples are cylindrical, hierarchically macro-, meso- and microporous silica monoliths with a length of several centimeters and a diameter ranging from 5mm to 1cm. They are built up by a disordered network of struts of 1 - 1.5 μm length and 200 - 400 nm diameter (**Figure 1 a**), which exhibit hexagonally ordered cylindrical mesopores with a diameter of 6 - 7 nm running along their long axis (**Figure 1 b**). The silica wall of these mesopores contains micropores which, if the structural correspondance to SBA-15 also holds on the microporous scale, are of chain or cylinder-like shape⁵⁷.

Samples, which were supercritically dried with CO_2 , exhibit in the as-prepared state mesopore walls decorated with residues of P123.³⁵ These residues seem to block certain vapors, such as water, from entering the micropores and consequently change adsorption characteristics⁵⁸. Amorphous silica surfaces exhibit dangling bonds such as silanol-groups. To stabilize the surface of the pores it is necessary to age the samples in a water atmosphere for 3 weeks at a temperature of 50°C³⁷. This allows for small conformal changes and restructuring of the silica surface, greatly enhancing experimental reproducibility against changes due to storage in ambient air.

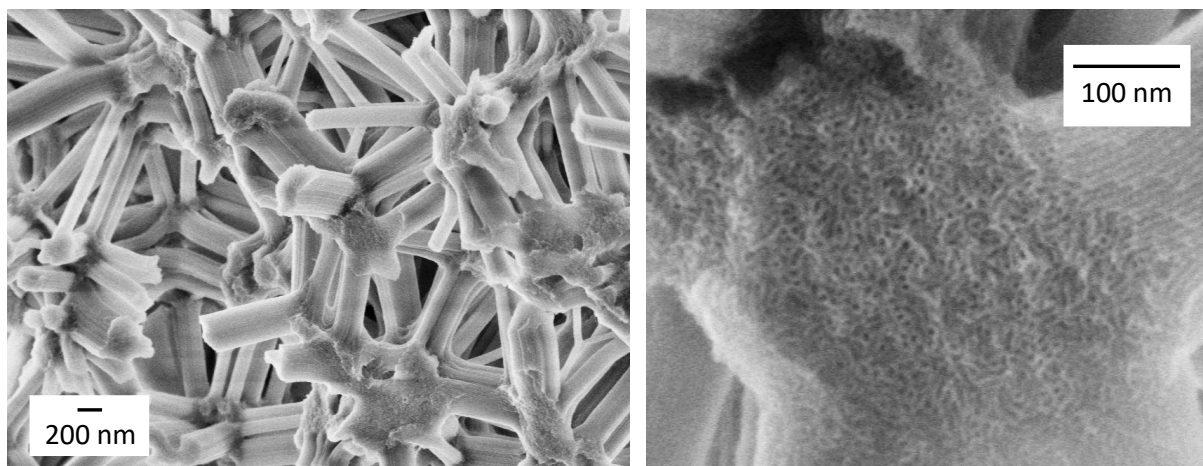


Figure 1: *The disordered strut-network of the hierarchically porous silica material is shown in a), with a zoom in the mesostructure of a singular strut where the individual cylindrical mesopores are distinguishable in top-view. Image supplied by Florian Putz and published in⁵⁹ (reprinted with permission from ACS publishing).*

Calcination of the material at 500 °C in air for a duration of 10 hours removes the organics inside and achieves accessibility of the micropores without removing them due to sintering processes. Still, densification of the silica matrix is observed⁶⁰ without considerable change in mesoporous structure. Further heating at a temperature of 750°C induces sintering of the material and removes most of the micropores in the sample. In the experiments performed in the thesis of Roland Morak⁵⁸, which were the basis for the simulations in this work, three samples at different stages of thermal treatment were investigated. Consequently, the notation used in Roland Moraks thesis was adapted, where S-A, S-C and S-S denote the as-prepared, calcined and sintered monolithic, hierarchically nanoporous silica samples respectively.

Adsorption induced deformation of all three samples was measured with two methods. Mesoscopic strains were determined with in-situ adsorption sorption Small Angle Neutron and X-Ray Scattering as established on a material exhibiting similar mesostructure in SBA-15. The monolithic nature of the materials investigated allows for determining the adsorption induced strain not only on a mesoscopic level, but also on a macroscopic level.

2.2 Nanoporous Carbon Materials

The carbon materials investigated in this work were synthesized by Florian Putz from the group of Dr. Nicola Hüsing (Paris-Lodron University, Salzburg). Their mesoscopic structure is similar to CMK-3 materials first synthesized in the late nineties of the last century⁶¹⁻⁶³.

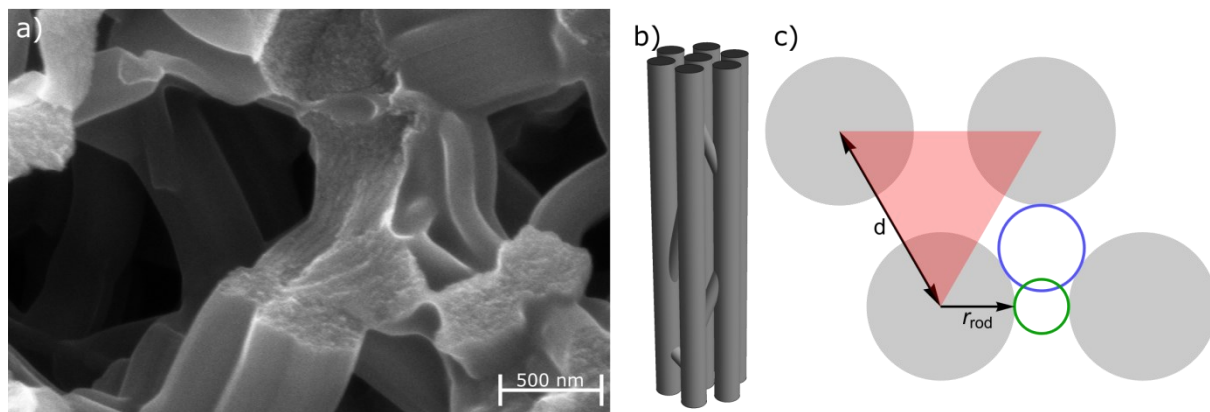


Figure 2: In a) a electron microscopy image of the macroporous structure of a monolithic hierarchically nanoporous carbon material is depicted, with b) being an idealized strut with interconnections between nanowires and c) showing the geometrical details of a unit cell. Depicted are the nanowire radius r_{rod} and their distance d , the smallest representative area by an opaque, red triangle and the largest and smallest inscribed radius inbetween three adjacent nanowires. The SEM picture was supplied by Simon Rumswinkel (Paris-Lodron University, Salzburg).

Synthesis of hierarchically nanoporous carbon monoliths was achieved by negative templating³⁹: Silica monoliths, produced as described above, were infiltrated with a resorcinol-formaldehyde solution which acted as the carbon source³⁹. After carbonization of the composite monoliths at 850°C³⁹, the silica was removed with hydrofluoric acid. Finally, a monolithic, hierarchically nanoporous, amorphous carbon skeleton results from the synthesis. The macroporous structure of the silica monolith is retained (**Figure 2**), whereas the cylindrical mesopores are replaced with carbon nanowires and the silica walls are exchanged with void space. In **Figure 2** a) the macroscopic structure built up from struts of around 1 μm length and 200 – 500 nm diameter is depicted in detail. These struts consist of an assembly of parallel, 2-D hexagonally ordered nanowires. A sketch of the mesoscopic structure is presented in **Figure 2** b) and c), where the former shows a small bundle of parallel, hexagonally ordered carbon nanowires connected by interconnections and the latter shows a top view of a smallest repeat unit with geometrical details highlighted. In general, the geometrical details from materials derived by a negative templating approach are closely related to the original. Hence, the carbon nanowire radius r_{rod} (~ 7 nm) and distance d (~ 10 nm) are similar to mean mesopore diameter and distance found in the monolithic, hierarchically nanoporous silica material described above.

A sample picture of the local three-dimensional structure is shown in **Figure 2** b), with a top-view image provided in **Figure 2** c). To characterize the material, Joo et al have applied physisorption analysis⁶², where the pore space was represented by the largest inscribed cylinder in-between three adjacent carbon nanowires as signified by the blue,

dashed circle in **Figure 2 c**). The results from this analysis were compared to results from transmission electron microscopy, which seemed to confirm the approach taken.

Although the individual carbon nanowires exhibit microporosity after removal of silica, their microporosity is enhanced with additional physical activation. This is achieved by activation with CO_2 at $925^\circ C$ ⁶⁴, a so-called ‘physical’ activation process. The chemical reaction underlying is the so called Boudouard reaction:



During this process, material is removed, called ‘burn-off’, which leads to the enlargement of existing micropores, revelation of closed microporosity and creation of new micropores. Consequently, the accessible microporosity is usually increased by this process, enhancing desired properties such as specific surface area and pore volume.

For the samples investigated in this work, the carbon is of turbostratic structure as found by Koczwara et al⁶⁵. Turbostratic carbon materials are built up from short stacks of graphene sheets constituting the small lateral dimension, forming a disordered arrangement of tiny graphite-like structural units. The investigations by Koczwara et al⁶⁵ were performed on samples prepared with the same procedure as the samples investigated in this work, with activation times of 0, 30, 120 and even 240 minutes, and can therefore directly compared. X-ray diffraction measurements revealed that with increasing activation time the mean stack height and in-plane crystallite size decreases, which was related to the formation of micropores in the carbon nanowires due to activation.

In this study the adsorption induced deformation of three monolithic, hierarchically nanoporous carbon materials was investigated with in-situ adsorption Small Angle Scattering and in-situ adsorption dilatometry. The samples differed by activation time: CN denotes the as-prepared sample, C30 the 30 minutes activated and C120 the 120 minutes activated sample respectively.

2.3 Biological Materials: Human Root Dentin

The human root dentin samples in this study were supplied by Paul Zaslansky from the Julius Wolff Institute, Charité, Berlin, in the form of 200 μm thick slices. The structure of root dentin is hierarchical and shares great similarity to bone. Its structure and composition is considerably more complex compared to the synthesized materials described above. Root dentin is a composite material with mean volume fractions of ~33 % organic matter, ~45 % hydroxylapatite and ~22 % water.^{45,66,67} Although it consists of a mixture of soft biological matter, water and mineral phases, its mechanical properties are comparable to engineering materials. Average mechanical properties are a Young’s modulus of 20 GPa, a tensile strength of 50 MPa and fracture toughness in the range of 1.5 to 3.5 $MPa\sqrt{m}$ ^{45,68}. Its combination of tensile strength and fracture toughness are similar to engineering polymers, whereas its strength and E-modulus are reminiscent of technical ceramics⁶⁹. These properties have drawn considerable interest due to combination of mechanical properties and the comparatively low mass density of $1.5 g/cm^3$ ⁷⁰. Engineering ceramics with comparable strength and fracture toughness have a typical mass density between 2 and 6 g/cm^3 ⁷¹, while engineering polymers usually exhibit mass densities of approximately 1 – 2 g/cm^3 . The origin of this favorable combination of

mechanical properties and low mass density is the composite nature of root dentin reaching over several levels of hierarchy.

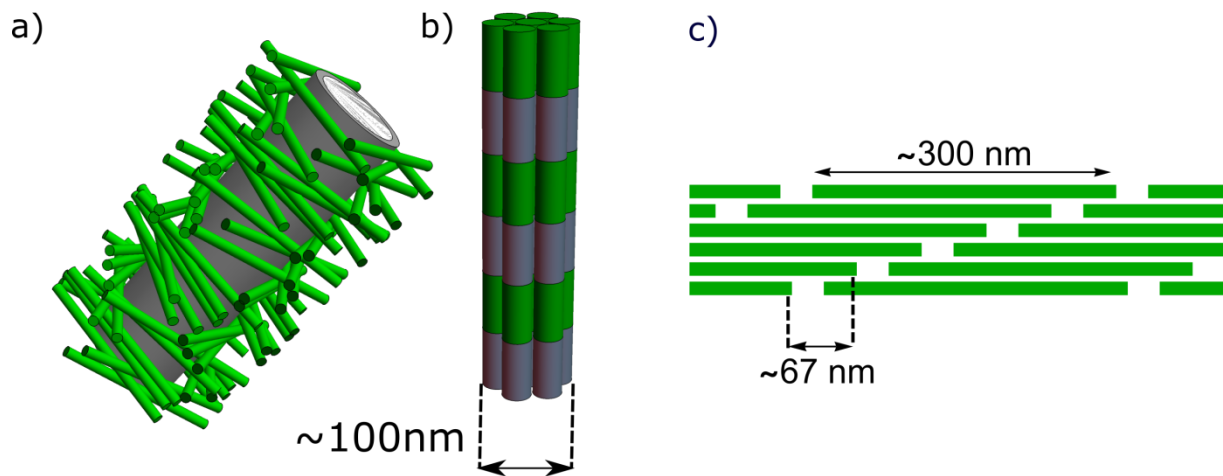


Figure 3: The microstructure of human root dentin is depicted, where in a) a microtubule with the surrounding peritubular dentin in gray and the tangential, relatively disordered intertubular dentin fibril as green cylinders are shown (after ⁷²). In b) a singular fibril with a mean diameter of around 100 nm is depicted with the green and gray areas corresponding to mineralized gap and non-mineralized overlap region. A detailed sketch of the arrangement of collagen in a fibril is provided in c), where the stacked order of the collagen molecules, pictured as green bars, are ordered in the Hodge-Petruska scheme⁷³.

Root dentin is situated between the root of the tooth and the enamel and cementum, which provide mechanical stability and protection through mastication. So-called microtubuli with a diameter of around one μm run diametral from the root to enamel coating of the tooth. The microtubuli, as shown in **Figure 3** a), are embedded in a matrix of intertubular dentin and coated with peritubular dentin. In contrast to the highly mineralized peritubular dentin which does not contain collagen, the intertubular dentin is built up from incremental layers of mineralized type I collagen fibrils normal to the long axis of the tubules. The plate-like mineral crystallites are around 2 to 5 nm thick and 60 nm long⁷⁴ and are situated either on the surface or are embedded in the collagen fibril along its long axis. Demineralization of intertubular dentin reveals a quite dense network of type I collagen fibrils, which is coated with so called non-collagenous proteins.

Peritubular dentin on the other hand exhibits mineral crystalites with a length of 36, breadth of 25 and thickness of 9.75 nm⁷⁴, forming a ring around the tubules. The detailed structure of peritubular dentin is revealed upon demineralization which reveals all organic phases left. These phases are primarily non-collagenous proteins and phospholipids forming a network among the mineral crystalites.⁷⁴

The mineralized collagen fibrils consist of a special arrangement of singular collagen molecules, which are arranged in the so-called Hodge-Petruska scheme⁷³ pictured in **Figure 3** b) and c). The length of a collagen molecule is around 300 nm, whereas the axial period of the collagen fiber is 67 nm, which is not an integer multiple. X-ray scattering measurements confirm that some sort of order exists along the long axis of the collagen fibrils. Hence, Hodge and Petruska⁷³ proposed a regular, staggered arrangement, where a gap region is introduced which allows for ordered, regular stacking. Every sixth collagen molecule is arranged perfectly parallel in lateral direction, which leaves a gap region of around 35 nm relative to its direct neighbors in axial direction as shown in **Figure 3** c).

Within this gap region, but not exclusively, mineral platelets of around 30 nm length⁷⁵, 35 nm breadth⁷⁶ and 2.5 to 3.5 nm thickness⁷⁷ are situated along with Glycosaminoglycans. These latter molecules are highly polar and consequently attract primarily cations and water⁷⁸.

Because water constitutes a considerable fraction of human root dentin and is mostly situated in the organic matter, it's role in the structure-property relationship could be of high interest. In contrast to adsorption in the silica and carbon materials introduced above, which is a surface process, volumetric uptake of water in the biological matter of human root dentin is the governing process. Consequently, in-situ water absorption small angle x-ray scattering of human root dentin could be valuable to shed light on structure-property relationships and distribution of water.

3 Theoretical Basics

In this section of this thesis a review of the theoretical basics of the concepts applied in this work is presented. First, the basics of small angle scattering are summarized, with a more in-depth discussion of the modelling of hierarchically macro-, meso- and microporous materials. Then a short introduction into physisorption and the modelling of adsorption and desorption of non-polar adsorbates in cylindrical mesopores by macroscopic thermodynamics is given. A different approach, based on the calculus of variation, is introduced and applied to adsorption in CMK-3 type materials. Further, the equivalence of the variational approach to traditional methods demonstrated on the example of cylindrical mesopores is shown. Finally, the theoretical and practical treatment of the concept of the disjoining pressure is introduced.

3.1 Small Angle Scattering

In this chapter a brief review the basics of small angle scattering (SAS) is provided. In particular, the SAS model of hierarchically porous silica is discussed and the Debye scattering formula for two dimensional arrangements is derived.

In contrast to most other techniques used to characterize nanometer sized objects, like transmission and scanning electron microscopy, SAS allows to measure a statistically significant number of scattering objects at once nondestructively. SAS also lends itself to in-situ experiments, of which in particular in-situ sorption experiments are of interest in this work. A general drawback of SAS is however its indirect nature, meaning we only get information on the shape, size, order or distribution of density heterogeneities in reciprocal space. Drawing conclusions from indirect information is usually more challenging than from direct methods. For instance, one needs to apply models based on considerable previous knowledge about the sample at hand to analyze data or collect additional information from other experimental techniques such as sorption analysis. Therefore, although SAS is a powerful technique which enables unique experiments, complementary methods are usually needed.

3.1.1 Basics of Small Angle Scattering

The term “Scattering” describes the elastic and inelastic interaction of quantum particles, i.e. x-Rays or neutrons, with matter. This thesis is only concerned with elastic scattering, which greatly simplifies the theoretical treatment. Due to the conservation of energy and large number of interaction events of the scattered beam, it can be accurately described by classical electrodynamics. In this thesis we are exclusively concerned with the scattering of parallel beams at low angles in transmission geometry, which is called Small Angle X-Ray or Neutron Scattering (SAXS and SANS respectively).

If a neutron or x-ray interacts with an object, its probability to interact with it is given by the interaction cross section σ_T . Usually, the overall total interaction is divided into several parts corresponding to the kind of interaction, which reads as⁷⁹:

$$\sigma_T = \sigma_{co} + \sigma_{inco} + \sigma_{abs} , \quad (3.0)$$

with σ_{co} and σ_{inco} denoting the coherent and incoherent scattering cross section and with σ_{abs} denoting the absorption cross section. Every single contribution is handled like a classical scattering cross section and can be deduced from an appropriate scattering length density (b_{co} and b_{inco}) or absorption length (b_{abs}) by:

$$\sigma_i = 4\pi b_i^2, \quad (3.1)$$

where i denotes the coherent, incoherent or absorption cross sections. The coherent and incoherent scattering cross section contribute directly to the scattering pattern, with their distinction being that the incoherent contribution scatters isotropically over the solid angle 4π and coherent scattering shows an angular dependence. From coherent scattering the distribution of atoms in a sample is obtained, whereas incoherent scattering gives information on single atom dynamics. On the other hand, the absorption cross section does not contribute to the elastic scattering and reduces the number of transmitted x-Rays/neutrons.

It is important to distinguish between the scattering cross sections in neutron and x-ray scattering experiments. Because x-rays interact with the electrons present in the material, the scattering cross section is directly proportional to the square of the elemental number and the materials density⁸⁰. In the case of neutrons, the interaction is defined by the properties of the nucleus, which is not trivially related to the atomic number of the element⁷⁹. This influences the interaction in as so far, that certain elements such as hydrogen exhibit negative scattering length densities, with it's isotope deuterium having a positive scattering length density. This allows for the design of experiments where certain phases, such as deuterated water at a certain mixing ratio, don't scatter coherently.

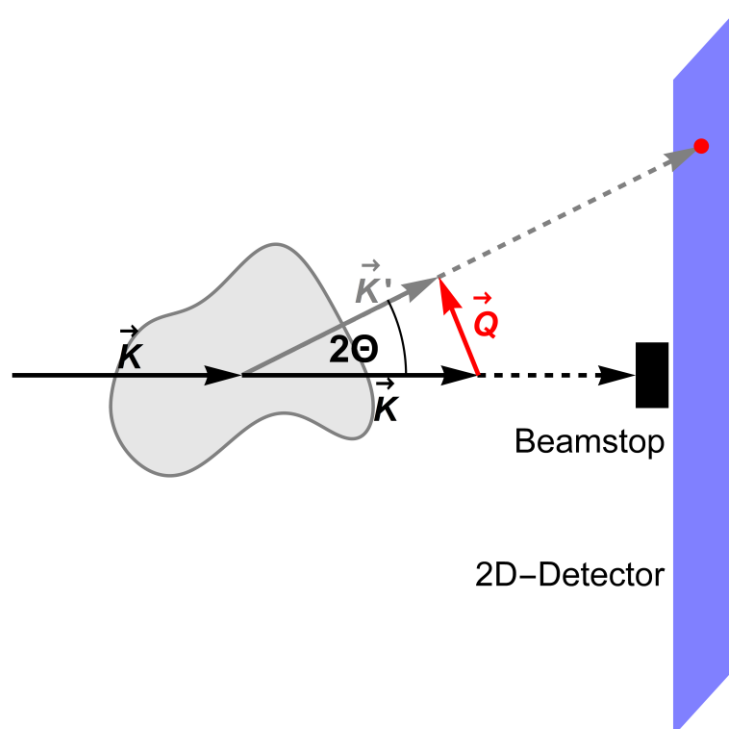


Figure 4: A sketch of a typical small angle scattering experiment is shown. The incoming beam is denoted by \vec{K} , while the scattered beam is \vec{K}' . The difference vector between transmitted and scattered beam is \vec{Q} , which results in a signal on the detector signified by the red dot.

A sketch of the geometry encountered in a typical small angle scattering experiment is shown in **Figure 4**. Per definition, the scattering angle is defined as the angle between the scattered and the incoming beam. Under the assumption of energy conservation, the momentum transfer vector Q can be deduced from **Figure 4**. It reads as⁸⁰:

$$Q = K' - K \quad (3.2)$$

where K and K' denote the incident and scattered wave vector. Alternatively, the momentum transfer vector Q is called the scattering vector in scattering experiments. Because elastic scattering is assumed, $|K| = |K'| = 2\pi / \lambda$, which gives for the length of the scattering vector as $|Q| = q = 4\pi \sin \theta / \lambda$ where θ denotes half of the scattering angle 2θ . In the case of scattering from an isotropic sample, the magnitude of the scattering vector q is also denoted as 'scattering vector' (which will be adapted below).

The total number of scattered x-rays or neutrons is usually set into relation to the illuminated sample volume and is denoted as the macroscopic scattering cross section Σ_{SAS} and can be computed if one knows the chemical composition and mass density of the sample. Alternatively, it is defined by the differential cross section per solid angle $d\Sigma_{SAS}/d\Omega$ with the unit $cm^{-1}sr^{-1}$. By defining the single scattered differential scattering cross section as:

$$I_1(Q) = \frac{d\Sigma_{SAS}}{d\Omega},$$

the macroscopic scattering cross section Σ_{SAS} can be obtained by integration of $I_1(Q)$ over the solid angle $d\Omega$. For an isotropic pattern, the scattering cross section per sample volume is then defined as the integral over the total momentum transfer q ⁸¹:

$$\Sigma_{SAS} = \int_{\Omega} I_1(Q) d\Omega = 2\pi \int_0^{\pi} \sin(\theta) I_1(q) d\theta = \frac{\lambda^2}{2\pi} \int_0^{4\pi/\lambda} q I_1(q) dq, \quad (3.3)$$

with λ being the wavelength of the incident and scattered beam and $I_1(q)$ being the measured, isotropic, single scattered intensity in units of $cm^{-1}sr^{-1}$. All discussions from here on out are related to isotropically scattering samples and necessitate that no multiple scattering occurs. Consequently, the measured, single scattered intensity $I_1(q)$ is simply denoted as $I(q)$.

As mentioned before, the differential cross section $d\Sigma_{SAS}/d\Omega$ is a function of the magnitude of the reciprocal space vector q . This angular dependence is related to the existence of different, well defined and homogeneous phases inside the illuminated sample volume with different scattering cross sections⁸⁰. Otherwise, no small angle scattering pattern would be observable in experiment. The coherent scattering cross section is responsible for the angular dependence observed in scattering patterns, whereas the incoherent scattering contribution gives a constant background⁸¹.

The measured intensity $I(q)$ is linked to the square of the scattering amplitude $F(q)$, which is obtained from the Fourier transform of the coherent scattering length density $b_{co}(r)$ of the sample:

$$F(q) \propto \int e^{-iqR} b_{co}(R) dR. \quad (3.4)$$

Generally, the scattering amplitude a complex function, although it only takes real values for the simple form factors considered in this thesis. The scattering amplitude alone usually does not determine the measured intensity. Only in dilute systems where no distance correlation between scatterers exists, the square of equation 3.2 is directly proportional to the measured intensity. If the scatterers are arranged in short- or long-range order, additional oscillations and/or peaks can be observed. Mathematically, this is represented by a convolution of the form factor squared $F^*(q)F(q)(= |F(q)|^2)$ with a so-called structure factor $S(q)$. In the case of isotropic, fairly homogeneous samples (variance $\sigma_{Size}^2 < 0.1$), this convolution operation reduces to a simple multiplication:

$$I(q) \propto |F(q)|^2 S(q). \quad (3.5)$$

The structure factor $S(q)$ can be obtained by means of Fourier transform of the real space distance distribution of scatterers, which is sometimes possible analytically⁸⁰. Following the definition given above, the structure factor for one species of scatterers in three dimensions can be calculated with:

$$S(q) = 1 + 4\pi \int_0^\infty (g(r) - 1) \frac{\sin(qr)}{qr} r^2 dr, \quad (3.6)$$

where $g(r)$ is the pair correlation function of the scatterers. Physically, the first term on the right-hand side, the additive factor 1, in equation 3.6 ensures that the scattering contribution $|F(q)|^2$ by individual scatterers is accounted for, whereas the second part describes the effect of their distance correlation. This additive property in equation 3.6 can be exploited in multiple ways to extract information from scattering patterns, as discussed below.

There are further inherent physical properties of small angle scattering which are valuable for analyzing scattering patterns, even if no modelling of the data is possible. One of these highly important properties is the second moment of the measured intensity \tilde{I} , also referred to as integrated intensity, and it describes the total overall scattered intensity:

$$\tilde{I} = \int_0^\infty I(q) q^2 dq. \quad (3.7)$$

Equation 3.7 can also be expressed by the difference in scattering length density to the mean scattering length density and the phase fractions within the sample⁸⁰. It is defined as:

$$\tilde{I} = 2\pi^2 \sum_{i=1}^k \phi_i (b_i - \bar{b}) \quad (3.8)$$

with ϕ_k being the phase volume fraction and b_k the scattering length density of the k th component of the sample. For two-phase systems, this can be highly simplified if one applies the facts that $\sum \phi_k = 1$ and that $\phi_k = V_k/V_{Total}$, which leads to:

$$\tilde{I} = 2\pi^2 (b_1 - b_2)^2 \phi_1 (1 - \phi_1). \quad (3.9)$$

Because \tilde{I} is only dependent on the difference of the scattering length densities and the respective volume fractions, it is independent of the geometry and distribution of any of the phases present in the sample. Consequently, it is also referred to as an integral parameter.

At large q , small angle scattering exhibits similar behavior as observed in other examples of scattering, such as Rutherford scattering⁸², in which the scattered intensity declines proportionally to q^{-4} . In small angle scattering this behavior originates from surface scattering of the sample and can be described for a sample with two phases by⁸⁰:

$$I(q) = [2\pi(b_1 - b_2)^2 A q^{-4}]_{q \rightarrow \infty} + C_{Laue}. \quad (3.10)$$

Here, b_1 and b_2 are the scattering length densities of the respective phases, A is the total surface between both phases present and C_{Laue} denotes the incoherent Laue scattering⁸³ of the atoms in the sample. In measurements the parameters b_1 , b_2 or surface S in equation 3.10 are not known, which is why the numerator in Equation 3.10 is abbreviated by the so-called Porod constant $P = 2\pi(b_1 - b_2)^2 A$. It can easily be obtained from a measured scattering pattern by multiplying the intensity by q^4 and plotting against q^4 . In **Figure 5** a Porod plot of a human root dentin measurement is shown, where the slope of the pattern at values larger than 10 nm^{-4} is fitted by a straight red line. Following equation 3.10, the slope of the red line represent the incoherent Laue scattering C_{Laue} and the intercept of the red line with the ordinate gives the Porod constant P . By subtraction of the incoherent Laue scattering, the q^{-4} behavior of the scattering pattern is retained. This ideal behavior is not observed for all surfaces, as fractal surfaces can show power law behaviors with the exponent varying from 3 to 4.⁸⁴

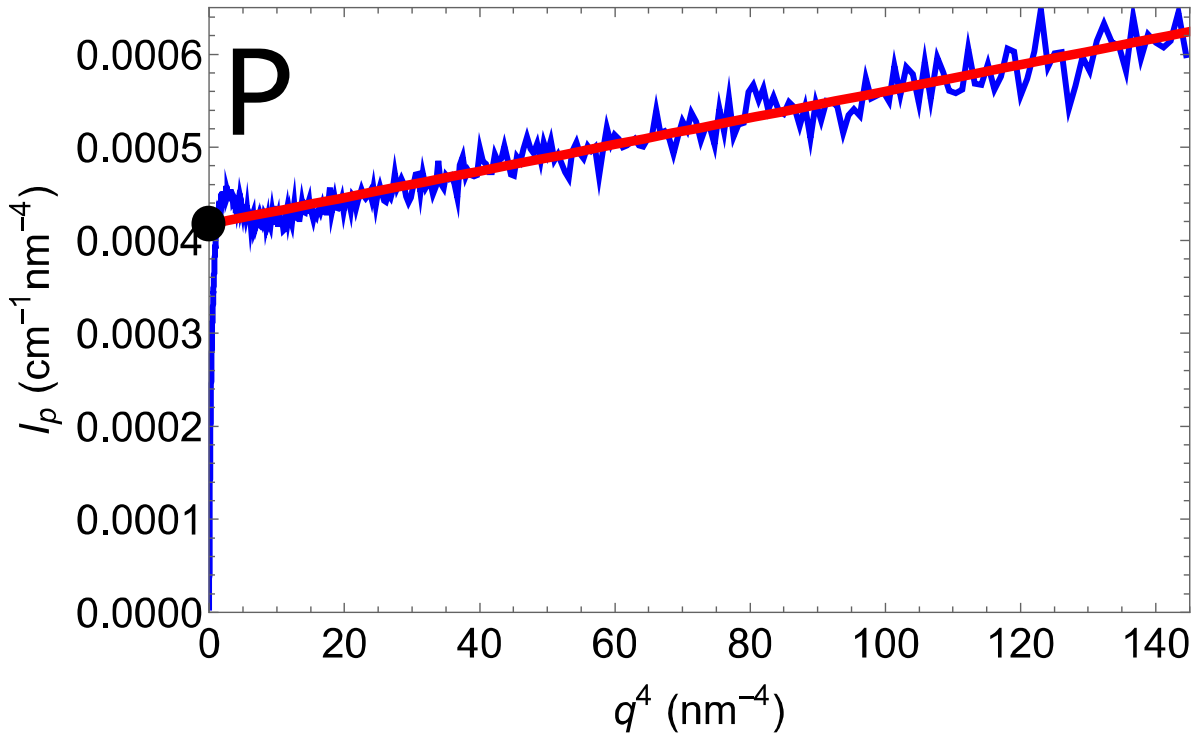


Figure 5: A Porod plot of a measured patterns is shown, where the red line indicates the linear fit of the high q part of the scattering pattern, which exhibits a slope greater than 0 due to Laue scattering. The black dot depicts the intercept between the ordinate and the red line, which determines the P -parameter.

Once the integrated intensity \tilde{I} and the total interface S are determined, the relation between both results in an average chord-length:

$$T = 4 \frac{\phi(1 - \phi)}{S}. \quad (3.11)$$

This factor, called the T -parameter, represents the average chord length of a two-phase material. To determine the average chord length of the components of a two-phase system, the T -parameter can be split into^{85,86}:

$$\frac{1}{T} = \frac{1}{l_1} + \frac{1}{l_2} = \frac{1}{\phi l_1} = \frac{1}{(1-\phi)l_2},$$

with l_1 and l_2 being the chord lengths of the respective phases. This directly implies that

$$\frac{1}{l_1} = \frac{\phi}{T} = \frac{S}{4(1-\phi)} \text{ and } \frac{1}{l_2} = \frac{1-\phi}{T} = \frac{S}{4\phi}.$$

By plugging these relations into the original definition

$$\frac{1}{T} = \frac{1}{l_1} + \frac{1}{l_2} = \frac{S}{4(1-\phi)} + \frac{S}{4\phi} = \frac{S}{4} \left(\frac{1}{1-\phi} + \frac{1}{\phi} \right) = \frac{S(\phi + 1 - \phi)}{4(1-\phi)\phi}$$

one arrives at:

$$\frac{1}{T} = \frac{1}{l_1} + \frac{1}{l_2} = \frac{S}{4\phi} + \frac{S}{4(1-\phi)} = \frac{S}{4\phi(1-\phi)}. \quad (3.12)$$

The great advantage of the T -parameter is its independence on shape and arrangement of the phases, which is often applied to random media such as microporous materials⁸⁷. It is also central in the study of biological materials, which are usually complicated composite materials, such as bone⁸⁵ or human root dentin⁸⁸.

3.1.2 Structural Model of Mineralized Biological Tissue

In the case of mineralized biological tissue, such as bone⁸⁵ and human root dentin⁴⁵, small angle scattering has been applied successfully in determining their meso- and nanoscale structure. Because water and biological tissue both have a relatively low x-ray scattering length density compared to the mineral platelets present, the former two phases are viewed as a homogeneous mixture.

Because only 2 phases are considered, the T -parameter can be applied to determine the chord length of the mineral crystallites. One can relate the surface of a rectangular crystalline platelet to its dimensions by:

$$T = 2 \frac{1-\phi}{\frac{1}{a} + \frac{1}{b} + \frac{1}{c}}, \quad (3.13)$$

with a being the thickness and b and c being the height and breadth. Because it can be assumed that $a \ll b, c$, the T -parameter is essentially directly proportional to the mineral plate thickness a .

In the case of bone and root dentin, a more sophisticated model, called the stack-of-cards model, was introduced by Fratzl et al⁸⁵, which models the scattering by bone. Its reasoning is based on the nanostructure of bone, where mineral platelets are situated inside the gap-regions of the aligned collagen molecules building up mineralized fibrils (see **Figure 3 c**). These mineral platelets can be thought of a succession of parallel 'cards' with biological molecules wedged in between them, which exhibit a characteristic scattering function. A

version of this model employs a rescaled function where a dimensionless parameter $x = qT$ is introduced:

$$G(x) = \frac{x^2 I\left(\frac{x}{T}\right)}{\tilde{T}^3}. \quad (3.14)$$

By applying a randomized one-dimensional two-phase model, where two phases ϕ_1 and ϕ_2 represented by quasi-infinite planes of randomized thickness t_1 and t_2 alternate, the nanostructure of bone is accurately modelled. Several situations pertaining to lateral correlation and distribution of plate-thicknesses can be described⁸⁵ and solved analytically. If wide thickness distributions but strong positional correlations are prerequisite, one gets:

$$G(x) = \frac{4}{\pi} \frac{x^2 + (\alpha - 1)(\alpha^2 - \beta^2)}{x^4 + 2(\alpha^2 + \beta^2)x^2 + (\alpha^2 - \beta^2)}, \quad (3.15)$$

where α and β must be real. The first parameter α describes the damping of the underlying correlation function and the second parameter β is closely related to the distance Δ between successive plates⁸⁵:

$$\Delta = \frac{2\pi T}{\beta}. \quad (3.16)$$

In relation to equation 3.12, the mean chord lengths, $l_1 (= \phi\Delta)$ and $l_2 (= (1 - \phi)\Delta)$, of both phases can then be determined if the phase fractions are known.

3.1.3 Hierarchical Model of Macro-, Meso- and Microporous Silica

The small angle scattering of the silica materials outlined in chapter 2.1 can effectively be modelled. Because no incoherent scattering or absorption of x-Ray/neutrons is considered here, all scattering lengths densities b are coherent. A thorough model of SBA 15¹⁵, a material with similar mesoscopic structure to the silica materials analyzed in this thesis, was developed by Gommers⁸⁹. It describes the small angle scattering pattern $I(q)$ of SBA-15 as the sum of intensities of the macro-, meso- and microporous hierarchical levels:

$$\begin{aligned} I(q) = & \left((1 - \phi_m)(1 - \phi_\mu) b_{SiO_2} \right)^2 \frac{2\pi A}{q^4} + \\ & + n \left(b_{SiO_2} (1 - \phi_\mu) \right)^2 \frac{\pi L}{q} S(q) F(q)^2 + \\ & + V_{grain} (2\pi)^3 b_{SiO_2}^2 (1 - \phi_m) \phi_\mu (1 - \phi_\mu) r_\mu^3 f_\mu(qr_\mu)^2. \end{aligned} \quad (3.17)$$

In the first term, denoting the surface scattering (see equation 3.10) of SBA-15 grain (see **Figure 6 a**), b_{SiO_2} is the scattering length density of bulk silica, reduced by the mesoporous and microporous volume fractions ϕ_m and ϕ_μ , and A is the grains surface. The second term describes the scattering of n mesopores (see **Figure 6 b**) in a grain of SBA-15 with length L , where $F(q)$ is the form factor of individual mesopores shown in **Figure 6 d**) and $S(q)$ their structure factor. The last term describes the scattering of the disordered,

spherical mesopores as depicted in **Figure 6 c)** of mean radius r_μ with the normalized form factor $f_\mu(qr_\mu)$.

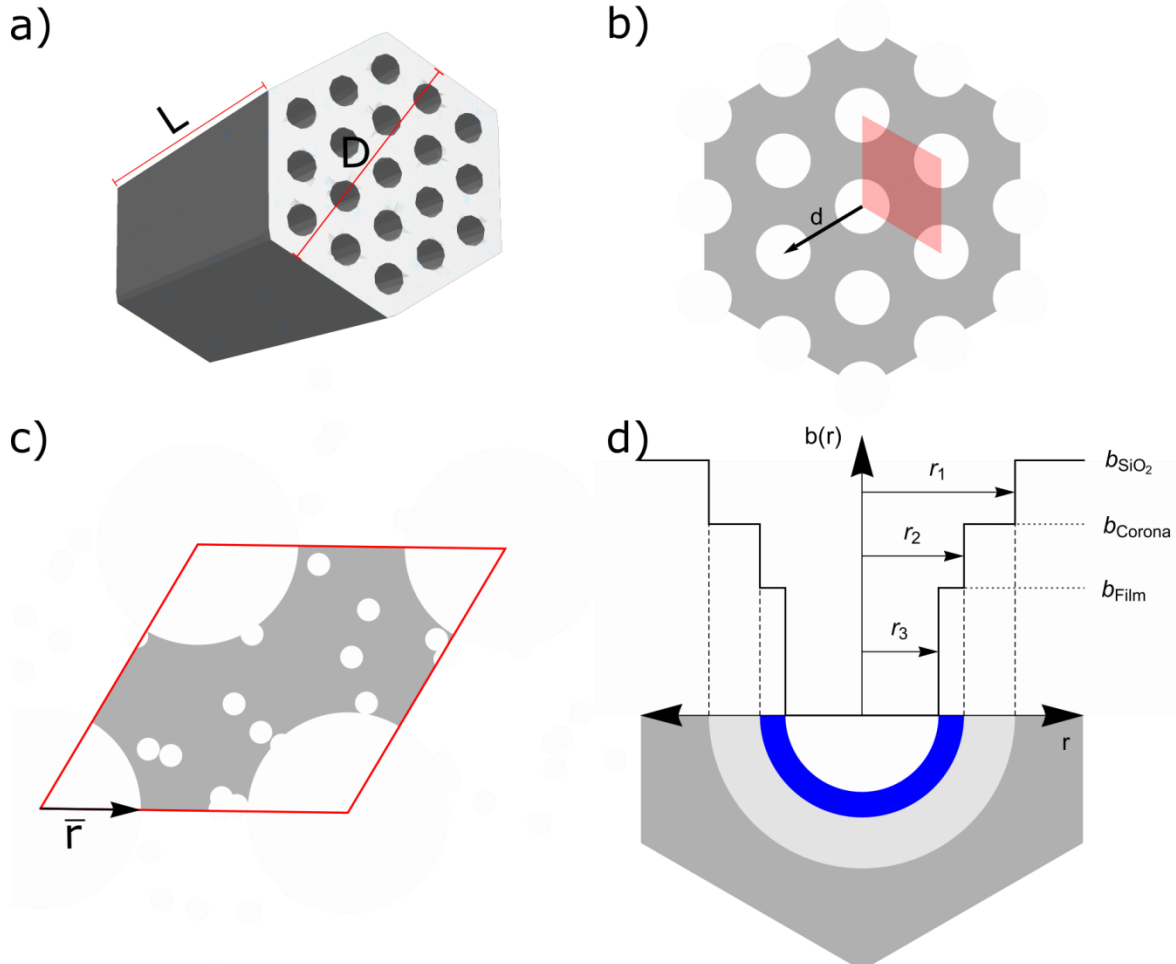


Figure 6: a) A sketch of a model grain/strut with diameter D and length L of the monolithic, hierarchically porous silica material is shown. In b) the hexagonal arrangement of the mesopores in the model of Gommers et al and Zickler et al, with the unitcell highlighted by a red rhomboid and the mesopore-distance d shown. The highlighted unitcell is shown in c), with mesopores of mean radius \bar{r} and micropores depicted as small, white disks. A detailed view of the pore model applied by Zickler et al with several scattering length density levels $b(r)$ and the associated radii of the phases is shown in d), where the blue and light-gray half-circles correspond to the adsorbed liquid film and the mesoporous corona respectively.

The parameter M_{hk} denotes the number of mesopore centers on a circle of radius $d_{10} \sqrt{h^2 + k^2 + hk}$ drawn around a single pore and $\delta(q - q_{hk})$ is the Dirac-delta function with q_{hk} being the scattering vector of a scattering peak with Miller indices hk . This scattering vector is defined as

$$q_{hk} = \frac{2\pi}{d_{hk}} = \frac{4\pi}{d\sqrt{3}} \sqrt{h^2 + k^2 + hk}, \quad (3.19)$$

with d being the lattice parameter of the hexagonal mesopore lattice and d_{hk} is the interplanar distance of the associated plane with Miller indices h and k .

Of note for the microporous intensity contribution is the prefactor to the form-factor $f_\mu(q)^2$, which describes the integrated intensity of microporous in a SBA-15 grain. Therefore, the form-factor must fulfill the following normalization relation⁸⁹:

$$\frac{1}{C} \int_0^\infty 4\pi q^2 f_\mu(q r_\mu)^2 dq = 1 . \quad (3.20)$$

For instance, if one chooses to implement a form factor describing spherical pores⁸⁰, the normalization constant C from equation 3.20 can be conveniently calculated analytically, giving a value of 6π .

An earlier approach to model analyze and model in-situ physisorption in cylindrical mesopores in SBA-15 was thoroughly implemented by Zickler et. al⁹⁰ (see **Figure 6 d**). In contrast to the model implemented by Gommès et al⁸⁹, only the Bragg peaks of the scattering pattern of SBA-15 were utilized. Because the scattering pattern can be viewed as a summation of the distinct macro-, meso- and microporous contributions, the influence of the coherent scattering can be well separated if one considers equation 3.6.

The scattering length densities **Figure 6 d**) are assigned to the silica pore wall, a microporous silica corona lining the mesopore wall, a liquid film on the corona and an empty void. The form factor utilized can be interpreted as a series of hollow cylinders with different scattering length densities stuck into a cylindrical cut-out in an infinite silica plane, which by application of equation 3.4 results in⁹⁰:

$$F(q) = 2 b_{SiO_2} \left((\alpha - 1) r_1^2 \frac{J_1(q r_1)}{q r_1} + (\beta - \alpha) r_2^2 \frac{J_1(q r_2)}{q r_2} - \beta r_3^2 \frac{J_1(q r_3)}{q r_3} \right), \quad (3.21)$$

with r_1, r_2 and r_3 being the mesopore, corona and liquid film distance-to-center and α ($= b_{Corona}/b_{SiO_2}$) and β ($= b_{film}/b_{SiO_2}$) being the relative scattering length densities of the corona and liquid film respectively. The expressions $2 J_1(q r_i)/q r_i$ denotes the form factor of an infinitely long cylinder, with J_1 being the Bessel function of the first kind and first order. With this form factor the integrated intensities of the Bragg peaks of the mesopore lattice resolved by a small angle scattering experiment can be fitted with the following formula⁹¹:

$$Min \left(\sum_{hk} (\tilde{I}_{hk} - c^* M_{hk} F(q)^2)^2 \right). \quad (3.22)$$

Here, \tilde{I}_{hk} is the integrated intensity of the associated peak and c is a constant which scales the model to the measurements. Ideally, if one chooses to fit equation 3.21 for multiple measurements at different relative pressures, c^* should remain constant because it should exclusively be related to the instrumental set-up, if the sample volume is not subject to big changes during experiment⁵⁹. In any case, the number of parameters retrieved, meaning the radii of the multi-step model and the associated relative densities, should not be greater than the number of peaks distinguishable in measurement. To remedy the situation if only a limited number of peaks is distinguishable in experiment and one seeks to track the evolution of the parameters of equation 3.21 as a function of relative pressure, one can fit the empty sample state and keep several parameters, in

general the scaling parameter, the mesopore and corona radius, constant for higher relative pressures. To fit relative pressures where a mixture of states, say a liquid film present on the mesopore wall and filled mesopores, a simple way to achieve this is a linear combination of appropriate form-factors with assigned weight summing up to one:

$$F(q) = Y_m F(q)_{\text{film}} + (1 - Y_m)F(q)_{\text{filled}}, \quad (3.23)$$

with Y , ranging from 0 to 1, being the weight of the empty pores and β assigned appropriately.

From the hierarchical pore model⁸⁹ and from the pore model by Zickler⁹⁰, the volume fraction of the mesopores and consequently the silica pore walls can be estimated with:

$$\phi_{\text{meso}} = \frac{2\pi\bar{r}^2}{\sqrt{3}a^2}. \quad (3.24)$$

The radius in the equation above is either obtained directly from the hierarchical model by Gommès⁸⁹, which considers only a simple mesopore model with a singular radius, or from the multistep model of Zickler⁹⁰, where the resulting radius \bar{r} ($= \sqrt{r_1^2 + (1 - \alpha)(r_2^2 - r_1^2)}$) is a weighted mean of the mesopore and corona radius. Although fair enough agreement between small angle scattering and physisorption measurements was achieved^{90,92}, the result from this analysis can be influenced by the relatively undefined amount of micropores. Zickler et al have already considered that the corona region is neither exclusively micro- nor mesoporous and is probably best described by a corrugated, microporous silica wall⁹⁰. In an analysis of the filling of the sample as a function of relative pressure from in-situ sorption small angle x-ray scattering, Findenegg et al⁹³ have also observed that micropores are present in the mesopore walls and corona, which complicates the exact determination of the mesoporous and microporous volume fractions.

3.1.4 Filling Fractions obtained from the hierarchical Pore-Model

The scattering of the hierarchically nanoporous silica can also be exploited to yield the microporosity and the filling fraction of the sample as a function of relative pressure in in-situ SAXS experiments. At large values of the magnitude of the scattering vector q , the microporous contribution dominates the scattered intensity⁸⁹ and the scattering pattern is essentially determined by the last term of equation 3.17:

$$I_\mu = V_{\text{grain}}(2\pi)^3 b_{\text{SiO}_2}^2 (1 - \phi_m) \phi_\mu (1 - \phi_\mu) r_\mu^3 f_\mu (qr_\mu)^2. \quad (3.25)$$

If f_μ and V_{grain} don't change considerably during adsorption, the change in I_μ can be modelled by exchanging $\phi_\mu(1 - \phi_\mu)$ with a suitable three phase description of the integrated intensity:

$$I_\mu(q) \propto \left((b_{\text{SiO}_2} - b_{\text{Void}})^2 \phi_{\text{SiO}_2} \phi_{\text{Void}} + (b_{\text{SiO}_2} - b_{\text{H}_2\text{O}})^2 \phi_{\text{SiO}_2} \phi_{\text{H}_2\text{O}} + (b_{\text{H}_2\text{O}} - b_{\text{Void}})^2 \phi_{\text{H}_2\text{O}} \phi_{\text{Void}} \right), \quad (3.26)$$

where all contributions of volume fractions ϕ and scattering length densities b are denoted by their respective subscripts. Of note is the interdependence of all volume fractions at all relative pressures, which is guaranteed by

$$1 = \phi_{\text{SiO}_2} + \phi_{\text{Void}} + \phi_{\text{H}_2\text{O}}. \quad (3.27)$$

By assuming that ϕ_{Void} at a relative pressure of 0, denoted here with ϕ_{pore} , is equivalent to ϕ_{H_2O} at the maximum relative pressure being > 0.95 , a filled fraction of the pores $x(p/p_0)$ can be introduced, which results in:

$$1 - \phi_{SiO_2} = \phi_{pore},$$

$$\phi_{H_2O} \left(\frac{p}{p_0} \right) = (1 - \phi_{SiO_2}) x \left(\frac{p}{p_0} \right),$$

$$\phi_{Void} \left(\frac{p}{p_0} \right) = (1 - \phi_{SiO_2}) \left(1 - x \left(\frac{p}{p_0} \right) \right).$$

By setting the void scattering length density to $b_{Void} = 0$, equation 3.26 can now be written as

$$I_\mu \left(q, \frac{p}{p_0} \right) \propto b_{SiO_2}^2 \phi_{SiO_2} (1 - \phi_{SiO_2}) \left(1 - x \left(\frac{p}{p_0} \right) \right) + (b_{SiO_2} - b_{H_2O})^2 \phi_{SiO_2} (1 - \phi_{SiO_2}) x \left(\frac{p}{p_0} \right) + b_{H_2O}^2 \phi_{SiO_2}^2 x \left(\frac{p}{p_0} \right) \left(1 - x \left(\frac{p}{p_0} \right) \right), \quad (3.28)$$

which reduces to the expected factors of the integrated intensity of the empty and filled pores at relative pressures of $p/p_0 = 0$ ($\rightarrow x = 0$) and $p/p_0 \gtrsim 0.95$ ($\rightarrow x = 1$):

$$I_\mu \left(q, \frac{p}{p_0} = 0 \right) \propto b_{SiO_2}^2 \phi_{SiO_2} (1 - \phi_{SiO_2}),$$

$$I_\mu \left(q, \frac{p}{p_0} \gtrsim 0.95 \right) \propto (b_{SiO_2} - b_{H_2O})^2 \phi_{SiO_2} (1 - \phi_{SiO_2}).$$

Because the volume fractions ϕ_{H_2O} and ϕ_{Void} are not easy to distinguish from scattering patterns alone, it is more convenient to divide the scattering at large q as $I_\mu(p/p_0 = 0)/I_\mu(p/p_0)$. This relation can easily be evaluated without knowledge of the size and distribution of micropores. By fitting this relation between scattering patterns one arrives at

$$\frac{I_\mu \left(\frac{p}{p_0} = 0 \right)}{I_\mu \left(\frac{p}{p_0} \right)} = \frac{b_{SiO_2}^2 \phi_{SiO_2} (1 - \phi_{SiO_2})}{b_{SiO_2}^2 \phi_{SiO_2} (1 - \phi_{SiO_2}) \left(1 - x \left(\frac{p}{p_0} \right) \right) + (b_{SiO_2} - b_{H_2O})^2 \phi_{SiO_2} (1 - \phi_{SiO_2}) x \left(\frac{p}{p_0} \right) + b_{H_2O}^2 \phi_{SiO_2}^2 x \left(\frac{p}{p_0} \right) \left(1 - x \left(\frac{p}{p_0} \right) \right)}, \quad (3.29)$$

which can be reduced to

$$\frac{I_\mu \left(\frac{p}{p_0} = 0 \right)}{I_\mu \left(\frac{p}{p_0} \right)} = \frac{b_{SiO_2}^2}{b_{SiO_2}^2 \left(1 - x \left(\frac{p}{p_0} \right) \right) + (b_{SiO_2} - b_{H_2O})^2 x \left(\frac{p}{p_0} \right) + b_{H_2O}^2 \frac{\phi_{SiO_2}}{1 - \phi_{SiO_2}} x \left(\frac{p}{p_0} \right) \left(1 - x \left(\frac{p}{p_0} \right) \right)}. \quad (3.30)$$

By taking the relation of scattering patterns at large angles, the ration on the left side of equation 3.30 is defined and the filling fraction x can be determined as a function of relative pressure.

3.1.5 Determination of Integrated Peak Intensities from ordered Mesopores

To correctly obtain second moments of the measured peak intensities, a short primer is given here. To ease evaluation, it is convenient to do so in a so-called Kratky representation of the pattern, meaning squaring the measured intensity by the angle squared ($=I(q)q^2$). Then a linear background is subtracted from a SAS pattern in the manner shown in **Figure 7** and can then be integrated numerically to obtain the second moment of the scattered intensity (see inset of **Figure 7**). But because any error in numerical integration is only related to the integrating algorithm itself and not the data treated, it can be advantageous to go a different route.

First, the peak is fitted with a Pseudo-Voigt function, which is a linear combination of a Gaussian and Lorentzian function:

$$P_V(x) = h \left(m \frac{1}{1 + \left(\frac{q - q_{hk}}{\tau}\right)^2} + (1 - m) e^{-\frac{1}{2} \left(\frac{q - q_{hk}}{\sigma}\right)^2} \right), \quad (3.31)$$

where h is a scaling factor, m is the weight ranging from 0 to 1, q_{hk} is the exact position of the associated peak, τ is the halfwidth of the Lorentzian and σ is the variation of the Gaussian contribution. This conveniently allows to not only determine the exact peak position, but also serves as an easy way to calculate the area under the peak analytically. Because the area under a Lorentzian is technically infinite, we simply assume that the only useful part is determined by the q -values of the flanks and arrive at:

$$A_{P_v} = (2\pi)^{0.5} \sigma (m - 1) h + 2 \tau h m \text{ArcTan} \left(\frac{q_{right} - q_{left}}{\tau} \right), \quad (3.32)$$

with q_{right} and q_{left} are the positions of the peak flanks selected. $h(m - 1)$ and hm represent the scaled heights of the Gaussian and Lorentzian contributions, as both are written in equation 3.31 to have a maximum value of 1.

This and the fact that the peak area can be calculated analytically also allows for the determination of the error of the second moment of the peak intensity analytically by Gaussian error propagation:

$$A_{P_v, err} = \sqrt{\left(\frac{\delta A_{P_v}}{\delta m} \Delta m\right)^2 + \left(\frac{\delta A_{P_v}}{\delta \sigma} \Delta \sigma\right)^2 + \left(\frac{\delta A_{P_v}}{\delta \tau} \Delta \tau\right)^2 + \left(\frac{\delta A_{P_v}}{\delta A} \Delta A\right)^2}, \quad (3.33)$$

with Δ denoting the error obtained from the fitting function.

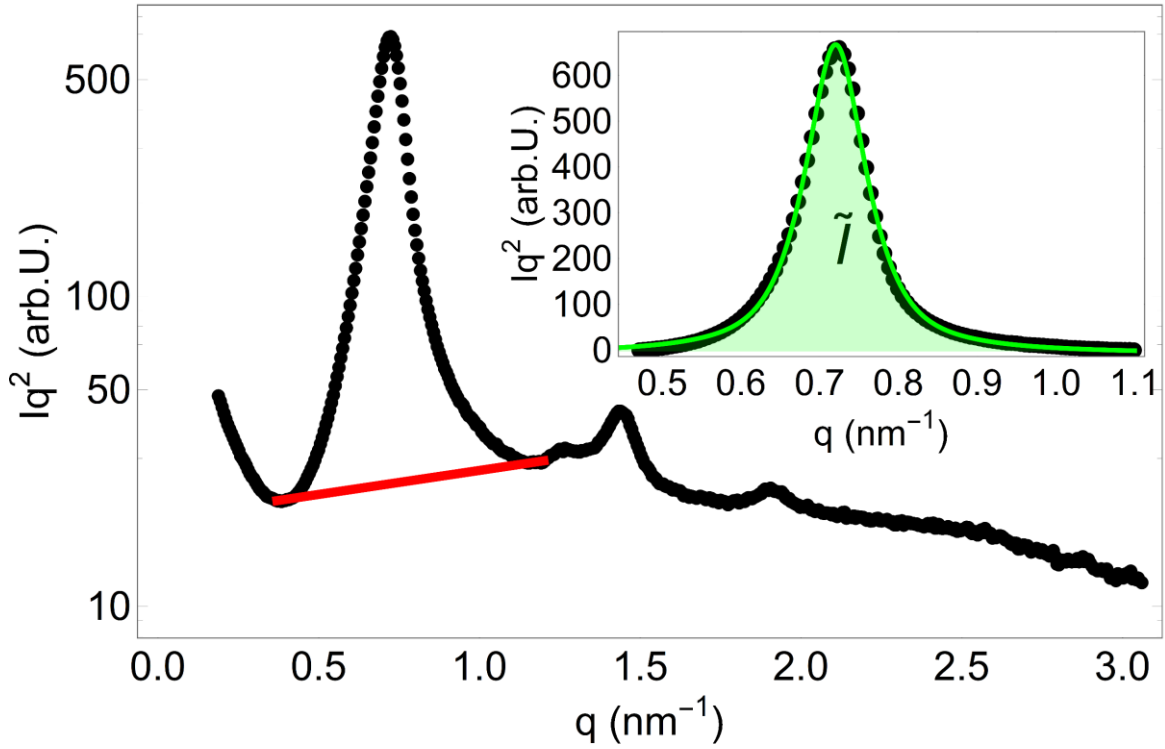


Figure 7: A sample SAXS pattern (black dots) of a calcined hierarchically nanoporous silica material in a Kratky-representation $I q^2$ is shown, with a linear background subtracted, signified with the red line, from the (10)-peak. The inset shows the subtracted peak, with the fit with a Pseudo-Voigt function (equation 3.31) shown as a green line. The area of the peak (green), is identical to the integrated intensity \tilde{I} (equation 3.7) of the peak and can be calculated analytically with equation 3.32.

The individual parts of the sum in the equation 3.33 are as follows:

$$\frac{\delta A_{P_v}}{\delta m} = (2\pi)^{0.5} h \sigma + h \tau \text{ArcTan} \left(\frac{q_{right} - q_{left}}{\tau} \right), \quad (3.34a)$$

$$\frac{\delta A_{P_v}}{\delta \sigma} = (2\pi)^{0.5} (m - 1) h, \quad (3.34b)$$

$$\frac{\delta A_{P_v}}{\delta \tau} = -h m \frac{q_{right} - q_{left}}{\tau \left(1 + \left(\frac{q_{right} - q_{left}}{\tau} \right)^2 \right)} + h m \text{ArcTan} \left(\frac{q_{right} - q_{left}}{\tau} \right), \quad (3.34c)$$

$$\frac{\delta A_{P_v}}{\delta h} = (2\pi)^{0.5} \sigma (m - 1) + 2 \tau m \text{ArcTan} \left(\frac{q_{right} - q_{left}}{\tau} \right). \quad (3.34d)$$

This relation can be used to calculate the error in integrated intensity from the Pseudo-Voigt function, which can be valuable if one performs form-factor fits as outlined in Zickler et al⁹⁰.

3.1.6 The Debye Scattering Formula for 3D and 2D

The hierarchical model by Gommès⁸⁹ introduced above is convenient to model materials which exhibit statistically random filling of mesopores, neglecting the existence of multilayer films on the mesopore walls. Simulation of the mesoporous scattering contribution with the Debye scattering equation⁹⁴ allows for more versatility in the modelling of hierarchically nanoporous materials. To derive the Debye scattering equation, the scattering amplitude of an assembly A of scatterers with individual form-factors $F(Q)_i$ is considered:

$$F(Q)_A = \sum_{i=1}^n F(Q)_i e^{-iQR_i},$$

where R_i is the position of the scatterer relative to the origin, giving the phase factor e^{-iQR_i} of the scatterer i in the assembly. The intensity of this assembly of scatterers is computed by multiplication of $F(Q)_A$ with its complex conjugate $F(Q)_A^*$:

$$I(Q) = F(Q)_A F(Q)_A^* = \sum_{j=1}^n \sum_{i=1}^n F(Q)_j F(Q)_i e^{-iQ(R_j - R_i)},$$

where $F(Q)_{i,j}$ denotes the scattering amplitude of the individual scatterers and $R_{i,j}$ the positional vectors of the respective scatterers i and j . In the case of isotropic scattering the form-factors are now a function of the magnitude q of the scattering vector Q . The exponential in the equation above needs to be spherically averaged, which is simplified if $Q(R_j - R_i)$ is substituted with $q r_{ji} \cos \gamma$, where r_{ji} denotes the scalar distance between scatterers and γ the angle of $(R_j - R_i)$ with respect to Q . After this manipulation the equation above reads as:

$$I(q) = \sum_{j=1}^n \sum_{i=1}^n F(q)_i F(q)_j \langle e^{-i q r_{ji} \cos \gamma} \rangle, \quad (3.35)$$

where the parenthesis denotes the spherical average. Calculating the spherical average in 3D leads to the so-called Debye scattering formula⁹⁴:

$$I(q) = \sum_{j=1}^n \sum_{i=1}^n F(q)_i F(q)_j \frac{\sin q r_{ji}}{q r_{ji}}, \quad (3.36)$$

which describes the isotropic scattering of any assembly of non-overlapping scatterers. If one applies atomic formfactors $f(q)_{i,j}$, this formula can describe the scattering by crystals if the atom positions align with a long-range ordered lattice⁹⁴.

The same procedure can be conducted to derive the scattering of (quasi-) 2-dimensional systems. An example of such a system would be an assembly of parallel, infinitely long, 2-D hexagonally ordered cylindrical pores as they are found in SBA-15 or the hierarchically nanoporous silica materials investigated in this theses. By applying radial averaging in a plane in equation 3.35, one arrives at

$$I(q) = \sum_{i=1}^n \sum_{j=1}^n F(q)_i F(q)_j J_0(q r_{ij}), \quad (3.37)$$

with J_0 being the Bessel function of the first kind and zeroth order. If this formula is applied, one obtains correct simulated scattering patterns for oriented 2-dimensionals system as shown later. Additionally, the scattering pattern obtained from this treatment perfectly describes the mesoporous contribution in equation 3.17 by application of equation 3.21.

3.1.7 Apparent Deformation

Strain isotherms can be obtained from in-situ physisorption measurements by different means⁹⁵, but the attention in this work is on small angle scattering. While dilatometry measures the expansion of a sample monolith, small angle scattering probes adsorption induced deformation on a nanometer level^{26,39}.

In the case of ordered mesoporous materials such as SBA-15, CMK-3 or the hierarchical silica and carbon materials in this thesis, adsorption induced deformation can be measured by exploitation of their ordered mesostructure. As in the discussion on the model of hierarchically porous materials, one can separate the (10) peak from the background scattering. The exact position of q_{10} can be obtained by fitting the peak with a function such as a Gaussian- or Pseudo-Voigt function if the peak is sufficiently symmetric³⁷, or by determining its center of mass²⁷. This needs to be done at every relative pressure at which a small angle scattering pattern is measured. The engineering strain is consequently defined by:

$$\varepsilon_{SAS} = \frac{d\left(\frac{p}{p_0}\right) - d\left(\frac{p}{p_0} = 0\right)}{d\left(\frac{p}{p_0} = 0\right)} = \frac{q\left(\frac{p}{p_0} = 0\right) - q\left(\frac{p}{p_0}\right)}{q\left(\frac{p}{p_0}\right)}, \quad (3.38)$$

where $q\left(\frac{p}{p_0} = 0\right)$ and $q\left(\frac{p}{p_0}\right)$ are the positions of the (10) peak in reciprocal space at a pressure of 0 and p respectively, whereas $d\left(\frac{p}{p_0} = 0\right)$ and $d\left(\frac{p}{p_0}\right)$ are the associated lattice parameters determined from q with equation 3.20.

In in-situ sorption small angle x-ray scattering strain measurements, Prass et al³⁸ have shown that the measured strain isotherm can exhibit artefacts which are not related to the actual strain induced in the mesoporous materials. In their work, adsorption induced deformation of several adsorbates on SBA-15 was measured in in-situ n-pentane, perfluoropentane and water adsorption synchrotron radiation experiments. In the relative pressure interval where capillary condensation was observed, the measured strain showed an artefact where the strain exhibited a positive spike close to the pressure of capillary condensation. The numerical and analytical analysis showed that it was due to the subsequent filling of the cylindrical mesopores at different relative pressures due to their distribution in diameter.

Later studies, where strain isotherms obtained from n-pentane in-situ sorption small angle x-ray scattering and dilatometry on a monolithic, hierarchically nanoporous silica material described in chapter 2.1 were performed³⁶, showed discrepancy between both obtained strain isotherms. Although they seem to behave similarly on a qualitative level, they are quantitatively different as they exhibit a difference in strain at a relative pressure of 0.95 by a factor of 2³⁶.

The apparent strain is consequently an effect which spans the entire range of relative pressures from 0 to 1 and is obviously closely related to the process of adsorption. Similarly, the concept developed by Prass and Mütter et al³⁸, it is highly likely that basic changes in fluid distribution, described by the theory discussed in the following section, are entirely responsible for the apparent strain effects observed in in-situ adsorption SAXS measurements.

3.2 Theoretical Basics on Macroscopic Thermodynamic Modelling of Physisorption

3.2.1 Short Introduction to Adsorption

Adsorption describes the adhesion of atoms, ions or molecules from a liquid, gaseous or dissolved phase on a surface⁹⁶. The reverse process, which means removal of adhered atoms, ions or molecules, is called desorption. Both processes are inherently surface phenomena and hence a consequence of interactions between atoms of the material constituting the surface, called adsorbent, and the adsorbed species, called adsorbate, adsorbing on it⁹⁷. Depending on the kind of interaction between adsorbate and adsorbent, physisorption⁹⁷, which is a reversible process, and chemisorption⁹⁸, an irreversible process, are distinguished. In this work, we are mainly concerned with the physisorption of highly polar (water) and non-polar (nitrogen, n-pentane) adsorbates. Absorption⁹⁸ on the other hand does not describe surface phenomenon, but usually involves the uptake of a certain atom, molecule or ion into a physical body. An example of absorption is the uptake of water in a biological material such as human root dentin.

Adsorption of an adsorbate on an adsorbent is usually measured at constant temperature and the uptake is characterized either by change of the sample weight or change of adsorbate volume as a function of the chemical potential ($\propto \log(p/p_0)$). The amount adsorbed as a function of relative pressure is typically set into relation to the dry weight of the adsorbent, which allows for the precise characterization of the pore space of the sample.

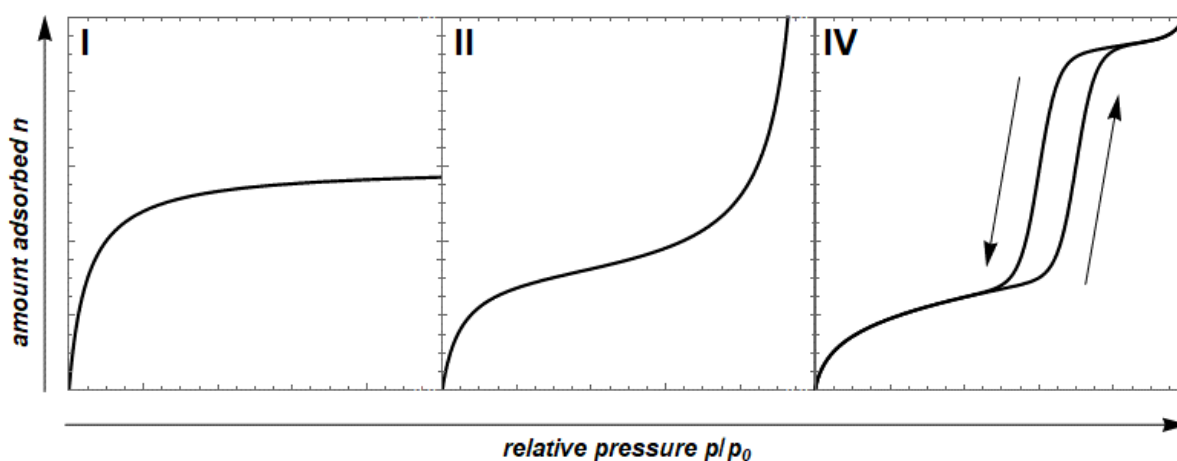


Figure 8: The relevant isotherm types in this work are shown. (adapted from Roquerol 2014)

To do so, one needs to analyze the shape of the recorded adsorption isotherms closely. In general, the shape of the isotherms is classified by the IUPAC⁵² and categorized into six different main classes. Of importance in this thesis are the isotherms I, II and IV (see **Figure 8**).

Sorption isotherms of class I as seen in **Figure 8** a) are typically observed in the adsorption in microporous materials or in chemisorption, which indicates a chemical reaction between the adsorbate and the surface of the adsorbent. To model such

isotherms the Langmuir⁸ or Freundlich⁹⁹ equation can be used. The Langmuir isotherm used later in this work is now introduced as:

$$\Phi_{Liquid} \left(\frac{p}{p_0} \right) = \phi_{\mu} \frac{b \frac{p}{p_0}}{b \frac{p}{p_0} + 1}, \quad (3.39)$$

where Φ_{Liquid} is the volume fraction of liquid in the micropores, ϕ_{μ} is the microporous volume fraction in the material and b is the interaction parameter. At a relative pressure of $1/b$ half of the micropores are filled as can be easily deduced from the equation above.

Isotherms of type II (see **Figure 8 b**) are typical of adsorption on non-porous or purely macroporous materials, where the increase in loading is only due to the existence and subsequent growth of a liquid layer. Typical models used to describe these types of isotherms are the Brunauer-Emmet-Teller (BET)⁹ equation for multilayer adsorption or the Frenkel-Halsey-Hill^{100,101} equation. These kinds of isotherms are also usually measured to determine thermodynamic parameters such as the disjoining pressure¹⁰² which are used to model the physisorption isotherms of materials exhibiting a more complex pore structure on the mesopore level.

Type IV isotherms, as depicted in **Figure 8 c**), are typical cases of materials exhibiting such a complex pore structure on the mesopore level. Typically, the sample associated with a type IV isotherm starts to fill by creation and subsequent growth of liquid layers on the mesopore walls with increasing relative pressure. Because a certain cost in energy is associated with the additional surface created by the liquid layer, it is energetically more favorable to change from a liquid layer to a different distribution of liquid or to fill the mesopore entirely after a certain relative pressure a distinct film thickness is reached as indicated by the upward tilted arrow in **Figure 8 c**). This is signified by the sharp increase in the amount adsorbed visible in **Figure 9**. The hysteresis shown is also characteristic of physisorption in mesoporous materials, although its origin is still not entirely clear today and different approaches are discussed^{11,12,103-105}.

3.2.2 Specific Pore Volumina

A sample nitrogen adsorption isotherm recorded on the silica material C-A is shown in **Figure 9**. The specific volume v_p in micro-/mesoporous materials at equilibrium vapor pressure is the sum of the specific micropore volume v_{μ} and specific mesopore volume v_m of the sample. From experiment it can be estimated by⁹⁷:

$$v_p = \frac{m_a}{\rho_a}, \quad (3.40)$$

where m_a is the specific mass adsorbed and ρ_a is the bulk density of the adsorbate. In the case of the sample isotherm in **Figure 9**, the specific pore volume of micro- and mesopores would be around $0.25 \text{ cm}^3/\text{g}$.

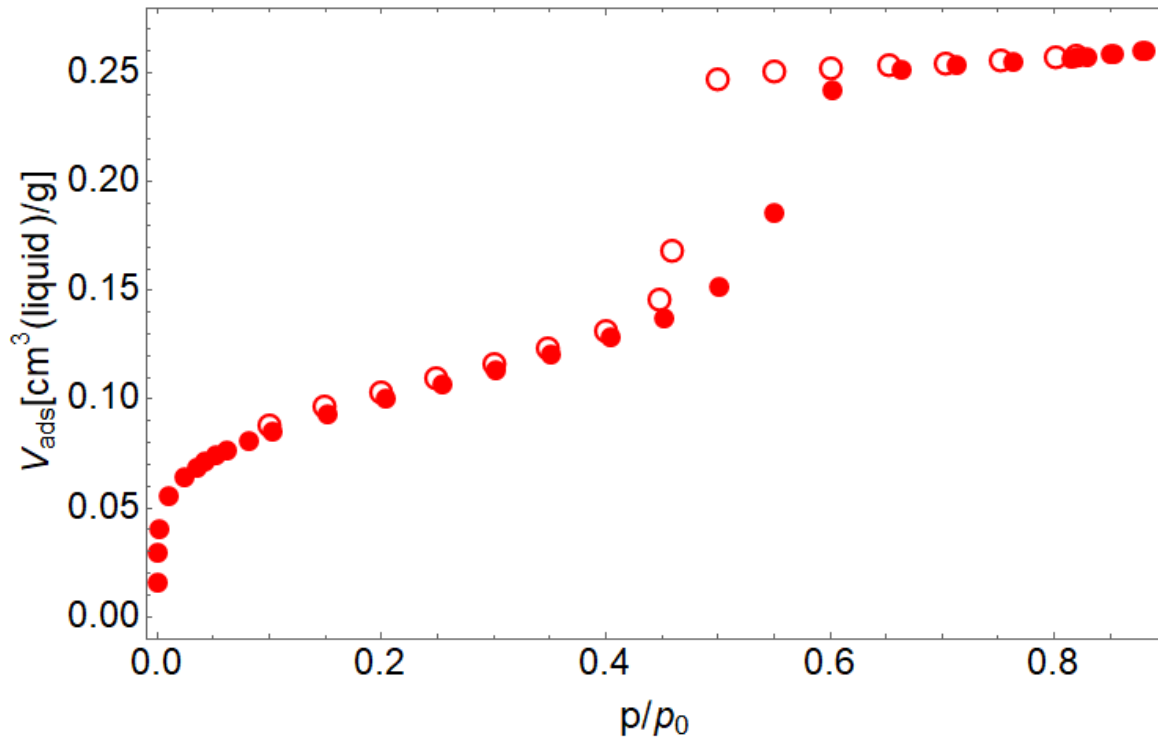


Figure 9: A sample nitrogen physisorption isotherm of a sintered, monolithic, hierarchically porous silica material measured at 77.4 K is shown, with the full and empty symbols depicting the adsorption and desorption branch respectively. The amount adsorbed is expressed as a liquid volume of nitrogen as a function of the relative pressure. (Isotherm recorded by Christian Balzer, ZAE Würzburg)

To distinguish between v_μ and v_m , the so-called t-plot analysis described in detail elsewhere⁵⁸ can be performed. In short, it is assumed that the thickness of an adsorbed liquid layer as a function of relative pressure is independent of mesopore size and shape. By plotting the amount adsorbed against the film thickness at corresponding relative pressures, a linear relationship exists between them for the relative pressure interval associated with growth of a liquid film in mesopores (**Figure 10**). For given adsorbate/adsorbent combinations, so called ‘universal t-curves’^{11,12}, which describe the film thickness t as a function of relative pressure p/p_0 on a flat surface, are used. If the material were purely mesoporous, this linear relationship would cross the origin, but the presence of micropores leads to deviations from this linear relationship at small relative pressures as shown in **Figure 10**. The intercept of the line describing this linear relationship with the ordinate is interpreted as specific micropore volume v_μ , whereas the slope is the specific mesopore surface S_{meso} . For the sorption isotherm shown in **Figure 9**, the specific micropore volume is $v_\mu \sim 0.02 \text{ cm}^3/\text{g}$ and $S_{meso} \sim 193 \text{ m}^2/\text{g}$. The specific mesoporous volume v_m can be calculated easily from v_p and v_μ ($v_m = v_p - v_\mu$).

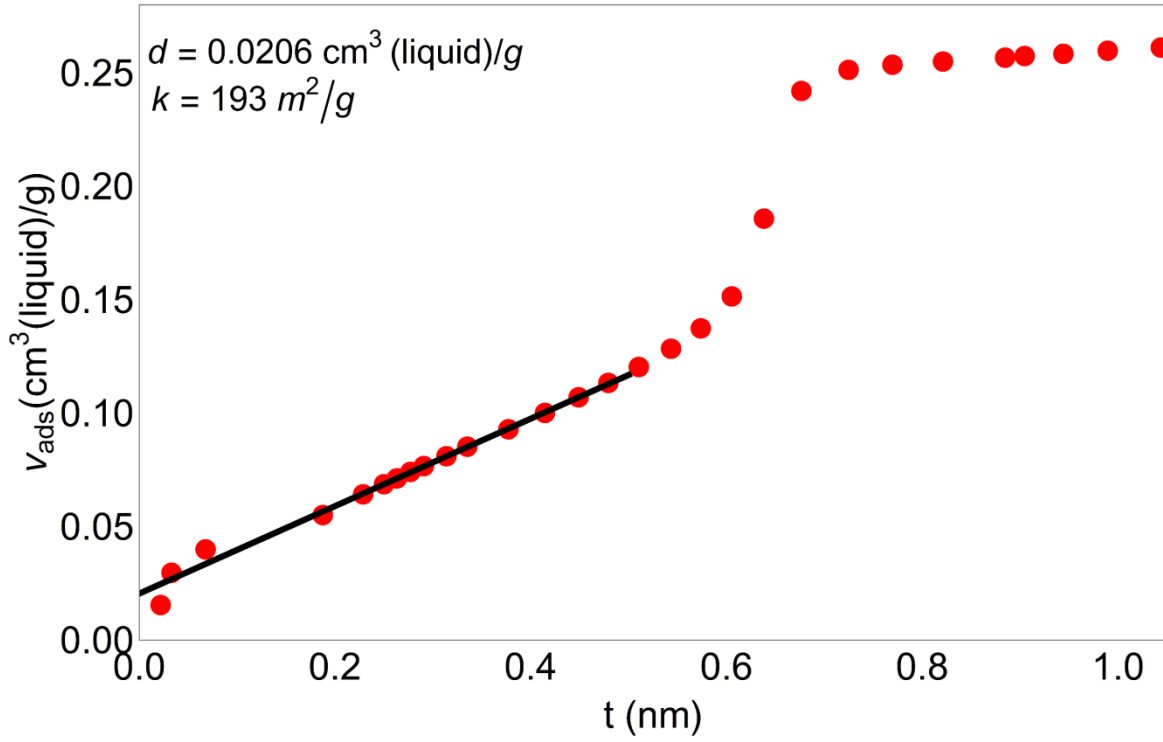


Figure 10: The t -plot of the adsorption branch of the nitrogen isotherm in **Figure 9** is shown, where the straight line denotes the film thickness on a flat substrate as function of relative pressure. (Isotherm recorded by Christian Balzer, ZAE Würzburg)

More information can be obtained if the skeletal density ρ_s of the porous material is determined by He-pycnometry, giving the total specific pore volume $v_t = \frac{1}{\rho_a} - \frac{1}{\rho_s}$. The macropore volume can then be estimated by subtraction of the porosity from the total pore volume ($v_{macro} = v_t - v_p$). After determination of the pore volume, the volume fraction of pores in the sample can be estimated by:

$$\Phi_t = \frac{v_t}{v_s} = \frac{v_t}{v_t + \frac{1}{\rho_s}}, \quad (3.41)$$

with v_s being the specific sample volume. For the simulations performed in this work, all volume fractions are usually defined on the strut/grain level of the porous material used and denoted in minuscule Greek letters.

The individual contributions based on the specific volumes and densities defined above are:

$$\phi_\mu = \frac{v_\mu}{v_m + v_\mu + \frac{1}{\rho_s}}, \quad (3.42a)$$

$$\phi_m = \frac{v_m}{v_m + v_\mu + \frac{1}{\rho_s}}, \quad (3.42b)$$

$$\phi_{SiO_2} = \frac{\frac{1}{\rho_s}}{v_m + v_\mu + \frac{1}{\rho_s}}, \quad (3.42c)$$

with the subscripts denoting the associated fractions. On a mesostructural level, the sum of all three volume fractions is equal to 1 ($= \phi_\mu + \phi_m + \phi_{SiO_2}$).

The sample adsorption isotherm depicted in **Figure 9**, wherein the specific adsorption of nitrogen on a sintered, hierarchically nanoporous silica sample as a function of relative pressure is shown, is of class IV. The characteristic shape of this isotherm is more closely classified by the IUPAC as a type IV isotherm with a H1 hysteresis⁹⁷, which is characteristic for mesoporous materials exhibiting cylindrical mesopores with micropores embedded in the pore walls.

For such a material exhibiting cylindrical mesopores with negligible specific microporosity, the mesopore radius r_{meso} can be evaluated with:

$$r_{meso} = \frac{2v_p}{S_{meso}}. \quad (3.43)$$

The approach taken with the equation above is a simple, yet relatively crude way to estimate the mesopore size. Other, state-of-the-art methods such as density functional theory approaches^{16,106-108} cannot be implemented easily and are usually part of commercial software packages implemented in commercial adsorption measurements devices (f.e. Micromeritics, Quantachrome). Older approaches based on macroscopic thermodynamic theories are easier to implement and will be discussed below.

3.2.3 Modelling of Sorption in Cylindrical Mesopores by Gibbs free energy

To develop a mathematical description of adsorption, it is convenient to apply macroscopic thermodynamics. Although state-of-the-art methods use simulations either on a molecular level, such as Grand Canonical Monte Carlo (GCMC), or density functional methods, such as the Non-Local and Quenched Solid Density Functional Method (NLDFT and QSDFT respectively)¹⁰⁸, approaches based on macroscopic-thermodynamic theory apply reasonably enough for mesoporous materials¹⁰⁷. Because adsorption is typically described by an isotherm as a function of relative pressure, the thermodynamic potential of choice is the Gibbs free energy^{11,12}. By omitting interplay between adsorption and the adsorbents change of potential due to adsorption induced stresses¹⁰⁹, it is sufficient to assume a two-phase system (vapor and liquid phases) at a given pressure p below the equilibrium vapor pressure p_0 .

In general, the theoretical treatment of adsorption was invented by Willard Gibbs and is still applied today⁷. The original problem was to accurately assess the amount adsorbed and the definition of surface between two phases. In adsorption of vapor on a solid, the surface between adsorbate and adsorbent is easily distinguished, but between adsorbed liquid and the vapor phase this is not immediately obvious (see **Figure 11 a**). Gibbs defined the so-called surface excess Γ ⁷, which is defined by a virtual surface separating vapor and liquid. The choice of the position of the surface defining the excess is arbitrary, which means that the surface excess Γ is not clearly defined and can even take negative values¹⁰⁹. To circumvent this problem, in the classical macroscopic thermodynamic treatment it is simply assumed that the density of the adsorbed liquid film with thickness t is at bulk value. This simplifies calculations significantly (see **Figure 11 b**) and clearly defines the surface excess $\Gamma (= t/v_{mol})$.

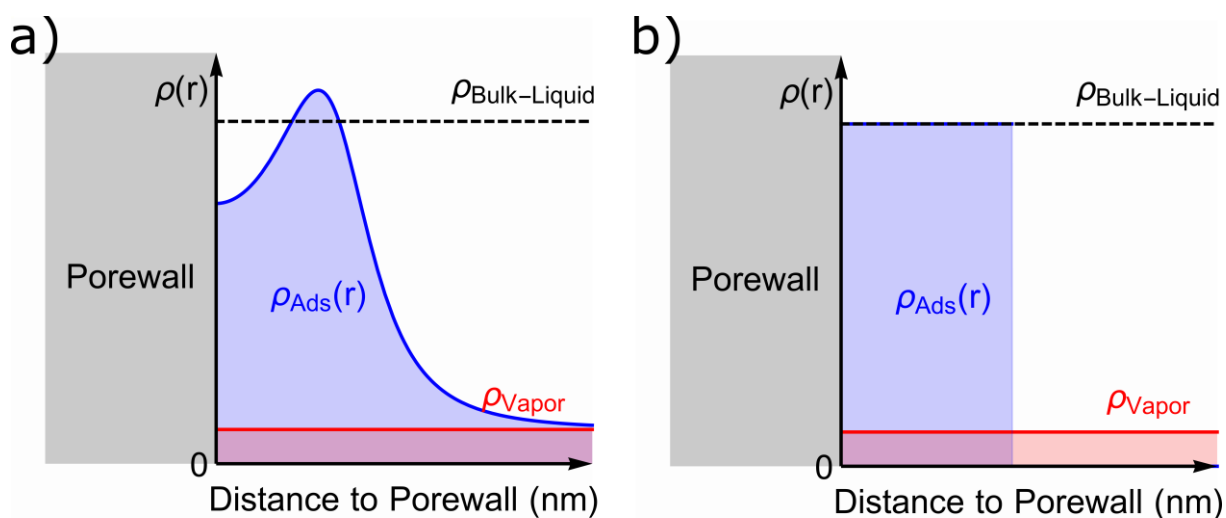


Figure 11: In a), the density profile of the adsorbed phase ρ_{ads} is plotted against the distance to the pore wall, with b) showing the density distribution assumed in the macroscopic thermodynamic treatment introduced by Broekhoff and DeBoer^{11,12}.

In the following discussion, the surface excess will be omitted and adsorption will be described in the amount adsorbed n in mol to match the nomenclature of Broekhoff and DeBoer^{11,12}. Surveying **Figure 11 b**), three contributions (liquid, gaseous and a surface phase between the former two) to the Gibbs free energy have to be considered.

In total, the Gibbs free energy is expressed as

$$G = G^c + G^v + G^S, \quad (3.44)$$

with G being the total Gibbs free energy. G^c , G^v and G^S are the contributions of the condensed liquid and the vapor phase and of the surface S between them. Written out, the sum of the contributions takes the following shape:

$$G_{p,T} = n_c \mu_c + n_v \mu_v + \gamma_{lv} S; \quad (3.45)$$

with n_i being the amount of the condensed and vapor phase present, μ being the chemical potential of the respective phases and S the interface area between the condensed and vapor phase with the surface tension γ_{lv} . To obtain the composition of a two-phase system at a given temperature T and pressure p , the minimum of the Gibbs free energy needs to be obtained by setting its derivative, with respect to the amount adsorbed, to zero.^{11,12} To arrive at such an expression, change of the Gibbs free energy by adsorption of a virtual amount of dn is explored. Under application of the second law of thermodynamics this leads to⁷:

$$dG_{p,T} = 0 = \mu_c dn_c + \mu_v dn_v + \gamma_{lv} dS. \quad (3.46)$$

To apply equation 3.46 to adsorption in cylindrical mesopores of radius r , where a liquid film of thickness t is adsorbed on the mesopore walls, several prerequisites are introduced. Small changes in the amount of condensed phase $dn_c = dn$ leads to an equal decrease dn_v of the vapor phase. For cylindrical pores, the third term on the right side of equation 3.46 can be related to dn by $dS = -\frac{v_{mol}}{(r-t)} dn$, with v_{mol} being the molar volume of the adsorbed fluid at bulk. Reformulating equation 3.46, the Kelvin equation for the cylindrical pore with a liquid film on the pore wall is derived¹¹⁰:

$$\mu_c - \mu_v = \Delta\mu = -R_g T \log\left(\frac{p}{p_0}\right) = \frac{\gamma_{lv} v_{mol}}{r-t}, \quad (3.47)$$

with R_g being the universal gas constant, T the absolute temperature, p the pressure under consideration and p_0 the equilibrium vapor pressure. As pointed out by Broekhoff and De Boer in a stability analysis by analyzing the second derivative of the Gibbs free energy^{11,12}, equation 3.47 does not allow for a coherent description of adsorption because a discontinuity in the properties of the adsorbed film is implied. Applying the second derivative of the Gibbs free energy with regard to dn , at a given temperature and pressure, to equation 3.46 for cylindrical pores gives:

$$\frac{d^2 G}{dn^2}_{p,T} = -\frac{\gamma_{lv} v_{mol}}{(r-t)^2} \frac{dt}{dn}. \quad (3.48)$$

Stability of the liquid film is ensured as long as equation 3.48 is larger than 0, which implies that either the first or second fraction on the right hand side is negative. The first fraction on the right hand side of equation 3.48 can't be negative, because of the square in the denominator. The second term on the right hand side is also positive in any case, because the film thickness t grows with an increase in the amount adsorbed dn . This in turn means that equation 3.48 is always negative and a liquid film phase on the pore wall were always unstable. Consequently, equation 3.47 is incorrect in describing adsorption in cylindrical pores. To correct the approach taken with equation 3.48, Broekhoff and de Boer applied a concept of Derjaguin¹⁰², called disjoining pressure, which assigns an additional energy term to the liquid film on the mesopore wall.

This reads as:

$$\mu_c = \mu_l - \Pi(t), \quad (3.49)$$

with $\Pi(t)$ denoting the disjoining pressure of a given liquid on a substrate. This pressure is felt by atoms, molecules or ions of the adsorbate via interaction forces with the adsorbent. These forces generally involve London-forces and electrostatic interactions¹⁰², which follow a d^{-6} and a d^{-2} behavior respectively, with d being the distance from the substrate. Although expressions for the disjoining pressure exist for cylindrical tubes and other geometrical shapes¹¹¹, the disjoining pressure of a flat surface approximates the potential well enough due to the short range of the interaction forces^{11,12}. Applying equation 3.49 to the analysis presented before, instead of equation 3.47 the following is obtained:

$$R_g T \log\left(\frac{p}{p_0}\right) = -v_{mol} \left(\Pi(t) + \frac{\gamma_{lv}}{r-t} \right). \quad (3.50)$$

This equation is called the Derjaguin-Broekhoff-de-Boer¹⁰⁻¹² equation and is generally used in the modelling of adsorption and desorption of cylindrical mesopores. Applying the stability analysis from before gives:

$$\frac{d\Pi}{dt} + \frac{\gamma_{lv}}{(r-t)^2} < 0, \quad (3.51)$$

which is equivalent to $\frac{d^2G}{dn^2_{p,T}} > 0$. In contrast to equation 3.48, this equation can take negative values. Because the disjoining pressure is dependent on forces described by inverse power laws, the dispersion and electrostatic forces decrease with growing film thickness resulting in a negative value of the derivative $\frac{d\Pi}{dt}$. The second term in equation 3.51 must be positive and grows with increasing film thickness t approaching r . As long the absolute value of the first term in equation 3.51 remains larger than the second term, the film phase remains stable. But once equation 3.51 reaches a value of zero or larger at a film thickness of t_c at a relative pressure p_c/p_0 , the film phase becomes unstable and capillary condensation sets in, filling the entire cylindrical pore.

Evaporation is handled differently historically and is thought to be an equilibrium process. Equilibrium between two phases is reached once their thermodynamic potential is the same. This can be calculated for a cylindrical mesopore of radius r and length L with the right-hand side of equation 3.46:

$$\begin{aligned} \Delta G_{p,T} = 0 &= \int_{n_{film}}^n (\mu_c - \mu_v) dn + \int_{A_{film}}^A \gamma_{lv} dA = \\ &= \frac{\pi L}{v_{mol}} \left(\int_{t_e}^r 2(\mu_c - \mu_g)(r-t) dt - 2\gamma_{lv}(r-t) \right) \end{aligned}$$

which can be simplified with equation 3.49. This yields the Derjaguin equation^{11,12}:

$$G_F - G_L = 0 = 2v_{mol} \left(\frac{\gamma_{lv}}{r-t_e} + \frac{1}{(r-t_e)^2} \int_{t_e}^r (r-t')\Pi(t') dt' \right) + R_g T \log\left(\frac{p_e}{p_0}\right), \quad (3.52)$$

with G_F and G_L denoting the Gibbs free energy of the filled and liquid layer phase, where the subscript e stands for the values of p and t at evaporation. Starting from a filled pore at $p/p_0 \sim 1$, the desorption process is interpreted as progressive receding of the meniscus at the end of the pore throats with decreasing pressure.^{11,12} For pressures below p_e , equation 3.50 is stable and represents the global minimum of the Gibbs free energy. Consequently, once the relative pressure of evaporation is reached in desorption, the mesopore empties and a liquid film on the mesopore wall is left.

Of note is the fact that $p_e < p_c$ for cylindrical mesopores, which is thought to be the origin of the hysteresis found in adsorption isotherms (see **Figure 9**)^{11,12}. This goes against the reasoning presented in the introduction of this section, where it was surmised that $\frac{dG}{dn_{p,T}} = 0$

would describe an equilibrium state if it were in a minimum. In fact, this is the case for relative pressures increasing from 0 until the film thickness t_e is reached, after which the filled phase exhibits a lower Gibbs free energy. With increasing relative pressure, the liquid film phase is stable as found through stability analysis (equation 3.51), but represents a local minimum. In general, as long as no nucleation event occurs for $p < p_{cap}$, capillary condensation won't ensue. Cole and Saam¹¹² discussed this circumstance in length and found that the liquid layer represents a metastable phase once $p/p_0 > p/p_e$. In the adsorption branch the activation barrier between the local and global minimum is too large to be overcome by thermal fluctuations alone until a film thickness t_c is reached¹¹². Hence, it is customary to describe the adsorption branch as metastable and the desorption branch as in equilibrium.

A fit of an experimental isotherm can be performed, if the thickness of the adsorbed layer is translated into the amount adsorbed via the following relations:

$$\frac{n_{film}\left(\frac{p}{p_0}\right)}{m} v_l = S_{meso} \left(t \left(\frac{p}{p_0}\right) - \frac{t \left(\frac{p}{p_0}\right)^2}{2r} \right), \quad (3.53)$$

$$\frac{n_{filled}}{m} v_l = \frac{1}{2} S_{meso} r, \quad (3.54)$$

where the quantity $\frac{n}{m} v_l$ is the liquid amount adsorbed and S_{meso} is the surface area of the mesopores. The mesopore radius r can be determined by analysis of the pressure of capillary condensation/evaporation by application of equation 3.51/3.52. Alternatively, the mesopore radius can be estimated by utilization of equation 3.43 if S_{meso} is known. Instead of a dedicated disjoining pressure isotherm, the universal t-curve popularized by Broekhoff and de Boer can be applied in equations 3.51 and 3.52^{11,12}. For this t-curve, it is assumed that the film thickness as a function of relative pressure does not vary strongly for most adsorbents. For nitrogen adsorption on amorphous silica the following relation was found empirically^{11,12}:

$$\Pi(t) = 2.303 R_g T \left(\frac{16.11}{t^2} - 0.1682 e^{-0.1137 t} \right). \quad (3.55)$$

To describe the adsorption in micropores, one can use the Langmuir isotherm (equation 3.39)⁸. To perform a fit with the procedure described, one needs to use the appropriate temperature ($T = 77.4 \text{ K}$) and specific surface energy ($\gamma = 8.72 \cdot 10^{-3} \text{ Nm}$) for nitrogen adsorption on the sintered, monolithic and hierarchically porous with a specific surface of $S_{BET} = 193 \text{ m}^2/\text{g}$, which results in **Figure 12**. Qualitative agreement is achieved, yet

quantitatively the fit is off due to the limited applicability of the universal t-curve especially in describing the film-state of the sample.

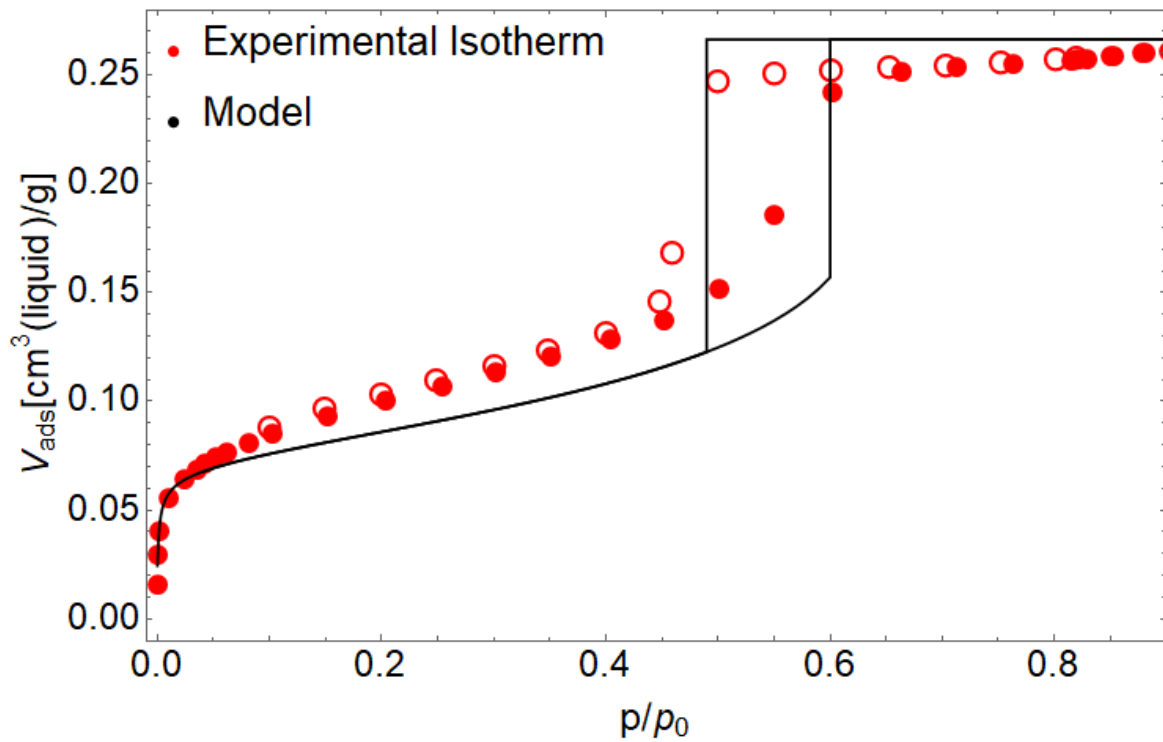


Figure 12: Physisorption isotherm of nitrogen at 77.4 K on monolithic, hierarchically porous sintered silica, with the full and empty circles denoting the ad- and desorption branch respectively. The full, black line represents the fit with the macroscopic, thermodynamic model under application of the universal t-curve.

3.2.4 Variational Approach to Physisorption in Complex Pore Geometries

Dobbs et al¹¹³ developed a variational approach of adsorption, which allows the description of physisorption in more complex geometries. Their method is based on the minimization of the grand potential Ω of defined phases with the Euler-Lagrange equation. In contrast to the geometrically simple case of cylindrical mesopores, where the amount adsorbed n directly scales with the film thickness t , the variational approach allows to determine liquid-vapor profiles for more complex substrate geometries. For instance: adsorption in materials exhibiting continuous pore spaces, such as the monolithic, hierarchically nanoporous carbon material investigated in this thesis (see chapter 2.2), can be effectively modelled with this approach.

The relevant equations were adapted from Dobbs et al¹¹³, where capillary bridging was described in parallel, quadratically arranged cylinders. Here, the formulism was extended to cover the case of adsorption between a 2-dimensional, hexagonal arrangement of parallel carbon nanowires of radius r_0 and lattice spacing d . (see **Figure 13**). Because of the high aspect ratio of the nanowires, adsorption is assumed to be independent of their axial dimension. Hence, all equations in this section were developed for the lateral dimension in 2-D (see **Figure 2 c**). Three different phase to model adsorption with were defined¹¹³:

- separated-phase: a simple liquid layer exists on every carbon nanowire
- bridged-phase: liquid bridges span the distance between neighboring carbon nanowires
- filled-phase: the entire void space is filled

To simplify calculations, Ω is derived in polar coordinates $\{l(\theta), \theta\}$. Two different origins were chosen for the separated-phase and bridged-phase. In **Figure 13** the geometry used is shown, where l_1 denotes the separated-phase (dark blue), with its origin set in the center of the nanowire, and l_2 denotes the bridged-phase (dark and light blue), with its origin set in the center of the void space wedged between three nanowires. To ease the notation, the implied dependence of l_1 as a function of θ_1 is not spelled out explicitly. Additionally, differentiation of l_1 by a variable is denoted with the appropriate subscript. Hence, Ω as a function of a profile l_1 is¹¹³:

$$\Omega(l) = 6 \int_0^{\frac{\pi}{6}} d\theta \gamma_{lv} (l_1^2 + l_{\theta_1}^2)^{\frac{1}{2}} - \frac{R_g T}{v_l} \log\left(\frac{p}{p_0}\right) \left(-\frac{\pi}{2} r^2 + 6 \int_0^{\frac{\pi}{6}} d\theta \frac{1}{2} l_1^2\right) + 6 \int_0^{\frac{\pi}{6}} d\theta V(l_1, \theta) \quad (3.56)$$

with γ_{lv} the liquid vapor surface tension and r the nanowire radius. Just as in the previous section, the adsorbed liquid is assumed to exhibit bulk properties. The first term of equation 3.56 describes the interfacial energy of a profile l_1 , the second term describes the energy due to the chemical potential of the adsorbate and the last term denotes the contribution due to the disjoining pressure of the adsorbed liquid film. $V(l, \theta)$ in equation 3.56 is similarly constructed to integral in the brackets in equation 3.52 and is defined as¹¹³:

$$V(l, \theta) = \int_l^{l_{\max}} \Pi(l', \theta) l' dl' \quad (3.57)$$

with Π being the disjoining pressure at a certain point $\{l, \theta\}$. To determine the disjoining pressure, the approach from Dobbs et al¹¹³ is adopted, where summation over all three contributions from every carbon nanowire is performed at every point $\{l, \theta\}$.

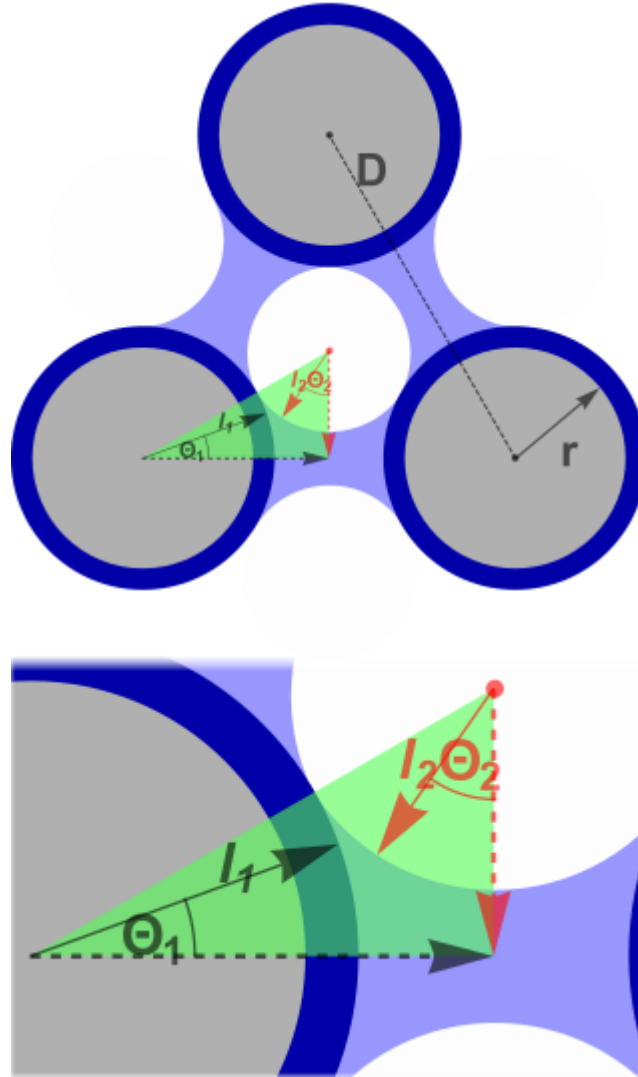


Figure 13: a) The geometry of a unit cell inside CMK-3 or the monolithic, hierarchically porous carbon material introduced in chapter 2.2 In b) a zoom in on the relevant part of the unicell is shown, where the polar geometry with subscript one describes the separated phase, indicated by the dark blue disk segment, and the subscript 2 denotes the geometry of the bridged phase, indicated by the opaque blue area.

The same calculation can be done for the bridged-phase, where the empty space in between neighboring carbon nanowires is spanned by a liquid bridge. Consequently, the grand potential takes the form:

$$\Omega(l_2) = 3 \int_0^{\frac{\pi}{3}} d\theta \gamma_{lv} (l_2^2 + l_{\theta_2}^2)^{\frac{1}{2}} - \frac{R_g T}{v_l} \log\left(\frac{p}{p_0}\right) \left(\frac{d^2}{4\sqrt{3}} - \frac{\pi}{2} r^2 - 3 \int_0^{\frac{\pi}{3}} d\theta \frac{1}{2} l_2^2 \right) + 3 \int_0^{\frac{\pi}{3}} d\theta V(l_2, \theta), \quad (3.58)$$

with d being the distance between adjacent nanowires.

Finally, the grand potential of the completely filled void space, which, due to lack of any liquid-vapor interface, trivially reads as:

$$\Omega = \frac{R_g T}{v_l} \log\left(\frac{p}{p_0}\right) \left(\frac{d^2}{4\sqrt{3}} - \frac{\pi}{2} r^2 \right). \quad (3.59)$$

Liquid-vapor interface configurations $l_{1,2}(\theta)$ are obtained by minimization of the appropriate grand potentials. This can be achieved by application of the Euler-Lagrange equation¹¹⁴:

$$\frac{d}{d\theta} \frac{\delta\Omega}{\delta l_\theta} = \frac{\delta\Omega}{\delta l}, \quad (3.60)$$

to equations 3.56 and 3.58 to obtain the respective profiles minimizing the grand potential. The resulting equation for the separated phase(if 3.60 is applied to 3.56) is:

$$-\gamma_{lv} \frac{d}{d\theta_1} \left(\frac{l_{\theta_1}}{(l_1^2 + l_{\theta_1}^2)^{\frac{1}{2}}} \right) + \gamma_{lv} \frac{l_1}{(l_1^2 + l_{\theta_1}^2)^{\frac{1}{2}}} + l_1 \left(-\frac{R_g T}{v_l} \log\left(\frac{p}{p_0}\right) - \Pi(\theta_1, l_1) \right) = 0. \quad (3.61)$$

Full differentiation of equation 3.61 leads to a non-linear ordinary differential equation of second order. A very similar result is achieved for the bridged-phase by application of equation 3.60 to 3.58:

$$-\gamma_{lv} \frac{d}{d\theta_2} \left(\frac{l_{\theta_2}}{(l_2^2 + l_{\theta_2}^2)^{\frac{1}{2}}} \right) + \gamma_{lv} \frac{l_2}{(l_2^2 + l_{\theta_2}^2)^{\frac{1}{2}}} - l_2 \left(-\frac{R_g T}{v_l} \log\left(\frac{p}{p_0}\right) - \Pi(\theta_2, l_2) \right) = 0. \quad (3.62)$$

Due to the angular dependence of the disjoining pressure, equations 3.61 and 3.62 need to be solved numerically. Because equations 3.61 and 3.62 are of second order, two conditions need to be known to solve them. These conditions can either be initial values or slopes at the angular boundaries of the respective profiles. The boundary conditions for the separated phase, with the origin fixed at the center of the rod, are given by:

$$l_{\theta_1}|_{\theta_1=0} = 0 \quad \text{and} \quad l_{\theta_1}|_{\theta_1=\frac{\pi}{6}} = 0 \quad (3.63)$$

Similarly, for the “bridged” phase the conditions read:

$$l_{\theta_2}|_{\theta_2=0} = 0 \quad \text{and} \quad l_{\theta_2}|_{\theta_2=\frac{\pi}{3}} = 0 \quad (3.64)$$

This leaves both Neumann boundary value problems to be solved numerically.

It has to be noted, that the grand potential in this work is no absolute value, as it is offset by a term containing the surface energy γ_s of carbon itself.¹¹³ Because this contribution is present in all three phases as a simple additive factor which is independent of $l(\theta)$, it has no influence on the shape determined by equations 3.61 and 3.62.

3.2.5 Equivalence between the Grand Potential and the Gibbs free energy description

Equivalence between the Gibbs free energy of adsorption and the grand potential description is shown on the example of adsorption in a cylindrical pore. This is achieved by application of the variational method to model adsorption in cylindrical mesopores. In principle, this means that equations 3.50, 3.51 and 3.52 can be derived with the variational method introduced above.

First, adsorption at relative pressures below capillary condensation by liquid layer growth is considered. This can be readily achieved by means of equation 3.62, after application of the radial symmetry of the cylindrical pore to it. Because it mustn't matter on which interval equation 3.62 is applied, the solution is independent on the angle θ . Also, the same boundary conditions as described in equation 3.64 can be applied. Application of the radial symmetry of a cylindrical mesopore necessitates $l_\theta = 0$, which transforms equation 3.62 to:

$$0 = -\gamma_{lv} \frac{d}{d\theta} \left(\frac{0}{l} \right) + \gamma_{lv} \frac{l}{(l^2 + 0^2)^{\frac{1}{2}}} - l \left(-\frac{R_g T}{v_l} \log \left(\frac{p}{p_0} \right) - \Pi \right)$$

$$\Delta\mu = -\frac{R_g T}{v_l} \log \left(\frac{p}{p_0} \right) = \left(\frac{\gamma_{lv}}{l} + \Pi \right), \quad (3.65)$$

which is exactly the same results as obtained in equation 3.50 with $l = r - t$.

Second, the condition for capillary condensation in cylindrical mesopores (equation 3.51) can be obtained with calculus of variations. Stability of a solution obtained with the Euler-Lagrange equation is evaluated with the second variation of the grand potential. The second variation can be developed by application of the Taylor approximation^{114,115} around an extremum found by the Euler-Lagrange equation to a given functional Ω in k variables l :

$$\Omega = \Omega_0 + \sum_{i=1}^k \frac{\delta\Omega}{\delta l_i} l_i + \frac{1}{2} \sum_{i,j=1}^k \frac{\delta^2\Omega}{\delta l_i \delta l_j} l_i l_j + \dots \quad (3.66)$$

Because only variations are of interest, the constant term Ω_0 on the right hand side can be dropped from equation 3.66. As the second variation is developed around an extremum found by the first variation, the second term on the right hand side is automatically 0. Higher order terms $\geq O(l_i)^3$ are usually of negligible influence¹¹⁵, which is why only the third term on the right hand side in equation 3.66 is of interest. In adsorption in a cylindrical mesopore only one variable $l(\theta)$ on an angular interval $0 < |\theta_b - \theta_a| \leq 2\pi$ is considered:

$$\delta^2\Omega = \int_{\theta_a}^{\theta_b} \left(v^2 \frac{\delta^2\Omega}{\delta l^2} + 2 v v' \frac{\delta^2\Omega}{\delta l \delta l_\theta} + v'^2 \frac{\delta^2\Omega}{\delta l_\theta^2} \right) \delta\theta, \quad (3.67)$$

with v being an arbitrary test function, which must at least be continuous and differentiable up to the second derivative. In contrast to the first variation, no differential equation defining stability is the result of the second variation and it has to be analyzed more closely¹¹⁵. Hence, the sign of equation 3.67 needs to be determined to identify the

stability of a given solution of the first variation. Equation 3.67 can be rewritten by quadratic expansion¹¹⁴ as:

$$\delta^2\Omega = \int_{\theta_a}^{\theta_b} \left(v^2 \left(\frac{\delta^2\Omega}{\delta l^2} - \frac{d}{d\theta} \left(\frac{\delta^2\Omega}{\delta l \delta l_\theta} \right) \right) + v'^2 \frac{\delta^2\Omega}{\delta l_\theta^2} \right) \delta\theta. \quad (3.68)$$

This form allows to discuss the stability of the liquid film phase in a cylindrical mesopore. To do so, the variations in equation 3.68 are explicitly calculated:

$$\frac{\delta^2\Omega}{\delta l^2} = -\Delta\mu + \Pi + l \frac{\delta\Pi}{\delta l} + \frac{\gamma_{lv} l_\theta^2}{(l^2 + l_\theta^2)^{\frac{1}{2}}} \quad (3.69)$$

$$\frac{\delta^2\Omega}{\delta l \delta l_\theta} = -\frac{\gamma_{lv} l_\theta l}{(l^2 + l_\theta^2)^{\frac{3}{2}}} \quad (3.70)$$

$$\frac{\delta^2\Omega}{\delta l_\theta^2} = \gamma_{lv} \frac{l^2}{(l^2 + l_\theta^2)^{\frac{3}{2}}} \quad (3.71)$$

It is convenient to start the analysis of equation 3.68 with the term proportional to v'^2 . To simplify calculation on whether an increase in loading would lead to instability, the prerequisite of radial symmetry is imposed on v . On any angular interval $0 < |\theta_b - \theta_a| \leq 2\pi$, hence $v(\theta_a) = v(\theta_b)$. This necessitates $v' = 0$ for any angular interval considered. Consequently variations v are only limited to changes in liquid layer thickness $t (= r - l)$. If this were not the case the second variation (equation 3.68) can under any circumstance only be positive, meaning that any variation of the liquid-vapor surface breaking radial symmetry is unfavorable.

The remaining term in equation 3.68 can be simplified with $l_\theta = 0$ and equation 3.65:

$$\begin{aligned} \int_{\theta_a}^{\theta_b} v^2 \left(\frac{\delta^2\Omega}{\delta l^2} - \frac{d}{d\theta} \left(\frac{\delta^2\Omega}{\delta l \delta l_\theta} \right) \right) \delta\theta &= \int_{\theta_a}^{\theta_b} v^2 \left(-\Delta\mu + \Pi + l \frac{\delta\Pi}{\delta l} \right) \delta\theta = \\ &= \int_{\theta_a}^{\theta_b} v^2 \left(-\frac{\gamma_{lv}}{l} + l \frac{\delta\Pi}{\delta l} \right) \delta\theta. \end{aligned} \quad (3.72)$$

The expression obtained now uniquely determines the sign of the second variation. For the film to be instable, the term in the bracket needs to be ≤ 0 :

$$-\frac{\gamma_{lv}}{l^2} + \frac{\delta\Pi}{\delta l} \leq 0.$$

This equation is for $l = r - t$ and $\delta l = -\delta t$ equivalent to the condition for capillary condensation in cylindrical mesopores (equation 3.51).

Evaporation in cylindrical mesopores as an equilibrium process can be derived by setting the grand potential between the liquid layer phase Ω_{film} and filled phase Ω_{filled} equal. The grand potential of both phases read as:

$$\Omega_{film}(l) = (\theta_b - \theta_a) \left(\gamma_{lv} + \gamma_s \frac{r}{l} \right) l - \frac{R_g T}{v_l} \log \left(\frac{p}{p_0} \right) (\theta_b - \theta_a) \frac{r^2 - l^2}{2} +$$

$$+(\theta_b - \theta_a) \int_l^0 \Pi(l) l dl \quad (3.73a)$$

$$\Omega_{filled} = (\theta_b - \theta_a) \gamma_s r - \frac{R_g T}{v_l} \log\left(\frac{p}{p_0}\right) (\theta_b - \theta_a) \frac{r^2}{2} \quad (3.73b)$$

These equations are set to be equal to find the equilibrium pressure p_e and the associated radial profile l_e :

$$\begin{aligned} \Omega_{filled} - \Omega_{film} = 0 = & -\frac{R_g T}{v_l} \log\left(\frac{p_e}{p_0}\right) \frac{l_e^2}{2} (\theta_b - \theta_a) - (\theta_b - \theta_a) \gamma_{lv} l_e - \\ & -(\theta_b - \theta_a) \int_{l_e}^0 \Pi(r-l) l dl \end{aligned}$$

This relation can be simplified to yield:

$$R_g T \log\left(\frac{p_e}{p_0}\right) = -\frac{2}{v_l} \left(\frac{\gamma_{lv}}{l_e} + \frac{1}{l_e^2} \int_{l_e}^0 \Pi(r-l) l dl \right) \quad (3.74)$$

By applying $l_e = r - t_e$, equation 3.74 finally gives:

$$R_g T \log\left(\frac{p_e}{p_0}\right) = -\frac{2}{v_l} \left(\frac{\gamma_{lv}}{r - t_e} + \frac{1}{(r - t_e)^2} \int_{t_e}^r \Pi(t) (r - t) dt \right),$$

which is equivalent to the condition for capillary evaporation in cylindrical mesopores (equation 3.52).

3.2.6 Disjoining Pressure

Here the concept of the disjoining pressure first explicitly mentioned in equation 3.49 in section 3 of this chapter is described. As defined by IUPAC¹¹⁶, disjoining pressure arises from an attractive interaction between two surfaces. Derjaguin introduced it already in 1936¹⁰² and described it as the difference between the pressure in a region of a phase adjacent to a surface confining it and the pressure of the bulk of the phase. It is the resistance felt if one were to peel off a flat plate from a substrate, when both were situated in bulk liquid. The resulting force F as a function of the pressure between the plate of area A and the substrate as a function of their distance t is directly calculated by¹¹⁷:

$$F = A \Pi(t) = -\frac{\delta \Omega}{\delta t_{T,A,\mu}} = -\frac{\delta G}{\delta t_{T,A,V}}. \quad (3.75)$$

The force can be derived by use of the grand potential Ω , although exactly the same result is reached by description in terms of the Gibbs free energy G ¹¹⁸. Incidentally, the explanation of the disjoining pressure by peeling off a flat plate is very similar to the original process the disjoining pressure was measured with¹¹⁹. In so called 'direct-force-measurements', two crossed cylinders (radius ~ 1 cm) of the same material with a well defined surface-to-surface distance (sensitivity < 0.1 nm¹²⁰) were positioned in vacuum or fluid. Their distance was measured with capacitance methods or interferometry and fine tuned with a piezoelectric actuator. Once a set distance between the cylinders was reached, their separation was carefully increased incrementally and the force as a

function of distance measured (sensitivity $\sim 10^{-8} N$)¹²⁰. Because of the defined geometry of the cylinders, $\Pi(t)$ was readily calculated.

Alternatively, the disjoining pressure is determined today by adsorption of a vapor of interest on a flat, non-porous surface of a material of interest. The Gibbs free energy of an equilibrium film with thickness t_0 is¹²¹:

$$G(t_0) = \int_{t_0}^{\infty} \Pi(t) dt \quad (3.76)$$

which can be derived from equation 3.46. The equation to determine the disjoining pressure from experiment is:

$$\Delta\mu = \frac{R_g T}{v_l} \log\left(\frac{p}{p_0}\right) = \Pi(t). \quad (3.77)$$

Hence, to determine the disjoining pressure the isotherm recorded on a flat surface is fit with an appropriate model, such as the Frenkel-Halsey-Hill isotherm^{100,101} mentioned in the introduction of this chapter.

As stated earlier in section 3 of this chapter, the disjoining pressure is a result of short-range forces between the substrate and the liquid film on it. Consequently, one can determine the disjoining pressure from theory for non-polar substrates if one introduces inverse power-law forces, such as the London force¹¹¹. This leads to the expression:

$$\Pi(t) = -\frac{2\pi\alpha}{(\epsilon - 2)(\epsilon - 3)} t^{3-\epsilon}, \quad (3.78)$$

with α being an interaction parameter between substrate and liquid and ϵ is the exponent of the interaction-force power law. An empirical form of equation 3.78 is the so-called Frenkel-Halsey-Hill equation of multilayer adsorption mentioned earlier^{100,101}:

$$\Pi(t) = -R_g T \frac{k}{\left(\frac{t}{t_0}\right)^m}, \quad (3.79)$$

where k and m are empirical parameters derived from so-called standard isotherms and $t_0 = 10^{-10} m$. Equation 3.79 is of the same structure as equation 3.78 where k represents the interaction strength between the adsorbate and adsorbent and $m = 3 - \epsilon$. In certain cases, a two parametric form of the disjoining pressure is used³⁰:

$$\Pi(t) = \Pi_1 e^{-\frac{t}{\lambda_1}} + \Pi_2 e^{-\frac{t}{\lambda_2}}, \quad (3.80)$$

with Π_1, Π_2, λ_1 and λ_2 being empirical parameters obtained from fitting the appropriate standard isotherm.

Philip¹¹¹ extended on the concept of equation 3.78 and applied it to non-planar surfaces. Analytical formulations of the disjoining pressure for several shapes, such as cylindrical tubes, cylinders, spherical cavities etc were determined by him. The form applied in this thesis represents the disjoining pressure on a singular cylinder:

$$\Pi(t) = -\frac{\pi^{\frac{3}{2}} \Gamma\left(\frac{\epsilon - 1}{2}\right)}{\Gamma\left(\frac{\epsilon}{2}\right)} \alpha r^2 (t + r)^{1-\epsilon} F_{2;1}\left(\frac{\epsilon - 1}{2}, \frac{\epsilon - 1}{2}; 2; \left(\frac{r}{t + r}\right)^2\right), \quad (3.81)$$

with Γ and $F_{2;1}$ being the gamma and general hypergeometric function respectively. All other parameters, except the cylinder radius r , are the same as in equation 3.78. Applying this more accurate description of disjoining pressure, one can achieve higher accuracy in modelling adsorption in mesoporous materials¹¹².

3.3 Adsorption Induced Deformation

Although first descriptions of adsorption induced deformation were introduced with Banghams law^{18,122}, the first calculations which also considered the pore geometry explicitly were developed by George Scherer¹²³ in the seventies and eighties of the last century. His work mainly focussed on the mechanics and not the thermodynamic origin of the strains observed. Further developments to deduce adsorption induced deformation of theoretical descriptions of the adsorption in porous materials were introduced by Neimark et al¹²⁴ and Gor et al²⁸⁻³⁰. On this basis, the thermodynamic model described in this chapter was developed by Balzer et al^{32,33}.

3.3.1 Origin of Surface Stress: Bangham Effect

The first work to deal with adsorption induced deformation theoretically was published by Bangham in the last century¹⁸. In it, the so-called Bangham effect is introduced, which relates the change in surface energy of the solid due to adsorption of vapor on its surface. In this context it is convenient to introduce the Gibbs adsorption equation⁷, which reads in this case as:

$$0 = d\gamma_{sv} + \Gamma d\mu \quad (3.82)$$

where γ_{sv} is the specific surface energy between the vapor and the solid, Γ is the surface excess and μ is the chemical potential. This equation can be interpreted as the change $d\gamma_{sv}$ in specific surface energy being compensated by the differential work of adsorption $\Gamma d\mu$. It can be reformulated to the Gibbs adsorption equation^{7,109}:

$$\Delta\gamma_{sv} = - \int_{-\infty}^{\mu} \Gamma d\mu, \quad (3.83)$$

Effectively, this can be imagined as shown in the sketch provided in **Figure 14**.¹²²

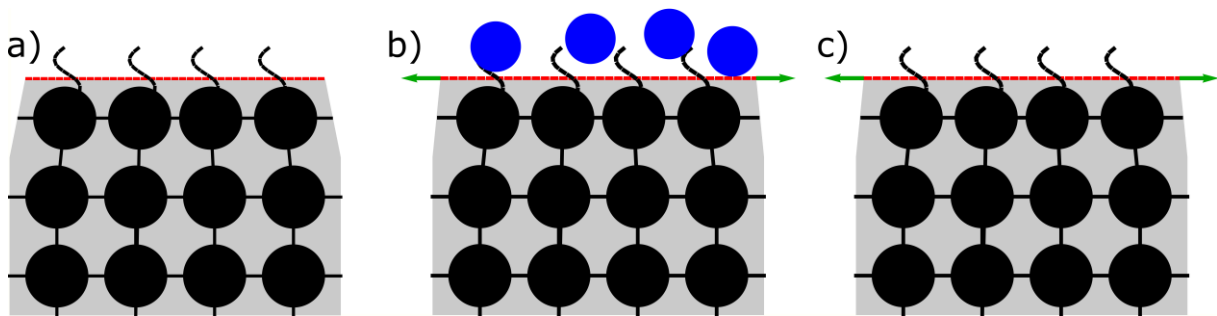


Figure 14: In a) the surface of a solid is shown (red line), where the black disks signify individual atoms and the black, wavy lines denote unsaturated bonds. In b) these bonds are occupied with adsorbed atoms changing the specific surface energy, which leads to a slight relaxation of the surface as denoted by the green arrows. Change of the specific surface energy can also be achieved if the surface is stretched, as shown in c).

In **Figure 14** a), an idealized surface (red line) of a material is shown. The black disks represent atoms of the solid, and the wavy lines unsaturated bonds. By assuming that a

total amount N_s of unsaturated bonds with energy e_b exist on a surface A of a material, the specific surface energy can be expressed as¹²²:

$$\gamma_s = \frac{e_b N_s}{A}. \quad (3.84)$$

This surface energy needs to be positive, else disintegration of the solid would be more favorable. Hence, the solid generally tries to minimize its surface by contraction¹²². Upon adsorption, several of these bonds are saturated with adsorbed atoms/molecules, which changes the overall surface energy to:

$$\gamma_{sv} = \frac{e_b N_s}{A} - \frac{e_l(N_l)N_l}{A} = \gamma_s - \frac{e_l(N_l)N_l}{A}, \quad (3.85)$$

where e_l is the binding energy between adsorbate and the solid as a function of the amount adsorbed N_l . Consequently, as sketched in **Figure 14 b**), this change in specific surface energy is directly associated with adsorption stress and the surface usually expands¹²² (illustrated with the green arrows). As $e_l(N_l)$ can be interpreted as the work gained from adsorbing a total amount N_l , it can be associated with the change in potential upon adsorption $d\mu$ by adsorption of Γ , leading to equation 3.82. With the Disjoining pressure Π being connected to $\mu(= -v_{mol}\Pi)$ and the amount adsorbed N_l to a surface excess $\Gamma (= N_l/A = t/v_{mol})$, Chuarev et al¹²¹ have shown that the Gibbs adsorption equation (Equation 3.83) can be reformulated in terms of the disjoining pressure $\Pi(= \mu/v_{mol})$:

$$\Delta\gamma_{sv} = \gamma_{sv} - \gamma_s = -\Pi(h)h + \int_0^h \Pi(h')dh'. \quad (3.86)$$

For adsorption, this can be set in relation to the surface stress f induced on the solid¹⁰⁹:

$$f = \frac{\delta\gamma_{sv}}{\delta\varepsilon}, \quad (3.87)$$

where the equation is written in Lagrangian coordinates¹⁰⁹. Equation 3.87 basically describes the amount of work done on the substrate by f by the deformation $\delta\varepsilon$ upon the change in surface energy $\delta\gamma_{sv}$. In principle, as described above, the specific surface energy is dependent on the density of surface atoms and consequently on the surface strain as A changes (see **Figure 14 c**). The materials in this thesis exhibit small strains in the range of per mille and below, hence it's influence on the specific surface energy is neglected^{109,124}. In this case: If γ_{sv} is known the surface stress from adsorption can be calculated, which is the origin of Bangham's law¹⁸.

3.3.2 Thermodynamic Model of Adsorption Induced Deformation

The macroscopic thermodynamic Derjaguin-Broekhoff-de-Boer theory^{11,12} can be used to describe the adsorption induced strain in cylindrical mesoporous materials^{28,29,32,33}. To develop the following theory, several assumptions were made in literature¹²⁵:

- the material follows Hooke's law
- no mutual influence of the strain energy and the grand potential

The grand potential per mesopore of volume V_{meso} can be related to the amount adsorbed n with the Gibbs equation¹⁰¹:

$$\Omega(p) = \Omega(0) - \int_{-\infty}^{\mu(p)} n(\mu') d\mu', \quad (3.88)$$

with $\Omega(0) = 2\pi r L \gamma_s$ being the reference state at zero pressure. This reference describes the grand potential due to the surface energy γ_s in a cylindrical pore of radius r and length L . The adsorption stress inside a pore can be calculated by differentiating the grand potential with respect to the mesopore volume V_p at constant temperature T and chemical potential μ :

$$\sigma_{ad} = - \frac{\delta \Omega}{\delta V_{p,T,\mu}}, \quad (3.89)$$

where σ_{ad} denotes the adsorption induced deformation. This formula was already used before in a similar context in equation 3.75. In the case of the cylindrical pore, one needs to distinguish between axial and radial stresses. Because the overall pore volume of a cylindrical mesopore with radius r and length L is defined as $V_p = V_{cyl} = r^2 \pi L$, the derivative with respect to the variable of the respective radial stresses σ_{\perp} and axial stresses σ_{\parallel} can be taken. This reads as^{28,32}:

$$\sigma_{\perp} = - \frac{1}{2\pi r L} \frac{\delta \Omega}{\delta r}, \quad (3.90)$$

$$\sigma_{\parallel} = - \frac{1}{\pi r^2} \frac{\delta \Omega}{\delta L} = - \frac{\Omega}{V_p}. \quad (3.91)$$

The axial stress σ_{\parallel} is not dependent on the length of the cylinder L and the derivative in equation 3.91 reduces to a simple division. For the radial stresses σ_{\perp} and axial stresses σ_{\parallel} in equation 3.90 and equation 3.91 two cases need to be differentiated: one where a liquid film covers the mesopore walls and one where the mesopore is filled after capillary condensation. Consequently, the axial and radial stresses are denoted with a subscript describing the state:

$$\sigma_{film,\perp} = - \frac{\gamma_s}{r} - \frac{t}{r} \Pi(t) + \frac{1}{r} \int_0^t \Pi(t') dt' - \gamma_{lv} \left(\frac{1}{r-t} - \frac{1}{r} \right) \quad (3.92a)$$

$$\sigma_{filled,\perp} = - \frac{\gamma_s}{r} + \frac{\gamma_{lv}}{r} + \frac{1}{r^2} \int_0^r (r-t') \Pi(t') dt' + p_0 + p_{cap} \quad (3.92b)$$

$$\sigma_{film,\parallel} = - \frac{2\gamma_s}{r} + \frac{2}{r^2} \int_0^t (r-t') \Pi(t') dt' - \Pi(t) \frac{t}{r} \left(2 - \frac{t}{r} \right) - \frac{t^2}{r^2} \frac{\gamma_{lv}}{r-t} \quad (3.93a)$$

$$\sigma_{filled,\parallel} = -\frac{2\gamma_s}{r} + \frac{2\gamma_{lv}}{r} + \frac{2}{r^2} \int_0^r (r-t')\Pi(t')dt' + p_0 + p_{cap} \quad (3.93b)$$

with γ_s being the surface energy of the dry mesopore wall, γ_{lv} the surface tension between vapor and liquid, p_0 the equilibrium vapor pressure and p_{cap} the capillary pressure²⁷. In both cases describing the film phase, $\sigma_{film,\parallel}$ (equation 3.93.a) and $\sigma_{film\perp}$ (equation 3.92.a), the first three terms describe the stress induced by the change of the surface energy of the mesopore wall, which is called Bangham effect¹²⁶ as described above. The last term describes the stress due to the curvature of the liquid film, called Laplace pressure³². In the filled state, the stress induced is mostly determined by the capillary pressure p_{cap} , which scales with the logarithm of the relative pressure²⁷. The factor 2 between the radial and the axial stresses is well known in the engineering of pipes and is due to the mechanical balance in the anisotropic geometry of the cylinder³². Because the available information on the surface energy of the dry mesopore wall can be missing, it is convenient to describe the calculated stresses in relation to the prestress ($\propto -\gamma_s/r$) without loss of generality. This is of course only applicable if the condition of a purely elastic behaviour is met.

The resulting strains can be obtained from the solution of the Lamé problem³²:

$$\varepsilon_{\perp} = \frac{1}{E} \frac{\phi_m}{1 - \phi_m} (2 \sigma_{\perp} - \nu \sigma_{\parallel}), \quad (3.94a)$$

$$\varepsilon_{\parallel} = \frac{1}{E} \frac{\phi_m}{1 - \phi_m} (\sigma_{\parallel} - 2\nu \sigma_{\perp}), \quad (3.94b)$$

where E is the elastic modulus of the mesopore wall and ν is Poisson's ratio.

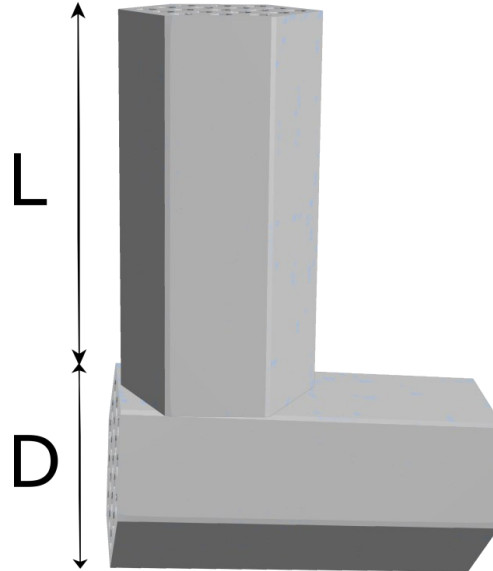


Figure 15: The geometry used to approximate the strains measured in dilatometry is shown (equation 3.96), where radial and axial contributions are summed with weights determined from the struts aspect ratio.

To model the macroscopic strain induced by adsorption in mesopores ε_{meso} , a linear approach is applied where the absolute deformation of a stack of a flat and standing strut (**Figure 15**) are added, which results in:

$$\varepsilon_{meso} = x \varepsilon_{\perp} + (1 - x) \varepsilon_{\parallel}. \quad (3.95)$$

The parameter x can be interpreted as:

$$x = \frac{D}{D + L}, \quad (3.96)$$

with D being the strut diameter and L being the strut length.

Balzer et al³³ have also introduced a model for the adsorption induced stress due to micropores present in the pore walls of SBA-15 and alike materials. The model describing the filling of the micropores is the Langmuir isotherm⁸, which leads to³³:

$$\sigma_{\mu} \left(\frac{p}{p_0} \right) = \frac{R_g T}{v_l} \left(\log \left(b \frac{p}{p_0} + 1 \right) + \frac{\delta b}{\delta \varepsilon_{\mu}} \frac{\frac{p}{p_0}}{b \frac{p}{p_0} + 1} \right), \quad (3.97)$$

with b being an empiric parameter which determines the relative pressure at which half of the micropores are filled. The first part in equation 3.97 is the adsorption induced strain due to micropores, which is modulated by the second part which describes the change in strain due to contraction/expansion of micropores^{33,122}. The associated strain is expressed as³³:

$$\varepsilon_{\mu} \left(\frac{p}{p_0} \right) = 3(1 - 2\nu) \frac{\phi_{\mu}}{E} \sigma_{\mu} \left(\frac{p}{p_0} \right), \quad (3.98)$$

where ϕ_{μ} is the volume fraction of the micropores. Because of the assumed isotropic nature of the adsorption induced strain from micropores, the contributions of the micro- and mesopores can be added:

$$\varepsilon_{ads} = \frac{1}{3} \varepsilon_{\mu} + \varepsilon_{meso}. \quad (3.99)$$

From the equations describing the stress of the filled sample states (equations 3.92b and 3.93b) the dominating term to the overall strain is p_{cap} , whereas all other terms remain constant. For both, the parallel and the perpendicular stresses, p_{cap} is the same, which results in them being near parallel at relative pressures where the sample is filled.

The capillary pressure p_{cap} can be calculated from the Kelvin equation:

$$\log \left(\frac{p}{p_0} \right) = \frac{\Psi v_l}{R_g T}, \quad (3.100)$$

where Ψ is the Laplace pressure. Is is formally defined as the difference in pressure between a liquid and vapor phase Δp ¹²⁷. The Laplace pressure can be derived from the momentum balance of a liquid in steady state, where for small film thicknesses the Laplace pressure takes the following, universal form¹²⁷:

$$\Psi = \Delta p = \gamma H - \Pi. \quad (3.101)$$

Here, Π is the disjoining pressure and H is the mean curvature. The mean curvature is defined as¹²⁷:

$$H = \frac{1}{\Delta\theta} \int_{\theta_a}^{\theta_b} \kappa(\theta) d\theta, \quad (3.102)$$

with κ being the signed local curvature, which reads in polar coordinates $\{l(\theta), \theta\}$ ¹²⁷:

$$\kappa = \frac{l^2 + 2l_\theta^2 - l_{\theta\theta}l}{(l^2 + l_\theta^2)^{\frac{3}{2}}}. \quad (3.103)$$

For a filled cylindrical mesopore with radius r and hemispherical menisci at its ends, the influence of the disjoining pressure in equation 3.101 can be omitted and takes the form:

$$\Psi = \frac{2\gamma_{lv}}{r}. \quad (3.104)$$

The fact that equation 3.92b and 3.93b are proportional to p_{cap} can be exploited in strain isotherms obtained from in-situ adsorption SAS experiments. For relative pressures where sample is filled, the measured strain can be related to the Laplace pressure by an effective Young's modulus, the so-called pore-load modulus M_{PL} ²⁷:

$$\varepsilon\left(\frac{p}{p_0}\right) = \frac{\Psi}{M_{PL}} = \frac{1}{M_{PL}} \frac{v_l}{R_g T} \log\left(\frac{p}{p_0}\right). \quad (3.105)$$

3.3.3 Adsorption Induced Stress on Carbon Nanowires

So far, only adsorption induced strains for cylindrical mesopores were considered by Balzer et al³². For a film phase, the same model can be applied for cylindrical nanowires, such as they are found in the hierarchically nanoporous carbon material discussed in Chapter 2. Due to the symmetry around the z -axis of a full cylinder, the stress tensor simplifies significantly¹²⁸ and only the hoop stresses $\sigma_\theta = \sigma_{radial} = \sigma_\perp$ and the axial stress $\sigma_z = \sigma_\parallel$ need to be considered.

Radial Stress: The grand potential is defined as in equation 3.88, where the pre-stressed reference state is defined as²⁸:

$$\Omega(0) = 2\pi r L \gamma_s, \quad (3.106)$$

with γ_s being the solid-vacuum surface energy of a nanowire of length L and radius r . The pore volume per representative unit (see **Figure 13**) $V_p (= (d^2\sqrt{3}/4 - r^2\pi/2)L)$ is dependent on two parameters d and r . Because it can be assumed that the influence of neighboring nanowires is negligible for small film thicknesses, the influence of d is neglected. Hence, the derivative is only taken with respect to r :

$$\sigma_\perp = -\frac{\delta\Omega}{\delta V_p} = -\frac{\delta\Omega}{\delta r} \frac{\delta r}{\delta V_p} = \frac{1}{r\pi L} \frac{\delta\Omega}{\delta r}. \quad (3.107)$$

The chemical potential can be derived if one applies equation 3.61 and assumes radial symmetry, which results in Derjaguins equation for sorption on a cylinder:

$$\mu = -v_l \left(\Pi(t) + \frac{\gamma_{lv}}{r+t} \right). \quad (3.108)$$

which allows to derive the normal and parallel stresses on a cylinder. The further steps taken in deriving the radial stress are very similar to the ones taken previously in other works (see²⁸ SI), but the outcome is very much the same except for the changed signs of the terms involving disjoining pressure. The derivative of the grand potential (equation 3.88) with respect to v_p yields:

$$\frac{\delta\Omega}{\delta r} = \pi L \gamma_s - \int_{-\infty}^{\mu^{(p)}} \frac{\delta n(\mu')}{\delta r} d\mu'. \quad (3.109)$$

To determine σ_{\perp} as a function of relative pressure, certain prerequisites are introduced just as in²⁸. First, one can conveniently define the amount adsorbed N as a function of the adsorbed film thickness t and nanowire radius r :

$$n = \frac{L\pi}{2v_l} ((r+t)^2 - r^2) = \frac{L\pi}{2v_l} (t^2 + 2rt), \quad (3.110)$$

which derives to the following expression if one keeps in mind that the adsorbed film thickness t is dependent on the nanowire radius r :

$$\frac{\delta n}{\delta r} = \frac{\pi L}{v_l} \left(t + (r+t) \frac{\delta t}{\delta r} \right). \quad (3.111)$$

Now, an expression for $\delta t/\delta r$ can be expressed as a function of r , if μ is viewed as an implicit function of t and r :

$$\frac{\delta t}{\delta r} = - \frac{\left(\frac{\delta\mu}{\delta r}\right)_t}{\left(\frac{\delta\mu}{\delta t}\right)_r} = \frac{\frac{\gamma_{lv}}{(r+t)^2}}{\frac{\delta\Pi}{\delta t} - \frac{\gamma_{lv}}{(r+t)^2}}. \quad (3.112)$$

The infinitesimal change in chemical potential can also be expressed as:

$$d\mu = \frac{\delta\mu}{\delta t} \delta t = -v_l \left(\frac{d\Pi}{dt} - \frac{\gamma_{lv}}{(r+t)^2} \right), \quad (3.113)$$

which is the last prerequisite to solve equation 3.109. Calculating the integral in equation 3.109 is achieved with application of equations 3.111, 3.112 and 3.113:

$$\begin{aligned} \int_{-\infty}^{\mu^{(p)}} \frac{\delta n(\mu')}{\delta r} d\mu' &= -\pi L \int_0^{t^{(p)}} \left(t + (r+t) \frac{\frac{\gamma_{lv}}{(r+t)^2}}{\frac{\delta\Pi}{\delta t} - \frac{\gamma_{lv}}{(r+t)^2}} \right) \left(\frac{d\Pi}{dt} - \frac{\gamma_{lv}}{(r+t)^2} \right) dt = \\ &= -\pi L \left(\int_{\Pi(0)}^{\Pi(t)} t d\Pi - \int_0^{t^{(p)}} t \frac{\gamma_{lv}}{(r+t)^2} dt + \int_0^{t^{(p)}} (r+t) \frac{\gamma_{lv}}{(r+t)^2} dt \right) = \\ &= -\pi L \left(\int_{\Pi(0)}^{\Pi(t)} t d\Pi + \int_0^{t^{(p)}} \frac{r \gamma_{lv}}{(r+t)^2} dt \right) = \\ &= -\pi L \left(\int_{\Pi(0)}^{\Pi(t)} t d\Pi - r \left(\frac{\gamma_{lv}}{r+t} - \frac{\gamma_{lv}}{r} \right) \right). \end{aligned} \quad (3.114)$$

By integration by parts of the remaining integral and defining $d\Pi = \frac{d\Pi}{dt} dt$ one arrives at:

$$\int_{-\infty}^{\mu^{(p)}} \frac{\delta n(\mu')}{\delta r} d\mu' = -\pi L \left(-t \Pi(t) + \int_0^t \Pi(t) dt - r \left(\frac{\gamma_{lv}}{r+t} - \frac{\gamma_{lv}}{r} \right) \right). \quad (3.115)$$

Combining equation 3.115 with 3.109 and plugging it into equation 3.107 one arrives at

$$\sigma_{\perp, film} = \frac{\gamma_s}{r} + \frac{t}{r} \Pi(t) - \frac{1}{r} \int_0^t \Pi(t) dt + \gamma_{lv} \left(\frac{1}{r+t} - \frac{1}{r} \right),$$

where every sign is reversed from equation 3.92a. This result is counterintuitive as it implies a radial contraction of the nanowires with a growing liquid film on it. Originally, equation 3.89 was applied to convex pore spaces and actually represents the magnitude of the normal component of the stress tensor at the pore wall. Consequently, an increase in pore volume in a cylindrical pore due to a liquid film on the mesopore wall indicates a tensile normal strain on the mesopore wall.

In the case of adsorption on a singular nanowire, the reverse is true. As the nanowire expands with increasing thickness of the liquid film on it, the mesopore volume decreases, which would indicate compressive stresses in the original picture. As shown by G. Scherer in qualitatively similar case¹²³, the carbon nanowires should expand upon sorption. Consequently, the normal component of the tensor is pointed outwards, into the void space. and the signs in the equation should be reversed:

$$\sigma_{\perp, film} = -\frac{\gamma_s}{r} - \frac{t}{r} \Pi(t) + \frac{1}{r} \int_0^t \Pi(t) dt - \gamma_{lv} \left(\frac{1}{r+t} - \frac{1}{r} \right), \quad (3.116)$$

Axial stress: As established by Balzer et al³², the stress parallel to the nanowire surface can be defined as:

$$\sigma_{\parallel} = -\frac{\Omega}{V_p} = -\frac{\Omega}{L \left(\frac{d^2 \sqrt{3}}{4} - \frac{r^2 \pi}{2} \right)}. \quad (3.117)$$

This expression can be simplified for our materials, if the pore volume is related to the mesoporous volume fraction:

$$\phi_m = 1 - \frac{\frac{r^2 \pi}{2}}{\frac{d^2 \sqrt{3}}{4}}, \quad (3.118)$$

which can be reformulated to express:

$$\frac{d^2 \sqrt{3}}{4} = \frac{1}{1 - \phi_m} \frac{r^2 \pi}{2}. \quad (3.119)$$

Plugging equation 3.119 into 3.117 by considering that $\phi_m \sim 0.5$ for CMK-3 materials for strains in the range of 1 % < gives

$$\sigma_{\parallel} = -\frac{\Omega}{V_p} \sim -\frac{\Omega}{\frac{L r^2 \pi}{2}}, \quad (3.120)$$

where $\Omega(0)$ is just as described in equation 3.106. But first the grand potential (equation 3.88):

$$\Omega(p) = \pi r L \gamma_s - \int_{-\infty}^{\mu(p)} n(\mu') d\mu',$$

where the integral can be simplified by integration by parts. Doing so gives:

$$\int_{-\infty}^{\mu(p)} n(\mu') d\mu' = [n(t)\mu(t)]_0^t - \int_0^t \frac{\delta n}{\delta t} \mu(t) dt. \quad (3.121)$$

Plugging equation 3.108 and 3.110 into equation 3.121, the following calculations can be performed:

$$\begin{aligned} \int_{-\infty}^{\mu(p)} n(\mu') d\mu' &= -v_l \left(\Pi(t) + \frac{\gamma_{lv}}{r+t} \right) \frac{L\pi}{2v_l} (t^2 + 2rt) - \\ &\quad - \int_0^t \frac{L\pi}{v_l} (r+t) \left(-v_l \left(\Pi(t) + \frac{\gamma_{lv}}{r+t} \right) \right) dt = \\ &= L\pi \left(-\frac{\Pi(t)}{2} (t^2 + 2rt) - \frac{\gamma_{lv} t^2}{r+t} - \frac{2rt \gamma_{lv}}{r+t} + \int_0^t (r+t) \Pi(t) dt + \gamma_{lv} t \right) = \\ &\quad L\pi \left(-\frac{\Pi(t)}{2} (t^2 + 2rt) + \frac{\gamma_{lv}}{r+t} \frac{t^2}{2} + \int_0^t (r+t) \Pi(t) dt \right) \end{aligned} \quad (3.122)$$

Applying equations 3.88 and 3.122 to equation 3.120 yields the final result:

$$\sigma_{\parallel} = -\frac{2\gamma_s}{r} + \frac{2}{r^2} \int_0^t (r+t) \Pi(t) dt - \Pi(t) \frac{t}{r} \left(2 + \frac{t}{r} \right) + \frac{\gamma_{lv}}{r+t} \frac{t^2}{r^2}, \quad (3.123)$$

where the sign of the fourth term is reversed compared to 3.93a. Here, the definition of equation 3.107 applies correctly, as an increase in length L of the nanowire leads to an increase in pore volume V_p .

To calculate strains due to adsorption on cylinders, the associated Lamé problem has to be solved. The constitutive equations for a full cylinder with radially homogeneous stresses applied on it's circumference were solved by G. Scherer¹²³ and read:

$$\varepsilon_{\parallel} = \frac{1}{E} (\sigma_{\parallel} - 2\nu\sigma_{\perp}), \quad (3.124)$$

$$\varepsilon_{\perp} = \frac{1}{E} (\sigma_{\perp} (1 - \nu) - \nu\sigma_{\parallel}), \quad (3.125)$$

where ε_{\parallel} and ε_{\perp} are the axial and radial strains respectively, ν is Poisson's ratio and E is the Young's modulus of the carbon nanowire.

3.3.4 Adsorption Induced Deformation of Slit Pores in the Mesopore regime

Because slit pores are usually associated with micropores, modelling of adsorption in them is treated with atomistic simulations such as QSDFT, NLDFT or Grand Canonical Monte Carlo simulations¹⁰⁸. In these simulations the potential overlap of the mesopore walls, the interaction between adsorbate atoms and their local density, which can vary significantly from bulk density¹⁰⁸, is explicitly taken into account. In the mesopore regime, hence for pore diameters $> 2 \text{ nm}$, these details are less influential and theoretical descriptions based on macroscopic thermodynamics, such as the DBdB-theory outlined in section 2.3 of this chapter, become valid once pore diameters of $> 4 \text{ nm}$ are reached¹⁰⁷. For small mesopores of size $\geq 2 \text{ nm}$, adsorption in a slit-pore geometry can be treated quite well with a macroscopic, thermodynamic approach developed by Derjaguin and Chuarev¹²⁹, where again the surface excess definition $\Gamma = t/v_l$ is applied (see **Figure 11**). A sketch of a slit-pore is provided in **Figure 16 a**), where H_{SP} is it's width and t is thickness of the adsorbed liquid. The stiffness of the material is signified by a spring with the effective Young's modulus E_{eff} . Due to the small pore size, defined by the wall-to-wall distance H_{SP} (see **Figure 16 a**), the solid-liquid potential P , described by the disjoining pressure Π , the solid-solid potential and liquid-liquid potential overlap. The associated grand potential is defined as:

$$\Omega_{SL} = -\frac{2t}{v_l}\Delta\mu + 2\gamma_{sl} + 2\gamma_{lv} - 2P(H_{SP} - t) + 2P(t) + F(H_{SP}) + W(H_{SP} - 2t), \quad (3.126)$$

with $F(H_{SP})$ denoting the contribution to the grand potential due to the attractive potential between both pore walls and $W(H_{SP} - 2t)$ being the potential between the adsorbed liquid films. $F(H_{SP})$ and $W(H_{SP} - 2t)$ are formally related to the solid-solid Hamaker-constant A_{SS} and the liquid-liquid Hamaker-constant A_{LL} respectively¹³⁰. Also, only London forces, sometimes also called dispersion forces, are considered. Then, the grand potential per surface unit takes the form:

$$\Omega_{SL} = -\frac{2t}{v_l}\Delta\mu + 2\gamma_{sl} + 2\gamma_{lv} + 2P(H_{SP} - t) + 2P(t) - 2\frac{A_{SS}}{12\pi H_{SP}^2} - 2\frac{A_{LL}}{12\pi(H_{SP} - 2t)^2}. \quad (3.127)$$

In this equation, it is implied that the any interaction potential, be it P , F or W as a function of the arbitrary distance variable x , can be obtained from a disjoining pressure isotherm Π ¹³⁰:

$$P(x) = \int_x^\infty \Pi(x')dx'. \quad (3.128)$$

For London forces, which can be assumed to follow a x^{-3} law for the self interaction potentials F and W , the leading term of the disjoining pressure is¹³⁰:

$$\Pi_{F,W} = -\frac{A_{SS,LL}}{6\pi x^3} + \dots \quad (3.129)$$

For the interaction between the pore wall and the fluid, the associated disjoining pressure will not be denoted by a subscript, hence will be called Π , accordingly to previous sections. The reason for this designation is that the disjoining pressure will be determined from experimental data and won't necessarily of the form in equation 3.129.

By taking the first derivative of equation 3.127 with respect to the adsorbed film thickness t , the film thickness can be determined as a function of the chemical potential $\Delta\mu$ with the following equation¹³⁰:

$$\Delta\mu = R_g T \log(p) = v_l \left(-\frac{A_{LL}}{6\pi(H_{SP} - 2t)} - 2 \Pi(H_{SP} - t) - 2 \Pi(t) \right). \quad (3.130)$$

The first term in the paranthesis in the equation above describe the influence of the adsorbed films between each other, while the interaction of the pore walls with the films on the opposing pore walls is described by the second term. For large slit pore widths H_{SP} , these first two terms in the parenthesis become very small and the influence of opposing pore walls on each other diminishes.

In accordance to the direct measurement of the disjoining pressure Π , described briefly in section 2.6 of this chapter, the pressure between two parallel pore walls due to adsorption can be calculated with¹³¹:

$$\sigma_{SL} = -\frac{\delta\Omega}{\delta H_{SP}},$$

which can be directly applied to equation 3.127:

$$\sigma_{SL} = -2 \frac{\delta\Pi(t)}{\delta H_{SL}} - 2 \frac{A_{SS}}{6\pi H_{SP}^3} - 2 \frac{A_{LL}}{12\pi(H_{SP} - 2t)^3}. \quad (3.131)$$

The pre-stress of the system is simply defined by the attractive interaction between both pore walls:

$$\sigma_{SL,0} = -2 \frac{A_{SS}}{6\pi H_{SP}^3}. \quad (3.132)$$

With the approach taken, the so-called solvation pressure approach¹⁰⁹, only the stresses normal to the mesopore wall are determined. These results found extensive use in Atomic Force Microscopy and have been confirmed experimentally since then¹³⁰.

However, because only the interaction between the pore walls in a slit pore is considered in the current discussion, effects of the surface stress f are neglected. In general, these effects are additive, as long as adsorption and adsorption induced deformation don't influence each other¹²². As A_{LL} and A_{SS} must take positive values¹³⁰, as well considering the fact that $\delta\Pi/\delta H_{SP}$ is automatically negative as briefly discussed in section 2.3 of this chapter, adsorption of a liquid film in a slit pore in the mesopore regime automatically leads to contraction of the sample. The condition for capillary condensation can be derived by taking the second derivative of Ω_{SL} with respect to the adsorbed film thickness t and setting it zero:

$$\frac{\delta^2\Omega}{\delta^2 t} = 0.$$

For slit pores in the mesopore regime, under the condition that only dispersion forces are in effect, this relation is nearly constant and the film thickness of adsorption t_{cap} fulfills the simple equation¹³⁰:

$$H_{SP} = 3.2 t_{cap}. \quad (3.133)$$

Once capillary condensation has set in, the grand potential takes the simple form¹³⁰:

$$\Omega_{SP, \text{filled}} = 2\gamma_{sl} - \frac{\Delta\mu}{v_l} H_{SP} - \frac{A_{SL}}{12\pi H_{SP}^2}. \quad (3.134)$$

where A_{SL} is the Hamaker constant for two surfaces with a liquid between them¹²⁰. Again, the adsorption induced stress, again in reference to the pre-stress described by equation 3.131, can be calculated:

$$\sigma_{SP, \text{filled}} = \frac{\Delta\mu}{v_l} - \frac{A_{SL}}{6\pi H_{SP}^3}. \quad (3.135)$$

This equation determines the pressure in the liquid as defined by the generalized Laplace equation 3.100, offset by the second term on the right-hand side of equation 3.133. For nitrogen adsorption at 77.4 K in a carbon slit pore of size $H_{SP} = 3 \text{ nm}$, the adsorption isotherm and calculated strain isotherm are shown in **Figure 16** b) and c). The film thickness was calculated with equation 3.130, with the critical thickness of capillary condensation t_{cap} being determined from equation 3.133. The parameters to model the adsorption and adsorption induced deformation of nitrogen in carbon slit pores at a temperature of 77.4 K are $A_{LL} = 3.2 \cdot 10^{-20} \text{ J}$ ¹²⁰, $A_{SS} = 1.1 \cdot 10^{-19} \text{ J}$ ¹³², $A_{SL} = (A_{LL}^{0.5} - A_{SS}^{0.5})^2 = 2.33 \cdot 10^{-20} \text{ J}$ and for the disjoining pressure as defined by the Harkins-Jurai equation¹³³.

In a material which purely exhibits slit pores, the effective Young's modulus E_{eff} is directly related to the materials bulk modulus K_b/ϕ_m ^{124,131}, but it is not considered in the example shown here. Still, adsorption of a non-polar liquid in slit-pore geometries can lead to compressive stresses in the film region even for small mesopores. Qualitatively, the strain isotherm in **Figure 16** c) corresponds to results from GCMC simulations on sheet silicate¹³⁴.

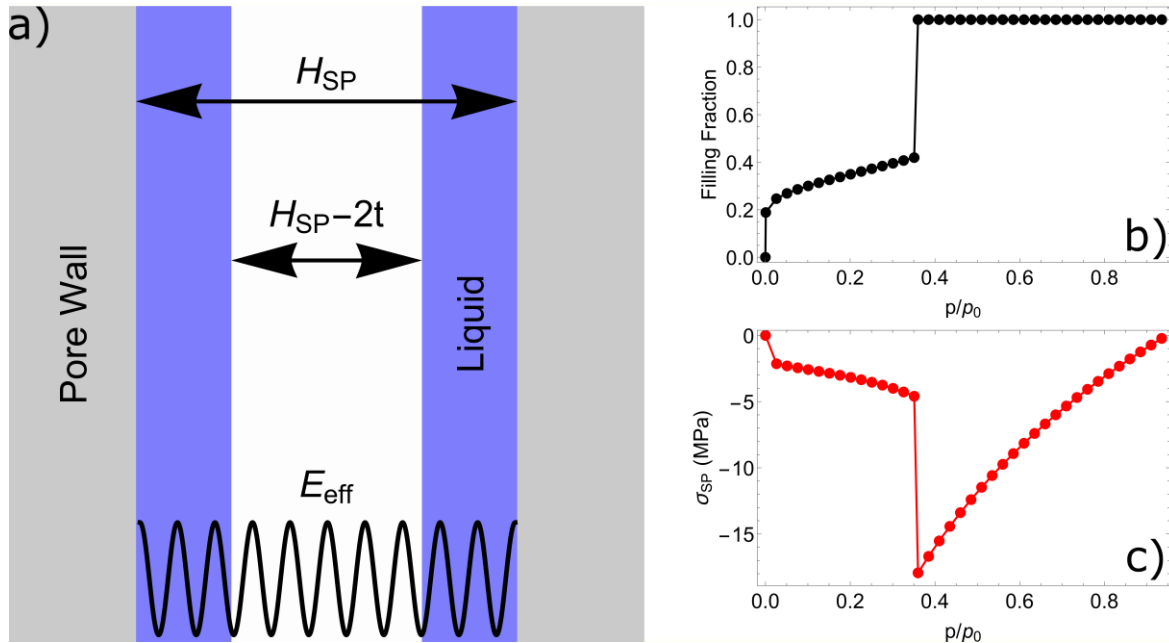


Figure 16: In a), the geometry considered in equation 3.126¹³² is shown, with H_{SP} being the slit pore width, t being the thickness of the adsorbed liquid and E_{eff} the effective Young's modulus of the material. In b), the nitrogen adsorption isotherm (77.4) in a carbon slit plot of 3 nm width is shown, where in c) the stress induced by nitrogen adsorption is shown.

4 Experimental Techniques and Procedures

The experiments performed in this work are related to in-situ adsorption- and absorption small angle scattering on the three different kinds of materials introduced in chapter 2:

- monolithic hierarchically macro-, meso- and microporous silica materials with different thermal histories: aged (S-A), aged and calcined at 550°C (S-C) and sintered at 750°C (S-S)
- monolithic hierarchically macro-, meso- and microporous carbon materials at various stage of activation: non-activated (CN), activated for 30 minutes (C30) and activated for 120 minutes (C120)
- human root dentin

Because the in-situ adsorption instruments used in experiments on silica and are already described in detail in the dissertation of Roland Morak⁵⁸, they will be only referred to in this thesis.

4.1 Ex-Situ Small Angle X-Ray Scattering

In house measurements for characterization or in-situ water absorption on root dentin were performed on the SAXS instrument Nanostar by Bruker (Karlsruhe, Germany). The x-ray generator was a microfocus source (μ -source) emitting CuK_{α} radiation at the characteristic wavelength $\lambda_{CuK_{\alpha}} = 0.15418 \text{ nm}$. The emitted X-ray beam was monochromized and focussed with Montel-optics and subsequently collimated by two scatterless pinholes (Scatex®). To achieve best spatial resolution only 300 μm pinholes were used in all experiments. The detector of the Nanostar used was a Vantec 2000 area detector with 2048x2048 pixels of 68 μm size. Because small scattering vectors were crucial in experiments involving root dentin, a 1.6 mm beamstop was mounted and adjusted. Due to the characteristic size of the mesopores in the carbon and silica materials of approximately 6 – 7 nm, the sample-detector distance was chosen to be 710 mm, which was accurately determined using Silver-Behenate as calibration standard.

In characterization measurements, samples were degassed for 2 hours in the sample chamber prior to experiment. All measurements collected were corrected for transmission using Glassy Carbon and for the background from the sample holder. Typical measurement times for silica samples of 1 mm thickness were 3600s for the sample and background measurements and 1800s for the sample and background measurements with Glassy Carbon. Due to the strong scattering, exposure time of the sample and sample holder was reduced to 2700s and 1400s respectively for characterization of carbon samples. The scattered intensity of Glassy Carbon was determined additionally for 600s after every sample measurements. Collected 2-D SAXS patterns were background and transmission corrected, as well as azimuthally integrated using Gerhard Popovski's custom written software 'Peak Fit'.

4.2 In-Situ Small Angle X-Ray Scattering – Human Root Dentin

The same instrumental set up was described above was also used for in-situ SAXS measurements on human root dentin performed during the course of this thesis. The in-situ water adsorption experiments on hierarchically nanoporous silica analyzed in this theses were performed by Roland Morak. In these experiments a custom-built **in-situ sorption unit** (ISSU) designed by Roland Morak was employed, where the details can be read elsewhere⁵⁸.

To obtain a well defined sample, defined slices of root dentin with known microstructure were manufactured by Dr. Paul Zaslansky (Julius Wolff Institute, Charité Berlin). The cut of root dentin with thickness of $350\ \mu\text{m}$ analyzed was taken from the center of the macroscopic sample, which yielded a well defined orientation of structures observed in SAXS. Outside experiments, the sample is stored at 4°C in water.

4.2.1 Vapor Dosing

The experimental procedure is simple in principle: loading of the sample with water is determined by the relative water pressure it is exposed to. To accurately determine this relative pressure, the sample holder containing the sample is exposed to a manifold filled with water vapor at a desired relative pressure. By changing the vapor pressure inside the manifold separately from the sample and subsequent exposition of the sample to the manifold, the water content of the sample can be manipulated. Because only the vapor pressure can be experimentally determined in the set-up used, no quantitative adsorption isotherms can be gathered during the experiment. The amount of water vapor inside the manifold is finite, hence large increases in loading of the sample, for instance due to capillary condensation, can deplete the manifold and the desired relative pressure is not reached. In this case, redosing of the manifold separately from the sample to the desired relative pressure and subsequent exposure of the sample to this pressure needs to be performed repeatedly. Once the system consisting of sample and manifold exhibit the desired relative pressure, SAXS measurements can be performed.

The sample was put into a custom sample holder designed by Maxim Erko¹³⁵, wherein the slice of root dentin was clamped tightly between two capton films inside the sample cell. The sample holder situated inside the NanoStar's sample chamber was connected to the self-built vapor dosing system outside the sample chamber through a flange. In contrast to ISSU used in water adsorption on hierarchically nanoporous silica, this simple system could not be thermally regulated. A symbolic sketch of the vapor dosing system used is supplied in **Figure 17** with the main parts highlighted. The part of the system situated outside the sample chamber is an assembly of connections which basically represent the manifold containing water vapor at a certain relative pressure measured by a dedicated pressure gauge.

Connected to the manifold are

- a water reservoir
- the feed to the sample holder inside the sample chamber
- a feed to two vacuum pumps

All parts were separated from the manifold by manual valves. The temperature in the laboratory was regulated by a climate unit to 297.85°K, which was also assumed to be the measurement temperature of the root dentin sample. The vapor pressure of water was determined by the Clausius-Clapyron equation, which is perfectly reflected by the maximum equilibrium pressure of 30.1 mbar measured at 297.85°K. The associated equation to determine the equilibrium vapor pressure in mbar reads as¹³⁶:

$$p_{sat H_2O} = 6.11 \text{ (hPa)} e^{6808 \left(\frac{1}{273.15} - \frac{1}{T} \right) - 5.09 \log \left(\frac{T}{273.15} \right)}, \quad (4.0)$$

where T is the temperature of interest in the experiment.

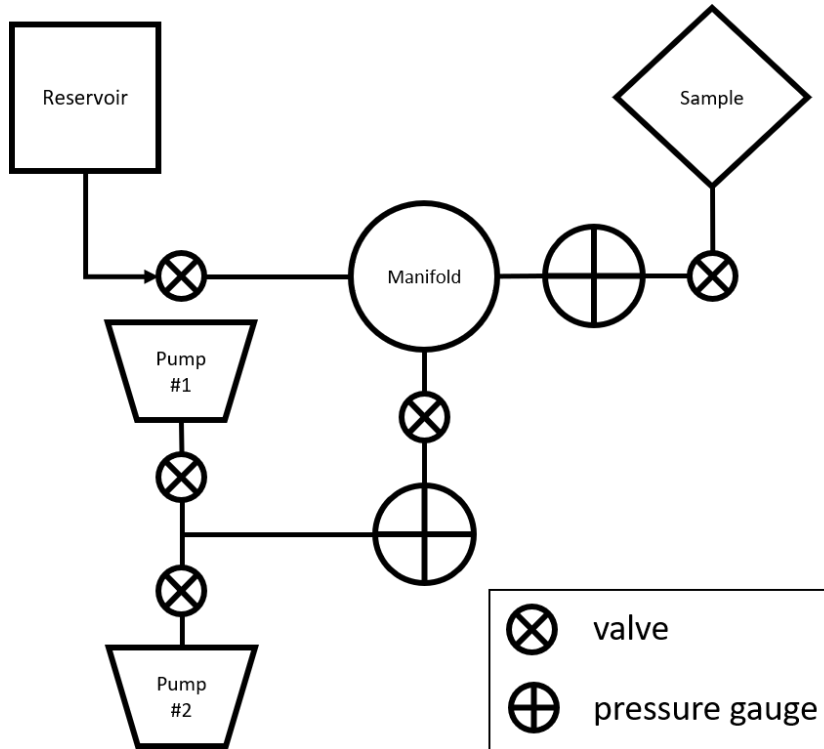


Figure 17: A diagram of the custom built vapor-dosing system used in the in-situ sorption experiments on human root dentin. Pump #1 is a simple membrane pump whereas Pump #2 is a turbo-molecular pump.

In adsorption the measurement procedure starts with evacuation of the manifold and sample holder containing the sample with a membrane pump (Pump 1 in **Figure 17**). Once 1 mbar is reached, Pump 1 becomes increasingly inefficient and is subsequently exchanged with a turbo molecular pump (Pfeiffer, Pump 2 in **Figure 17**). During this part of evacuation, the reservoir is disconnected from the rest of the dosing system. Due to the small size of the manifold and sample holder, pressures down to 10^{-5} mbar were achieved with Pump 2. This pressure was sustained for several hours after the pumps were disconnected, proving the empty state of the root dentin sample.

Once the sample was degassed, the adsorption process began. During adsorption the pumps stayed disconnected and the vapor pressure inside the manifold was manipulated with the water reservoir. During the first dosing step, the sample chamber was disconnected and the manifold carefully exposed to the vapor pressure supplied by the reservoir. Because a high precision manual valve (Pfeiffer) was used, the pressure could

be carefully calibrated until a dedicated pressure value was reached. After the manifold was disconnected from the reservoir, it was subsequently equilibrated for about 300 seconds to reduce the effect of thermal and pressure fluctuations due to expansion of the water vapor into the manifold. Afterwards, the sample holder was connected to the manifold and stayed connected until the pressure of the sample between the sample holder-manifold system equilibrated. Of note is the fact that absorption in biological matter such as root dentin seems to be a diffusion driven process, which led to equilibration times in the range of 4 hours. However, these equilibration times were entirely dependent on the relative pressure in the manifold before the sample was connected to it. Once the pressure of the sample holder-manifold system changed with a rate below of 0.01 mbar/h , SAXS measurements were performed. If the desired relative pressure was not reached, another dosing step was performed (with the sample evacuation skipped!). After the first SAXS measurement at a given relative pressure was performed, the steps mentioned above were repeated with evacuation of the sample being skipped.

For desorption, the process is essentially exactly as described above in reverse. The main difference is that the pressure in the manifold is now regulated with Pump 1, with the water reservoir staying disconnected throughout desorption.

4.2.2 In-Situ water absorption SAXS measurements in Human Root Dentin

In SAXS measurements, the following configuration and procedure was used: Because the mean thickness of mineral platelets in bone and human root dentin is about 3 nm ^{85,88} which gives features in the range of $q \sim \pi/3 \sim 1 \text{ nm}^{-1}$, the sample-detector distance was initially chosen to be 710 mm. This leads to a spread in scattering vector magnitude of $0.1 \text{ nm}^{-1} < q < 3.5 \text{ nm}^{-1}$ for measurements on the SAXS instrument. Preliminary measurements showed that a sample and background measurement time of 4500s and 2700s respectively was needed to guarantee sufficient quality of the azimuthally integrated scattering patterns. The recorded scattering patterns were reduced to absolute units ($\text{cm}^{-1}\text{sr}^{-1}$) by using water as calibration standard¹³⁷. The necessary water measurement was performed at a relative pressure $p/p_0 = 100\%$, where the empty space between capton films next to the sample is filled with water, with the thickness of the of the water film determined from the samples thickness ($\sim 350 \mu\text{m}$). All relative pressures used in the experiment are depicted in **Table 1**.

Table 1: Absolute pressure p and relative pressure p/p_0 values of the experiment on water absorption in human root dentin, where the same pressures were achieved for ab- and desorption.

p_{ads} (mBar)	0	0.64	1.28	1.92	2.56	3.83	5.11	7.67	12.78	30.1
p/p_0 (%)	0	2.12	4.25	6.37	8.5	12.72	16.98	25.48	42.46	100

To determine relevant sample positions for the experiment, rasterized transmission measurements, called nanography, of the dry sample with a stepsize of $300 \mu\text{m}$ were performed. A sketch of the nanography of the sample, with the selected measurement positions highlighted, is provided in **Figure 18 a)**. The elliptical shape of the 2-D SAXS

patterns observed in **Figure 18** b) and c) implies an anisotropic arrangement of scatterers within the sample.

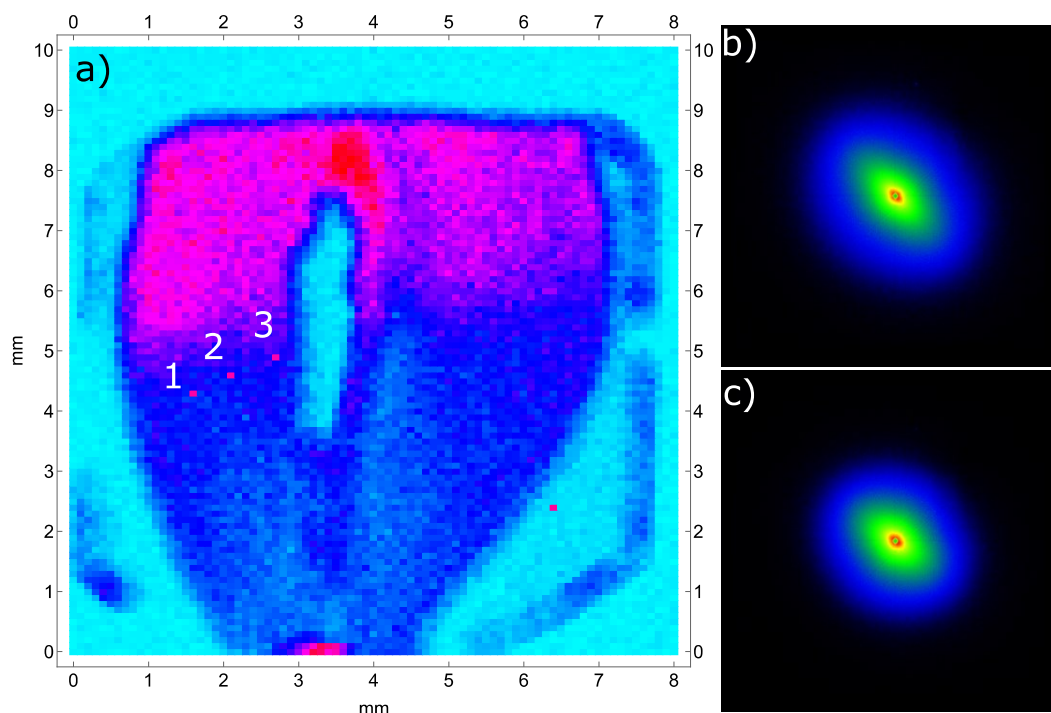


Figure 18: The nanography of one of the root dentin slices is shown in a), with the three measurement positions highlighted by the numbers, with 1 and 3 corresponding to the 2-D SAXS patterns b) and c). The red dot at the bottom right hand of the tooth is the position at which the background was determined.

4.3 In-situ water and n-pentane adsorption SANS on Carbon

The in-situ water and n-pentane physisorption experiments were conducted at the SANS-1 beamline¹³⁸ at the FRM2 at the MLZ Garching, Munich. Similar to the measurements on hierarchically porous silica published elsewhere earlier^{37,58,59}, a custom in-situ sorption system built by Stephan Braxmeier (ZAE, Bayern) was used. The structure of this particular vapor dosing system is essentially the same as the one described and shown above in **Figure 17**, except that an additional pressure gauge is installed close to the sample position.

Three monolithic, hierarchically porous carbon samples at different stages of activation (CN, C30, C120) were measured during the beamtime. Activation of the C30 and C120 samples was performed with CO_2 at $925^\circ C$ for 30 and 120 minutes respectively. Water and n-pentane were used in this experiment and in both cases the coherent scattering length density was tuned to zero by utilizing deuterated water and n-pentane. The mixtures used can be easily obtained by a simple linear model of the values in **Table 2** (taken from¹³⁹) and are for a C_5H_{12}/C_5D_{12} mixture 0.9068/0.0932 and for a H_2O/D_2O mixture 0.9195/0.0805.

Table 2: The specific mass density ρ (g/cm^3) at 20°C , coherent scattering length density σ_{co} ($10^{-6}/\text{\AA}^2$) and incoherent scattering length density σ_{inco} ($10^{-6}/\text{\AA}^2$) are shown for H_2O , D_2O , C_5H_{12} and C_5D_{12} respectively¹³⁹.

Material	H_2O	D_2O	C_5H_{12}	C_5D_{12}
ρ (g/cm^3)	1.00	1.11	0.62	0.71
σ_{co} ($10^{-6}/\text{\AA}^2$)	-0.56	6.40	-0.63	5.78
σ_{inco} ($10^{-6}/\text{\AA}^2$)	21.18	3.32	20.07	2.94

Due to the high fugacity of n-pentane a controlled desorption process was not possible with the sample cell used, which is why the measurement protocol for both adsorbates only included the adsorption branch of the physisorption isotherm. All samples were conditioned in the respective deuterated n-pentane mixtures for several weeks before experiment to ensure that potential surface groups containing non-deuterated n-pentane or water molecules to be of the same scattering length density. The thicknesses and diameters of the individual samples are shown in **Table 3**.

Table 3: The sample thicknesses $t_{Sample}^{C_5H_{12}}$ as well as the sample diameters of sample slices $D_{Sample}^{C_5H_{12}}$ are shown for the non-activated (CN), 30 minutes activated (C30) and 120 minutes activated (C120) carbon samples.

Sample	CN	C30	C120
$t_{Sample}^{C_5H_{12}}$ (mm)	0.381	0.381	0.398
$D_{Sample}^{C_5H_{12}}$ (mm)	6	6	6

Dilatometry

In-situ n-pentane adsorption dilatometry data shown in this work was collected by Christian Balzer (ZAE Bayern) in a commercial vapor sorption instrument (SPS-11 μ , prohumid). Prior to measurement, all samples were degassed for 24h at 50°C in a nitrogen stream (purity 5.0).

4.3.1 Vapor Dosing

The sample holder itself is a custom machined aluminum block with a circular cutout covered with a thin quartz window in up-stream direction, meaning away from the detector, and 0.1 mm thin aluminum window in downstream direction. Both materials were chosen due to their limited interaction with neutrons (activation) and hence their negligible effect on the experiment conducted. The quartz window was necessary to check the alignment of samples within the sample cell. In the sample holders center the samples are mounted on a flat aluminum disk with three evenly spaced holes of around 6 mm diameter, where the monolithic carbons samples are held in place. This particular sample holder also allowed for cooling of the sample with water by an external thermostat (Huber) and to track sample temperature with a thermocouple. In this experiment, the temperature was set to be 17°C , as to directly compare the effects of two different

adsorbates, once deuterated water and once deuterated n-pentane, on the deformation of the monolithic, hierarchically porous carbon introduced in chapter 2.2.

The experiment itself was controlled externally by a personal computer as all necessary components, the magnetic valves, the temperature and pressure read out, allowed connection via a RS-232 serial port. A custom script, written by and with Stefan Braxmeier (CAE Bavaria), was used to communicate with the controlsystem of the SANS-1 beamline, which allowed for a fully automatic conduction of the experiment.

In the first step, the samples and adsorption system were degassed for one hour. To ensure that no water adsorbed from air humidity was left after degassing, the samples were heated to 50°C. Except for the reservoir holding the O-SLD liquid, all components of the adsorption system were connected to a pump to remove all remaining fluid from the manifold and sample during degassing. Dosing of O-SLD water and n-pentane was performed following the same principle as described for in-situ absorption SAXS on human root dentin above. At the beamtime, dosing was performed automatically by a custom script. Short dosing bursts were used to reach the desired pressure in the manifold. Then, the samples were exposed to the vapor in the manifold. During the first 300 seconds of equilibration between sample and manifold the pressure at the sample was continuously measured. If the measured pressure fell below 2% of the desired pressure within these 300 seconds, another short dosing step was performed. Once measured pressure was within 2% of the desired pressure after 300 seconds, the system was allowed to equilibrate for a full 1800 seconds. After equilibration, the SANS measurement at the given relative pressure started. Once all SANS data were collected for a given relative pressure, the next pre-programmed pressure was reached by the procedure described above.

4.3.2 SANS

To cover as much of the reciprocal space as possible, two different sample-detector distances, 1.111m and 5 m, were used at a neutron wavelength of 0.55 nm. As a result, scattering vectors q ranging from 0.1 nm^{-1} to 5.4 nm^{-1} were covered in the experiment. Because adsorption induced strain was the focus of this beamtime, the (10) peak of the carbon mesostructure (**Figure 2 b**) had to be resolved well. For an approximate lattice parameter $d \sim 10$ of the 2-D hexagonally arranged carbon nanowires, the scattering vector of interest was $\sim 0.72 \text{ nm}^{-1}$ (equation 3.19). Large scattering vectors $q > 3 \text{ nm}^{-1}$ were also deemed important to accurately determine and correct the incoherent background scattering due to the material and the adsorbed liquid. Measurement protocol was determined by the need to measure data in absolute intensity units (scattering length density per volume and solid angle $\text{cm}^{-1} \text{sr}^{-1}$ ($= \frac{\text{cm}^2}{\text{cm}^3} \text{sr}^{-1}$)). Correction and azimuthal integration of measured data was performed with 'BerSans'¹⁴⁰, a software developed to treat SANS data. The formula to correct collected 2-D patterns read from an area detector is implemented in 'BerSans'¹⁴⁰ and reads as:

$$\frac{d\Sigma}{d\Omega}(q) = \frac{\frac{S_{ij} - C d_{ij}}{\tau(S)} A(S) - \frac{SB_{ij} - C d_{ij}}{\tau(SB)} (1 - p(S)) SF(W)}{\frac{W_{ij}}{\tau(W)}} \frac{SF(S)}{SF(S)}. \quad (4.1)$$

Here $\frac{d\Sigma}{d\Omega}(q)$ is the differential scattering cross section, S_{ij} , Sb_{ij} , W_{ij} and Cd_{ij} are the intensity values at the detector pixel $\{i, j\}$ of the sample, empty cell, water standard and cadmium absorber respectively. Cadmium, which is used to block the incoming neutron beam completely, is 'measured' to determine parasitic scattering from nearby sources not related to the incoming neutron beam and is subtracted from the sample and empty cell 2D patterns. The scaling parameters $A(s)$ and $p(s)$ are the attenuation factor and multiple scattering probability, $SF(W)$ and $SF(S)$ are scaling factors of the sample and water intensities. Finally, $\tau(s)$, $\tau(SB)$ and $\tau(W)$ are the transmissions of the sample, empty cell and water standard which compensate absorption and attenuation effects to scale measurements to the same transmitted neutron flux.

The measurement times for 5m were 1800 seconds for data collection and 300 seconds for transmission determination, whereas for the 1.111m sample-detector distance the measurement time was reduced to 900 seconds. It was deemed sufficient to determine transmission solely for the 5m distance. Transmission was determined by removal of the beamstop and setting attenuation from 'open' to 'x1000'. The same measurement was performed without sample to determine the incoming neutron flux. Hence, the sample transmission was determined as $\tau_s = I_{sample}^{Att}/I_{beam}^{Att}$. Similarly, transmission of the background was determined by measuring transmission on an empty cell.

To scale and correct the obtained 2D patterns, water filled in a so-called Helma©-cell (thickness 1mm) were measured for 3600s. Further, the empty Helma©-cell was measured for 1800 seconds. The measured 2D -scattering data was transmission corrected, background corrected and scaled in 'BerSans' and consequently azimuthally integrated to yield 1-D patterns with absolute intensity in $cm^{-1}sr^{-1}$ vs q in nm^{-1} .

4.4 In-situ water adsorption SANS on Silica

The in-situ water adsorption SANS experiments on hierarchically nanoporous silica are already published in Roland Morak's dissertation. Hence, experimental details are not discussed here and the focus lies on the correction of azimuthally averaged 1-D in-situ water adsorption SANS data.

The data reduction of the S-C sample is well documented in Morak et al³⁷, hence it will be omitted here. The S-A and S-S samples were collected at a different beam time than the S-C data, where only a reduced spread in scattering vector $0.1 nm^{-1} < q < 2.45 nm^{-1}$ was obtained in measurement. In these measurements it is critical to accurately subtract incoherent background scattering due to the sample and the adsorbed liquid, as it can distort the true position of the (10)-peak used to determine strain isotherms. Unfortunately large $q > 3 nm^{-1}$ are needed to accurately determine the incoherent background scattering. But because the water adsorption isotherms of the S-A and S-S samples are determined, the incoherent scattering of the sample can be estimated as a function relative pressure with the following equation³⁷:

$$\frac{d\Sigma^{inc}}{d\Omega}\left(\frac{p}{p_0}\right) - \frac{d\Sigma^{inc}}{d\Omega}(0) = \frac{\rho_s M_w}{\rho_w v_m} v_{ads} \left(\frac{p}{p_0}\right) \frac{d\Sigma^{inc}}{d\Omega}_{H_2O=1mm} \quad (4.2)$$

The parameters ρ_s and ρ_w are the specific densities of the macroscopic silica sample and water respectively, M_w and v_m are the molar weight and volume of water and $v_{ads}(p/p_0)$

is the adsorption isotherm of the sample. $\frac{d\Sigma^{inc}}{d\Omega_{H_2O=1mm}}$ is the incoherent scattering cross section of one mm of water and $d\Sigma^{inc}/d\Omega (p/p_0)$ is the incoherent scattering cross section of the sample at a relative pressure p/p_0 . The incoherent scattering cross section of the sample at a relative pressure of zero $d\Sigma^{inc}/d\Omega (0)$ remains undetermined as it cannot be determined with the given experimental SANS set up.

Fortunately SANS measurements from an earlier beamtime (see⁵⁸) on S-A and S-S samples from the same batch allowed to determine $d\Sigma^{inc}/d\Omega (0)$. With equation 4.2, the incoherent scattering background of the recorded SANS patterns was corrected as shown in **Figure 19 a)**. Exact positions q_{10} of the (10) peak due to the 2-D hexagonally ordered mesopores were obtained by fitting it with a Pseudo-Voigt-function (equation 3.31) in the intensities Kratky representation⁸⁰ (**Figure 19 b)**. Because these peaks were fit in the Kratky representation ($= q$ vs $I(q)q^2$), the area underneath it is the integrated intensity of the peak which can be calculated with equation 3.32.

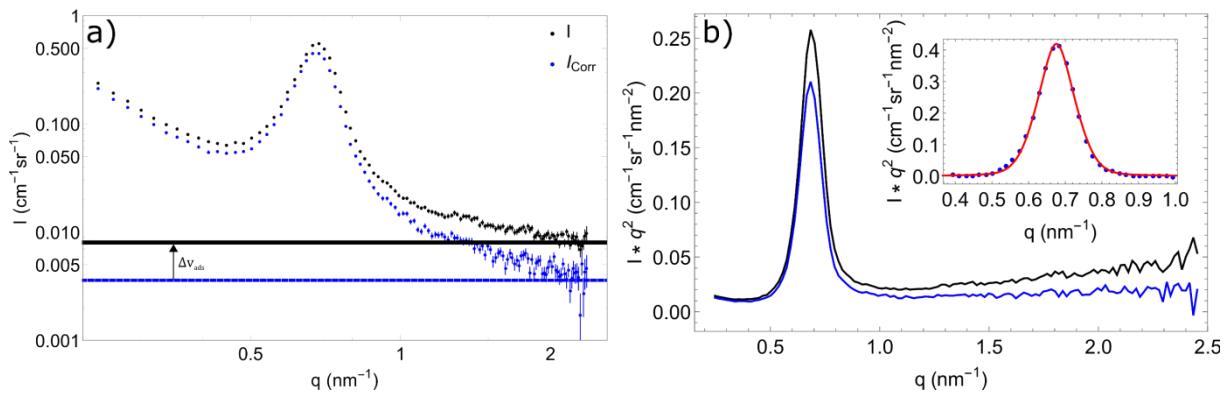


Figure 19: In a), the uncorrected and corrected SANS pattern of the S-A sample at $p/p_0 \sim 0.95$, where the black line corresponds to the original incoherent background from measurement and the blue line corresponds to the incoherent background of the empty sample. Their difference in intensity is directly related to the amount adsorbed v_{ads} through equation 4.2. Of note is the clearly distinguishable (10) peak of the 2-D hexagonally ordered cylindrical mesopores. In b) the uncorrected and corrected SANS pattern in the Kratky representation are depicted. In the inset, the fit (red line) of the visible (10) peak (blue dots) with a Pseudo-Voigt-function (equation 3.31).

5 Modelling of strains and apparent strains in hierarchical Silica

In this chapter the results and discussion of the SANS and SAXS in-situ sorption measurements (all performed by Roland Morak⁵⁸) are presented. In the first part, modelling of strain induced by water adsorption on monolithic, hierarchically nanoporous silica is performed. This first part is already published, hence all figures and tables presented are taken or derived from⁵⁹.

In the second part, models of apparent strain found in water in-situ adsorption SAXS measurements of the S-C sample are developed and their connection to the process of adsorption discussed. During the course of this section, simple mathematical tools to evaluate the micro- and mesoporosity in hierarchically nanoporous materials are introduced. The results of this second part are published in¹⁴¹.

5.1 In-situ small-angle neutron scattering investigation of adsorption-induced deformation in silica with hierarchical porosity

5.1.1 Experimental Results and Modelling

The experimental results section is divided into characterization of the S-A, S-C and S-S samples by nitrogen adsorption and additional water adsorption measurements. These experiments, in addition to He-pycnometry to determine the samples skeletal density, and their analysis were conducted by Christian Balzer at ZAE Bayern. The SANS data shown here was collected in dedicated in-situ water adsorption SANS experiments designed by Roland Morak, with the sorption system experimentally realized with the help of Stefan Braxmeier, ZAE Bayern. Stephan Braxmeier, Gudrun Reichenauer, Florian Putz and I provided assistance to Roland Morak at the allocated SANS beamtimes at the MLZ Garching.

5.1.1.1 Nitrogen and Water Adsorption

The experimental results of this section are already published fully in the dissertation of Roland Morak⁵⁸, partially in Morak et al³⁷ and Ludescher et al⁵⁹. They are shown to allow for sufficient discussion.

All three sample were characterized by water and nitrogen sorption, as shown in **Figure 20**. Both, the nitrogen and water adsorption isotherms, are of type IV⁹⁷ indicating cylindrical mesopores with micropores embedded in the mesopore walls. From nitrogen adsorption were the Gurvich volume v_{ads} (equation 3.40) and mesopore diameter d_{meso} (equation 3.43) determined. From the t-plot analysis⁹⁷ the specific external surface area S_{ext} , the specific micropore and mesopore volumes v_{μ} and v_m were determined. With equations 3.42a and 3.42b the micro- and mesopore volume fractions ϕ_{μ} and ϕ_m were calculated.

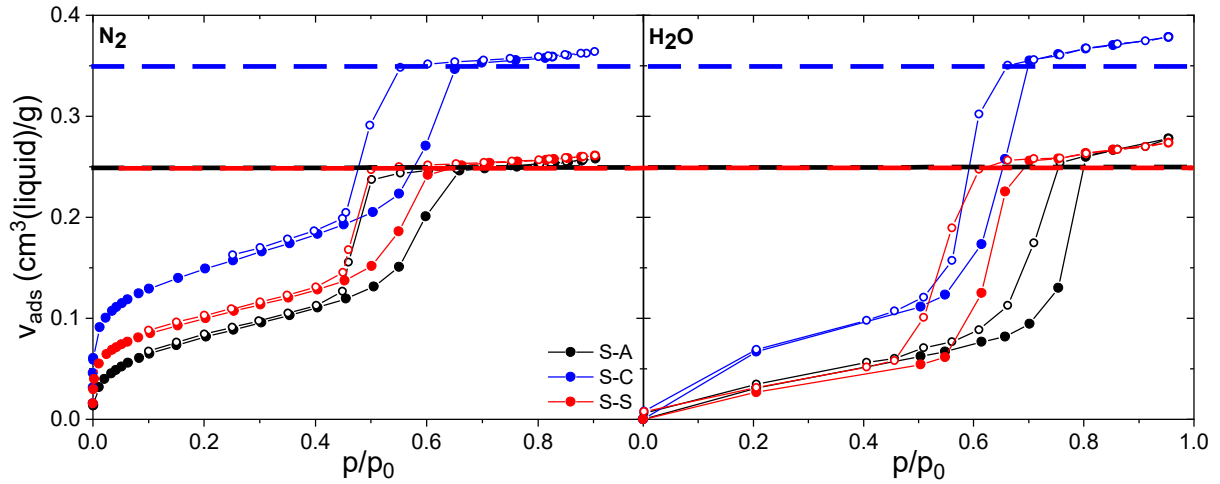


Figure 20: Nitrogen (left) and water (right) adsorption isotherms on monolithic, hierarchically nanoporous silica materials S-A (black), S-C (blue) and S-S (red). Absolute temperature of the measurements was 77.4 K and 290.15 K for nitrogen and water adsorption respectively. The adsorbed volume for all three samples are highlighted by dashed lines in the respective colours associated with the samples. (reprinted with permission from ACS publishing)

Additionally the sample density ρ and skeletal density ρ_s were measured in dedicated experiments. The results of the analysis of the nitrogen isotherms for all three samples are already published elsewhere^{58,59}, but they are shown again in a **Table 4** due to their relevance to the analysis of strain isotherms conducted later.

Table 4: Results for densities and pore space characteristics obtained from the nitrogen isotherms shown in **Figure 20**: the macroscopic sample density ρ , the adsorbed specific volume v_{ads} and the associated specific micro- and mesopore volumes v_μ and v_m , the external surface area S_{ext} , the mean cylindrical mesopore diameter d_{meso} and the volume fractions ϕ_m and ϕ_μ of the respective hierarchical levels. The skeletal density ρ_s was obtained from He-pycnometry.

Sample	ρ [g/cm ³]	ρ_s [g/cm ³]	v_{ads} [cm ³ /g]	v_μ [cm ³ /g]	v_m [cm ³ /g]	S_{ext} [m ² /g]	d_{meso} [nm]	ϕ_m	ϕ_μ
S-A	0.421	1.74	0.258	0	0.258	211	4.9	0.31	-
S-C	0.372	2.21	0.364	0.05	0.314	243	5.2	0.38	0.06
S-S	0.465	2.21	0.261	0.02	0.241	197	4.9	0.34	0.03

With the structural data v_{ads} , v_μ , v_m , S_{ext} and d_{meso} listed in **Table 4**, modelling of water isotherms was performed for the calcined sample S-C and sintered sample S-S. The necessary parameters such as the specific liquid tension γ_{lv} ($= 0.073 \text{ N/m}$), molar volume v_{mol} ($= 1.8 \cdot 10^{-5} \text{ m}^3/\text{mol}$) of water and the disjoining pressure isotherm (equation 3.80) are listed in **Table 5**. The values of the disjoining pressure parameters of water on amorphous silica were inferred from the values for nitrogen on silica³² (see **Table 5**) by Christian Balzer (ZAE Bayern) by modelling adsorption. Because it can be assumed that organics decorate the mesopore walls in the sample S-A³⁵, the interaction between water and the mesopore wall is undetermined and consequently no modelling was performed.

Table 5: Parameters Π_1 , Π_2 , λ_1 and λ_2 used for modeling of N_2 and H_2O sorption isotherms for the calcined and sintered samples are listed. This table is taken from Ludescher et al⁵⁹ (see SI).

	N_2 - calcined & sintered	H_2O - sintered	H_2O - calcined
Π_1 [MPa]	178	120	420
λ_1 [nm]	0.23	0.27	0.25
Π_2 [MPa]	68	200	-
λ_2 [nm]	0.073	0.05	-

The adsorption isotherms were modelled the following way: For the adsorption branch, for relative pressures below capillary condensation the film thickness of the adsorbed film $t(p/p_0)$ in a cylindrical pore of radius r was calculated with equation 3.50 as a function of relative pressure and translated into specific liquid loading in $cm^3(liquid)/g$ with equation 3.53. The relative pressure of capillary condensation p_{cap}/p_0 was determined with the condition described in equation 3.51. For all filled states $p/p_0 > p_{cap}/p_0$ the loading of mesopores was determined with equation 3.54. Modelling of the desorption branch follows the exact same procedure, only that the transition from filled mesopores to empty mesopores with a liquid layer is described with equation 3.52. Filling of micropores is handled independently from adsorption in mesopores and is added to the mesoporous contribution to the adsorption isotherm. It is modelled with Langmuir's isotherm (equation 3.39), where the empiric interaction parameter b was determined to be roughly 10^1 (for exact values see **Table 6**). The results of the modelling of water adsorption isotherms samples S-C and S-S are shown below in **Figure 21**.

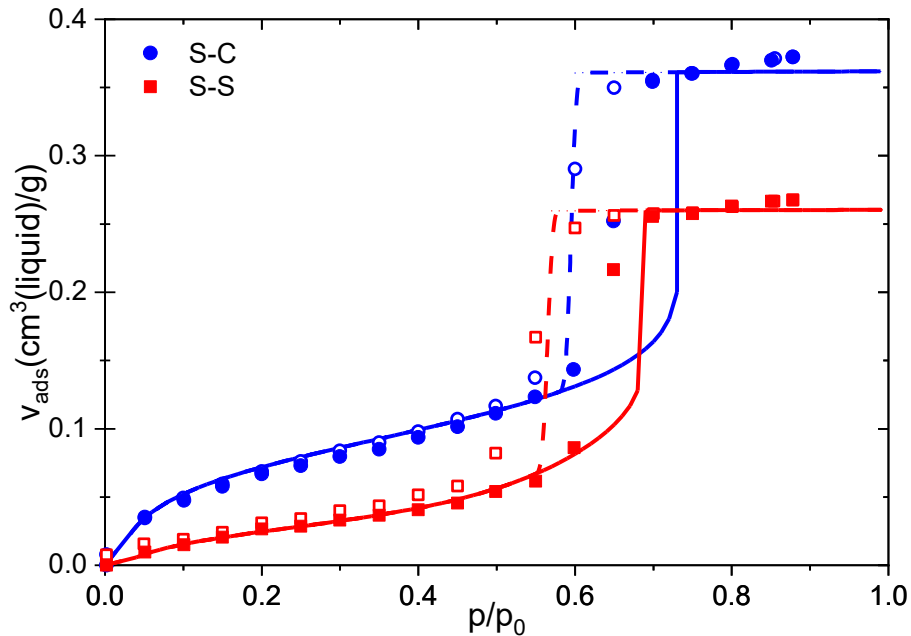


Figure 21: Water adsorption isotherms of the S-C (blue disks) and S-S (red rectangles) recorded at 290.15 K are shown, where filled symbols denote the adsorption branch and empty symbols the desorption branch. Fits of the adsorption isotherms with the DBdB model^{10,11} performed with equations 3.50-3.54 and parameters from **Table 4** and **Table 5** are

shown, with full lines denoting adsorption and broken lines desorption. (reprinted with permission from ACS publishing)

5.1.1.2 In-situ water adsorption SANS

All in-situ water sorption SANS and SAXS data was measured by Roland Morak and are published in his dissertation⁵⁸. Further, are all SANS, SAXS and dilatometry strain isotherms already published in Roland Moraks dissertation. Because these data sets are vital to the discussion, they are presented again and evaluated. The exact experimental details can be found in the References^{37,58} and ⁵⁹.

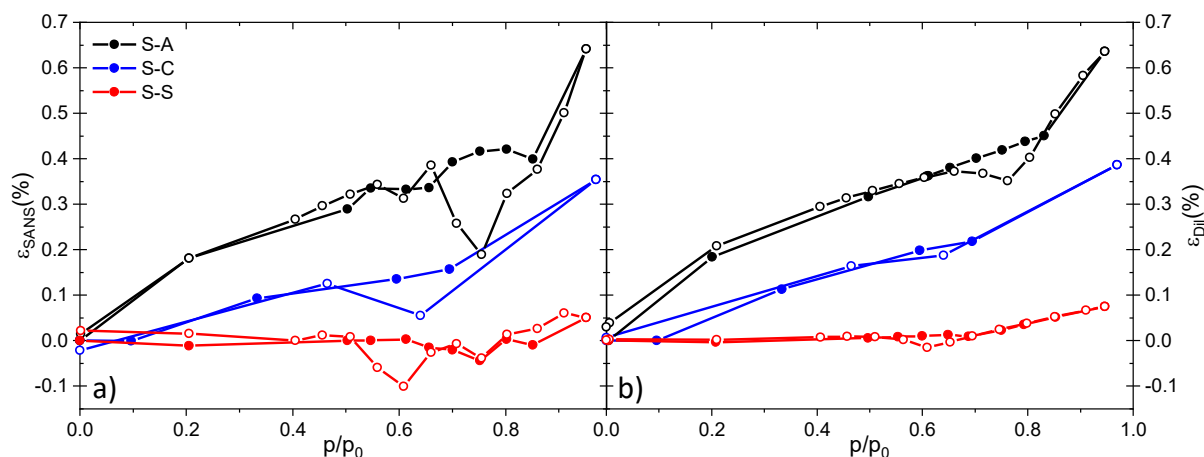


Figure 22: In a), the strains derived from in-situ water adsorption SANS of the S-A (black), S-C (blue) and S-S (red) samples are shown as a function of relative pressure. In b) water adsorption induced strains measured with dilatometry of samples from the same batch are presented. (reprinted with permission from ACS publishing)

In **Figure 22**, strain isotherms for samples S-A, S-C and S-S obtained from in-situ water sorption SANS and dilatometry are presented. The SANS water-adsorption strain isotherms were obtained fits of the (10)-peak with a Pseudo-Voigt function (equation 3.31), whereas evaluation of dilatometry data can be read up in References^{37,58,125}. For all three samples, the maximum strain at $p/p_0 \sim 0.95$ associated with complete filling of micro- and mesopores is equal between SANS and dilatometry and decreases from S-A ($\sim 0.68\%$) to S-C ($\sim 0.35\%$) and finally S-S ($\sim 0.05\%$). All strain isotherms, whether they were measured by SANS or dilatometry, exhibit a pronounced hysteresis, where position and breadth of hysteresis mirrors results from water adsorption (see **Figure 20**). With the structural data of all three samples (**Table 4** and **Table 5**) obtained from nitrogen adsorption and the modelled adsorption isotherms of the calcined sample S-C and sintered sample S-S, strain isotherms for SANS and dilatometry can be modelled.

It is convenient to model the mesoporous contribution to the strain isotherms first and deal with the microporous contribution later. From equations 3.92a (film phase) and 3.92b (filled phase) the adsorption induced stresses perpendicular $\sigma_{\perp, film/filled}$ to the long axis of the cylindrical mesopore are calculated. The axial adsorption induced stresses $\sigma_{\parallel, film/filled}$ are determined with equations 3.93a (film phase) and 3.93b (filled phase). A critical input for equations 3.92a and 3.93a is the associated film thickness $t(p/p_0)$ already used in the modelling of the adsorption isotherms (**Figure 21**) (obtained from equation 3.50). Once these stresses are calculated, the strains ϵ_{\perp} , ϵ_{\parallel} and ϵ_{meso} can in principle be determined. Unfortunately, the Young's modulus E and the factor x weighing

radial and axial strains to obtain ε_{meso} are not a priori known. These parameters can be later obtained from fitting equations 3.94a ($=\varepsilon_{\perp}$) and 3.94b ($=\varepsilon_{\parallel}$) plugged into equation 3.95 ($=\varepsilon_{meso}$) to measured dilatometry strain isotherms of the samples S-C and S-S. To model the radial deformations probed by SANS, equation 3.95 was modified to give:

$$\varepsilon_{SANS} = \frac{1}{3} \varepsilon_{\mu} + \varepsilon_{\perp}. \quad (5.0)$$

The microporous contribution to the adsorption induced strain isotherm ε_{μ} is calculated with equation 3.98, after the stresses σ_{μ} as a function of relative pressure are determined with equation 3.97. The filling of the micropores is modelled with Langmuir's isotherm in equation 3.97, with the necessary empiric interaction parameter b derived from fits of the water adsorption isotherms shown in **Figure 21** and listed in **Table 6**. The undetermined parameter $\delta b/\delta \varepsilon_{\mu}$ also needs to be determined from fits to the measured strain isotherms.

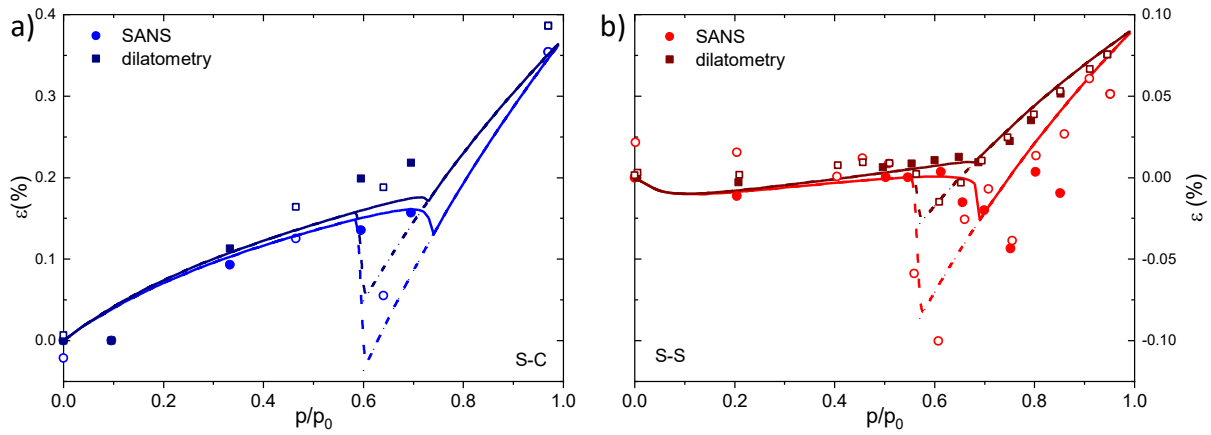


Figure 23: Fits of the in-situ water sorption SANS (disks) and dilatometry (rectangles) strain isotherms for the calcined sample S-C (a) and sintered sample S-S (b). Open and closed symbols, as well as full and dashed lines, correspond to the adsorption and desorption branch respectively. (reprinted with permission from ACS publishing)

From fits of the water adsorption SANS and dilatometry strain isotherms (see **Figure 23**), the Young's modulus E , the factor x and $\delta b/\delta \varepsilon_{\mu}$ are determined for the samples S-C and S-S. All fits were performed with the *NonlinearModelFit* function implemented in *Mathematica 11.3*©, because its algebraic language eases implementation of equations to be fit to data. In contrast to previous works by Balzer et al^{32,33} the factor x was left to be determined by the fit and was not set to a value of 0.33. The resulting parameters E , x and $\delta b/\delta \varepsilon_{\mu}$ are listed in **Table 6** below.

Table 6: Parameter b used for modeling adsorption and strain isotherms for the sintered and the calcined samples and the parameters E , x and $\delta b/\delta \varepsilon_{mic}$ obtained from the fit to the strain isotherms. The Poisson ratio was fixed to $\nu = 0.2$ for all strain calculations.

	nitrogen isotherms calcined & sintered	water isotherms sintered sample	water isotherms calcined sample
b	500	20	30
$\delta b/\delta \varepsilon_{mic}$	-	-70	-15
E [GPa]	-	40	20
x	-	0.5	0.65

5.1.2 Discussion of Results

First, nitrogen adsorption results for the S-A and S-C samples are discussed (**Table 4**). For the S-A sample the skeleton density $\rho_s = 1.74 \text{ cm}^3/\text{g}$ is significantly lower than the density of amorphous silica found in literature ($\rho_s \sim 2.1 \pm 0.1 \text{ cm}^3/\text{g}$)⁹⁰. The reason for this low skeletal density is the residual organics which are thought to decorate the mesopore walls³⁵. Calcination removed these residual organics and $\rho_s (\sim 2.2 \text{ cm}^3/\text{g})$ becomes comparable to amorphous silica³⁵. This increase in skeletal density upon calcination is accompanied with a loss of approximately $\sim 25 \text{ wt}\%$ attributed to the removed organics³⁵. Because the decrease of the samples density ρ between the S-A and S-C sample (see **Table 4**) is below 25%, shrinkage of the monolithic disks is indicated in parallel to mass loss. The increase in specific external surface area S_{ext} and specific mesopore volume v_m , as well as mesopore diameter d_{meso} , upon calcination found through nitrogen adsorption are only in the order of 10%. The specific microporosity present in the S-C sample is assumed to be already present in the S-A sample, but is blocked by the organic residuals which are removed upon calcination.

Sintering of the samples obviously reduced shrinking of material at all length scales when comparing S-S to S-C: the bulk density of the monolithic samples increases, while the average mesopore diameter and the specific mesopore volume decrease. A decrease in microporosity is also observed, which was the expected effect of continued thermal treatment.

Because both adsorbates, nitrogen and water (see **Figure 20**), exhibit the same specific pore volume v_{ads} in adsorption after capillary condensation has occurred, it can be assumed that they fill the same pore volumes. Compared to nitrogen adsorption, significantly higher relative pressures of capillary condensation are observed for water adsorption. Also, in contrast to nitrogen adsorption where all three samples exhibit similar relative pressures of capillary condensation, in water adsorption capillary condensation occurs at higher relative pressures. The S-A sample exhibits an even higher relative pressure of capillary condensation compared to the S-C and S-S samples. Additionally, loading of the samples right before capillary condensation is consistently lower in water adsorption than in nitrogen adsorption. This points to a different loading mechanisms of water in the silica materials and/or presumably stronger interaction between water and silica for S-C and S-S, which is most pronounced for the S-A sample. In this case, residual organics decorating the mesopore walls seem to increase hydrophobicity, which leads to higher pressures of capillary condensation even compared to the S-C and S-S samples. It can also be assumed that not adsorption but absorption of water in these residual organics is the leading loading mechanisms in the as-prepare sample S-A.

The water adsorption strain isotherms obtained with SANS and dilatometry (see **Figure 22**) show the typical shape associated with adsorption induced deformation in mesoporous solids^{26,27,36}. Between both measurements, SANS and dilatometry, a pronounced hysteresis is observed. The fact that strain isotherms obtained with dilatometry and SANS are of the same magnitude in the film state and arrive at practically the same value for complete loading of the micro- and mesopores ($p/p_0 \sim 0.95$) (see **Figure 22**) was predicted by Balzer et al³³ and already reported by Morak et al³⁷. This shows that an earlier work by Balzer et al³⁶, where in-situ pentane sorption SAXS and

dilatometry were compared and no accordance in magnitude of strain between both measurements was observed, was severely influenced by so-called apparent strains³⁸ in in-situ adsorption SAXS. In the case of SANS with Z-SLD water this effect is explicitly excluded and the strains measured should represent actual adsorption induced strains in the material.

For a quantitative description of the experimental strain isotherms obtained from in-situ water adsorption SANS and dilatometry the macroscopic thermodynamic model from Balzer et al^{32,33} introduced in chapter 3.3 is applied. First, the sintered sample S-S is considered, which shows the best agreement with the applied theoretical framework, since it contains no organic residuals and only little specific microporosity. First, the modeling of the water adsorption isotherm on the S-S sample (see **Figure 21**) is performed. Satisfactory agreement between experiment and model can be observed, although some deviations in the position and width of the hysteresis exist.

In **Figure 23 b)**, the fit of the model to in-situ water adsorption SANS and dilatometry strain isotherms is shown, where SANS data was modelled first because of its independence from influences of the strut network. Consequently, the Young's modulus E and $\delta b/\delta \varepsilon_\mu$ are determined from SANS, whereas x is obtained from fits of dilatometry data. The resulting fitted parameters E , x and $\delta b/\delta \varepsilon_\mu$ are presented in **Table 6** (the Poisson's ratio was set to $\nu \sim 0.2$). The latter parameter strongly determines the slope of the strain isotherm in the film regime and correctly predicts the slightly negative strains at relative pressures below capillary condensation. This non-monotonic behavior of the strain isotherms at low relative pressures could be explained by contraction of micropores upon water adsorption. This effect is notably different when compared to studies on a similar materials with nitrogen adsorption induced strain³³, where a consistent increase of strain was observed for small relative pressures. The young's modulus $E = 40 \text{ GPa}$ obtained from the fit is close to the value of $E = 42 \text{ GPa}$ obtained from the nitrogen strain isotherm of a sample with similar thermal history but a different drying process³³. A discrepancy for $x \sim 0.5$ between this thesis and an earlier work of Balzer et al^{32,33}, where $x = 0.33$, was found. Although x should be well determined from the aspect ratio of the silica struts building up the monolith and should be ≤ 0.33 , no satisfactory fit to the strain isotherms of the S-S sample was achieved with a value of $x = 0.33$. Possible reasons for this deviation will be discussed later below.

To better understand the effect of micropores in the strain isotherms, the strain modelling of the S-C sample (shown in **Figure 23**) is now discussed. Again, the water adsorption isotherm on the S-C sample is modeled first (**Figure 21**). The water adsorption isotherm agrees satisfactorily with measurement, although position and width of hysteresis doesn't reflect experimental data well. Of note in this regard is the difference in parameters describing the disjoining pressure between the S-S and S-C sample. These discrepancies regarding the description of hysteresis, which are also present for the S-S sample, are most likely due to inaccuracies of the parameters of the disjoining pressure (**Table 5**). or due to omittance of influences of local pore structure, such as corrugations^{105,142,143}, which most likely differ between both samples.

Modeling of the SANS and dilatometry water adsorption strain isotherms of the S-C sample yields satisfactory agreement between model and experiment as shown in **Figure 23**. The Young's modulus $E = 20 \text{ GPa}$ is in fair agreement with results from nitrogen adsorption on a sample with similar thermal history ($E = 27 \text{ GPa}$ ³³). Although a dip in

the strain isotherm of the S-C sample is observed for small relative pressures in SANS and dilatometry (see **Figure 22** and **Figure 23**), the parameter $\delta b/\delta \varepsilon_\mu$ could not be adjusted while ensuring a satisfactory fit to the strain isotherm at higher relative pressures. Also, the parameter $x = 0.65$ is nearly a factor of 2 larger than expected from the geometry of the struts and from nitrogen adsorption³³ where $x = 0.33$. With the aspect ratio of the struts being around 3:1 between strut length and diameter, the axial strain ε_\parallel should dominate the macroscopic strain measured with dilatometry (see equation 3.95). But as shown below, modelling of strain isotherms with x fixed at the value of 0.33 (see **Figure 24** a) and b) yields unphysical results where parts of the adsorption and desorption branch of ε_{dil} cross.

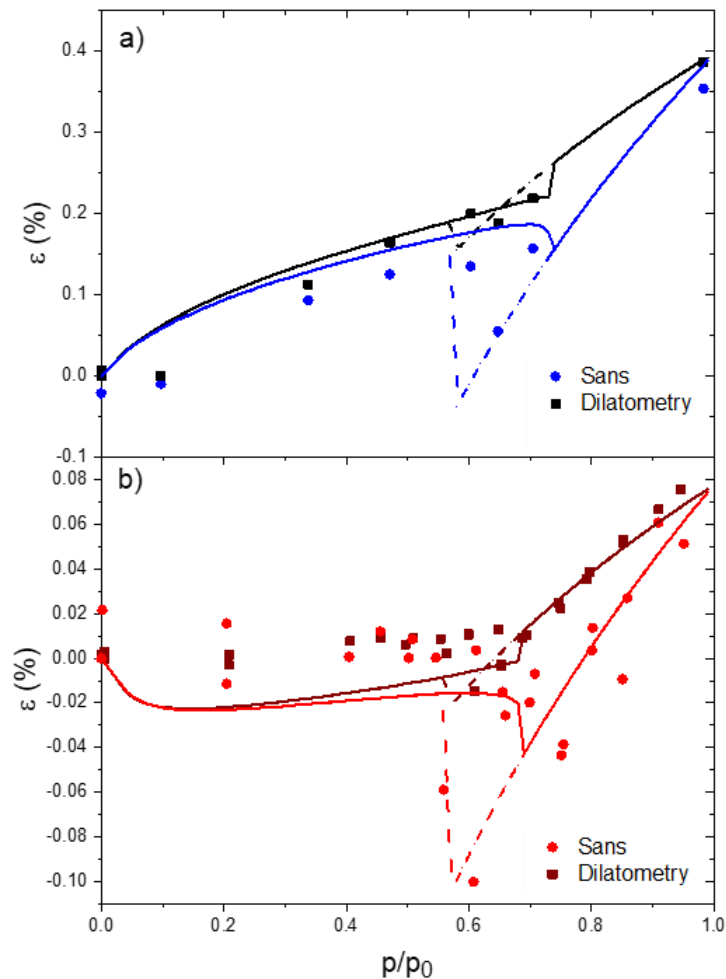


Figure 24: In a) and b) alternative fits of the in-situ water adsorption SANS and dilatometry strain isotherms for the samples S-C (a) and S-S (b) are presented. (reprinted with permission from ACS publishing)

A possible reason for this discrepancy could be the insufficient modelling of the adsorption isotherm in the relative pressure interval where capillary condensation takes place (**Figure 21**). Alternatively, one could surmise that the aging process softens the joints which connect individual struts together and that higher strains induced by water adsorption lead to deformations not covered by equation 3.95.

Finally, the as-prepared silica sample S-A is discussed. Since the interaction between water and organic residues is not easily quantified, no modelling of this sample was performed. Still, the overall shape of the adsorption strain isotherm is qualitatively similar

to the S-C sample, while the magnitude of strain is a factor 2 larger (**Figure 21**). This suggests that either the organic residuals lower the Young's modulus of the mesopore walls, or that these organic residuals absorb water and swell. The scenario of absorption is so far not covered by the macroscopic thermodynamic model developed by Balzer et al^{32,33}.

5.2 Hierarchically Nanoporous Silica: Adsorption Isotherm and Adsorption-Induced Deformation from Small-Angle X-ray Scattering

The SAXS patterns and in-situ water adsorption experiments analyzed in this part of the thesis were all performed by Roland Morak, with the results partially published in his PHD-thesis⁵⁸. Because the results from nitrogen adsorption are already presented and discussed in the section above (see **Table 4**), they are only referred to here. Additionally, apparent strains are only analyzed for the S-C sample. The sample S-A was not suitable because the interaction of water with organic residuals decorating the mesopore walls is undefined, whereas no complete data set of water adsorption and desorption was available for the sintered sample S-S. This section was published in Reference¹⁴¹ and all figures and tables are taken from it or have been altered slightly for the purpose of presentation in this thesis.

5.2.1 Experimental Results:

SAXS and SANS scattering data for the same S-C sample are shown in **Figure 25** for the completely empty sample state ($p/p_0 = 0$) and for a sample state where all micro- and mesopores are filled with liquid water ($p/p_0 \sim 0.95$). The 2-D hexagonal order of cylindrical mesopores is confirmed by the clear Bragg reflections in the SANS/SAXS scattering patterns. Due to the lower resolution of SANS experiments, higher order peaks are smeared out and considerably broadened. For both samples a constant background was subtracted and the Porod law at high q ($> 2.5 \text{ nm}^{-1}$) enforced. The SANS data shows almost no intensity change as a function of relative pressure, which is a direct consequence of adjusting the adsorbate to Z-SLD. In contrast, a large drop in intensity at large q can be observed, while at low q an increase in intensity can be observed. This effect can only be due to the change of scattering length density in the sample as a consequence of adsorption. Interestingly, filling of micro- and mesopores doesn't result in a uniform shift of intensity to smaller values for the SAXS curves. This is a direct consequence of the hierarchical structure of the material. Because only the micro- and mesopores are filled at $p/p_0 \sim 0.95$ with water, only large and intermediate q - values exhibit a decrease in intensity with loading and consequent decrease in scattering contrast between pore and silica matrix. The macropores on the other hand are not filled at $p/p_0 \sim 0.95$, which leads to an increase in mean scattering length density of the strut with loading of micro- and mesopores. This leads to a larger scattering contrast between the strut and the empty macropores surrounding it, which results in a relative increase in intensity in relation to the empty sample state at $p/p_0 \sim 0$.

In the insets in **Figure 25** a) and b) the (10) peak shifts are shown for SANS and SAXS respectively. Whereas a pronounced shift of the (10) peak to lower q can be observed for SANS, which indicates expansion of the sample (also check **Figure 22**), no clear shift in (10) peak position can be seen for the SAXS data. The strain isotherm for the calcined sample S-C was determined by fitting the (10)-peak of the 1-D patterns and is shown along with the SANS strain isotherm in **Figure 26** a).

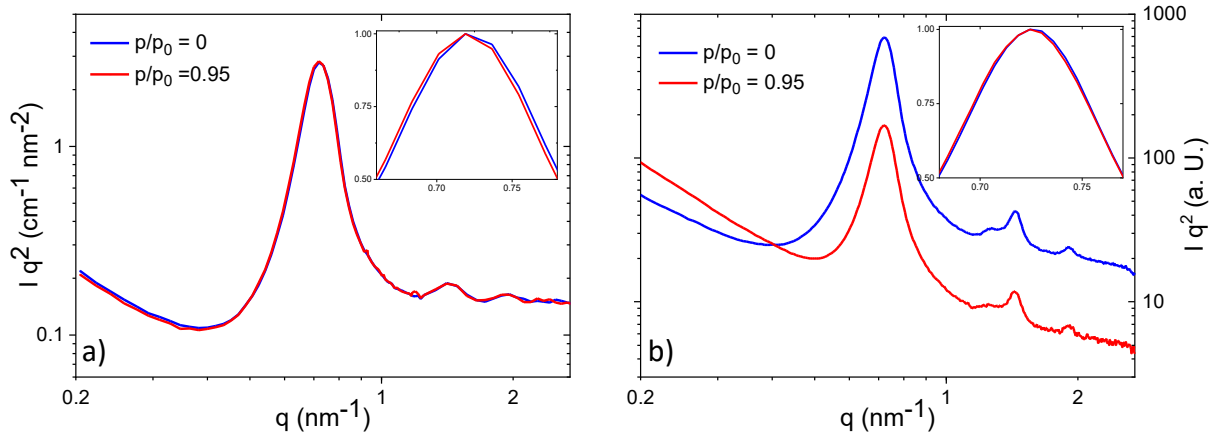


Figure 25: (a) In-situ SANS and (b) in-situ SAXS profiles in a Kratky plot representation for two different relative vapor pressures of Z-SLD water. The insets show the normalized (10) peaks to visualize the peak shifts. (reprint from Ref.)

There are pronounced differences between both strain isotherms, where, after a similar increase in strain for small relative pressures, a significantly larger drop in strain is observed for SAXS than is for SANS. Once capillary condensation is complete, both strain isotherms show again similar, yet constantly off-set increases in strain until all micro- and mesopores are filled at $p/p_0 \sim 0.95$. Similar results have been reported by Balzer et al³⁶ where in-situ n-pentane adsorption SAXS was compared to dilatometry. But the macroscopic, thermodynamic model^{32,33} applied above has correctly described that dilatometry and SANS should yield the same strains once micro- and mesopores are filled⁵⁹.

Consequently, it can be deduced that the SAXS strain isotherm in **Figure 26 a)** is strongly affected by so-called apparent strains³⁸ which are a function of the pore filling. The SANS strain isotherm in **Figure 26 a)** can be thought to be a correct reflection of the true adsorption induced strains in the material. In a first approximation, the strains from SAXS are assumed to be a simple sum of true and apparent strains. Hence, the apparent strain isotherm can be calculated with:

$$\varepsilon_{\text{apparent}} = \varepsilon_{\text{SAXS}} - \varepsilon_{\text{SANS}}, \quad (5.1)$$

where individual strain contributions are denoted by their subscript. The measured apparent strains of the S-C sample, as determined from SAXS and SANS strain isotherms with equation 5.1, are shown in **Figure 26 b)**. The errorbars in this figure are a consequence of the limited resolution in relative pressure and strain in the SAXS and SANS experiments and are consequently larger, the larger changes in one or both strain isotherms are. Below capillary condensation the apparent strains are relatively small, but once mesopores fill a large jump to compressive apparent strains is observed. At relative pressures above capillary condensation no significant changes in apparent strain occur, as most if not all micro- and mesopores are completely filled with condensed liquid. Still, the apparent strain in filled sample states is not equal to zero as one would expect. In the following, two models are developed and applied to qualitatively and quantitatively predict apparent strains over the whole relative pressure range used in adsorption experiments. In Model 1 the simplified case of adsorption of liquid on perfectly smooth, cylindrical mesopore walls omitting the influence of micropores is treated, whereas in Model 2 micropores are explicitly taken into account as well.

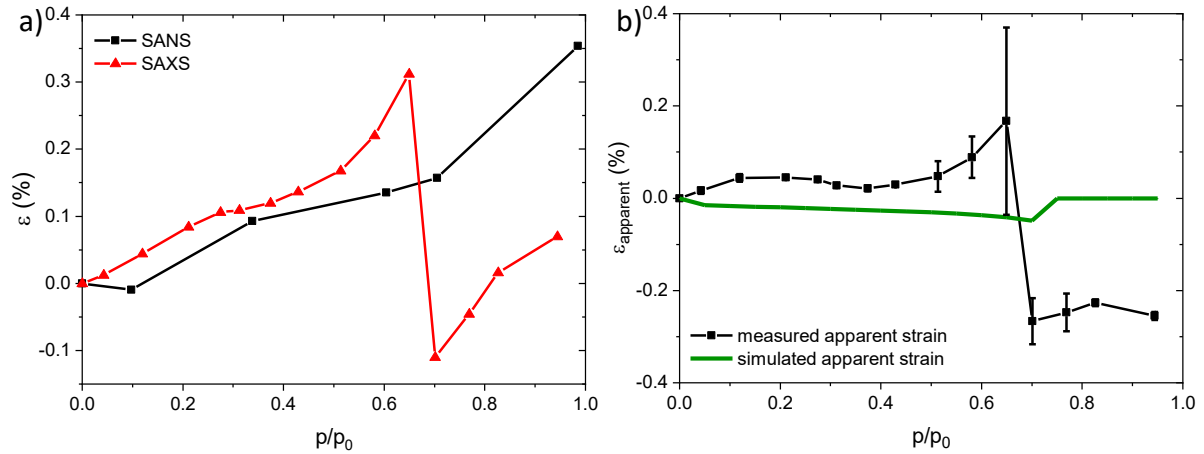


Figure 26: a) Experimental SANS (black symbols) and SAXS (red symbols) adsorption strain isotherms obtained from the shift of the (10) Bragg reflection. In b) the measured apparent strain isotherm (black symbols) is determined from the data in a) by Eq. 1. The green curve is the simulated apparent strain isotherm using a model for a purely mesoporous system (Model 1). (reprint from Reference ¹⁴¹)

5.2.2 Theoretical Modelling

The approach of Prass et al³⁸, who only modelled apparent strains in the relative pressure region of capillary condensation both numerically and analytically, is extended to model apparent strains over the whole range of relative pressures $0 < p/p_0 \leq 0.95$. This is achieved by simulating SAXS patterns of a single, mesoporous model strut with microporous walls. The loading of this model strut is adjusted with relative pressure to reflect adsorption of water in the S-C sample. The SAXS pattern at each relative pressure is then evaluated for strains by tracking the shift of the (10)-peak, while keeping the lattice parameter d constant.

5.2.2.1 SAXS from a hexagonal lattice of cylindrical mesopores

To model SAXS from a purely mesoporous strut, the Debye scattering formula is applied. Because the length of the struts is much larger than the diameter of the mesopores, a two dimensional approach is sufficient (equation 3.37). The form factor of the circular mesopore cross-section is approximated with the step-density model adapted from Zickler et al⁹⁰, introduced with equation 3.21. At the dry reference state this allows to obtain information on the structure complementary to nitrogen adsorption (see **Table 4**). For the S-C sample, four peaks are distinguishable (see **Figure 25**), confirming 2-D hexagonal order of cylindrical mesopores. At $p/p_0 = 0$, the film radius $r_3 = r_2$, the inner corona radius, and equation 3.21 takes the form:

$$F(q) = k \left((\alpha - 1)r_1^2 \frac{2 J_1(qr_1)}{qr_1} - \alpha r_2^2 \frac{2 J_1(qr_2)}{qr_2} \right), \quad (5.2)$$

with r_1 and r_2 being the outer and inner radii of the corona. With equation 5.02, the peak intensities of the SAXS pattern of the S-C sample at $p/p_0 = 0$ can be fit⁹⁰ to determine $\alpha(p/p_0 = 0)$ (from here-on abbreviated with α_0) and the radii r_1 and r_2 . With these parameters an 'equivalent' mesopore radius $\bar{r} = \sqrt{r_2^2 + (1 - \alpha_0)(r_1^2 - r_2^2)}$ can be determined, which is listed in **Table 7**. Further, with the lattice parameter d calculated from the position of the (10)-peak q_{10} , the mesoporous volume fraction ϕ_m can be

determined with equation 3.23. Similarly, the volume fractions of the corona $\phi_{corona} = (2\pi/3) ((\bar{r}^2 - r_2^2)/d^2)$ and the remaining mesopore space outside the corona $\phi_{m,0}$ can be calculated.

Table 7: Mesopore parameters obtained from SAXS patterns of the empty sample S-C: outer and inner corona radii r_1 , r_2 , relative corona electron density α_0 , equivalent radius \bar{r} , and mesoporosities $\phi_m (= \phi_{corona} + \phi_{m,0})$. From adsorption the variance σ_m of mesopore radii which are assumed to be normal distributed is presented. (reprint from Reference ¹⁴¹)

r_1 (nm)	r_2 (nm)	α_0	\bar{r} (nm)	d (nm)	ϕ_m	ϕ_{Corona}	$\phi_{m,0}$	σ_m (nm)
3.81	2.39	0.5	3.19	10.1	0.36	0.16	0.20	0.09

To simulate SAXS patterns of the whole strut, a single mesoporous strut of quadratic cross section hosting an assembly of 30 x 30 two-dimensional hexagonally arranged cylindrical mesopores. This corresponds roughly to a strut of 350 nm which is of similar size as in the real material (see **Figure 1 a**). At each position of the lattice a mesopore of a randomly chosen size is seeded with a normal distribution, where the mean radius \bar{r} is obtained from SAXS at $p/p_0 = 0$ (see **Table 7**) and the variance σ_m is obtained from the water adsorption isotherm as follows. In **Figure 20**, capillary condensation occurs between relative pressures of 0.55 and 0.7 p/p_0 . This can be translated into mesopore radii by solving equations 3.50 and 3.52 simultaneously at these relative pressures with a simple root finding algorithm. This results in a minimum radius of 2.25 nm at $p/p_0 = 0.55$ and a maximum radius of 3.75 nm at $p/p_0 = 0.7$. By assuming a normal distribution of mesopore radii, this interval can be interpreted to be of total width $6\sigma_m$. Hence, the mean variance $\sigma_m = 0.25$ is defined and can be used as input for the simulation.

Additionally, to model static disorder of the mesopore lattice¹⁴⁴, each mesopore center is slightly, randomly offset. This is modelled with a normal distribution with a mean value of 0 and variance σ_{DW} of 0.09. This specific value was determined empirically to match the number of peaks differentiable in the simulated SAXS patterns with experiment. The scattered intensity from the mesoporous model strut is then calculated numerically with the two-dimensional Debye scattering equation (equation 3.17).

5.2.2.2 Model 1: Film growth and capillary condensation in cylindrical mesopores

In this model cylindrical mesopores with perfectly smooth mesopore walls are assumed, while micropores are omitted. The filling of the mesopores with water is modelled with the DBdB-formalism¹⁰⁻¹² introduced in chapter 3, hence under the assumption of a growing liquid film until complete filling of the pore with capillary condensation. The form factor applied reads as:

$$F(q) = k \left((\beta - 1)r_1^2 \frac{2 J_1(qr_1)}{qr_1} - \beta r_2^2 \frac{2 J_1(qr_2)}{qr_2} \right), \quad (5.3)$$

with β being the relative scattering length density of bulk water ($\rho \sim 1.01 \text{ cm}^3/\text{g}$) in relation to bulk silica ($\rho = 2.2 \text{ cm}^3/\text{g}$). Radius r_1 corresponds to the equivalent mesopore radius \bar{r} (see **Table 7**) and r_2 to the film radius $r_{film} = \bar{r} - t(p/p_0)$, with $t(p/p_0)$ being the film thickness of the adsorbed multimolecular film and the only quantity in equation 5.3 dependent on relative pressure. The film thickness $t(p/p_0)$ is calculated with equation 3.50, with the disjoining pressure parameters taken from **Table 5** and $\gamma_{lv} = 0.073 \text{ N/m}$ and $v_{mol} \sim 1.8 \cdot 10^{-5} \text{ m}^3/\text{mol}$. Once this relative pressure is reached r_2 is set to 0, the second term in the brackets in equation 5.3 becomes 0. The pressure of capillary

condensation was modelled using equation 3.52 for reasons discussed later. Because the mesopore radii are seeded randomly, the adsorption isotherm for every single mesopore needs to be calculated and taken into account. A sketch of this mesopore model is supplied in **Figure 27 a)**.

Figure 27 b) shows simulated SAXS patterns for the empty state ($t = 0$), for a film with thickness $t = 0.34 \text{ nm}$ and completely filled mesopores. A slight, apparent shift in position of the (10) peak is observable for $t = 0.34 \text{ nm}$ in the inset of **Figure 27 b)**, however the peak positions of the empty and filled sample align perfectly. This is evident from equation 5.3: a relative pressure $p/p_0 = 0$ necessitates $r_{film} = \bar{r}$, which cancels all terms proportional to β and only the first term in the form factor $F(p/p_0 = 0)$ is left; but once r_{film} is 0 for $p \geq p_{cap}$, the form factor $F(p/p_0 = 0)$ is retained, scaled down by $(\beta - 1)$. SAXS curves were simulated using the form factor equation 5.3 for 20 distinct, evenly spaced relative pressures between 0 and 95%. From these simulated SAXS patterns, the apparent strains were determined from the shift of the center of mass of the (10) Bragg peak. These apparent strains are shown in **Figure 26 b)** with the corresponding measured apparent strains. It is obvious that the simulated apparent strain fails to predict the measured apparent strain of S-C both in direction and magnitude. The simulated apparent strain takes exclusively negative values in the film regime, contrasting the positive apparent strains of the S-C sample in the film regime. Measured apparent strains show a pronounced negative offset in the filled pore regime, whereas simulated apparent strains are effectively 0. From these observations it can be concluded that the model applied is too simple to determine apparent strains in a hierarchical micro-/mesoporous material. However, this model could be applicable to model apparent strains in purely mesoporous materials with reasonably smooth pore walls.

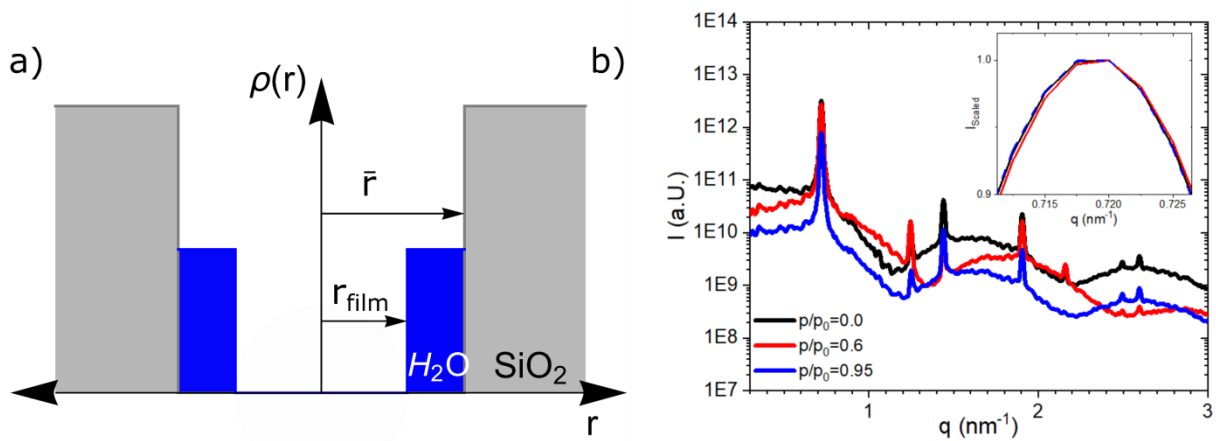


Figure 27: a) Step density model for mesopore filling. b) Simulated scattering patterns using Eq. 3 for four different relative pressures corresponding to various film thicknesses ($t = 0 \text{ nm}$, $t = 0.34 \text{ nm}$ and $t = R_m$), with the inset depicting a zoom of the (10) peaks scaled to 1 for better visibility of the apparent strains. (reprint from Reference ¹⁴¹)

5.2.2.3 Model 2: Hierarchical pore model

To model apparent strains more accurately, the hierarchical pore model by Gommès et al ⁸⁹ introduced in chapter 3 is applied. In it the SAXS intensity is assumed to be an incoherent superposition of macro- (I_M), meso (I_m) and microporous (I_μ) scattering

contributions (equation 3.17). To implement the dependence of this model on relative pressure, the macro- and microporous contributions need to be reformulated.

Because the macroporous scattering $I_M(q)$ is assumed to result from the surface scattering of the strut, it is sensitive to the mean scattering density inside⁸⁹. This leads to

$$I_M(q, p/p_0) = 2\pi \left((1 - \phi_m)(1 - \phi_\mu) \rho_{\text{SiO}_2} + \phi_{\text{H}_2\text{O}}(p/p_0) \rho_{\text{H}_2\text{O}} \right)^2 \frac{A_g}{q^4}, \quad (5.4)$$

with ϕ_m and ϕ_μ being the mesopore and micropore volume fractions, ρ_{SiO_2} and $\rho_{\text{H}_2\text{O}}$ being the bulk silica and bulk water electron densities in e^-/nm^3 and A_g being the strut surface. The dependence of equation 5.4 on relative pressure is introduced with $\phi_{\text{H}_2\text{O}}(p/p_0)$, which is the volume fraction of adsorbed liquid water as a function of relative pressure. Of note is the fact that the surface scattering obtained from application of the Debye equation (equation 3.37) gives an incorrect contribution to mesoporous patterns obtained from simulation. The origin of this effect is found in the fact that all applied mesopore form factors (equation 3.21)⁹⁰ were derived as if the mesopore were situated in an infinite silica volume. As implied according to equation 3.10, the surface scattering of the strut is directly proportional to the square of the difference in scattering length density between its inside and outside. By application of equation 3.37, the outside of the simulated strut is bulk silica and not vacuum as is the case in our materials (see **Figure 1 a**). The incorrect surface scattering must be subtracted and substituted with the correct surface scattering covered with equation 5.4.

The microporous scattering contribution $I_\mu(q, p/p_0)$ is modelled with an assembly of uncorrelated spherical mesopores within the mesopore walls (see equation 3.17 and 3.20). The resulting equation reads as⁸⁹:

$$I_\mu(q, p/p_0) = 8 \pi^3 V_G K(p/p_0) (1 - \phi_m) \phi_\mu (1 - \phi_\mu) f_\mu^2(q, r_\mu, \sigma_\mu) \quad (5.5)$$

which closely resembles the expression reported by Gommers et al⁸⁹ except for the fact that a dedicated form factor representing polydisperse, spherical micropores is applied. Consequently, the form factor $f(q, r_\mu, \sigma_\mu)$ depends on a mean micropore radius r_μ and the standard deviation σ_μ . The only term depending on relative pressure in equation 5.5 is the scattering contrast $K(p/p_0)$. It is dependent on the micropore filling fraction $Y_\mu(p/p_0)$ which is determined with Langmuir's isotherm (equation 3.39) in this thesis. The scattering contrast is expressed as the linear combination between empty and filled micropores:

$$K(p/p_0) = (1 - Y_\mu(p/p_0)) (\rho_{\text{SiO}_2})^2 + Y_\mu(p/p_0) (\rho_{\text{SiO}_2} - \rho_{\text{H}_2\text{O}})^2. \quad (5.6)$$

In the simulation it is assumed that all micropores fill instantaneous and also independent of each other.

The mesopore contribution to the SAXS intensity is essentially the same as outlined in the previous section. In contrast to growth of a liquid film which dictates filling for relative pressures below capillary condensation in a purely mesoporous material (Model 1), it is not obvious how filling in mesopores exhibiting a microporous corona proceeds as a function of relative pressure. Hence, a detailed analysis of the scattering patterns of the associated in-situ water adsorption SAXS experiment carried out by Roland Morak⁵⁸ was performed.

5.2.2.4 *In-situ water adsorption SAXS analysis*

The in-situ water adsorption SAXS patterns were evaluated for mesoporous and microporous volume fractions, as well as for the filling fraction as a function of relative pressures. In total, 15 SAXS patterns at various pressures measured in the adsorption branch of the isotherm, were analyzed. To obtain the integrated intensities of the individual peaks they were fit with a Pseudo-Voigt function (equation 3.31) in a Kratky-representation of the intensity⁸⁰. This conveniently allows to determine their integrated intensity and its error due to the fitting procedure with equations 3.32 and 3.33 respectively. Form factor fits⁹⁰ of the integrated peak intensities were performed for all 15 SAXS patterns. In these fits, both, the relative corona density $\alpha(p/p_0)$ and the film radius $r_3(p/p_0)$ in equation 3.21, were allowed to be varied with relative pressure. To limit the number of variables to be fit, the inner and outer corona radii r_1 and r_2 , as well as the relative electron density of water $\beta = \rho_{H_2O}/\rho_{SiO_2}$, in equation 3.21 were set to be constant.

These form factor fits at relative pressures $p/p_0 > 0$ reveal the distribution of liquid inside the mesopores as a function of relative pressure. Effectively, equation 3.21 describes loading of the corona with liquid by increase of $\alpha(p/p_0)$ and growth of a liquid film for pressures $p < p_{cap}$ (see **Figure 6**) by decrease of the film radius $r_3(p/p_0)$. To perform fits of the relative corona density and liquid film radius r_3 (with a set relative electron density of $\beta = \rho_{H_2O}/\rho_{SiO_2}$), the inner and outer corona radius r_2 and r_1 were taken from the reference state (**Table 7**) and held constant. Interestingly, for relative pressures below capillary condensation, a progressive increase of α (**Figure 29 a**) with relative pressure was sufficient and no film was needed to satisfactorily fit the integrated intensities (see **Figure 29 c** and **d**). This points to a pore filling mechanism of water in highly corrugated silica mesopores different from the usual film formation mechanism. The different shape of the water isotherm as compared to the nitrogen isotherm in **Figure 20** seems to support this hypothesis.

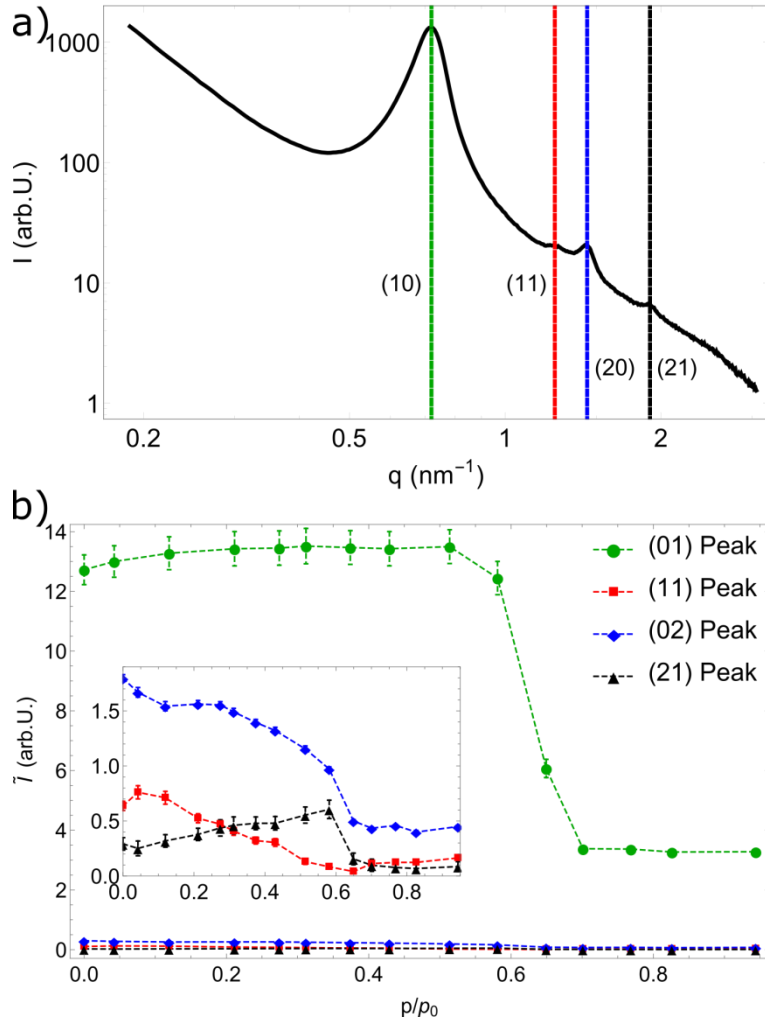


Figure 28: In a) the calcined samples SAXS pattern in its dry reference state is shown, with all four discernible peaks ((10), (11), (20), (21)) highlighted by colored lines. Integrated peak intensities and their associated errors for all four peaks versus relative pressure are shown in b).

For pressures $p \geq p_{cap}$ equation 3.23 was utilized to fit integrated peak intensities. For these fits the relative corona electron density α of the mesopore fractions in the filled and liquid film state, as well as the filled mesopore fraction Y_m were fitted (see **Figure 29** e and f). For the filled sample states for $p > p_{cap}$, the α -values approach the theoretical values for $\alpha = \alpha_0 + (1 - \alpha_0 \rho_{H_2O} / \rho_{SiO_2})$ of ~ 0.76 as indicated by the red line in **Figure 29** a). Similarly, the fraction of mesopores in the filled state Y_m reaches 1 in the an intervall of 0.6 to 0.75 p/p_0 .

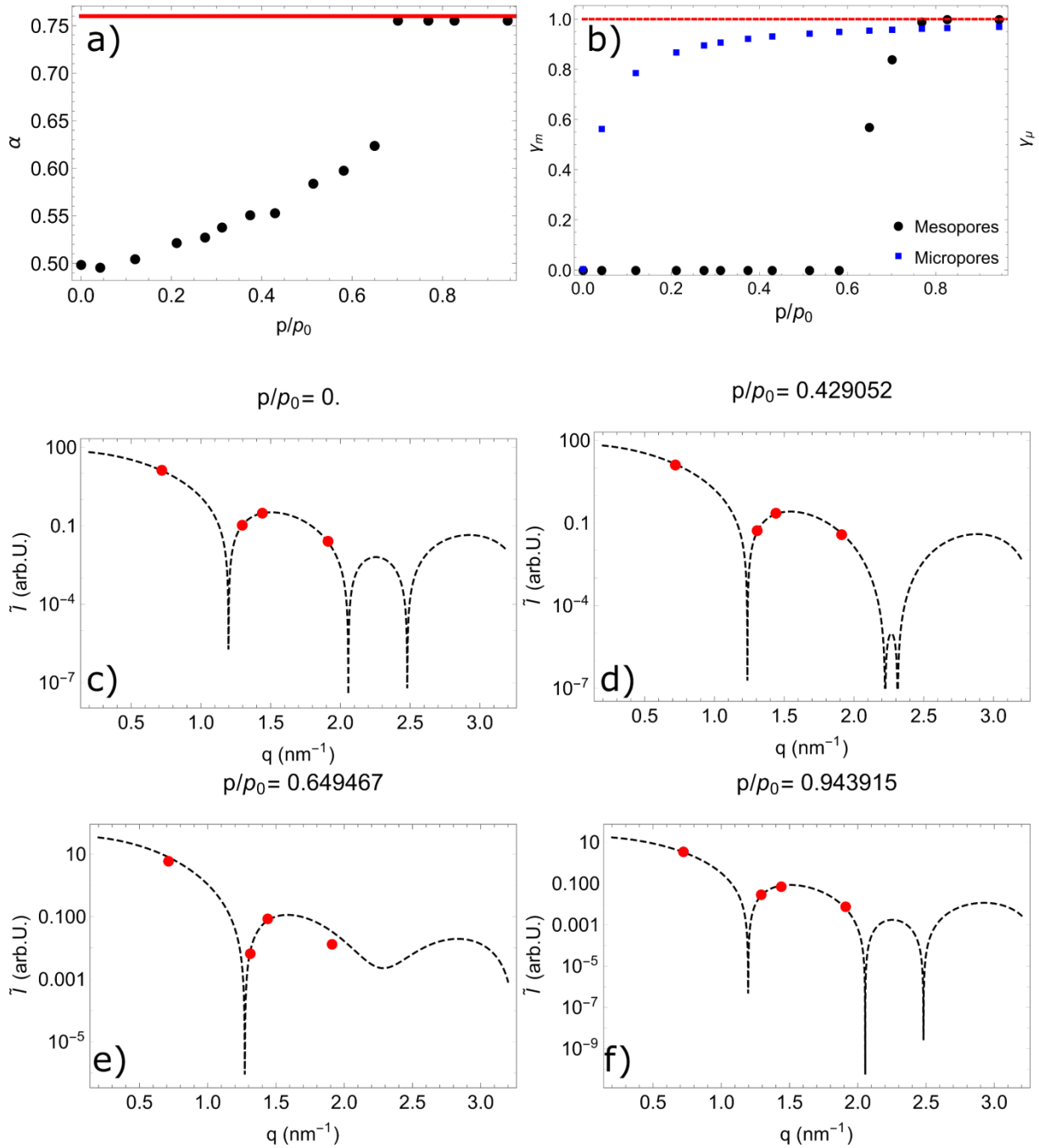


Figure 29: $\alpha(p/p_0)$ values obtained from the fit of the corona model with varying relative scattering length densities are shown in a), with the red dashed line indicating the theoretical maximum value of the filled corona. In b) the filling factors of mesopores Y_m and Y_μ are depicted. In c) to e) fits of the applied model (equation 3.21) to the integrated intensities of the peak intensities, marked as red dots, is shown as a black, dashed line for several relative pressure. (reprint from Reference ¹⁴¹)

By exploiting the hierarchical structure of the S-C material, the micropore volume fraction and sorption isotherm can be evaluated. Because all three levels of hierarchy are well separated in size, their scattering contributions can be roughly discriminated by q -intervals. Two limiting cases, i.e. the intensity at large and small scattering vector lengths, are analyzed. By denoting the water filling fraction with $x(p/p_0)$ (the dependence of x on p/p_0 will be seen as implied from here on), the ratio of equation 5.5 for the empty sample

($\phi_{H_2O} = 0$) and for the sample containing the volume fraction ϕ_{H_2O} at a relative pressure p/p_0 reads as:

$$\frac{I_M(0)}{I_M(p/p_0)} = \frac{\rho_{SiO_2}^2 (1 - \phi_\mu)^2 (1 - \phi_m)^2}{\left(\rho_{SiO_2} (1 - \phi_\mu)(1 - \phi_m) + \rho_{H_2O} (1 - (1 - \phi_\mu)(1 - \phi_m)) x(p/p_0) \right)^2}, \quad (5.7)$$

By assuming that the macroporous surface scattering is dominant for small q values of measured SAXS profiles, the intensity ratio in principle allows to determine the water adsorption isotherm by solving equation 5.7 if the meso- and microporous volume fractions ϕ_m and ϕ_μ are known. Conversely, if the filling fraction $x(p/p_0)$ and mesoporous volume fraction ϕ_m are known, the microporous volume fraction ϕ_μ can be determined. For relative pressure $p/p_0 \gtrsim 0.95$ it can be assumed that all micro- and mesopores are filled and $x = 1$. Because the mesoporous volume fraction $\phi_m^{(SAXS)}$ is known from the form factor fit (see **Table 7**) and $x \sim 1$ for $p/p_0 \gtrsim 0.95$, ϕ_μ can be determined. The result listed in **Table 8** agrees well with the one obtained from nitrogen sorption listed in **Table 4**. Because some of the micropores are probably attributed to the mesoporosity $\phi_m^{(SAXS)}$ determined from SAXS due to the corona model, this discrepancy can be expected.

From the second limiting case of large scattering vectors q ($\geq 2.5 \text{ nm}^{-1}$) the ratio between the sample at reference state $p/p_0 = 0$ and any state of pore filling can be analyzed with a three-phase model (which includes silica, water, empty space). To simplify such an expression, the term $K \left(\frac{p}{p_0} \right) \phi_\mu (1 - \phi_\mu)$ in equation 5.5 can be substituted with a three phase model of the integrated intensity (see equation 3.8):

$$\frac{I_\mu(0)}{I_\mu(p/p_0)} = \frac{\rho_{SiO_2}^2}{\rho_{SiO_2}^2 (1 - x) + (\rho_{SiO_2} - \rho_{H_2O})^2 x + \rho_{H_2O}^2 \frac{\Phi_{SiO_2}}{1 - \Phi_{SiO_2}} x (1 - x)}. \quad (5.8)$$

The detailed derivation of equation 5.8 is given in chapter 3.1.4. Assuming that the scattering at the largest q -values is dominated by the micropore scattering and knowledge of ϕ_μ (for example from nitrogen adsorption as listed in **Table 4** or equation 5.7), the isotherm can be reconstructed by solving equation 5.8 for x . As can be seen in **Figure 30** the adsorption isotherm obtained from large scattering vectors q is in fair agreement with the water adsorption isotherm measured ex-situ.

To model SAXS patterns over the whole range of relative pressure, the volume fraction of water in micro- and mesopores needs to be determined as a function of relative pressure. The filling factor of micropores Υ_μ (**Figure 29 b**) is obtained from the water adsorption isotherm using the Langmuir isotherm (equation 3.39). Filling of mesopores happens in two stages: first the filling of the corona, described by the parameter $\alpha(p/p_0)$ (see **Figure 29 a**), and second capillary condensation in mesopores described by the filling fraction $\Upsilon_m(p/p_0)$ ($0 \leq \Upsilon_m \leq 1$). Because both are obtained from fits of the Bragg reflections, they can be used along with the micropore filling fraction to model the water adsorption isotherm in terms of the adsorbed volume fraction of water:

$$\phi_{H_2O} = \frac{\frac{\alpha(p/p_0) - \alpha(0)}{\alpha(1) - \alpha(0)} \phi_{\text{Corona}} + \Upsilon_m(p/p_0) \phi_{m,0} + \Upsilon_\mu(p/p_0) \phi_\mu}{\phi_m + \phi_\mu}. \quad (5.9)$$

The resulting total pore filling fractions is presented in **Figure 30**, also providing a reasonable description of the adsorption isotherm of the sample S-C especially for $p/p_0 \leq 0.25$.

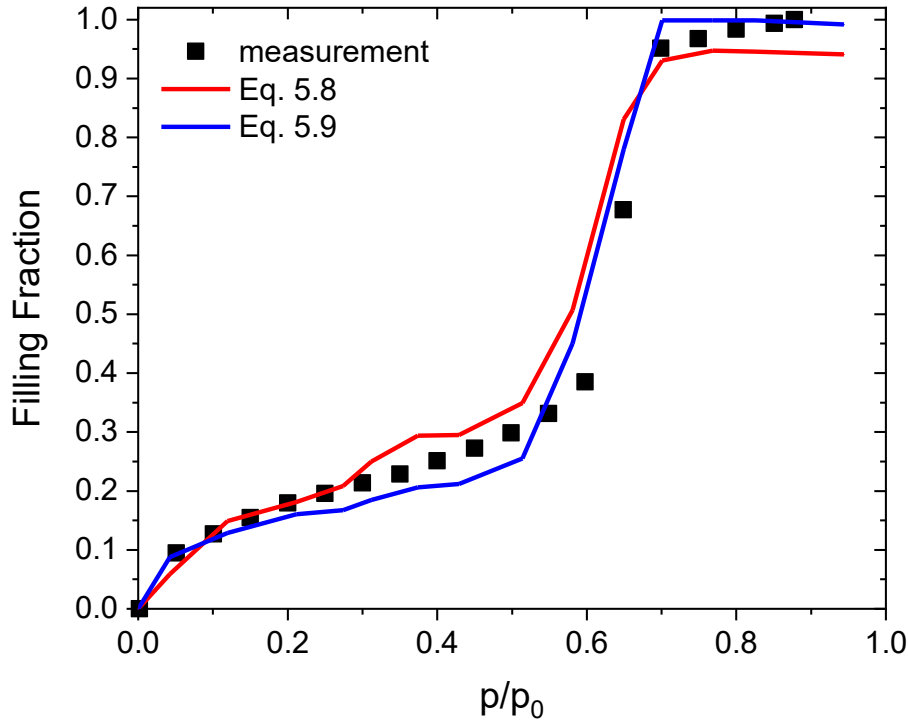


Figure 30: Adsorption isotherms in terms of filling fractions obtained from SAXS with equation 5.8 and 5.9 are shown along with the measured isotherm. (reprint from Reference 141)

Additionally, by fitting the sample at reference state $p/p_0 = 0$ with the hierarchical model by Gommes (equation 3.17)⁸⁹ a rough estimate of the mean micropore size $2r_\mu$ and its variance σ_μ can be obtained. In **Figure 31** a fit of the S-C data at reference state is shown as a dashed, purple line, with the macro- and microporous scattering contributions I_M and I_μ as blue and red curves respectively. In contrast to Gommes et al⁸⁹, the microporous contribution wasn't modelled with a generalized Guinier-Porod model but with a polydisperse, spherical form factor. A table of all relevant parameters extracted from SAXS with the electron densities ρ_{SiO_2} and ρ_{H_2O} used in the simulations is assembled below.

Table 8: Electron densities of silica ρ_{SiO_2} (e^-/nm^3) and bulk water ρ_{H_2O} (e^-/nm^3) taken from Zickler et al, specific microporosity $\phi_\mu^{N_2}$ determined from nitrogen adsorption and ϕ_μ^{SAXS} obtained with equation 5.8 and micropore diameter $2r_\mu$ with variance σ_{2r_μ} obtained from SAXS pattern of the empty sample. (reprint from Reference 141)

$\rho_{SiO_2} \left(\frac{e^-}{nm^3} \right)$	$\rho_{H_2O} \left(\frac{e^-}{nm^3} \right)$	$\phi_\mu^{N_2}$	ϕ_μ^{SAXS}	$2r_\mu$ (nm)	σ_{2r_μ} (nm)
654	333	0.06	0.056	1.1	0.28

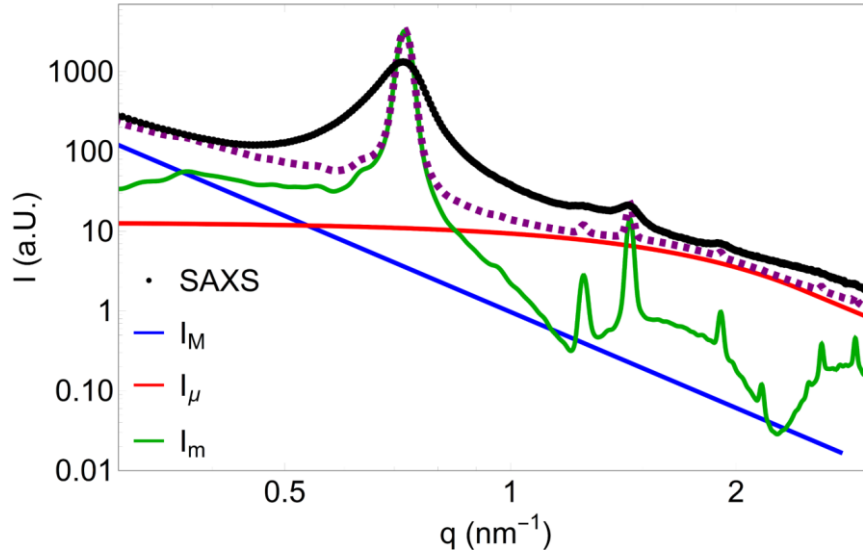


Figure 31: A fit (dashed-purple) of the S-C sample with the hierarchical model by Gommès⁸⁹. The macroporous (blue) and microporous (red) scattering contributions I_M and I_μ were obtained from the fit of equation 3.17 to the scattering data. The mesoporous scattering I_m (green) was supplied from simulation with equation 3.37. (altered reprint from Reference ¹⁴¹)

5.2.2.5 Model Set-Up

The simulations of the SAXS curves in Model 2 were performed as follows:

Initialization of Mesopores and Lattice: A lattice of $n \times n$ pores is constructed and the pore size for each lattice site is determined by a normal distribution with width σ_m , where both, radii R_1 and R_2 are independently seeded and a corona density of $\alpha = 0.499$ is assigned to every pore. To simplify computation, the mesopore and corona radii are stored in a $n^2 \times 2$ array. For simplicity, the α values shown in **Figure 29** a), were interpolated for $p \leq p_{cap}$ by linear regression and are set to the maximum α (~ 0.76) value once their individual capillary pressure value, determined by the assigned pore size, is reached. To model capillary condensation, a workaround to the method applied in Model I is needed. Because the DBdB-theory is not applicable anymore (no film growth), the radius $\bar{r} \left(= \sqrt{r_2^2 + (1 - \alpha_0)(r_1^2 - r_2^2)} \right)$ is used as critical radius for capillary condensation in 3.52 with the film thickness being $t = 0$.

Initialization of Micropores: From the fit of the measured scattering pattern of the sample at $p/p_0 = 0$ with Eq. 3.17, the approximate micropore size distribution is determined (see **Table 8**). By setting the filled volume fraction according to the Langmuir isotherm, the filled and empty phase fractions in equation 5.6 are determined and implemented. Consequently, the micropore contribution is calculated for every relative pressure considered.

Simulation of Mesoporous Scattering: By application of the Debye equation (equation 3.37), the scattering pattern is determined at all relative pressures considered.

Filling Fraction and Strut Scattering: The mesoporous scattering I_m of the model strut is corrected as follows: The incorrect surface scattering is subtracted from the data. Then,

the correct surface scattering (equation 5.4), with the loading ϕ_{H_2O} known as a function relative pressure, is added to the simulated scattering patterns. The micropore scattering contribution calculated using Eq. 5.6 is added accordingly.

In **Figure 32** b) and c) two SAXS patterns at $p/p_0 = 0$ and $p/p_0 = 0.95$ obtained through simulations of Model 2 are shown. In both cases, the hierarchical contributions to the simulated SAXS patterns are drawn as well. In **Figure 32** d) a zoom on the (10)-peak of SAXS patterns at $p/p_0 = 0, 0.6$ and 0.95 is provided, where a strong shift between the former two patterns to positive strains can be observed. In contrast to simulations of Model 1 (**Figure 27** b), the original position of the (10) peak is not retained once capillary condensation has occurred. From the shift of the (10)-peak, the apparent strain isotherm of the simulation is determined (**Figure 33**).

5.2.3 Discussion

Upon inspection of **Figure 32** b) and c), the essential characteristics of the SAXS curves presented in **Figure 25** b) are retained. Between simulation and measurement, filling of mesopores and micropores leads to a relative increase in surface scattering of the struts and a pronounced decrease in scattering of meso- and micropores. The apparent strain isotherm derived from simulations of Model 2 qualitatively and quantitatively mirror the measured apparent strain isotherms given the simplicity of the model and experimental errors. Even the large negative offset of the apparent strain above capillary condensation is well reproduced. Additionally, the magnitude of the positive apparent strains at pressures below capillary condensation is satisfactorily covered as opposed to Model 1 (see **Figure 27** b). The deviation in the region of capillary condensation originate in the large errors due to the coarse density of measured and simulated points, as well as the steep increase in loading of the sample due to capillary condensation. Evaluation of the apparent strains of Model 2 before the microporous and macroporous scattering contributions are added to the simulated mesoporous SAXS pattern in **Figure 32** (blue line) indicates that the positive apparent strains below capillary condensation are dominated by changes in the form factor. For pressures above capillary condensation the form factor doesn't contribute significantly to the apparent strain, whereas the significant change in background scattering of the macroporous and microporous SAXS contributions seems to cause the large negative offset in apparent strain. The measured apparent strain also takes largely constant values, as loading of the sample doesn't change significantly once capillary condensation has occurred. On the other hand, if a purely mesoporous materials strain isotherm were to be investigated, Model 1 should be sufficient to correct apparent strains in in-situ sorption SAXS experiments. Still, a constant offset should be then considered, as the mechanism leading to the offset, meaning the increase in surface scattering in relation to mesoporous scattering, still exists. These observations also show that earlier approaches to characterize nanoporous materials, such as the so-called pore-load modulus M_{PL} ²⁷ give correct values as long as the apparent strain remains constant in the pressure region of interest.

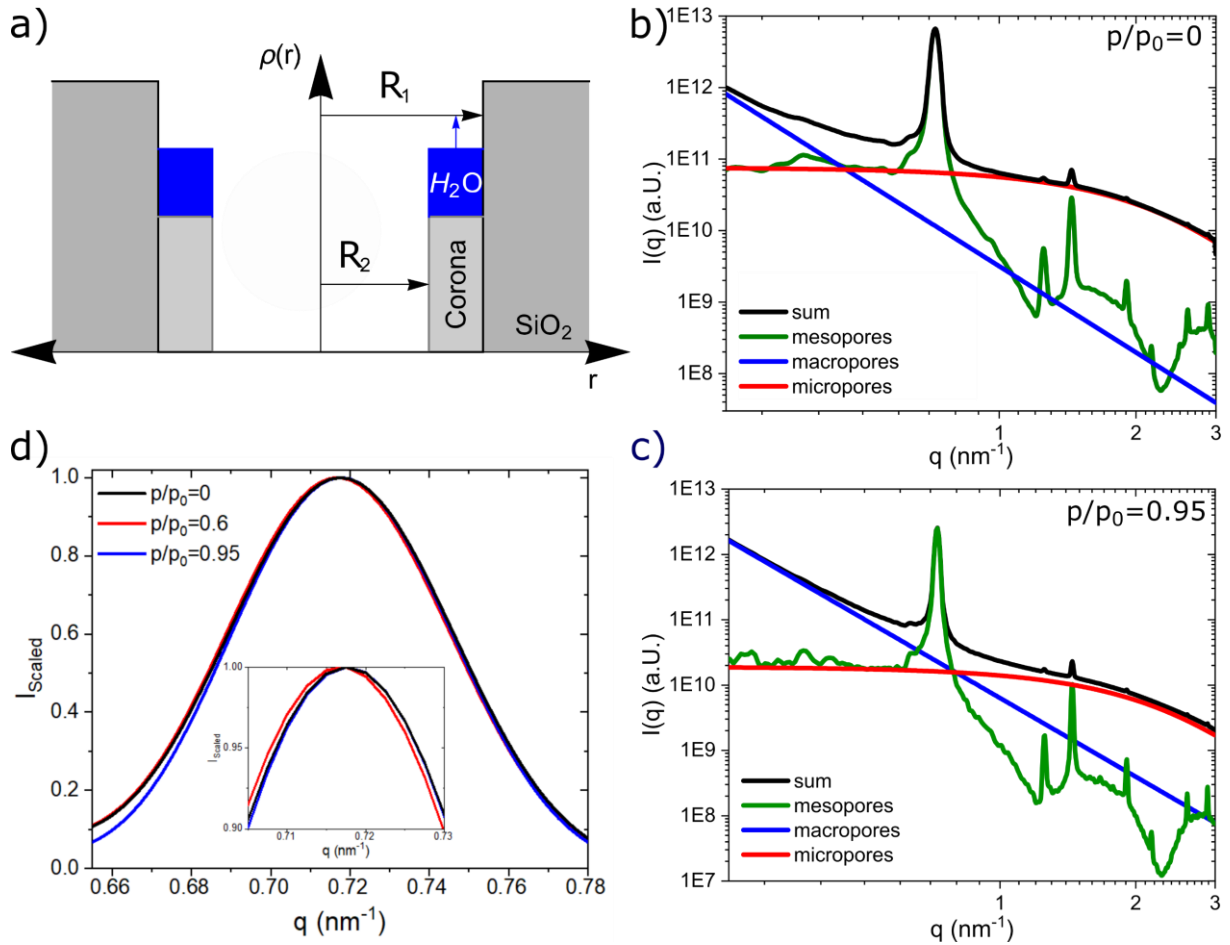


Figure 32: Electron density profile ρ as a function of the distance to pore center for Model 2. The result of the simulation using the hierarchical pore model (Eq. 3.17) is shown in b) and c) for relative pressures of $p/p_0 = 0$ and $p/p_0 = 0.95$, with the individual contributions highlighted. In d), the (10)-peak shift for three relative pressures ($p/p_0 = 0, 0.6$ and 0.95) is shown, with a zoom on the peak in the inset, scaled to one for better visualization. (reprint from Reference ¹⁴¹)

Of particular interest in this regard is the fact that the simulations have shown that apparent strains due to liquid film formation and growth at $p < p_{cap}$ exclusively result in negative apparent strains. Change of the electron density of the corona on the other hand exclusively leads to positive apparent strains. This again points to a loading mechanism of the meso- and micropores of the S-C sample which is not governed by film formation and growth. This becomes especially clear once the mean film thickness in a mesopore of 3.2 nm diameter is considered by simple arithmetic. Comparing the nitrogen and water adsorption isotherm in **Figure 20**, the loading of the S-C sample is considerably less for water than for nitrogen. With a specific external surface of $243 \text{ m}^2/\text{g}$ (**Table 4**) and an assumed monolayer thickness of 0.3 nm , the specific loading in the case of monolayer coverage of the specific external surface can be calculated with equation 3.53. By addition of micropores ($\sim 0.5 \text{ cm}^3(\text{liquid})/\text{g}$), the overall specific loading comes out at approximately $0.12 \text{ cm}^3(\text{liquid})/\text{g}$. This is roughly the value at which capillary condensation occurs (see **Figure 20**), which means that until then monolayer coverage is not achieved. This seems to confirm the approach taken in Model 2, where no liquid film was considered in the form factor (equation 3.21) and all loading for $p < p_{cap}$ was attributed to the filling of the corona.

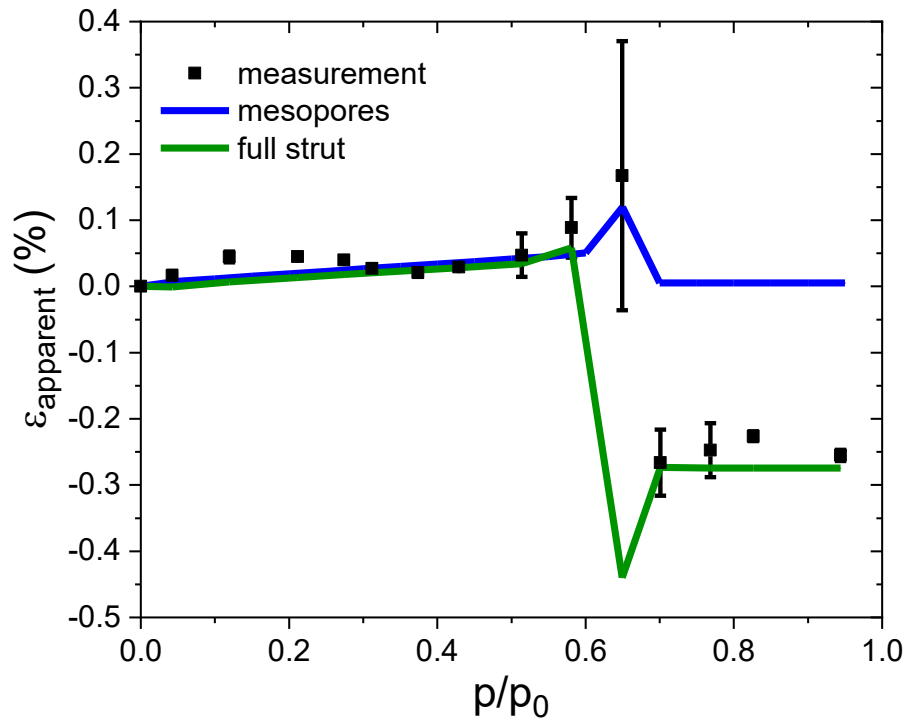


Figure 33: Measured- (black symbols) and simulated (green and blue lines) apparent strains. All apparent strains were calculated from the shift of the (10) reflections in simulated SAXS profiles. The apparent strain due to mesoporous effects alone was determined before the micro- and macroporous scattering contributions (equations 5.5 and 5.4 respectively) were added. (reprint from Reference ¹⁴¹)

6 Adsorption and Adsorption induced deformation in hierarchical carbons with concave pores

In this chapter adsorption induced deformation by n-pentane and water in monolithic, hierarchically nanoporous carbon materials is analyzed. Three monolithic, hierarchically porous carbon materials at different states of physical activation were investigated:

- non-activated, non-thermally annealed carbon (CN)
- thermally annealed and for 30 minutes activated carbon (C30)
- thermally annealed and for 120 minutes activated carbon (C120)

This chapter is split into two main parts:

In the first part, a model for adsorption in the concave void space of the monolithic, hierarchically porous carbon materials investigated in this thesis was developed. In this model, three different distributions of adsorbed liquid were proposed to describe adsorption isotherms over the whole relative pressure interval $0 \leq p/p_0 \leq 1$. Numerical calculations on the basis of a macroscopic, thermodynamic model developed by Dobbs et al¹¹³ were conducted (see chapter 3.4) to determine adsorption isotherms of nitrogen and n-pentane. Computational results for both adsorbats are compared to ex-situ adsorption isotherms and SAXS measurements. This first part was published in Reference ¹⁴⁵ and all figures and tables are reprinted within the guide lines of the Creative Commons CC BY license (check journal guidelines: *Springer-Adsorption*).

The second part deals with adsorption induced deformation of the monolithic, hierarchically porous carbon materials CN, C30 and C120 due to adsorption of n-pentane and water. Results from in-situ adsorption SANS experiments performed during the course of this thesis and from dilatometry experiments (performed by Christian Balzer, ZAE Bayern) are presented and compared. N-pentane strain isotherms are then interpreted and quantified using the model of adsorption developed in the first part.

6.1 Capillary Bridge Formation between Hexagonally Ordered Carbon Nanorods

6.1.1 Characterization

6.1.1.1 Small Angle X-Ray Scattering

The ordered mesopore structure of the C30 sample was characterized by SAXS using the laboratory set-up described in the experimental section. Scattering measurements were conducted at several positions on a cylindrical slice of a monolith with a diameter of 6 mm and 0.5 mm thickness, synthesized and supplied by Florian Putz (PLUS, Paris-Lordron-University, Salzburg). A SAXS pattern of one of the positions is supplied in **Figure 34**, where the Bragg peaks of the cylindrical nanowires confirm their 2-D hexagonal order. Five peaks (which are (10), (11), (20), (21), (30)) are clearly distinguishable, which allows to determine the mean carbon nanowire radius with a multi-step-density model⁹⁰. An outer and inner corona radius r_2 and r_1 , as well as a relative corona density α_c are determined, which is translated to a mean carbon nanowire radius r (=

$\sqrt{r_2^2 + (1 - \alpha_c)(r_1^2 - r_2^2)}$). The value determined for the mean carbon nanowire radius r was $3.9 \pm 0.4 \text{ nm}$. From the (10)-peak position $q_{10} \sim 0.73 \text{ nm}^{-1}$, the mean lattice parameter was determined with equation 3.19 to be $d = 10.1 \pm 0.1 \text{ nm}$. These values result in a mean d/r – ratio of 2.6 ± 0.05 , which is used to characterize the mesopore structure.

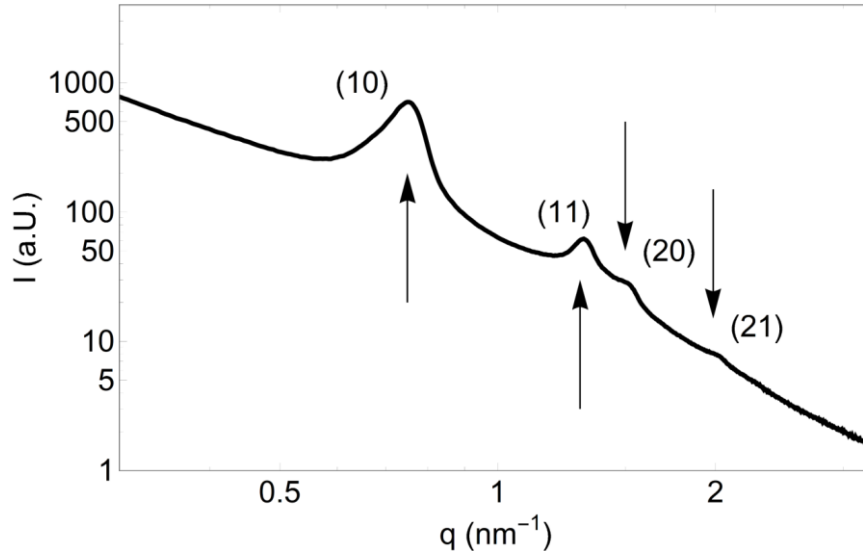


Figure 34: A representative SAXS pattern of the C30 sample is depicted, where the (10), (11), (20) and (21) peaks used for mesopore structure determination⁹⁰ are marked with black arrows. (reprint from Reference ¹⁴⁵)

6.1.1.2 Adsorption

Adsorption isotherms of the CN sample were obtained for nitrogen at 77 K and n-pentane at 290 K, using a volumetric adsorption instrument (ASAP2020, Micromeritics). Prior to measurement, the sample was degassed for several hours at 300°C within the sample holder. All adsorption experiments were performed by Christian Balzer (ZAE Bayern). The resulting nitrogen and n-pentane adsorption isotherms are plotted together in **Figure 35** and fit the classification of type IV⁹⁷. This indicates defined, cylindrical mesoporosity with micropores embedded in the carbon nanowires. As the adsorbed specific volume of both adsorbates is practically the same, they seem to occupy the same pores. Nitrogen enters the micropores at lower relative pressures compared to n-pentane as indicated by the latter's shallow slope at $p/p_0 < 0.1$. Capillary condensation occurs at lower relative pressures for n-pentane at $p/p_0 \sim 0.2$, whereas for nitrogen capillary condensation happens approximately at $p/p_0 \sim 0.35$. For nitrogen, a slight shoulder appears at higher relative pressures of $p/p_0 \sim 0.7$, which could indicate a second capillary condensation event.

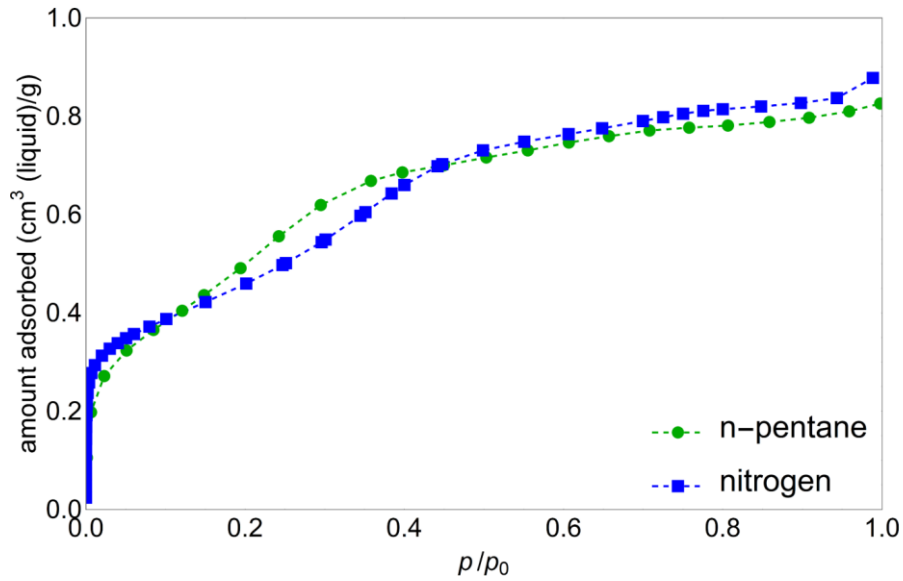


Figure 35: The adsorption isotherms of nitrogen (blue squares) and n-pentane (green disks) on the CN-sample are shown together. All measurements were performed by Christian Balzer (ZAE Bayern). (reprint from Reference ¹⁴⁵)

6.1.1.3 Reference Isotherms

The interaction between both adsorbates, nitrogen and n-pentane, with carbon are determined by fitting reference isotherms as outlined in chapter 3. For nitrogen/carbon several reference isotherms are published with minute qualitative and quantitative differences, where one of the most recent ones published¹⁴⁶ was selected. N-pentane/carbon reference isotherms have not been published so far to the authors knowledge. However, to estimate the interaction between n-pentane and carbon, an adsorption isotherm of n-pentane on carbon xerogel measured at 273.15 K (from Christian Balzer, ZAE Bayern¹²⁵) exhibiting close to no microporosity ($\sim 0.01 \text{ cm}^3(\text{liquid})/\text{g}$) and large mesopores with $d_{\text{meso}} > 10 \text{ nm}$, was utilized. As both disjoining pressure isotherms were collected on flat surfaces or materials with low curvature, they were fit with the Frenkel-Halsey-Hill equation for multilayer adsorption^{100,101} (equation 3.79). For both, nitrogen and n-pentane, sufficient agreement was found as shown in **Figure 36 a)** and **b)**. The deviation of the fit of the n-pentane reference isotherm observable in **Figure 36 b)** for relative pressures $p/p_0 > 0.6$ is due to the mesoporosity inside the material.

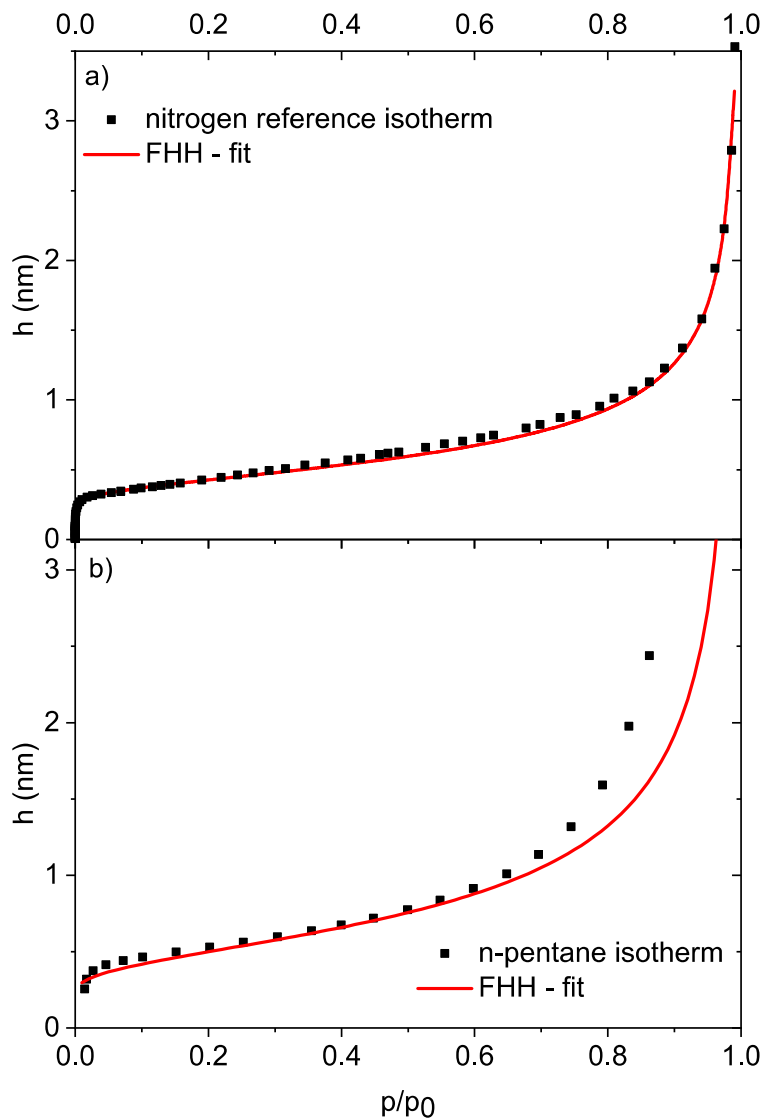


Figure 36: In a) the adsorption reference isotherm of nitrogen on annealed, activated carbon black collected at 77.4 K from [118] with the Frenkel-Halsey-Hill isotherm (equation 3.79) is shown. In b) the same is shown for a reference isotherm of n-pentane on carbon xerogel measured by Dr. Christian Balzer at 273.15 K. (reprint from Reference ¹⁴⁵)

Although the disjoining pressure isotherm for n-pentane was recorded at a temperature of 273.15 K compared to the simulation temperature at 290.15 K, the interaction parameters derived should still apply sufficiently well¹⁴⁷. The results obtained from these fits and other parameters needed in the simulation are shown below in **Table 9**.

These parameters were then used to more accurately calculate the disjoining pressure of a singular carbon nanowire, where the derived solution for such a case by Philip (equation 3.81) was used. To model the disjoining pressure in a 2-D hexagonal lattice, contributions from the three nanowires forming a smallest representative volume (see **Figure 2 b**) or **Figure 13**) are summed up at each point of consideration in the simulation.

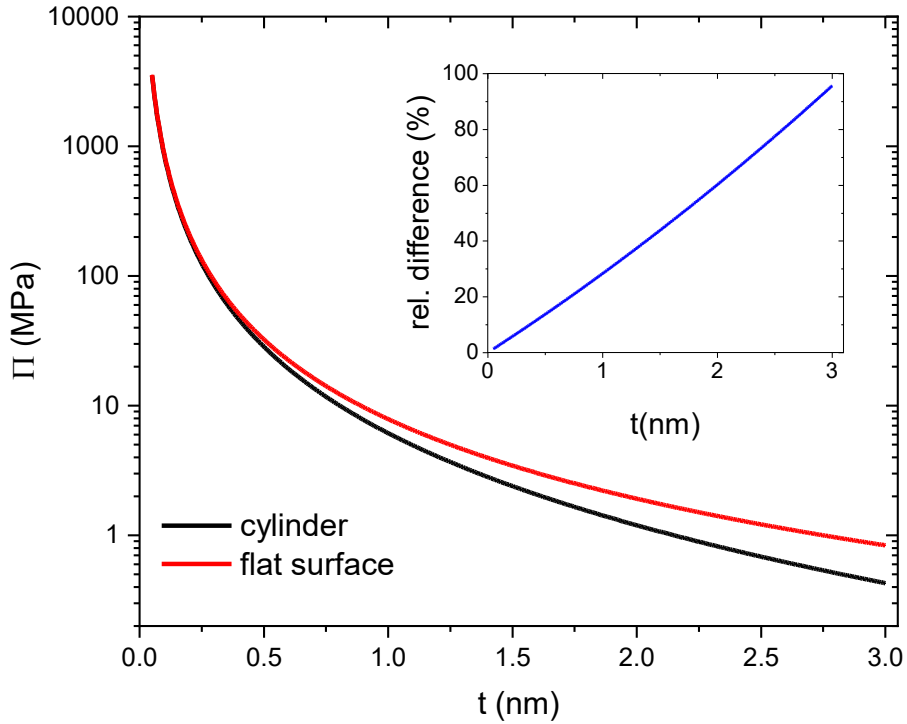


Figure 37: The disjoining pressures in MPa of *n*-pentane on carbon on a flat surface (red) and a single cylindrical nanowire (black) of radius 3.7 nm versus film thickness *t* is shown. To highlight the difference between both potentials, the relative difference in percent is shown in the inset. (reprint from Reference ¹⁴⁵)

In **Figure 37** the effect of the substrates geometry is illustrated, where the disjoining pressure from a cylindrical carbon nanowire is compared to disjoining pressure originating from an infinite substrate. The relative difference is depicted in the inset of **Figure 37**, where already at around 0.5 nm multimolecular film thickness the deviation is around 15 – 20 %. If one considers adsorption on a single cylinder, the balance between the chemical potential μ and the surface energy consisting of the liquid/vapor surface tension γ_{lv} and the disjoining pressure contribution Π , reduced film thicknesses should result. The origin of this difference is the reduced amount of substrate over which is integrated over to derive the appropriate description of the disjoining pressure¹¹¹ due to a single cylinder.

Table 9: Fitting parameters of the FHH isotherm (see equation 3.79) to the reference isotherms taken from¹⁴⁶ for nitrogen on annealed activated carbon at 77 K, and from measurement for *n*-pentane on an annealed carbon xerogel at 273.15 K. Fluid surface tension values were taken from Refs.³⁰ and ¹⁴⁸ and molar volumes calculated.

Adsorbate	<i>k</i>	<i>m</i>	γ_{lv} [mN/m]	v_{mol} [cm ³ /mol]
<i>n</i> -pentane	38.96	2.04	15.28	116.264
nitrogen	61.7	2.514	8.72	34.68

6.1.2 Computational Details and Results

Once the interaction between adsorbate and adsorbent is defined, the simulation can be set up. Solutions of the separated and bridged phases introduced in chapter 3.4 can be obtained by solving the differential equations for each case (equations 3.61 and 3.62 respectively). A Python script (version 3.7) was developed where an implemented least squares algorithm minimizes the response of an initial solution provided to the algorithm. Due to the nonlinear nature of equations 3.61 and 3.62, the initial solution provided to the algorithm should be at least close to the final solution. The geometrical data needed to do so, defining the geometry of the unitcell with the nanowire distance d and rod radius r , was determined with SAXS.

To construct an initial solution, the following procedure was conducted. For the separated phase a constant layer with its thickness t determined by Derjaguin's equation and values from **Table 9** for sorption on a single cylinder:

$$R_g T \log\left(\frac{p}{p_0}\right) = -v_{mol} \left(\Pi(t) + \frac{\gamma}{r+t} \right), \quad (6.0)$$

was supplied as it automatically satisfies the boundary conditions of $l_\theta(\theta = 0) = l_\theta(\theta = \pi/6) = 0$.

For the bridged solution a distorted cosine was used, where the argument was scaled to yield $l_\theta(\theta = 0) = l_\theta(\theta = \pi/3) = 0$, $\cos(0) = 1$ and $\cos(\pi/3) = -1$. The boundary values for $\theta = 0$ and $\theta = \pi/3$ were also derived using equation 5.8 by defining $l(\theta = 0) = \sqrt{3}/4 d - 2t$ and $l(\theta = \pi/3) = d/\sqrt{3} - r - t$, with t obtained from equation 6.0.

To improve on the stability of the solution, the differential equations 3.61 and 3.62 were divided by γ_{lv}/r as this leads to a dimensionless representation which is easier to handle for the solver used¹¹³. Best results were obtained using the 'least_squares' method in the 'scipy.optimize' package in Python, where the step size of the Jacobian was set to values larger than 10^{-3} . Convergence of the solutions was determined by the parameter 'gtol', which analyzes the vicinity of the solution by means of the Jacobian and breaks the iteration process once a sufficiently small value is reached.

Temperatures in the simulations were 77.4 K and 290.15 K for nitrogen and n-pentane respectively, according to the temperatures at which adsorption measurements were performed. The differential equations 3.61 and 3.62 were solved for the separated and bridged phase for previously defined nanowire distance to radius ratios d/r at 20 distinct, equally spaced relative pressures p/p_0 ranging from 0% to 95%. The lattice parameter d was held constant at the value determined from SAXS, whereas the nanowire radius r was set to values ranging from 3.2 to 4.4 nm in 0.05 nm steps, leading to a spread in d/r ratio from 2.3 to 3.15.

From the interface profiles $l(\theta)$ obtained from the simulations, grand potentials were calculated with equations 3.56 for the separated, 3.58 for the bridged and 3.59 for the filled case. For nitrogen, in a system determined by $d = 10.1$ nm and a rod radius of 3.8 nm, the grand free energies of the separated, bridged and filled phase are plotted vs the relative pressure in **Figure 38 a)**. The lowest grand potential Ω at each relative pressure considered yields the resulting phase in equilibrium if spinodal phase transitions are omitted. **Figure 38 a)** shows that the separated phase is stable for low relative pressures, followed by the bridged phase and finally the filled phase. The solutions found also allow

to construct an adsorption isotherm for $d/r = 2.7$ shown in **Figure 38 b)**, which only bears qualitative semblance to the recorded isotherm presented in **Figure 35**. In **Figure 38 c)**, corresponding profiles for the bridged phase at varying relative pressures corresponding to the blue dots in **Figure 38 b)** are shown. With increasing relative pressure, the empty void space shrinks and the mean profile curvature progressively increases until the bridged-to-filled transition happens.

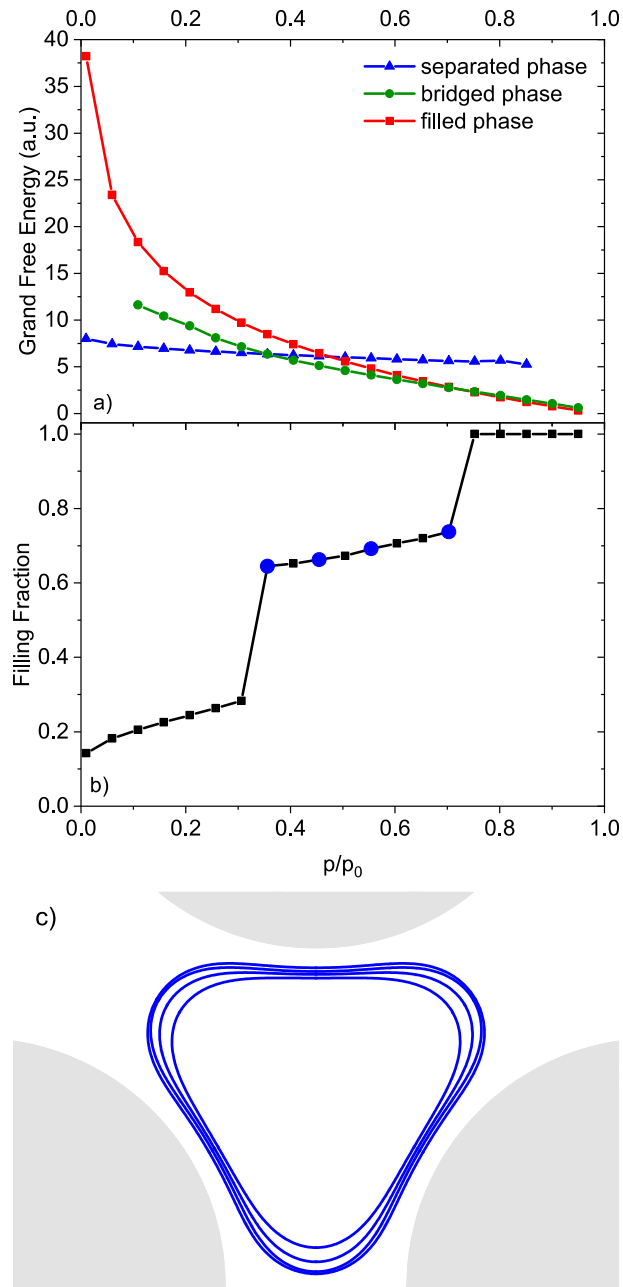


Figure 38: In a) grand free energies for the three phases considered are shown as a function of relative pressure. At relative pressures where a different phase is more favorable, we surmise that condensation events takes place, which leads to the sorption isotherm shown in b). the blue dots in b) signify the profiles of the bridged phase shown in c). (altered reprint from Reference ¹⁴⁵)

From the isotherms determined at different d/r – ratios phase diagrams can be extracted, showing the range of stability of the respective phases as a function of relative pressure and d/r – ratio. The phase diagrams for nitrogen (**Figure 39 a)** and n-pentane

(**Figure 40 a**) are shown, where for all calculations a fixed nanorod distance $d = 10.1 \text{ nm}$ were used. In both diagrams the green area is the separated, the white area the bridged and the red area the filled phase. Both phase diagrams show a similar trend overall, where both show bridging transitions at low relative pressures for small d/r – ratios, which corresponds to small gaps between neighboring nanorods. With increasing d/r , the separated-to-bridged transition occurs at progressively higher relative pressures. Whereas the transition from a separated to a bridged phase is sensitive to the nanowire radius r , the transition to the filled phase appears at very similar relative pressures for all radii investigated and the resulting phase boundary is essentially vertical. The location of the phase boundaries are clearly different between nitrogen and n-pentane, reflecting the different solid-fluid interaction and surface tension γ_{lv} . Higher values of surface tension γ_{lv} make bridging less favorable as a higher energy cost is associated with creating larger surface areas, whereas disjoining pressures with lower exponents m (see **Table 9**) lead to increased adsorption which favors bridging. For instance no bridged phase was stable for nitrogen at d/r – ratios corresponding to high mesoporous volume fractions (> 0.62), while for n-pentane the bridged phase is still stable over a broad range of relative pressures.

6.1.2.1 Comparison to Experiment

Although some experimental hints for two condensation transition were present in the earliest paper on CMK-3 carbons^{61,149}, which exhibit the same mesostructure as the C30 sample, and corresponding “bimodal” pore size distributions were obtained from adsorption analysis, the idea of a bridged phase was not confirmed. The reason might be that the two steps are not always unambiguously seen in adsorption datasets of CMK-3 due to heterogeneity of samples or pronounced disorder on the mesoporous scale which would smear out these transitions.

The C30 sample in this thesis exhibits two slight shoulders in nitrogen and n-pentane adsorption. By taking the derivative of the adsorption isotherms local maxima corresponding to two inflection points indicate capillary condensation events are observable, which correspond to $p/p_0 \sim 0.35$ and $p/p_0 \sim 0.7$ for nitrogen (see **Figure 39**) and $p/p_0 \sim 0.2$ and $p/p_0 \sim 0.6$ for n-pentane (see **Figure 40**). The uncertainty shown as a broad, opaque grey region was determined from the error in position of the fit, where an original error in $\Delta p/p_0 \sim 0.025$ and $\Delta v_{ads} \sim 2 \text{ cm}^3(\text{vapor})/g$ were considered. This is consistent with an earlier study by Gor et al¹⁵⁰, where a high resolution nitrogen adsorption isotherm recorded on CMK-3 clearly exhibits two step-like features in adsorption, but only one capillary evaporation event in desorption. This is in qualitative agreement with nitrogen adsorption experiments on CMK-3 in the very first publications reporting on this material^{61,149}, but no values for the lattice spacing d were provided in any of these publications.

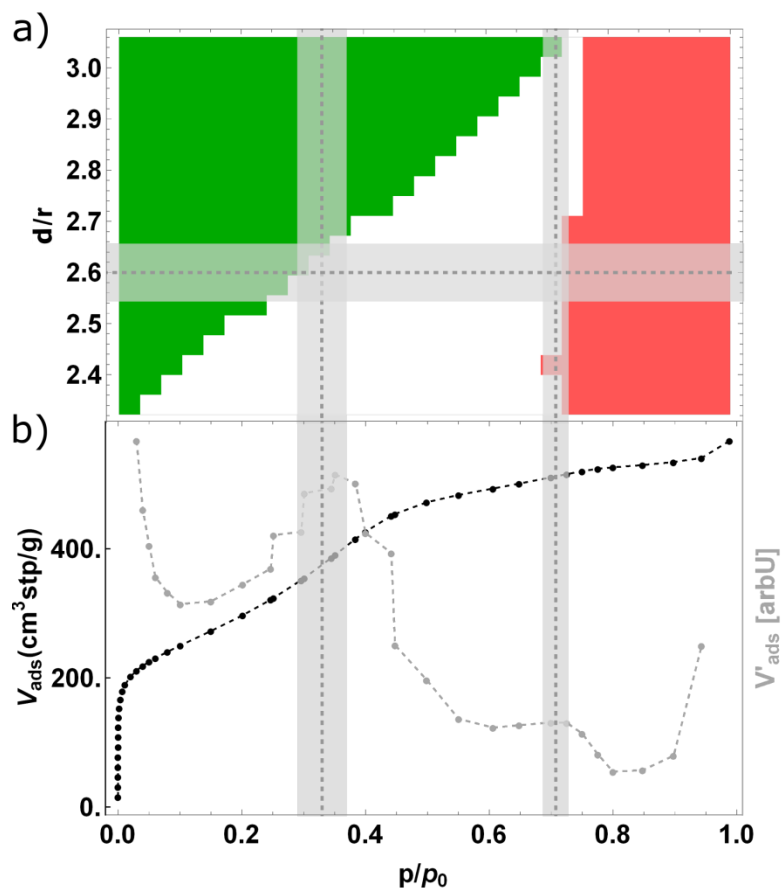


Figure 39: a) Calculated phase diagram for nitrogen on the C30 sample at 77.4 K showing the separated phase (green), the bridged phase (white), and the “filled” phase (red). (b) nitrogen (77.4 K) adsorption isotherm of the C30 sample (black), and the derivative of the isotherm (grey). Vertical lines are drawn at the relative pressure of the two local maxima of the derivative, indicating the pressure of the separated-to-bridged phase transition and the bridged-to-filled phase transition in this sample. The grey region represents the uncertainty of the maximum derived from the experimental isotherm. The horizontal line in panel (a) indicates the ratio d/r of 2.6 measured with SAXS for the present sample, with the grey region representing the uncertainty of the experimentally determined ratio d/r . (reprint from Reference ¹⁴⁵)

Vertical dashed lines in **Figure 39 b)** and **Figure 40 b)** denote the experimental transition pressures determined by the maxima of the derivative, where the grey intervals represent the uncertainty range. The horizontal dashed line in **Figure 39 a)** and **Figure 40 a)** represents the d/r – ratio of 2.6 determined from SAXS, with the opaque, grey bars again representing the experimental uncertainty. For nitrogen and n-pentane the intersections between the vertical and horizontal dashed lines agree well with phase boundaries between the separated/bridged and bridged/filled transitions. The d/r – ratio for n-pentane was approximately 2.7 and for nitrogen 2.65, which corresponds well with the ratios determined from SAXS within the experimental errors.

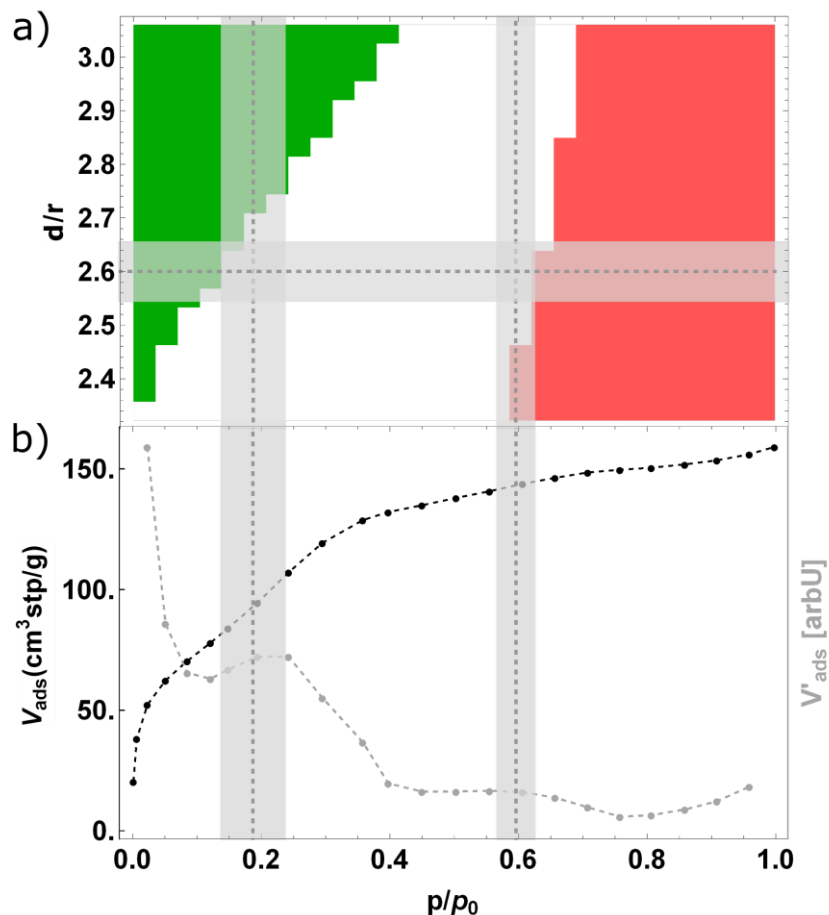


Figure 40: a) Calculated phase diagram for *n*-pentane on the C30 sample at 290.15 K showing the separated phase (green), the bridged phase (white), and the “filled” phase (red). (b) *n*-pentane (290.15 K) adsorption isotherm of the C30 sample (black), and the derivative of the isotherm (grey). Vertical lines are drawn at the relative pressure of the two local maxima of the derivative, indicating the pressure of the separated-to-bridged phase transition and the bridged-to-filled phase transition in this sample. The grey region represents the uncertainty of the maximum derived from the experimental isotherm. The horizontal line in panel (a) indicates the ratio d/r of 2.6 measured with SAXS for the present sample, with the grey region representing the uncertainty of the experimentally determined ratio d/r . (reprint from Reference ¹⁴⁵)

6.1.3 Simplified Capillary Bridge model

In the light of this model, it is well suited to compare the results found here with an analysis of the nitrogen and *n*-pentane isotherm collected on the sample with the Kelvin-Cohan¹¹⁰ equation. In accordance with Jun et al⁶¹, the Kelvin-Cohan equation for adsorption is employed¹³³:

$$-\frac{R_g T}{v_{mol}} \text{Log} \left(\frac{p}{p_0} \right) = \frac{\gamma_{lv}}{r - t}. \quad (6.1)$$

Originally, t was adjusted with an additive factor 0.3 to correct for inaccuracies in the Harkins-Jurai equation determining the statistical film thickness t of nitrogen on the substrate. However, the interaction between nitrogen and carbon and n-pentane and carbon have been determined above. Hence, t is calculated using equation 6.0 for both nitrogen.

The radius inside the interstitial r_c (as defined by $r_c = d/3^{0.5} - r$) was determined with SAXS to be approximately 4 nm. Plugging this value into equation 3.79 in conjunction with equation 6.1, the pressure of capillary condensation is $p/p_0 = 0.68$, which is close to the value of the bridged-to-filled transition for nitrogen proposed above. For n-pentane, the pressure of capillary condensation predicted is approximately $p/p_0 = 0.57$, which is again close to the values predicted and found in **Figure 39 a**).

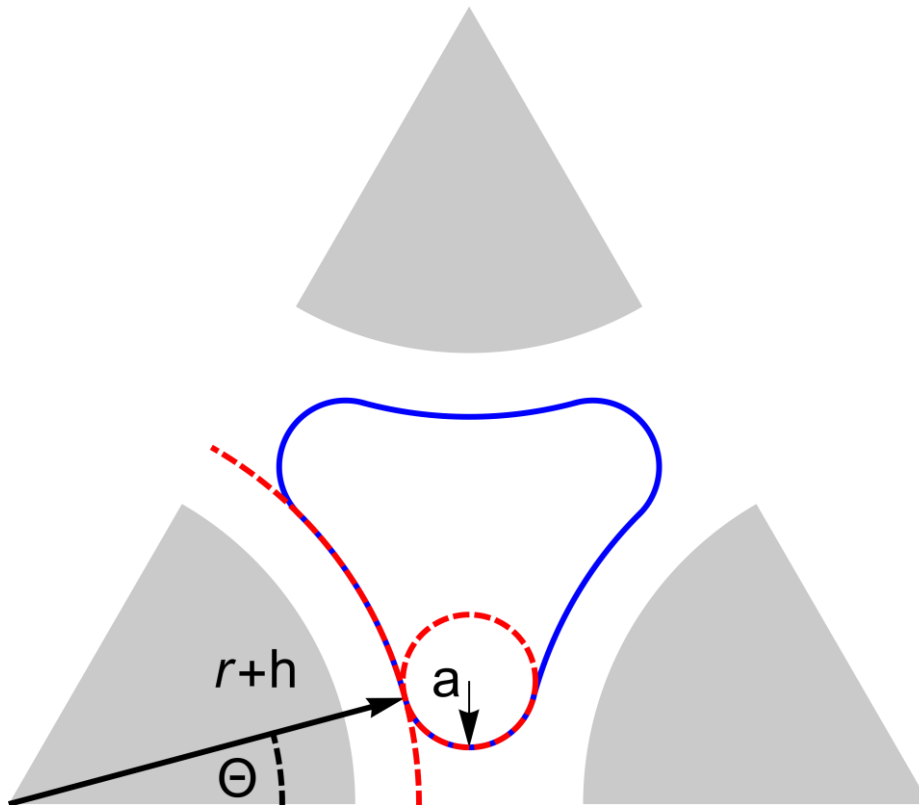


Figure 41: A sketch of the simplified “bridged” model is shown, with the approximated profile shown as the blue, closed curve. The two radii defining the profile, a and $r_c = r + h$ are shown (red dashed circles), with the angle θ at which they meet. (reprint from Reference 145)

The gap between neighboring carbon nanowires can be approximated by adsorption between two flat carbon surfaces with distance $2r_{gap} = D - 2r$. Again, the classical Kelvin-Cohan equation can deliver approximate results¹⁵¹ for relative pressures of capillary condensation if the D/r - ratio is relatively close to 2. For $D = 10.1 \text{ nm}$ and $r = 3.7 \text{ nm}$, the pressure of capillary condensation comes out at $p/p_0 = 0.5$ for Nitrogen and

$p/p_0 = 0.3$ for n-Pentane. Of note is the fact, that for $D/r = 2.6$ the approximation of two flat carbon surfaces doesn't hold anymore, hence these values are only a very rough approximation. However, this analysis has proven that the classical Kelvin-Cohan equation (equation 6.1) gives similar values for adsorption in the small gap between neighboring carbon nanowires, equivalent to a "separated-to-bridged" transition, and in the interstitial in-between three hexagonally arranged nanowires, corresponding to a "bridged-to-filled" transition to the results from the model introduced above.

To shed light on the physics of the model of adsorption introduced above, a simplified model of adsorption was adapted¹⁵² which should still capture essential properties. In this model, summarized in **Figure 41**, the bridged profile is approximated with two radii of curvature, one defined as $r_c = r + t$ and one as $a = \gamma_{lv}/\Delta\mu$, related by $\cos(\theta) = \frac{D}{2(r_c+a)}$. With h calculated from equation 3.79 and $\Delta\mu$ from equation 6.1, the profile is uniquely determined by the relative pressure p/p_0 . The grand potential of this approximated "bridged"-profile is defined as:

$$\Omega\left(\frac{p}{p_0}\right) = \gamma_{lv}6\left((r_0 + t)\left(\frac{\pi}{6} - \theta\right) + \left(\frac{\pi}{2} - \theta\right)a\right) + \Delta\mu 6\left(\frac{(2r_0t + t^2)}{2}\left(\frac{\pi}{6} - \theta\right) + \frac{D^2}{8}\tan(\theta) - \frac{a^2}{2}\left(\frac{\pi}{2} - \theta\right) - \frac{r_0^2}{2}\theta\right), \quad (6.2)$$

where the first parenthesis describes the liquid-vapor surface energies contribution and the second parenthesis the change in potential due to the liquid adsorbed. For the separated phase, the grand potential reads as:

$$\Omega\left(\frac{p}{p_0}\right) = \gamma_l (r + t)\pi + \Delta\mu 6 ((r + t)^2 - r^2) \frac{\pi}{4}. \quad (6.3)$$

In this model, the contribution of the disjoining pressure Π to Ω , outside of the determination of t from the Frenkel-Halsey-Hill equation, is completely omitted, which entails that only vapors with weak, short range interaction (ideally $m \sim 3$ in equation 3.79) with the substrate can be satisfactorily modelled. Consequently, only nitrogen adsorption was modelled as n-pentane couldn't be modeled properly due to its relatively strong long-range interaction ($m \sim 2$ in equation 3.79). Because $m \sim 2.5$ for Nitrogen in equation 3.79 (see **Table 9**), only qualitative agreement between the "simplified-bridged" and the exact model is expected. Again, a phase diagram (see **Figure 42**) was constructed for Nitrogen as shown in **Figure 39 a**). The overall shape of the phase diagram is close to **Figure 39 a**), with some deviations due to the simplified geometry of the bridge profile especially at higher relative pressures. Still, the similar shape demonstrates that the phase diagrams from 2D-hexagonally arranged carbon nanowires are substantially different from nanowires arranged in a square as considered by Dobbs et al¹¹³.

Of note is the fact that the equilibrium pressure of the "bridged-to-filled" transition coincides with $\theta = \pi/6$ (see **Figure 41**), hence when one empty, cylindrical void space has formed at the center of the interstitial space for all d/r - ratios. In the numerical calculations, this is equivalent to the fact that the profile of the "bridged" phase exhibits curvature of exclusively one sign as evident in **Figure 38 c**), yet not constant numerical values of curvature. Because the residual void space in the "bridged" phase is small in

diameter, the grand potential is similar in numerical value to the filled case and is dominated by the change in potential due to the liquid adsorbed. Also, because the shape of the bridged phase is now mainly described by the Kelvin-Laplace equation due to the (approximately) cylindrical shape of the residual void space, it's grand potential also exhibits a logarithmic shape due to the influence of the second term on Ω (see equation 6.2), similar to the grand potential of the filled phase shown in **Figure 38 c**). In **Figure 42** we also included the predictions for capillary condensation in the gap between neighboring nanowires as a black dashed line and in the interstitial between three carbon nanowires as a blue dashed line. The results of the Kelvin-Cohan equation for the proposed “bridged-to-filled” transition align well with the simplified model, yet they deviate significantly for the “separated-to-bridged” transition with increasing d/r – ratio as described above. The calculation with the “simplified-bridged” model show, that the Kelvin-Cohan equation of adsorption indeed captures the essentials of our model, but only once it's conditions, meaning that an empty, cylindrical residual void space of the “bridged” phase is left, are met.

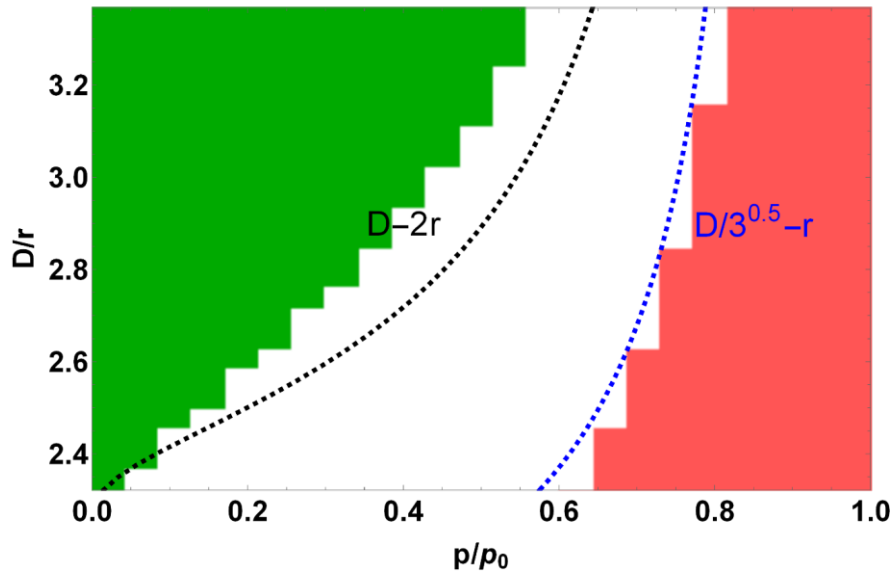


Figure 42: Calculated phase diagram for nitrogen in C30 carbon at 77.4 K showing the “separated” phase (green), the “bridged” phase (white), and the “filled” phase (red). The dashed lines correspond to pressures of capillary condensation for the “separated-to-bridged” (black) and “bridged-to-filled” (blue) transitions. (reprint from Reference ¹⁴⁵)

The overall shape of the bridged phase is not only determined by the surface tension γ_{lv} , but also by the landscape of the disjoining pressure Π in the void space. A plot of the equipotential lines of n-pentane on 2D-hexagonally arranged carbon nanowires ($d = 10.1 \text{ nm}$ and $r = 3.9 \text{ nm}$) is shown in **Figure 43** along with the numerically calculated profiles at $p/p_0 = 0.3$ and 0.6 . At smaller curvatures, the profiles cross regions of higher disjoining pressure, whereas for higher curvatures regions of smaller disjoining pressure are crossed. Due to the relatively higher surface tension of n-pentane versus nitrogen (see **Table 9**), the curvature of nitrogen bridged phase profile is higher if one compares **Figure 38 c**) versus **Figure 44**. Consequently, the simplified model doesn't apply well to n-pentane adsorption on 2D-hexagonally arranged carbon nanowires as the balance of disjoining pressure and surface tension is not well approximated.

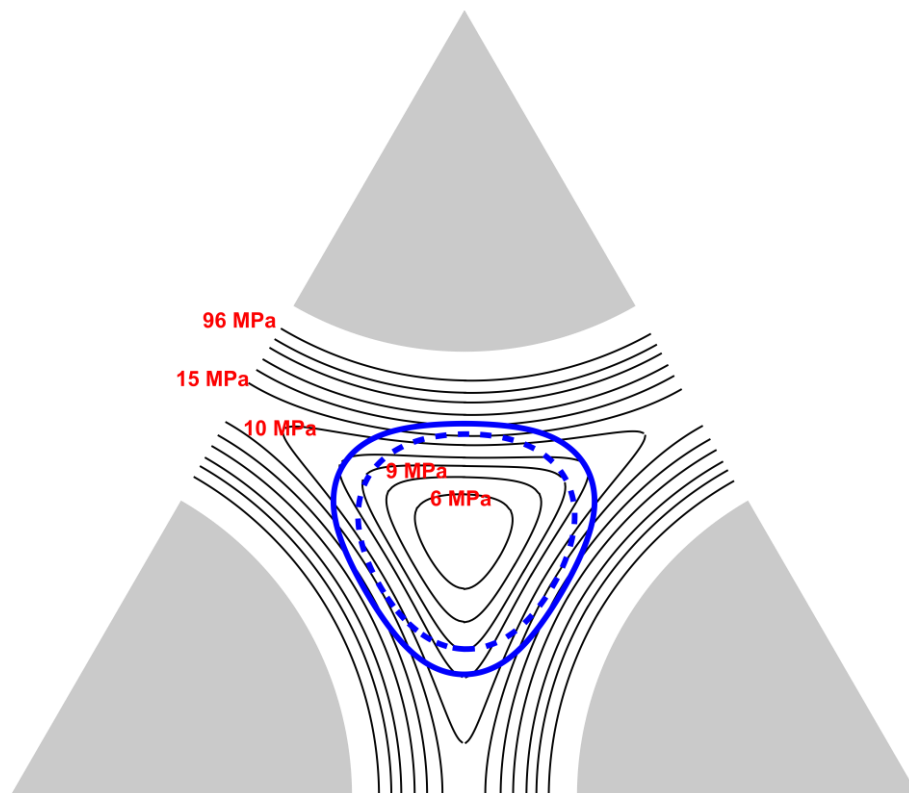


Figure 43: Equipotential lines for the disjoining pressure Π of n-pentane on carbon nanowires (black lines) are drawn along with the bridged profiles (blue lines) at p/p_0 equal 0.25 (full line) and 0.6 (dashed line). The geometric parameters of this system represent the one found experimentally for the sample C30 at $d/r = 2.6$ with $d = 10.1$ nm and $r = 3.9$ nm. The equipotential lines were calculated from the disjoining pressure (equation 3.79)

6.1.4 Discussion

Adsorption in CMK-3 materials was simulated with several state-of-the-art computational methods such as GCMC^{153–155} or QSDFT¹⁵⁰, but a bridged phase was never considered. The reason for the dismissal of this phase in these studies could be the fact that only spinodal phase transitions were considered in adsorption, whereas the transitions determined experimentally in this thesis aligned well with equilibrium transitions from simulations for both adsorbates. Although macroscopic thermodynamic approaches deviate from more exact microscopic simulations at small pore diameters < 5 nm, qualitative agreement is still reached. The step heights in the adsorption isotherms predicted in this work (see **Figure 38** b) unfortunately do not agree with measurement. However, the transition pressures for the separated-to-bridged and bridged-to-filled transitions are in good agreement with experiment. There are two main reasons why the adsorption isotherm is not predicted correctly. First, the mean-field theory applied here omits density variations of the adsorbed liquid, which leads to more abrupt transitions. Second, local disorder, such as pore corrugations, is not considered in the simulations which could lead to an increased filling fraction at low relative pressures. Yet, this local disorder could be important in the description of adsorption presented in this thesis. Jain et al¹⁵⁴ introduced interconnections in between nanowires (see **Figure 2** b) to shift the capillary condensation transition to lower relative pressures for CMK-3, which hints towards a

possible condensation mechanism in the C30 material. Small structures are considered to be situated inbetween carbon nanowires in CMK-3, which stabilize the mesostructure¹⁵⁵. A more realistic sketch of the 2D-hexagonally arranged carbon nanowires is provided in **Figure 44 a)**. In the C30 material such interconnections are expected to exist too, which could show some sort of capillary condensation transition at low relative pressures (see **Figure 44 b)**). Once the bridged phase is stable, these sites could serve as nucleation sites, essentially shifting capillary transition pressures towards equilibrium¹⁵⁴. Due to local disorder, some interstitial void spaces wedged in-between three hexagonally ordered carbon nanowires could fill below the proposed bridged-to-filled transition as shown in **Figure 44 d) I**. In reality, the bridged phase might look considerably more complicated than in **Figure 13**, although in principle the model geometry might exist locally enabling the proposed separated-to-bridged transition (see **Figure 44 d) II**). The fact that no spinodal transition was needed to determine the relative pressures of condensation sheds light on the underlying physical processes and their relation to the actual structures present in the material.

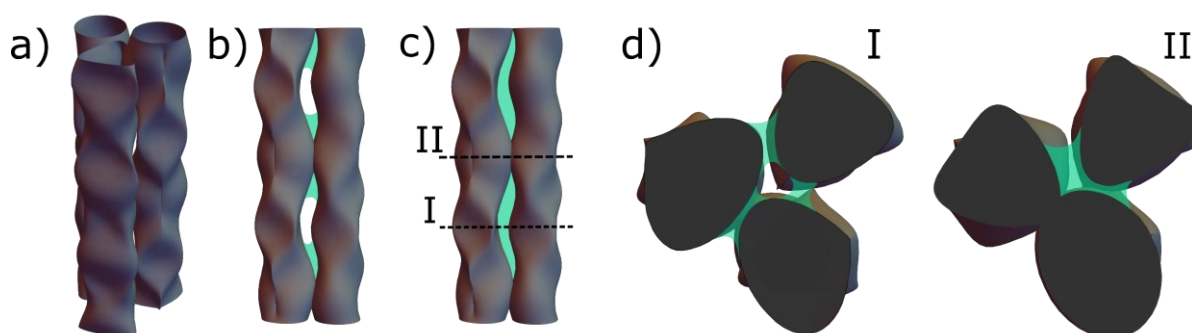


Figure 44: Sketch of a “realistic” 3D model of the carbon nanorods a), their mean distance and radius corresponding to the values obtained from SAXS. b) and c) show sketches of vertical cuts for pressures below (b), and above (c) the “separated-to-bridged” transition, with the liquid adsorbate shown in opaque green. The liquid-like film covering the nanorods is omitted in c) for better visualization, and only condensed regions in small “constrictions” are shown, which will act as nucleation sites for the “bridged” phase. In d), two top-view sketches at cuts through the positions I and II in c) are shown, demonstrating the local existence of the “bridged” and the “filled” phases in different regions along the rod axis. (reprint from Reference¹⁴⁵)

6.2 Adsorption induced deformation in monolithic, hierarchically nanoporous carbon with concave mesoporosity

In this part of chapter 6, in-situ SANS experiments on deformation induced by adsorption of 0-SLD n-pentane in monolithic, hierarchically nanoporous carbon materials are evaluated. These data sets are complemented with in-situ adsorption dilatometry measurements performed by Christian Balzer (ZAE Bayern) to elucidate deformation mechanisms in monolithic carbon materials exhibiting concave mesoporosity. In the experiments, three different carbon materials CN, C30 and C120 which are described in Chapter 2.2 are investigated. These experiments are, to the authors knowledge, the first of their kind on these kinds of materials and pose an interesting perspective due to the mesoscopic geometry, shown in **Figure 2**, of the carbon materials investigated.

6.2.1 Experimental Results

6.2.1.1 Characterization: Adsorption and SANS

Adsorption experiments, shown in **Figure 45**, of nitrogen and n-pentane were conducted on all three samples and carefully evaluated to quantify the specific volumes of micro- and mesopores by the t-plot method (by Christian Balzer). All isotherms were measured using a volumetric adsorption instrument (ASAP2020, Micromeritics) by Christian Balzer (ZAE, Bayern). The nitrogen and n-pentane data were collected at the respective temperatures of 77.4 K and 290.15 K. The shape of the adsorption isotherms is similar to materials with micropores and cylindrical mesopores, and therefore fit the classification of type IV⁹⁷.

The relatively sharp increase in specific loading seen at $p/p_0 \sim 0.35 - 0.4$ for nitrogen and $p/p_0 \sim 0.2-0.3$ for n-pentane are generally associated with capillary condensation and filling of the entire void space in literature^{149,150}. Yet, in the model introduced in a previous work¹⁴⁵, it was shown that these steps can be related to two distinct phase transitions. These transitions take place between a separated film phase to a so-called bridged phase, spanning the void space between adjacent carbon nanowires, and a second capillary condensation event occurring at higher relative pressures from the bridged to a filled phase. Between all three samples, capillary condensation is independent of activation time and occurs at higher relative pressures for nitrogen as compared to n-pentane. The broad relative pressure interval associated with capillary condensation for nitrogen and n-pentane implies disorder and/or distributed pore sizes on the mesoporous scale (see **Figure 2**). Comparing the maximal specific loading of nitrogen and n-pentane adsorption in all samples, only the CN sample fails to reach the same value at $p/p_0 \sim 0.95$. Hence, only for the C30 and C120 sample nitrogen and n-pentane access the same pore structures, whereas for CN approximately $0.2 \text{ cm}^3(\text{liquid})/\text{g}$ remain unoccupied between n-pentane and nitrogen adsorption. This coincides quite well with the amount of micropores, listed in **Table 10**, found by the t-plot method. Generally, n-pentane seems to enter micropores at clearly higher relative pressures compared to nitrogen adsorption, as indicated by the shallow slope of the isotherm for relative pressures $p/p_0 < 0.1$.

Sample activation increases specific micropore volume, whereas the specific mesopore volume decreases (see **Table 10**). The mesoporous and microporous volume fractions $\phi_m (= v_m/(v_m + v_\mu + 1/\rho_s))$ and $\phi_\mu (= v_\mu/(v_\mu + v_m + 1/\rho_s))$ were determined with the specific volumes listed in **Table 10**. A significant distinction related to the dependency of

specific micro- and mesoporosity at activation time occurs because longer activation times increase the specific microporosity for all samples, whereas specific mesoporosity stays the same between C30 and C120. The micropore volume fraction ϕ_{μ}^* in reference to the specific amount of carbon in the sample, as defined by $v_{\mu}/(v_{\mu} + 1/\rho_s)$, is also listed. From equations 3.42a and 3.42b the micro- and mesoporous volume fractions were estimated and are presented in **Table 10**, where a typical value of 2.05 g/cm^3 for the skeletal density ρ_s of carbon¹⁵⁰ was used. As found by Koczwar et al⁶⁵ for samples synthesized with the same method, the skeletal density does not change by more than $\pm 0.04 \text{ g/cm}^3$ with increasing activation time and can be assumed to be constant in a first order approximation. The porous volume fractions of the struts, composed of micro- and mesopores ($= \phi_m + \phi_{\mu}$) volume fraction, seems independent on activation time with a value of $\phi_{pore} = \phi_m + \phi_{\mu} \sim 0.64 \pm 0.02$. An estimate of the pore size can be given if the largest inscribed cylinder in-between three nanowires is defined as the pore size¹⁴⁹ see **Figure 2 c**).

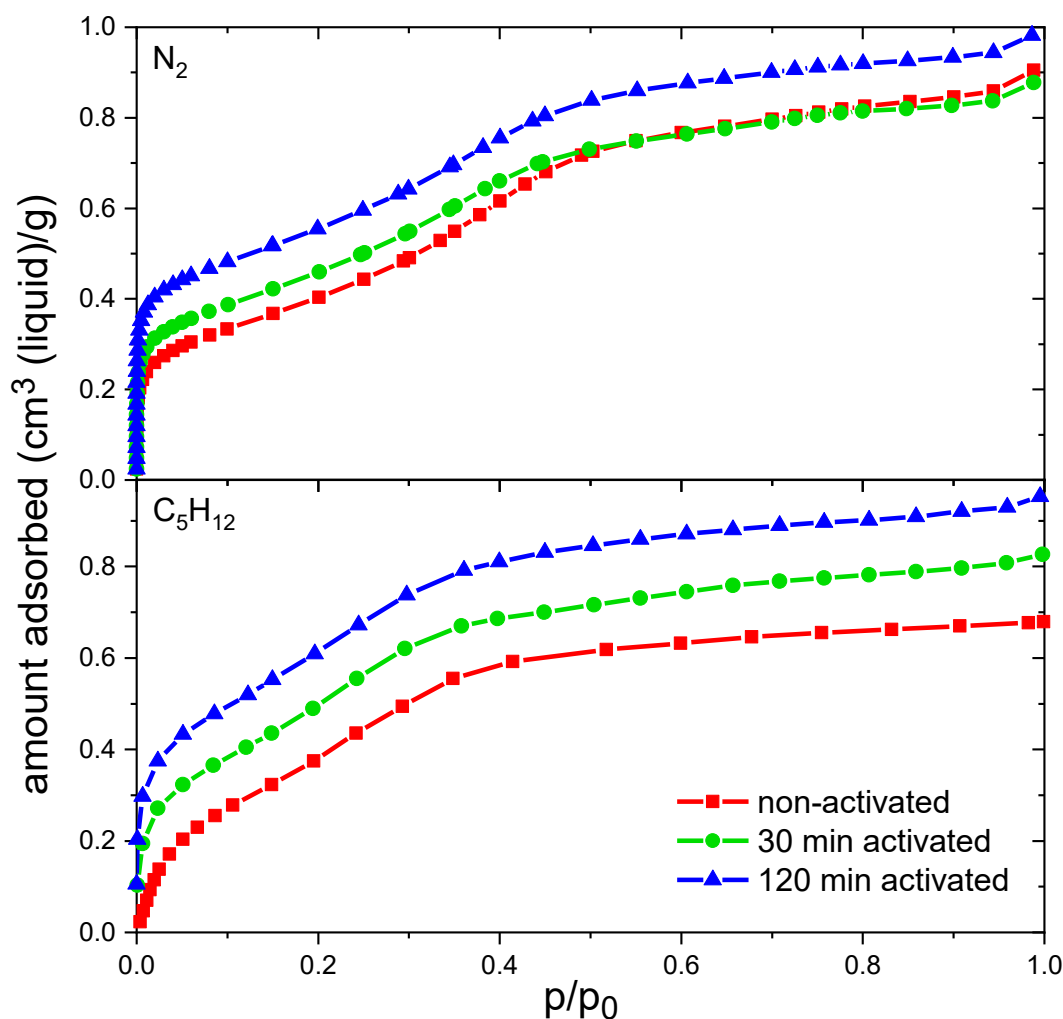


Figure 45: In the upper part nitrogen and in the lower part *n*-pentane adsorption isotherms of three different samples of monolithic, hierarchically porous carbon material of different stages of physical activation are shown (provided by Christian Balzer, ZAE Bayern).

With the lattice constants derived from SANS (see **Table 11**) and an assumed skeletal density ρ of 2.05 g/cm^3 for carbon one arrives at¹⁵⁰:

$$w_m = d \left(\frac{4}{3} - c \left(\frac{\frac{1}{\rho} + v_\mu}{v_m + \frac{1}{\rho} + v_\mu} \right) \right). \quad (6.4)$$

In equation 6.4, c is a constant characteristic of 2D-hexagonally arranged cylindrical mesopore geometry with a value of 1.213. The results obtained are all very well within the range of typical pore sizes reported for CMK-3¹⁵⁰ and allow the calculation of the carbon rod radius r by application of elementary geometry displayed in **Figure 2 c**):

$$r = \frac{d}{\sqrt{3}} - \frac{w_m}{2}. \quad (6.5)$$

The values resulting from this basic adsorption analysis are compiled in **Table 10**.

Table 10: Structural parameters related to the SANS experiment, obtained from nitrogen sorption and structural parameters such as the total amount adsorbed v_{ads} and the values v_{micro} and v_{meso} constituting it, the mean largest cylinder w_{meso} inscribed in-between three adjacent nanowires, ϕ_m , ϕ_μ and ϕ_μ^* are displayed.

Sample	v_{ads} [cm ³ /g]	v_μ [cm ³ /g]	v_m [cm ³ /g]	w_m [nm]	ϕ_m [/]	ϕ_μ [/]	ϕ_μ^* [/]
CN	0.85	0.18	0.67	4.8	0.5	0.14	0.27
C30	0.83	0.25	0.57	4.3	0.43	0.19	0.34
C120	0.92	0.34	0.58	4.15	0.42	0.24	0.41

SANS patterns of all three samples, CN, C30 and C120, were collected. In **Figure 46** the SANS patterns of the CN, C30 and C120 samples at a relative pressure $p/p_0 = 0$ are shown, where the hexagonal order of the carbon nanowires is evident by the position of the (10),(11) and (20) peaks. Due to the relatively low resolution of SANS experiments, the latter two peaks are not resolved well enough and merge into a single peak-like feature.

Data treatment for all collected 2D-patterns was the same as applied to SANS data of the silica samples (Chapter 5) and was performed with BerSans¹⁴⁰. A constant, incoherent background was subtracted to achieve a q^{-4} behavior of 1-D patterns at large q ($q > 4 \text{ nm}^{-1}$)⁸⁰ and the (10) peak is fitted with a Pseudo-Voigt function. Although the (11) and (20) peaks overlap extensively, they can be separated by fitting two individual Gaussians to the subtracted spectrum in $1 \text{ nm}^{-1} < q < 1.7 \text{ nm}^{-1}$ to obtain the integrated intensity of their individual intensities. This decomposition into two peaks is aided by the knowledge of the peak positions in q from the (10) peak by equation 3.19. With the integrated intensities of the (10), (11) and (20) peaks an estimate of the diameter of the carbon nanorods can be given⁹⁰ using the step-density model described in chapter 3.1 (equation 3.21). Because only three peaks are discernible, the overall amount of information retrievable is limited to three distinct parameters, which means that only a solid cylinder without corona can be fitted to arrive at a rough estimate of the pore geometry. The results of the fits of the integrated intensities of all samples investigated at $p/p_0 = 0$ are shown in **Table 11** below, where the result from SAXS for the C30 sample (see **Figure 34**) is replicated within experimental errors.

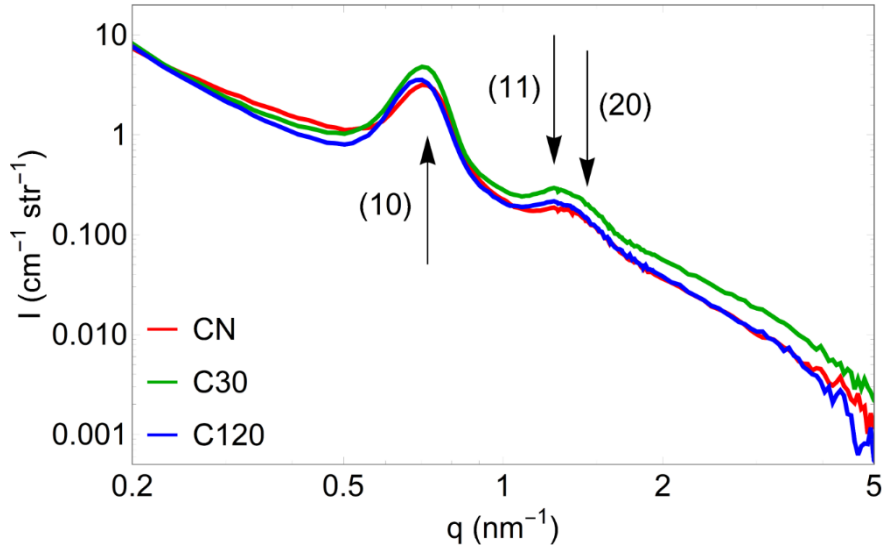


Figure 46: SANS patterns of all three hierarchically porous carbon samples at a relative pressure $p/p_0 = 0$ are shown after correction of the incoherent background was performed. The positions of the (10), (11) and (20) peaks are highlighted by black arrows.

The compared values of the structural parameters obtained between SANS and nitrogen adsorption are similar in magnitude, but the calculated mesopore volume fractions ϕ_m and $\phi_m^{(SANS)}$ evolve quite differently. For nitrogen adsorption, the mesoporous volume fraction decreases consistently with increasing activation time, whereas in SANS it remains constant within the given experimental resolution. The origin for this difference in values could be the simplified models used to determine the carbon nanowire radius r from SANS (equation 3.21) and nitrogen adsorption (equation 6.4 and 6.5). Whereas equation 3.21 considers a highly simplified model of a nanowire with no corona, the cylindrical pore model in equation 6.4 dismisses the concave shape of the void space.

Table 11: Structural parameters obtained from SANS: the lattice parameter d , the nanowire diameter r_{SANS} and variance σ_{SANS} and the largest inscribed radius in-between three nanowires $w_{ads}^{(SANS)}$, the mesopore fraction $\phi_m^{(SANS)}$ and the rod radius from in-situ nitrogen sorption r_{ads} are also listed.

Sample	d [nm]	r_{SANS} [nm]	$\sigma_{r_{SANS}}$ [nm]	$w_{ads}^{(SANS)}$ [nm]	$\phi_m^{(SANS)}$ [/]	r_{ads} [nm]
CN	10.08	3.5	0.07	4.7	0.55	3.4
C30	10.18	3.8	0.07	4.1	0.48	3.7
C120	10.3	3.7	0.06	4.4	0.52	3.9

In in-situ adsorption SANS, the change in relative incoherent background as a function of relative pressure can be related to the adsorption isotherm of the adsorbate on the adsorbent³⁷. Because the samples macroscopic density was not determined, the incoherent background scattering can only be interpreted in terms of relative filling fractions. By evaluating the incoherent scattering from n-pentane (see **Figure 48**), defined steps in the filling fractions at relative pressures $p/p_0 \sim 0.3$ and 0.6 were found for all three materials investigated. Comparing **Figure 48** with **Figure 45**, the general

resemblance between the incoherent backgrounds as a function of relative pressure for n-pentane and with the associated adsorption isotherms proves the proportionality between incoherent background and sample loading for the materials investigated. The main difference between the n-pentane isotherms recorded ex-situ and in the in-situ adsorption SANS experiment, is the pronounced step at $p/p_0 \sim 0.6$ which is not as pronounced, but still discernible in ex-situ measurements. For the sample C30, this step is most pronounced in ex-situ n-pentane adsorption, whereas it is less visible for CN and C120. If one assumes a macroscopic sample density of around 0.5 g/cm^3 , as was found by Koczwar et al⁶⁵ for similar monolithic carbon samples, around 10 mg of sample (thickness tabulated in **Table 3**) are situated in the neutron beam with diameter of 6 mm. In contrast, in the dedicated ex-situ adsorption measurements, around 100 mg are needed. Because the carbon samples are probably quite inhomogeneous structurally, the incoherent background in **Figure 48** represents the filling of a more homogeneous sample than in ex-situ n-pentane sorption due to the reduced sample volume.

6.2.1.2 Adsorption induced deformation: SANS and Dilatometry

Deformation of the samples in SANS was determined by subtractions of a linear background from beneath the (10) peak (as shown in **Figure 19 b**) and fitting of the exact peak position with a Pseudo-Voigt function³⁷. The strains of the individual samples were then determined from the shift of the (10) peak by equation 3.38. The error in strain was determined from the errors in peak position q_{10} , taken from the covariance matrix supplied by the used fitting function “NonlinearModelFit” (Mathematica 11.3©).

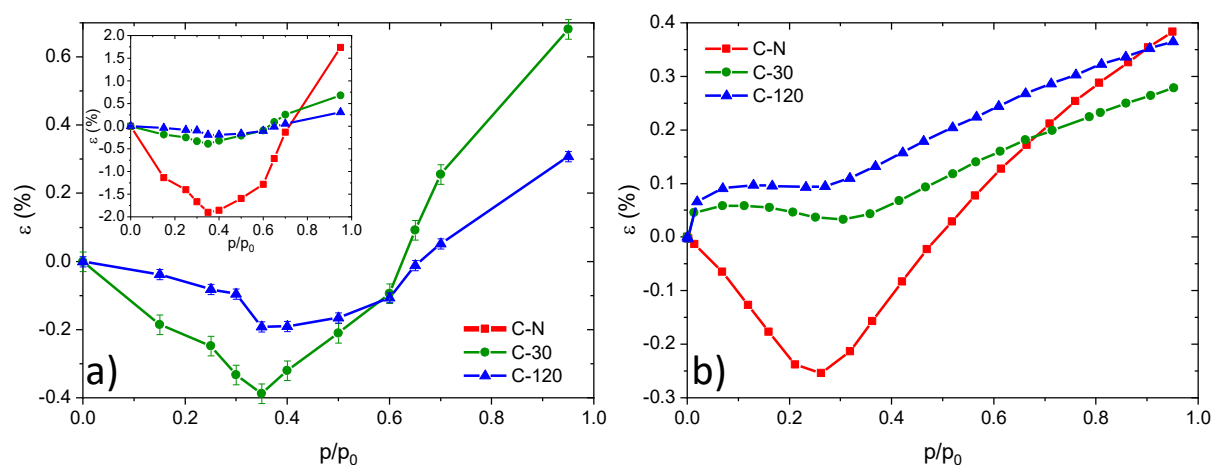


Figure 47: In-situ n-pentane sorption strain isotherms collected with SANS (a) and dilatometry (b) for the three samples with differing states of activation.

As shown in **Figure 47 a**), all three carbon samples showed qualitatively the same deformation behaviors upon n-pentane adsorption. At low relative pressures $p/p_0 < 0.35$ samples contracted, until maximum contraction was reached at $p/p_0 \sim 0.35$. For higher relative pressures the sample started to expand until at a relative pressure of $p/p_0 \sim 0.6$, where a second distinct change in deformation behavior is observed. From there on, the samples strongly expanded until the previous net-compression was compensated and tensile strains were reached. Generally, with increasing activation time the magnitude of

contraction and expansion of the samples decreases, while qualitative agreement is retained. Of note is the drastic decrease in strain magnitude upon activation, where between the CN and C30 sample maximum strains at $p/p_0 \sim 0.95$ differ by a factor of 3 to 4. Between the C30 and C120 samples a further decrease by a factor of 2 is observed.

The position in relative pressure of the step-like features in the incoherent background, and therefore the samples loading, (see **Figure 48**) align well with the changes of deformation behavior observed in the samples strain isotherms in **Figure 47 a**). This behavior can be explained with the existence of an independent phase for $0.3 < p/p_0 < 0.6$, which further substantiates the existence of the bridged phase in the model of adsorption; proposed in the previous section. Important to note is the fact that the strain isotherms collected share little to no resemblance to strain isotherms found for silica materials^{37,59}. Still, nitrogen adsorption isotherms for silica (see **Figure 22 a**) and carbon in **Figure 45** seem similar in shape upon first glance and are therefore classified similarly as type IV⁹⁷.

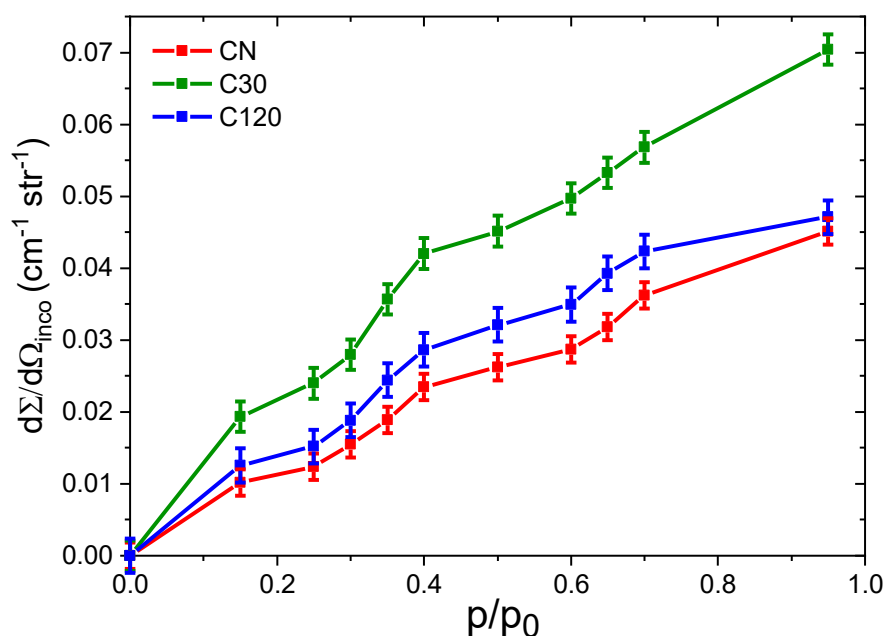


Figure 48: Incoherent backgrounds and errors fitted from SANS on all three samples investigated for the adsorbates *n*-pentane is plotted versus the relative pressure.

In dilatometry the CN sample is the only one where compressive strains were reached, with a pronounced minimum in adsorption induced strain of $\varepsilon \sim -0.25\%$ at $p/p_0 = 0.25$. In contrast, the C30 and C120 samples exclusively exhibit expansive deformations, with a sharp increase in strain occurring already at small relative pressures $p/p_0 < 0.1$. For all three samples, a defined dip in the strain isotherm was observed in the relative pressure range $0.25 < p/p_0 < 0.35$. For larger relative pressures a steady increase in strain occurred, until similar tensile strains $\varepsilon \sim 0.3 - 0.4\%$ were reached between all three samples. In comparison to SANS deformational data, the CN and C30 strain isotherms were by a magnitude of 4 and 2 smaller, whereas similar strains were observed for the C120 sample between both techniques.

6.2.1.3 Adsorption induced strain modelling

Unfortunately, no analytical or computational model which describes adsorption induced deformation of materials with similar mesostructure to the carbon materials investigated in this thesis, such as CMK-3, exists to the authors knowledge. The strain data of the three carbon materials investigated in this thesis, shown in **Figure 47**, are analyzed in the light of the model of adsorption proposed in Chapter 6.1. In this model three phases are considered: a separated phase with wetting films cover nanowires, a bridged phase with liquid bridges between neighboring nanowires and a completely filled phase.

First, an analytical form for the adsorption induced strain on a singular nanowire corresponding to strains shown in **Figure 47 a)** for $p/p_0 \lesssim 0.3$, was developed. This is achieved with the macroscopic, thermodynamic approach of Balzer et al³², as multilayer adsorption on carbon nanowires can be well approximated with equation 6.0. Although it is not clear how adsorption induced deformation of nanowires translates to strains measured in SANS and dilatometry, the results from modelling could help elucidate physical processes. To derive analogous equations to 3.92a and 3.93a, where strains induced by multilayer adsorption in cylindrical mesopores are modeled, multilayer adsorption on a single nanowire is considered. The resulting equations 3.124 and 3.125 are valid for small film thicknesses, where the influence of neighboring carbon nanowires on adsorption is negligible. These equations were already derived in the introduction, where again a radial stress component σ_{\perp} (Equation 3.116) and a component parallel to the long axis of the carbon nanowires σ_{\parallel} (Equation 3.123) describes the stress state unambiguously. Both equations correspond to the equations derived by Balzer et al³², as expected. The axial and parallel stresses on a single nanowire induced by adsorption of n-pentane at 290.15 K, on a carbon nanowire radius of 3.7 nm are shown in **Figure 49**. The values of the disjoining pressure Π and surface tension γ_{lv} to perform calculations were taken from **Table 9**.

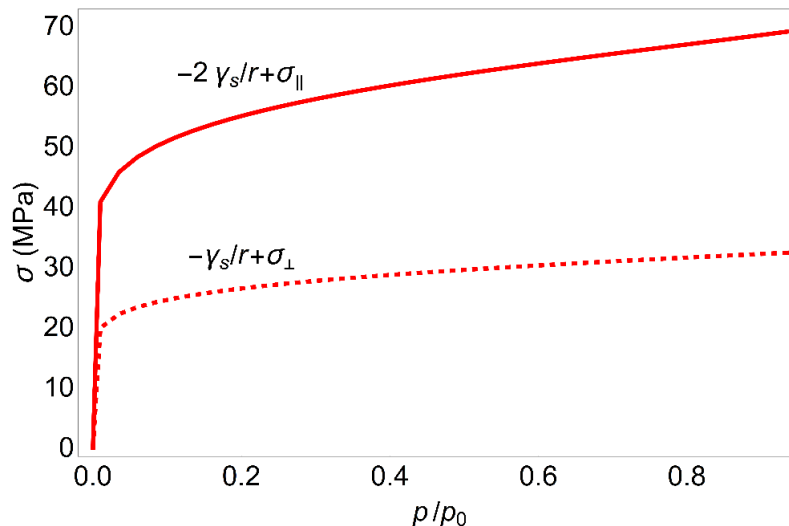


Figure 49: The adsorption induced stresses of n-pentane adsorption on a single carbon nanowire at 290.15 K are shown, with the full red line being the axial and the dashed red line being the radial stresses respectively. All stresses are shown in relation to the pre-surface stress γ_s/r for the radial and $2\gamma_s/r$ for the axial stresses, where γ_s is the specific surface energy of carbon.

The radial stresses are tensile and are smaller by a factor of 2 than the axial stresses, which resembles the relation between radial and axial stresses found in a thick walled tube³². At the proposed separated-to-bridged transition, the axial stresses are approximately 55 MPa for the axial and 25 MPa for the radial stresses as shown in **Figure 49**. A clear difference between adsorption induced strains in cylindrical mesopores and on cylindrical nanowires is the solution of the associated Lamé problem¹²³. Here, axial strains from equation 3.124 and 3.94b are exactly the same, whereas the radial strains in equation 3.125 are approximately by a factor of 2 smaller than for a thickwalled tube (see equation 3.94a). For a model carbon nanowire of radius $r = 3.7 \text{ nm}$, a Young's modulus E of 10 GPa and a Poisson's ratio ν of 0.25, situated in a model system with a mesoporous volume fraction of $\phi_{meso} \sim 0.5$, radial and axial strains due to adsorption of n-pentane at 290.15 K are shown in **Figure 50**.

In contrast to strains induced by a liquid film in cylindrical mesopores in Balzer et al³², the difference between radial and axial strain is larger, due to the different structure of equations 3.125 and 3.94a. However, the results in **Figure 50** indicate that the resulting strain is, in any case, positive which mirrors results from G. W. Scherer¹²³. This is not reflected in the SANS strain isotherms (**Figure 45 a**), where for relative pressures corresponding to multilayer adsorption on cylindrical nanowires compression is observed. Possible origins of adsorption induced strain in the hierarchically nanoporous carbon materials will be discussed below.

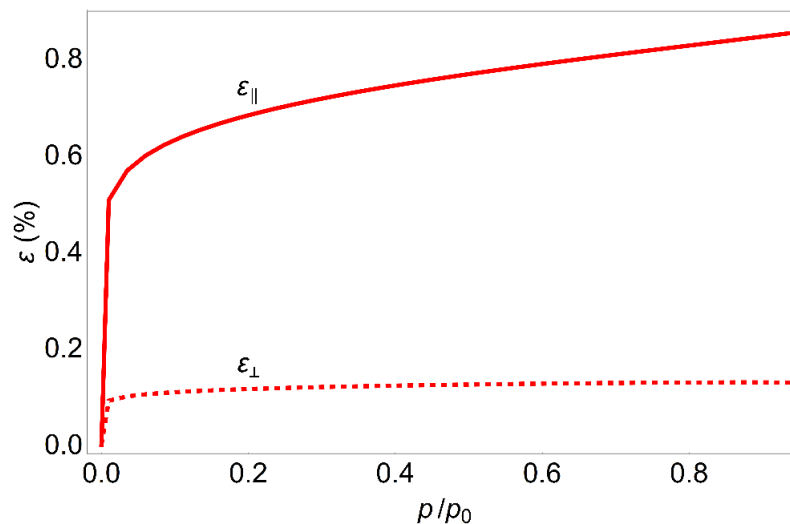


Figure 50: The axial and radial strains induced by adsorption of n-pentane on a carbon nanowire with a radius of 3.7 nm, a Young's modulus of 10 GPa and a Poisson ratio ν of 0.25.

An additional contribution to deformations, induced by a film phase on carbon nanowires, is the mutual attraction between neighboring nanowires due to film formation and growth (see Chapter 3.3.4). An adequate approximation for the void space between adjacent nanowires, to conduct qualitative calculations, is a slit pore of similar width. The filling fraction ($= 2t/H_{SP}$) was calculated with the film thickness t . It was determined with equation 3.130 and the film thickness at which capillary condensation sets in was determined with equation 3.133. Stresses induced by the film phase were calculated using equation 3.130, whereas stresses from the filled phase were determined with equation 3.135. The necessary parameters to model adsorption of n-pentane in such a representative carbon slit pore are the slit pore width $H_{SP} = 2.3 \text{ nm}$ (for $d = 10.1 \text{ nm}$ and $r = 3.9 \text{ nm}$) and the Hamaker constants at a temperature of 290.15 K between n-

pentane–n-pentane ($A_{LL} = 3.75 \cdot 10^{-20} \text{ J}^{120}$), carbon-carbon ($A_{SS} = 1.164 \cdot 10^{-19} \text{ J}^{132}$) and carbon-n-pentane-carbon $A_{SL} = (A_{LL}^{0.5} - A_{SS}^{0.5})^2 = 2.37 \cdot 10^{-20} \text{ J}^{120}$. The small pore width $H_{SP} = 2.3 \text{ nm}$ is close to the value of 2 nm , differentiating micro- and mesopores, but the physics should still qualitatively agree with molecular simulations. The disjoining pressure, describing the interaction between carbon and a n-pentane film, is described with an inverse power-law (equation 3.79), with the parameters taken from **Table 9**, and is the only experimentally determined interaction term. Therefore, the calculations conducted do not necessarily reflect the exact values for the pressures induced by adsorption of n-pentane in a carbon slit pore, but they at least represent a qualitative assesment on the magnitude of these pressures.

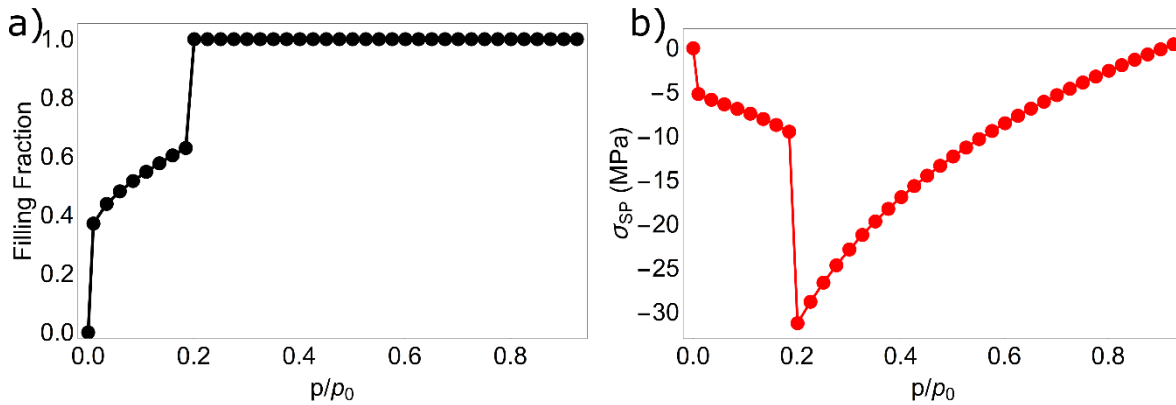


Figure 51: In a), the filling fraction of n-pentane adsorption in a carbon slit pore of 2.3 nm width is shown as a function of relative pressure. In b), the normal stress induced on the slit pore walls by n-pentane adsorption as a function of relative pressure is plotted.

The resulting adsorption isotherm is shown **Figure 51 a)**. Naturally, the filling fraction does not apply to the real system of 2D-hexagonally arranged nanowires, but it qualitatively describes the relative pressure of capillary condensation of n-pentane between carbon nanowires and aligns well with values found from numerical calculations performed on 2D-hexagonally ordered carbon nanowires in Chapter 6.1. In the numerically simulated system, the jump in contractive stress upon capillary condensation is also different in magnitude as no filled but a bridged phase comes into existence. However, in accordance with computational¹³⁴ and experimental¹³⁰ studies on stresses in slit pores in the mesopore regime, the small mesopores with a slit-like geometry, such as the porespace between carbon nanowires, contract upon adsorption. Consequently, the spaces in-between carbon nanowires see a negative stress upon adsorption which should contract the material, barring the surface stress effects considered above. Because all Hamaker constants used are literature values, the stresses in **Figure 51 b)** reproduce stresses in the materials investigated in this thesis only qualitatively.

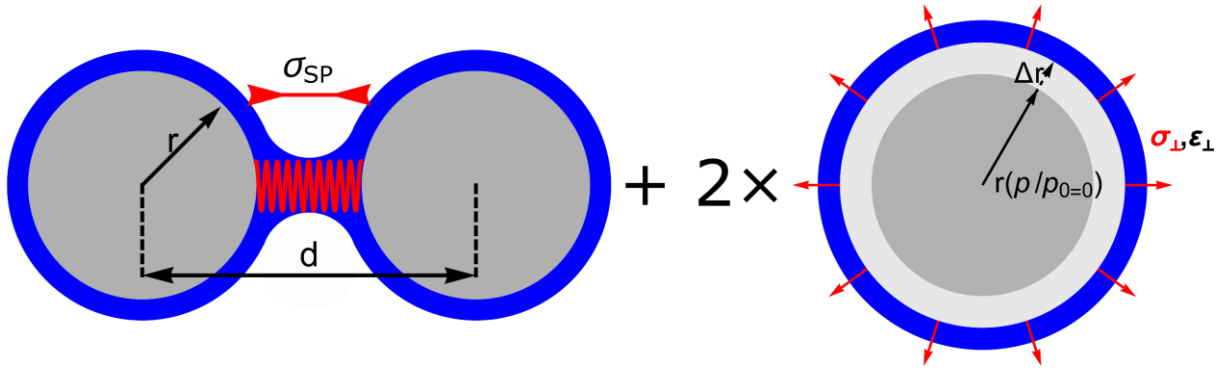


Figure 52: The proposed deformation mechanism is shown, where on the left the contribution due to the contraction of the nanowire distance d due to the stress σ_{SP} , which acts on interstitial structures signifies by the red spring. On the right, the contribution σ_{\perp} of the solvation pressure to the deformation, which is added two times as both nanowires forming the gap contribute equally.

As both effects, expansion of individual nanowires and contraction of the 2D-hexagonally arranged lattice of nanowires due to film formation, occur simultaneously, both need to be considered. As a zeroth order approximation we assume that the surface stress on and the normal stress between nanowires do not influence each other or the process of adsorption in a notable fashion¹³⁴. It has to be pointed out, that such a model does not cover the intricacies of the interplay between the stresses induced on structures in the interstitial space by the expansion of the nanowires and the stresses due to film formation in the gap between nanowires. A sketch of the proposed zeroth order approximation to the deformation mechanism is shown in **Figure 52**.

In this model, the deformation of the carbon nanowires ε_{\perp} is dependent on the nanowires Young's modulus, whereas the deformation due to film formation and bridging is dependent on the stiffness of structures in the space between adjacent nanowires. Here, the analysis stays qualitative, as technically a weighted pore size distribution should be used to model the contraction through film formation and condensation between nanowires. The corresponding formula to calculate strain, as implied from **Figure 52**, reads as:

$$\varepsilon_{sep} = \frac{\sigma_{SP}}{M_{PL}} + 2 \varepsilon_{\perp} = \frac{\sigma_{SP}}{M_{PL}} + 2 \frac{2}{E_{c,eff}} (\sigma_{\perp} (1 - \nu) - \nu \sigma_{\parallel}), \quad (6.6)$$

with σ_{SP} being the stress induced due to film formation and growth between nanowires, σ_{\perp} and σ_{\parallel} the stresses in the nanowires due to film formation, M_{PL} an effective pore-load modulus of the structures connecting neighboring nanorods, $E_{c,eff}$ representing Young's modulus and ν the Poisson's ratio of the carbon nanowires. Later, the modulus $E_{c,eff}$ will be determined roughly and an estimate of ε_{sep} will be provided.

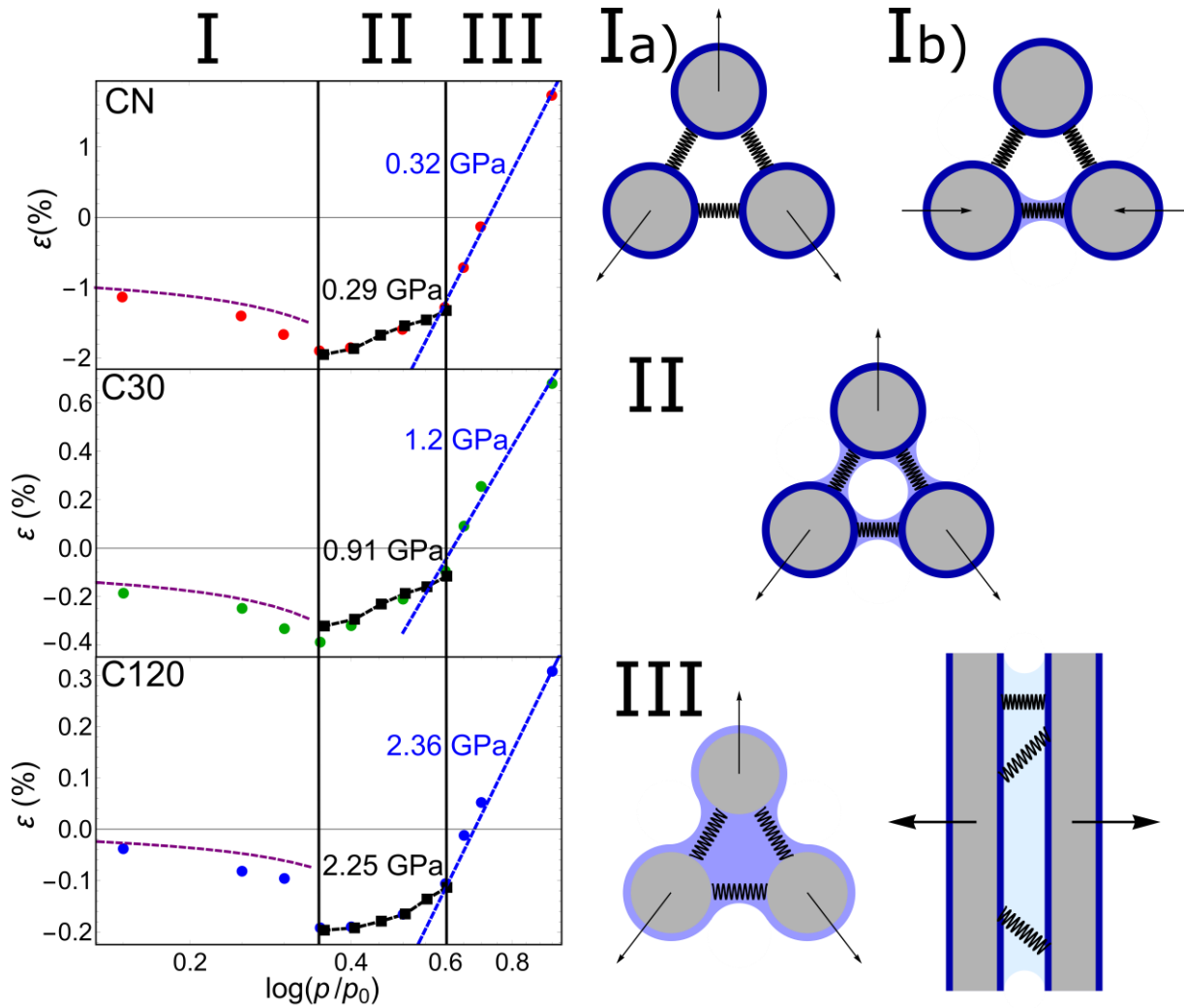


Figure 53: The strain isotherms of the CN, C30 and C120 samples are plotted against the logarithm of the relative pressure on the left hand side. On the right hand side theorized mechanisms inducing adsorption induced strain are depicted. The roman numerals correspond to the intervals of relative pressure where the associated mechanism (I separated phase, II bridged phase, III filled phase) is dominant. Along with experimental values, fits of the measured strain isotherms and the resulting pore-load modulus are shown for all samples. The dashed purple, black, and blue lines correspond to the separated (equation 6.6), bridged (equation 3.101) and the filled phases (equation 3.100) respectively.

To model strains associated with the bridged phase, which is assumed to be stable for pressures $0.3 \leq p/p_0 \leq 0.6$, the generalized Laplace equation (equation 3.101) is applied. For a liquid at rest the stress tensor inside the liquid has no shear components and the pressure inside is equivalent to the hydrostatic part of the stress tensor¹⁰⁹. The hydrostatic of the stress tensor is then equivalent to the normal stress acting on the carbon nanowires. In the present case, even where the thickness of the adsorbed liquid of the bridged phase is above 0.7 nm, the contribution of the disjoining pressure in equation 3.101 cannot be omitted due to the long-range nature of the potential (m in Equation 3.79 ~ 2 , as listed in **Table 9**). The mean curvature H used to calculate the Laplace pressure (equation 3.100) was determined from numerical simulations of the liquid-vapor profile for the bridged phase (see Chapter 6.1) for appropriate d/r values (see **Table 11**). The disjoining pressures influence varies with film thickness, which in the mean results in an

offset to compressive strains as a function of relative pressures. By analyzing the profiles with respect to curvature and disjoining pressure more closely, the curvature's contribution to the Laplace pressure in equation 3.101 varies from $\sim 5.9 \text{ MPa}$ to $\sim 10 \text{ MPa}$ for $p/p_0 = 0.3$ and $p/p_0 = 0.6$, while the contribution of the disjoining pressure changes from $\sim -13 \text{ MPa}$ to $\sim -11 \text{ MPa}$. Two n-pentane profiles ($d = 10.1 \text{ nm}$ and carbon nanowire radius $r = 3.9 \text{ nm}$) at $p/p_0 = 0.3$ and 0.6 are shown along with equipotential lines of the disjoining pressure Π in **Figure 43**.

The resulting stresses are fit to measured strains in the interval $0.3 \leq p/p_0 \leq 0.6$ in **Figure 47 a)**, where the bridged phase is expected to be stable. The strain isotherm's slope of the bridged phase is related to the inverse of an effective modulus M_{PL} , which is in principle the same as the so-called pore-load-modulus²⁷. The offset needed to fit the measured strain data is not discussed in detail, as it depends on factors, such as the surface stress and the change in interaction between carbon nanowires due to the presence of n-pentane between neighboring carbon nanowires, which are not covered by the generalized Laplace equation (equation 3.101). In the case of the bridged phase, the effective modulus M_{PL} most likely depends on the Young's modulus of the carbon nanowires and the amount and structure of the interconnections between neighboring nanowires. The results of these evaluations are shown in **Figure 53**. The fit between the measured and the theoretical strain isotherms of the bridged phase is satisfactory for all

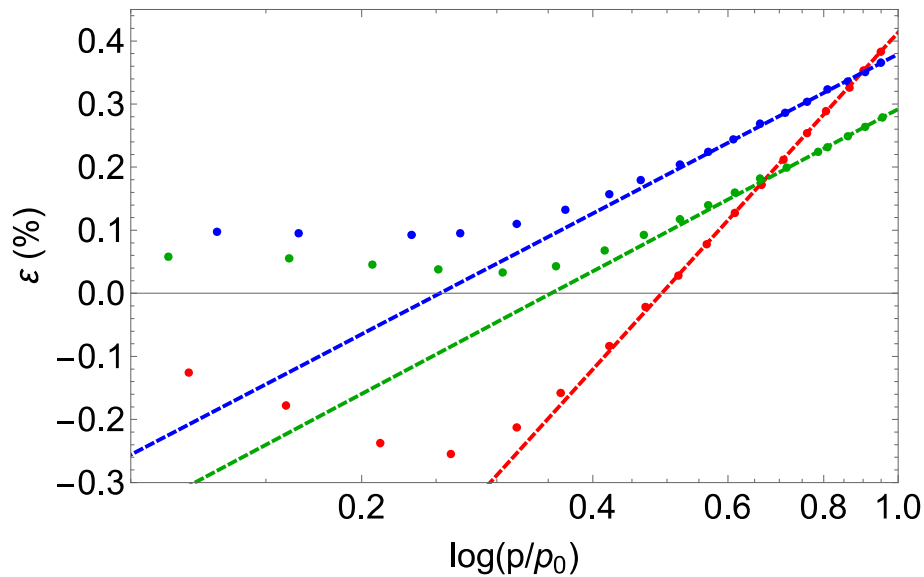


Figure 54: *In-situ n-pentane adsorption dilatometry strain isotherms of the CN (red), C30 (green) and C120 (blue) samples are shown. The straight, dashed lines are the fits with equation 3.105 which determines the system modulus M_{DIL} .*

three samples. Additionally, with increasing activation time, the pore load modulus M_{PL} increases by a factor of 3 to 4 between CN and C30 and as well as by a factor of ~ 2 between C30 and C120. This trend in magnitude is exactly in reverse to the decrease in maximal strains at $p/p_0 \sim 0.95$ found for all three samples.

Strains in the pressure interval $p/p_0 > 0.6$ corresponding to the filled phase were modelled with the Kelvin equation (equation 3.100). Again, an effective Young's modulus M_{PL} was used to convert stresses due to capillary pressure to adsorption induced strains. The filled pore regime is well approximated with equation 3.100 for all three samples, as indicated by the straight line fitting strains at $p/p_0 > 0.6$ in **Figure 53**. Compared to results from the bridged phase, values for the pore-load-modulus M_{PL} , presented in **Table**

12, are of similar magnitude and increase with activation time as well. Because the structures which constitute M_{PL} are unknown and more dedicated experiments are needed to fathom its precise physical origin, no attempt to derive an analytic form of the pore-load modulus was made.

Because strains measured with in-situ adsorption dilatometry should be proportional to capillary pressure in the filled pore regime, the Kelvin equation (equation 3.100) was used to fit strain isotherms of all samples for $p/p_0 \geq 0.6$. Again, a linear relationship was found between capillary pressure and strains in the filled pore regime, as shown in **Figure 54**. The proportionality constant, which converts the capillary pressure to the measured strains, is introduced as M_{dil} and used to clearly differentiate between the pore-load-modulus M_{PL} which is used for SANS-data. M_{dil} is presented along M_{PL} for the bridged and filled phase in **Table 12**. The effective Young's modulus M_{dil} found in dilatometry approximately doubles between CN and C30, but remains practically constant with longer activations time between C30 and C120. In general, the effective Young's moduli obtained from dilatometry are considerably larger than results found with SANS.

Table 12: The pore load modulus M_{PL} obtained from SANS for the bridged and filled phase, as well as the effective Young's modulus M_{dil} found in dilatometry measurements and the nanowires effective Young's modulus $E_{c,eff}$ are listed for the CN, C30 and C120 carbon materials.

Sample	CN	C30	C120
$M_{PL \text{ bridged}}$ (GPa)	0.29	0.91	2.25
$M_{PL \text{ filled}}$ (GPa)	0.32	1.20	2.36
M_{dil} (GPa)	3.53	7.51	7.79
$E_{c,eff}$ (GPa)	29.3	24	19.2

6.2.1.4 Analysis of Pore-Load Modulus M_{dil}

Here, a more detailed analysis of the pore-load moduli obtained from dilatometry is conducted. Only pressure intervals which can be described with the Kelvin equation (equation 3.100), and therefore parts of the strain isotherms associated with the filled phase, are considered. First, a simple model, relating the measured dilatometric modulus to the geometry of the void space, is developed. To do so, the concept of the spreading tension λ needs to be introduced¹⁰⁹. This concept describes the force exerted on a nanowire through the line tension at the necks of the meniscus after complete filling of the void space due to capillary condensation. Gor et al¹⁰⁹ have shown that it can be related to the Laplace pressure Ψ in the pore space by considering the force equilibrium between the line tension and the pressure acting on the area of the pore. Defining the pore area and nanowire surface according to **Figure 2 c)**:

$$\lambda r\pi = -\Psi \left(\frac{3^{0.5}d^2}{4} - \frac{r^2\pi}{2} \right), \quad (6.7)$$

results for $d = 10.1 \text{ nm}$ and $r = 3.9 \text{ nm}$ in $\lambda \sim -2\Psi$. This implies, that the line tension effectively "pulls" the nanowires into the liquid¹¹⁰, which is to be interpreted as axial compression of nanowires. With increasing relative pressure, the menisci at the pore throats round out and λ decreases in magnitude, hence the material extends in axial direction. Because the aspect ration of the nanowires is high, λ acts only locally at the

menisci. By Saint Venant's principle, this is equal to a constant effect of λ over the whole length of the nanowire and local stress amplitudes, for instance at the meniscus' throat where the line tension acts on carbon nanowires, can be neglected.

But λ can also be directly related to a simplified, mean axial stress σ_{\parallel}^* by a force balance. Considering the geometry in **Figure 2 c)**, this reads as:

$$\lambda r\pi = -\frac{1}{2}\sigma_{\parallel}^* r^2\pi, \quad (6.8)$$

which means that the Laplace pressure Ψ and the exerted axial stress σ_{\parallel}^* can be set into relation as the left hand sides of equation 6.7 and 6.8 are equal. This leads to:

$$\sigma_{\parallel}^* = \Psi \frac{\left(\frac{3^{0.5}d^2}{4} - \frac{r^2\pi}{2}\right)}{\frac{r^2\pi}{2}} = \Psi \frac{1}{1 - \phi_m}. \quad (6.9)$$

For the materials investigated, the mesoporous void fraction ϕ_m is close to 1/2, which means that the simplified axial stress σ_{\parallel}^* is approximately twice the Laplace pressure.

To obtain the Young's modulus of the carbon nanowires, the dilatometric modulus M_{dil} can be approximated by equation 3.95. Here, the parameter x purely takes the form of a scaling parameter between radial and axial deformations, but it should still be somewhere in the range of 0.1-0.6^{32,59}. No mechanical parameter is assigned to M_{dil} or M_{PL} , but the axial deformation should be indirectly proportional to an effective Young's modulus of the nanowires $E_{c,eff}$. Further, it is assumed that the line tension, which is acting on the surface of the nanowires, results in a constant axial stress across the cross section of the carbon nanowires.

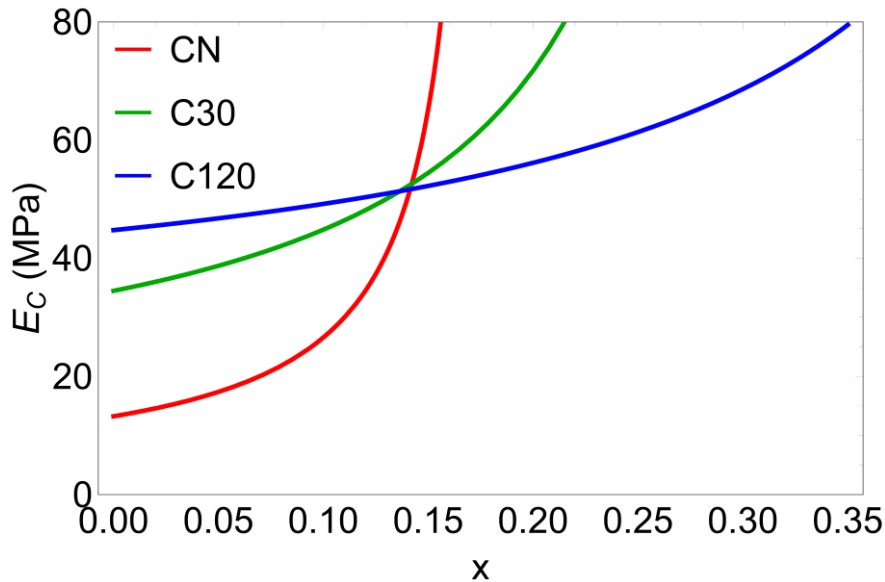


Figure 55: The axial Young's modulus for all three samples investigated, CN, C30 and C120, versus the scaling parameter between axial and radial deformations x . The functional relationship is determined with equation 6.8 below, with a clear intersection point at $x \sim 0.14$ and $E_c \sim 53$ MPa.

Additionally, the simple relationship between the measured and actual axial effective Young's modulus $E_{c,eff} = E_c(1 - \phi_\mu^*)$ is assumed to apply as to simplify calculations. Then, with using³²:

$$\varepsilon_{dil} = x \varepsilon_\perp + (1 - x)\varepsilon_\parallel,$$

to model the monolith's deformation and inserting the relationship used to fit the strain isotherms for the filled phase (equation 3.101) one arrives at:

$$\frac{\Psi}{M_{dil}} \sim x \frac{\Psi}{M_{PL}} + (1 - x) \frac{\sigma_\parallel^*}{E_{c,eff}} \sim x \frac{\Psi}{M_{PL}} + 2(1 - x) \frac{\Psi}{E_c (1 - \phi_\mu^*)^2}. \quad (6.10)$$

For simplicities sake, the relation between axial strains and the axial and radial stresses, applied in equation 3.125, is omitted in the definition $\varepsilon_\parallel \sim \sigma_\parallel^*/E_{c,eff}$ and it is further assumed that $\sigma_\parallel^* \sim 2\Psi$ (with $\phi_m \sim 0.5$ in equation 6.9). Then, this formula can be rearranged to obtain the nanowires axial Young's modulus:

$$E_c = 2(1 - \phi_\mu^*)^{-2} (1 - x) \left(\frac{1}{M_{dil}} - x \frac{1}{M_{PL}} \right)^{-1}. \quad (6.11)$$

With the factor $(1 - \phi_\mu^*)^2$, E_c of all three samples can be compared. If the relationship in equation 6.11 holds, all three samples should exhibit the same x and E_c . A simple way of solving equation 6.11 for all three samples is graphically. By plotting equation 6.11 for all samples simultaneously, hence with the according ϕ_μ^* , M_{dil} and M_{PL} , a unique x and E_c exist if all three graphs intersect at one point. Plotting equation 6.11 with the appropriate values for the moduli M_{dil} , M_{PL} (see **Table 12**) and micropore volume fractions ϕ_μ^* (see **Table 10**), indeed a crossing point between all three samples can be observed in **Figure 55**. This intersection point is situated at $x \sim 0.14$ and $E_c \sim 53 \text{ MPa}$, with the effective axial Young's modulus being decidedly larger than the other effective moduli found. This result shows that all three samples originally exhibit an axial Young's modulus of 53 MPa , which reduces due to the microporosity present in the carbon nanowires. With increasing activation time, as more micropores are created in the carbon nanowires, the effective Young's modulus $E_{c,eff}$ decreases further. The values of the effective axial Young's moduli $E_{c,eff}$ are listed in **Table 12** for all three samples.

With the values for $E_{c,eff}$ obtained, equation 6.6 is used to calculate the strains induced for the separated phase by adsorption of n-pentane on 2D-hexagonally ordered nanowires. It has to be pointed out, that capillary condensation in slit pores is not considered. Hence, for pressures $p/p_0 > 0.2$, the slit-pore model is not applicable anymore as capillary condensation has set in for the considered pore width $H_{SP} = 2.3 \text{ nm}$ (see **Figure 51 a**). This means that the calculations represent only a qualitative estimate of strains induced by the separated phase. The stress σ_{SP} in the gap between nanowires was calculated with 3.131, whereas the strain ε_\perp on the nanowires due to film formation were calculated using equation 3.125. The mechanical parameter utilized to convert σ_{SP} to strain ε_{sep} was the pore-load modulus M_{PL} fitted from the filled phase, whereas the nanowires effective Young's modulus $E_{c,eff}$ was used to determine ε_\perp (both listed in **Table 12**). The geometrical parameters of the material were chosen to coincide with the simulations of the bridged phase for each sample (see **Table 11**). The results of the calculations are shown as dashed purple lines in **Figure 53** in the relative pressure intervall associated with the separated phase. Although the zeroth order model itself is only qualitative in nature, it describes the strains of the separated phase quite well for all

three samples investigated. Deviations for relative pressures $p/p_0 \gtrsim 0.2$ are resulting from the increasing formation of the bridged phase due to capillary condensation, which is not covered by the slit-pore model. However, the magnitude of the compressive strains of the separated phase, found with SANS, is well approximated.

6.2.2 Discussion

With the data and analysis presented a simple model of adsorption induced deformation of the monolithic, hierarchically nanoporous carbon materials investigated can be constructed. The SANS and dilatometry n-pentane adsorption strain isotherms recorded in the CN, C30 and C120 samples (shown in **Figure 47**) look qualitatively different than strain isotherms obtained on silica (Chapter 5.1). This is due to their structural differences on the mesoscale, where the silica materials exhibit convex, cylindrical mesopores (**Figure 6**), whereas the pore space of the carbon samples is concave in nature. This difference can be explained with a model explicitly considering the concave nature of the void space on a mesoporous scale.

In accordance with the model of adsorption proposed in Chapter 6.1, three distinct intervals, each exhibiting specific deformation behavior as a function of relative pressure, can be identified. In SANS, the bridged, $0.3 \lesssim p/p_0 \lesssim 0.6$, and the filled phase, $0.6 \lesssim p/p_0 \lesssim 0.95$, can be satisfactorily described, where the strain in the bridged phase can be described by application of the generalized Laplace equation 3.101 to the bridged profiles obtained from numerical calculations and the filled phase can be evaluated with the Kelvin-Laplace equation 3.100. Effective pore-load moduli M_{PL} obtained from SANS data for the bridged and filled phase align well for all three samples, which indicates that both phases act on the same structures. Interestingly, M_{PL} increases with longer activation time, which seems counterintuitive at first, especially as an increase in micropores due to activation should lead to a decrease in measured modulus. Also, because all three samples exhibit very similar pore sizes and geometries, the stresses induced in the bridged phase are similar in magnitude and differences in M_{PL} due to different magnitudes in stress are ruled out. Therefore, the change in M_{PL} between all three samples can only be due to structural changes induced by activation. Evaluation of the pore-load modulus from dilatometry also shows an increase in modulus M_{dil} from the CN sample. But between the samples with 30 and 120 minutes activation, M_{dil} practically stays constant.

Although this trend in M_{dil} also seems contradictory as more micropores, due to activation, should lead to softening, the model of deformation shown in **Figure 53** can be applied to explain this behavior. If the compliance of structures between nanorods is considerably higher than of the carbon nanowires themselves, most of the deformation found in SANS is mediated by interstitial structures between carbon nanowires (see **Figure 52**). A simple estimation of the adsorption induced strains in the separated phase regime, where the nanowires modulus $E_{c,eff}$ is set to the value of M_{PL} , proves this assertion by contradiction. It can be assumed, that the normal and axial stresses induced by the surface stress during adsorption are purely positive and quite large ($\sim 0.1\%$ in **Figure 51** for $E = 10 \text{ GPa}$) compared to compressive stresses induced by adsorption in the gap between adjacent nanowires. If the associated modulus of the CN sample, $M_{PL} \sim 0.3 \text{ GPa}$ (**Table 12**), would be applied to the calculated stresses on a nanowire shown in **Figure 49** (with considering the factor 2 due to symmetry in **Figure 52**) a total positive deformation of around 6% would be observed. Considering the stresses induced

in a slit pore of width $H_{SP} \sim 2.3 \text{ nm}$ (for $d/r \sim 2.6$ with $d = 10.1 \text{ nm}$) upon capillary condensation, their resulting strain can be estimated to be of $\sim -0.4\%$ for a maximum stress of $\sim -12 \text{ MPa}$ (**Figure 51 b**) and $M_{PL} \sim 0.3 \text{ GPa}$. Summing these contributions up, an expansion of $\sim 5.5\%$ should be observed. As this is not the case (see **Figure 47 a**), the modulus of the carbon nanowires must be considerably higher than M_{PL} . Analysis of the pore-load moduli to extract effective axial Young's modulus $E_{c,eff}$ shows that it is indeed considerably larger than the associated value of M_{PL} and decreases with physical activation. For the CN and C120 samples $E_{c,eff}$ is by a respective factor of 90 and 8 larger than M_{PL} . Now, the change of M_{dil} with activation time can be explained. Due to stiffening of interstitial structures between nanowires and softening of nanowires with activation, M_{dil} is roughly constant between C30 and C120.

With the values for M_{PL} and E_c from SANS and dilatometry, the strains induced by the separated phase were calculated. Although the model applied (equation 6.6) is only a zeroth order approximation, it seems to cover the essential mechanism as the magnitude of strains found with SANS could be satisfactorily reproduced. Hence, the simple assumption that three phases form during adsorption allows to qualitatively describe the adsorption strain isotherms found with SANS and conceptually analyze strain isotherms obtained with dilatometry. An additional result is the fact that deformation of the mesopore space in SANS is mostly dictated by the compliance of structures situated between nanowires. Because the interconnections number density, structure and geometrical alignment relative to the nanowires long axis, all of which likely determine M_{PL} , are not known, M_{PL} is not equal to the Young's modulus of an individual interconnection and only represents a rough mean value of the Young's moduli of all affected structures.

With the findings presented in the previous paragraphs, a simple model of adsorption induced deformation can be constructed. At relative pressures associated with the separated phase, a liquid film covering the carbon nanowires leads to their expansion and also induces compressive stresses in the gaps between neighboring nanowires. In total, these effects lead to a compressive strain in the separated phase regime. Additionally, small condensation events occur in-between carbon nanowires, which probably lead to an additional compressive strain contribution¹²⁴ as shown in **Figure 53 I**. Filled regions in-between adjacent nanowires grow with increasing relative pressure, until they serve as nucleation sites for the bridged phase once the relative pressure of equilibrium transition between the separated and bridged phase is reached. Qualitative calculations of the strain induced by adsorption in the separated phase indicate that a separated phase exists and that local film instabilities¹³⁰ could also serve as sufficient nucleation points of the bridged phase. For n-pentane and nitrogen the relative pressure at which these instabilities are sufficiently large to initiate capillary condensation in a slit pore of similar width to the spacing between neighboring nanowires is close to values obtained from numerical calculations performed in Chapter 6.1 (see **Figure 39** and **Figure 40** respectively). From here-on, the strain isotherm can be approximated satisfactorily with pressures described by the generalized Laplace equation. With increasing relative pressure the mean curvature of the liquid-vapor profile decreases, which results in a relative increase in strain as shown in **Figure 47**. Once the equilibrium phase transition between bridged and filled phase has occurred, liquid-vapor interfaces at the pore throats, spanning the pore space in-between nanowires, lead to stresses that can be described by the Kelvin equation (equation 3.100). With increasing relative pressure the menisci at the ends of the nanowires round out and the pressure difference reduces, resulting in a net expansion of the lattice as pictured in **Figure 53 III**.

Strain isotherms measured with dilatometry can also be interpreted and discussed qualitatively with this model. All three strain isotherms can also be divided into three intervals, which approximately align with the phase boundaries of the separated, bridged and filled phase. The strain isotherms of the CN and C30, C120 sample differ for $p/p_0 < 0.3$, as the latter two exhibit clear dilation compared to the former which shows compression (similar to SANS strain isotherms). A possible origin of this behavior can be found if the nitrogen and n-pentane adsorption isotherms, presented in **Figure 45**, are compared for the CN sample. The difference in loading recorded between nitrogen and n-pentane is close to the amount of microporous, which leads to the conclusion that micropores in the CN sample don't fill substantially with n-pentane. Therefore, the stark expansion of the C30 and C120 samples at low relative pressures is most likely related to the filling of micropores. Because the positive strain at $p/p_0 \sim 0.05$ is larger for the C120 sample than for the C30 sample, the magnitude of this dilation seems to roughly scale with the specific microporosity (see **Figure 47**). The local minimum/saddle point observable at $p/p_0 \sim 0.3$ can be interpreted as the approximate phase boundary between the separated and bridged phases. The fits of the dilatometric strain isotherms with the Kelvin-Laplace equation reveal that only parts of the isotherm associated with the filled phase, hence for $p/p_0 \gtrsim 0.5 - 0.6$, can be well described with it. The lowest pressure at which good accordance between the Kelvin-Laplace equation and measured data is found defines the bridged-to-filled phase boundary. Between the separated and filled phase intervals, the bridged phase interval should exist according to the strain isotherms measured with SANS. In contrast to SANS strain isotherms, the shape of the strain isotherms measured with dilatometry cannot be interpreted as clearly. This is probably due to the network deformation measured in dilatometry where radial and axial deformations contribute to different degrees. In the proposed bridged phase regime loading does not change considerably (see **Figure 45**) and the nanowires are surrounded by liquid. The specific surface energy of the nanowires $\Delta\gamma_{sv}$, which is related to the surface stress acting on the nanowires, should therefore not vary considerably with relative pressure. Once the entire void space has filled upon the transition from the bridged to the filled phase, the spreading tension λ , which is directly proportional to the Laplace pressure Ψ , acts on the nanowires. As the radial and axial deformations are proportional to the Laplace pressure, the strains measured with dilatometry in the filled regime are directly proportional to Ψ (see equation 6.10).

To understand the increase in M_{PL} , the following process occurring during activation is proposed. It can be assumed that certain areas in the mesostructure are of lower mass density than on the mean. These areas with lower mass density can also be expected to be mechanically softer than areas with higher mass density. Once these compliant structures are removed via activation, effectively increasing the lattice parameter d (see **Table 11**), stiffer links are retained and the stiffness of the material seems to increase, even if the nanowires' mechanical parameters, such as E_c , decrease with physical activation. Indeed, the deformation measured in SANS is largest for the CN sample and subsequently decreases with activation time as evident from **Figure 47 a**).

7 Human Root Dentin

7.1 Experimental Results

The objective, of the in-situ water absorption SAXS studies on human root dentin performed during the course of this thesis, was to track deformation of the collagen matrix sandwiched between mineral platelets. The investigated sample was a slice of approximately $200\ \mu\text{m}$ of human tooth after the removal of the enamel crown. Preliminary in-situ water absorption SAXS measurements showed that most of the relevant structural changes are due to humidity which seem to happen at the relative pressures interval: $p/p_0 < 0.5$. The experimental water vapor pressures are listed in **Table 1**.

The evaluation of the measured scattering patterns was performed by azimuthal integration of the collected 2D SAXS patterns. The data collected was corrected regarding transmission, the sample cell's background was then subtracted and the 2D-SAXS patterns scaled to absolute units ($\text{cm}^{-1}\text{sr}^{-1}$) with water taken as calibration standard. The resulting one dimensional, radial patterns of the three measurement positions (see **Figure 18 a**) are shown below in **Figure 56**. The presented curves display the typical shape of radially averaged scattering patterns of mineralized collagen¹⁵⁶, indicating parallelly aligned mineral platelets within mineralized collagen¹⁵⁷. The parallelly aligned mineral platelets show a defined shoulder in 1-D scattering patterns at around $1\ \text{nm}^{-1}$ (**Figure 56**), where the shoulders position indicates a thickness of $\frac{\pi}{q} \sim \frac{\pi}{1} \sim 3\ \text{nm}$.

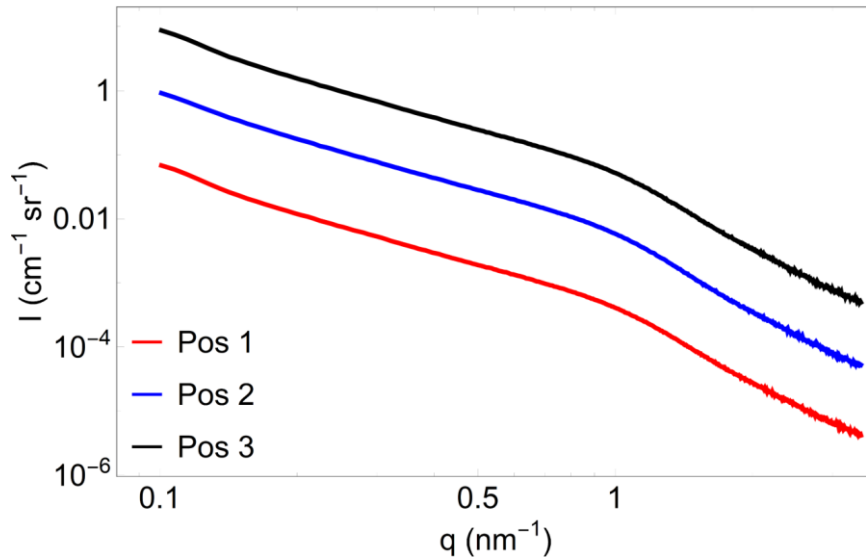


Figure 56: One-dimensional scattering patterns obtained from radially averaging the 2-D patterns at the positions highlighted in **Figure 24 a**) at a relative water pressure of 0. Positions 2 and 3 are scaled by a factor of 10 and 100 respectively for better visualization.

For the exact mineral platelet thickness determination the T-parameter, which results from the ratio \tilde{I}/P (see equation 3.11), was calculated. Therefore, the integrated intensity \tilde{I} of the scattered intensity was assessed first (equation 3.9) and then, by using the Porod plot (see equation 3.10), the P-parameter was calculated. Because every measurement

position investigated showed the same behavior as a function of relative pressure in scattering, it is sufficient to only show the results from Position 1. As water and collagen (or most biological materials) are relatively similar in X-ray scattering length density, other than the significantly denser mineral phase, a two-phase system between mineral and water/organics can be assumed. Consequently, the T-parameter should, according to previous assumptions, represent a mean chord length^{68,80} and closely represent the mineral platelets thickness (equation 3.13). In **Figure 57** a) the evolution of the integrated intensity as a function of relative pressure is displayed. After a sharp drop-off in integrated intensity at relative pressures $p/p_0 \leq 0.2$, a linear decline with regard to the decrease in density of measurement points can be observed. Assuming that the platelets embedded in the collagen matrix are fixed in position and that absorbed water is integrated into the collagen matrix and thereby effectively enhancing its scattering length, the area between the mineral platelets and the collagen matrix does not change. The P –parameter is then only proportional to the square of the difference in scattering length density (see equation 3.10) of the organics containing water and the mineral. Therefore P , as a function of relative pressure, should correspond to the amount of water absorbed.

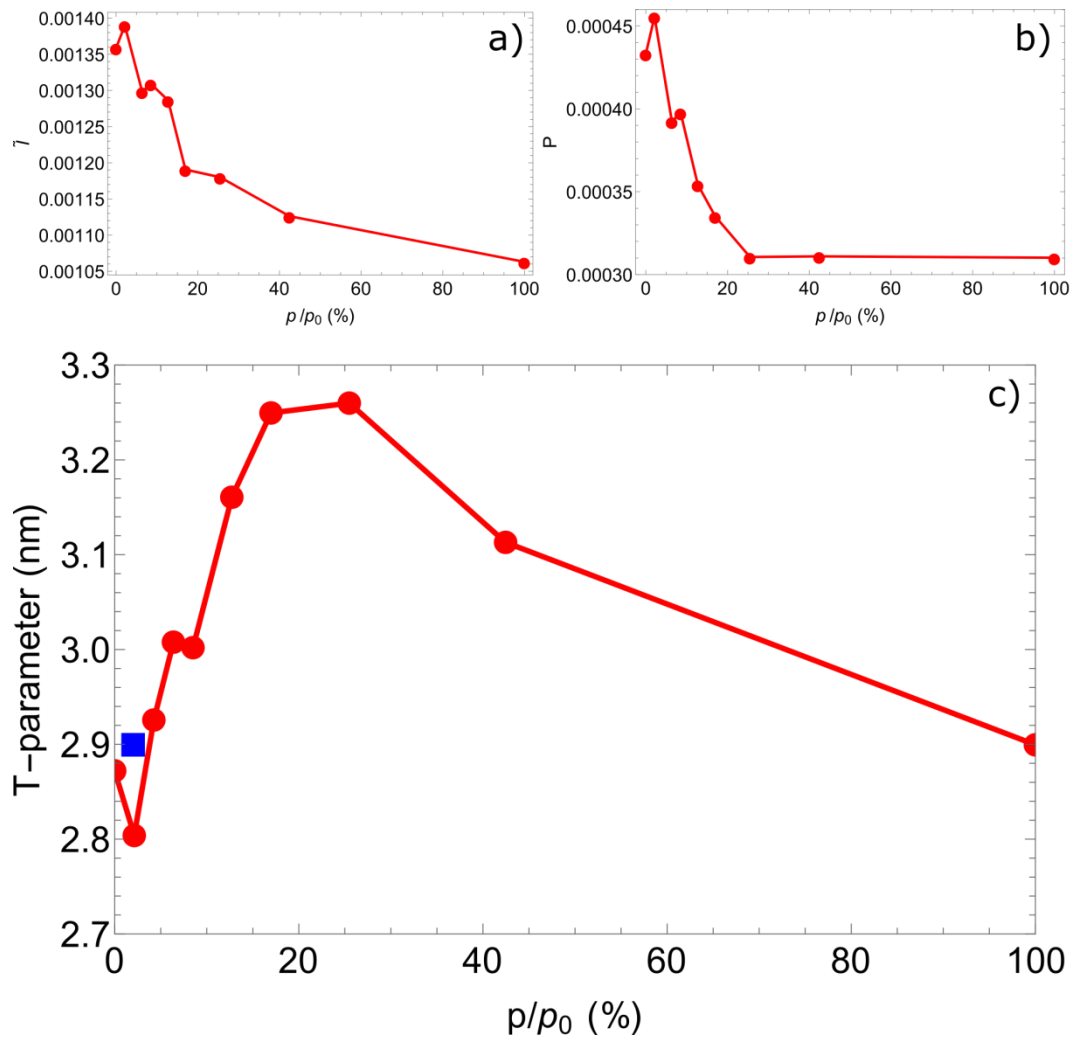


Figure 57: The integral parameters \tilde{I} and P are derived from the scattering patterns of position 1 at different relative pressures are shown, with integrated intensity in sub-figure a), the P -parameter in sub-figure b) and the resulting T -parameter in sub-figure c). The T -parameter value in desorption after evacuation of the sample is represented by the blue square.

The integrated intensity \tilde{I} , which is also proportional to the difference in scattering length density squared (equation 3.10), is not in direct correlation with the water content as different hierarchical levels contribute to it. Therefore, the Porod scattering at high q –values originates from the mineral platelets only. Hence, the hierarchical structure of human root dentin prohibits the use of the integrated intensity to track the water content unambiguously. As can be seen in **Figure 57 b)**, the P –parameter drops off significantly at low relative pressures and levels off at $p/p_0 = 0.25$, thus indicating the filling of the collagen matrix inbetween mineral platelets with water. The resulting T –parameter as a function of relative pressure is shown in **Figure 57 c)**, where a relatively steep increase at low relative pressures can be observed until the trend reverses and a slow decrease down to the original value of T is retained. As in desorption only slight changes of the T -parameter are visible due to the experimental resolution in pressure, analysis of it was omitted. After evaluation of the sample following adsorption, the original T –parameter value (indicated by the blue square in **Figure 57 c)** is retained.

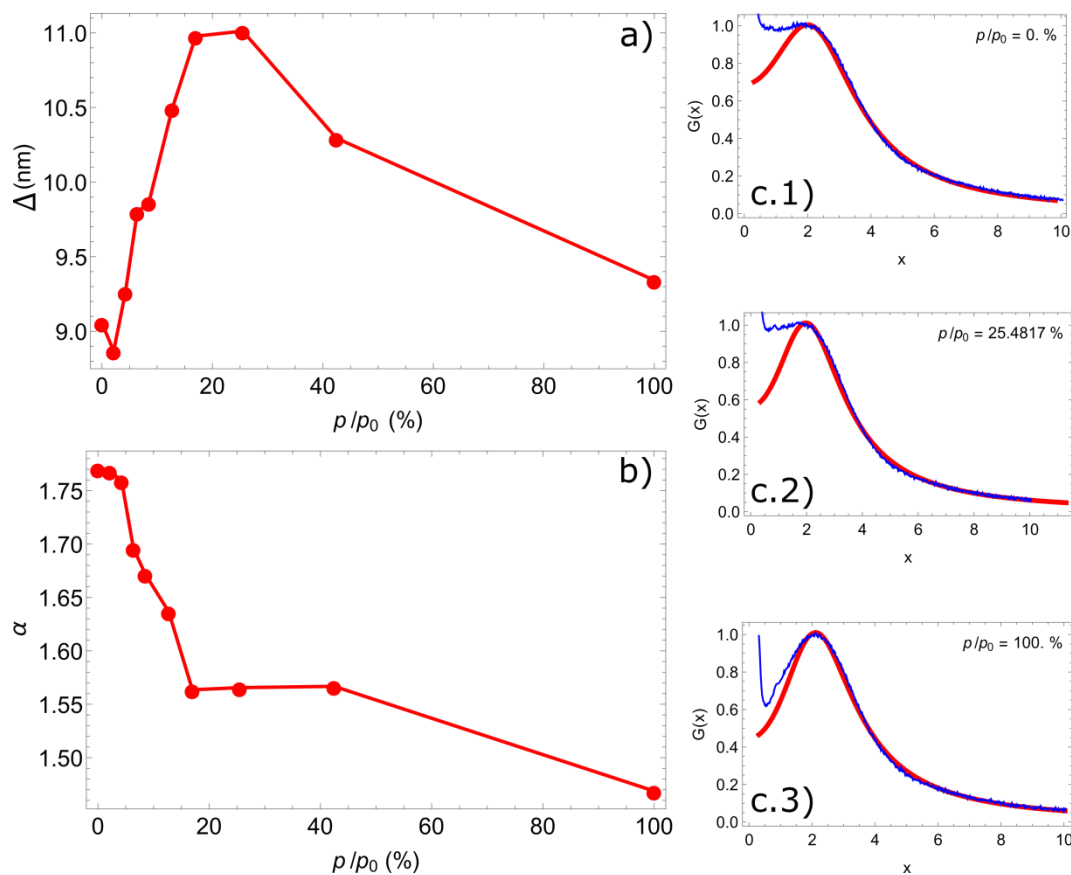


Figure 58: In sub-figures a) and b) the evolution of mean platelet distance and disorder with increasing relative pressure is shown. In sub-figures c.1) to c.3) fits of the $G(x)$ curves at select relative pressures are provided, where the full blue line depicts the measurement and the dashed red line is the fitted function.

After analyzing the platelets thickness, the dimensionless $G(x)$ function⁸⁵ was applied to the scattering patterns. These patterns were fitted with equation 3.15 to obtain parameters $\beta \left(\frac{p}{p_0}\right)$ and $\alpha \left(\frac{p}{p_0}\right)$, which indicate the mean distance between mineral platelets and their respective long range order. To mitigate effects of contrast changes, all $G(x)$ curves were scaled to the T -parameter of the wet sample, because it should most reliably represent the actual value found in other studies. To minimize the effect of the integrated

intensity, all curves were scaled to 1 at $x \sim 2$. The resulting parameters α and $\Delta = 2\pi T/\beta$ are plotted in **Figure 58** a) and b) as a function of relative pressure. In **Figure 58** c) best fits are presented, where the curve cannot be fit satisfactorily when considering data at $x < 2$. Comparing fits to scattering data, transformed to $G(x)$ in **Figure 58** c), one can see that the scattering data at $x < 2$ significantly deviates from the fitted functions of $G(x \geq 2)$. As $x \sim 2$ corresponds to the q – position of the shoulder in the scattering patterns presented in **Figure 56**, data at $x \geq 2$ exclusively originates from the mineral platelets scattering. The shape of the fitted $G(x)$ curves then dictates α and β . The distance parameter Δ and the T -parameter evolve similarly as a function of pressure. Long-range disorder of the system as characterized with α follows the trends of the integrated intensity \tilde{I} and Porod-parameter P in **Figure 57** b) and c).

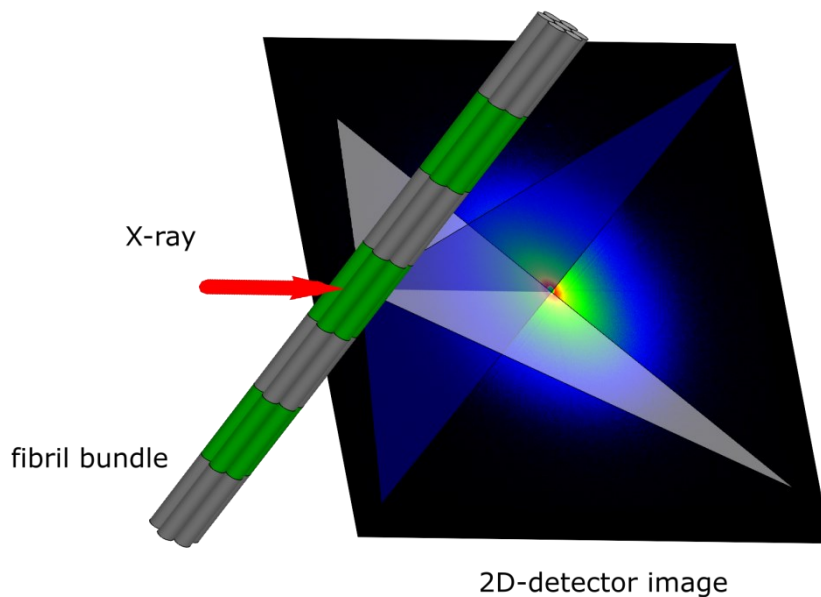


Figure 59: A schematic sketch of the relation between the collagen fibril orientation with respect to the obtained scattering pattern is shown. The alternating black and green parts of the fibril bundle denote the gap regions filled with mineral plateletes and the collagen overlap region respectively, whereas the opaque white triangle perpendicular to the fibril axis denotes the equitorial and the parallel aligned blue triangle denotes the meridional scattering directions.

Sectoral Evaluation: The anisotropic shape of the measured 2-D SAXS patterns can be directly related to the texture of the human root dentin sample. As the mineralized collagen fibrils in human root dentin are well aligned and arranged in bundles of approximately cylindrical shape (see above in **Figure 61**), their scattering pattern shows the characteristic non-isotropic 2-D intensity distribution, shown above in **Figure 59**. The anisotropic scattering of the parallel closed-packed cylindrical objects shows different features according to their geometrical arrangement in relation to the laboratory system. For instance, sectors of the 2-D scattering pattern parallel to the fibrils arrangement should show scattering characteristics of the Hodge-Petruska scheme, introduced in Chapter 2 (see **Figure 3**), whereas sectors perpendicular to the preferred orientation of collagen fibril bundles should exhibit correlation peaks of the fibrils packing. The mineral plateletes scattering should be visible in directions parallel and perpendicular to the collagen fibrils orientation, due to the helical alignment of platelets within fibrils and the radial distribution of fibrils in the plane perpendicular to the detector as well as parallel

to the fibril orientation (see for reference **Figure 3** or blue plane in **Figure 59**). By integrating sectors of the 2-D SAXS pattern, associated with either the scattering parallel (blue plane in **Figure 59**) or perpendicular (white plane in **Figure 59**) direction described above, alignment of collagen fibrils, 1-D SAXS data specific to the structure dominating scattering in these sectors can be obtained. Because the collagen fibrils are usually not aligned perfectly parallel, sectoral cake integration with a spread of $\pm 15^\circ$ around the intersections of the blue (parallel) and white (perpendicular) plane with the detector is performed (for reference see **Figure 59**).

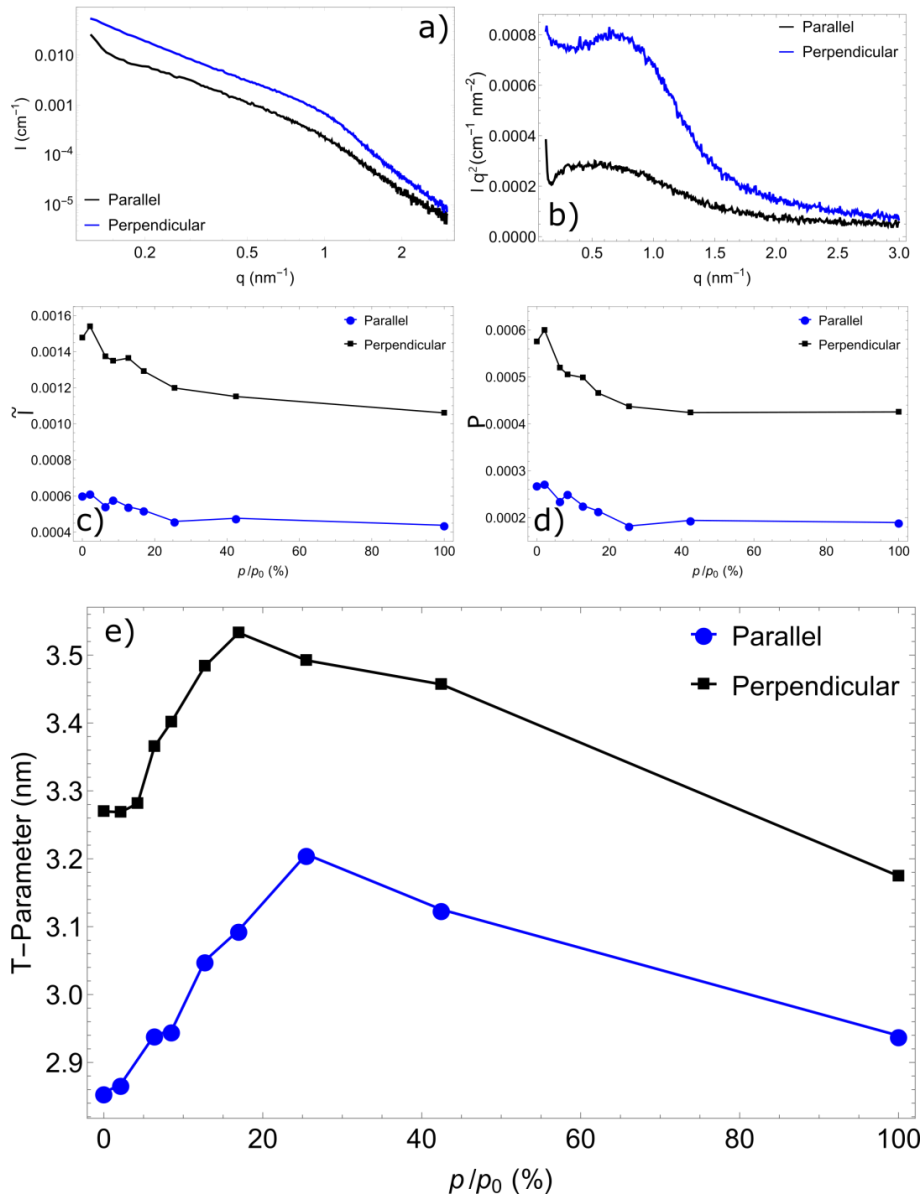


Figure 60: In sub-figures a) and b) the double logarithmic and Kratky plot of the 1-D patterns at a dry sample state is obtained from cake integration parallel and perpendicular to the main orientation of collagen fibrils found. Integral parameters, those being the second moment of the recorded intensity, Porod parameter and T-parameter, derived from both patterns are compared at a function of relative pressure

Comparing these 1-D scattering patterns in **Figure 60** a) and b), clear differences are evident. Along the long axis of the collagen fibers, the onset of a peak-like feature is visible at small q . Also, the recorded intensity is vastly different between the parallel and

perpendicular directions, with the latter being around a factor of 2 to 3 larger. The P-parameter shows a similar trend, although the ratio is significantly smaller.

Further investigation is conducted by again transforming the data from the parallel axis and from the perpendicular direction, to the dominant collagen orientation, into $G(x)$ curves and subsequent fitting with the Stack-of-Cards model. The largest changes to the recorded scattering pattern are expected to happen at low angles, where large changes in contrast and structure were observed in the $G(x)$ curves of the radially averaged data. Therefore only partitions of the curve where $x > 2$ corresponding to $q \geq 0.6 \text{ nm}^{-1}$ were fit.

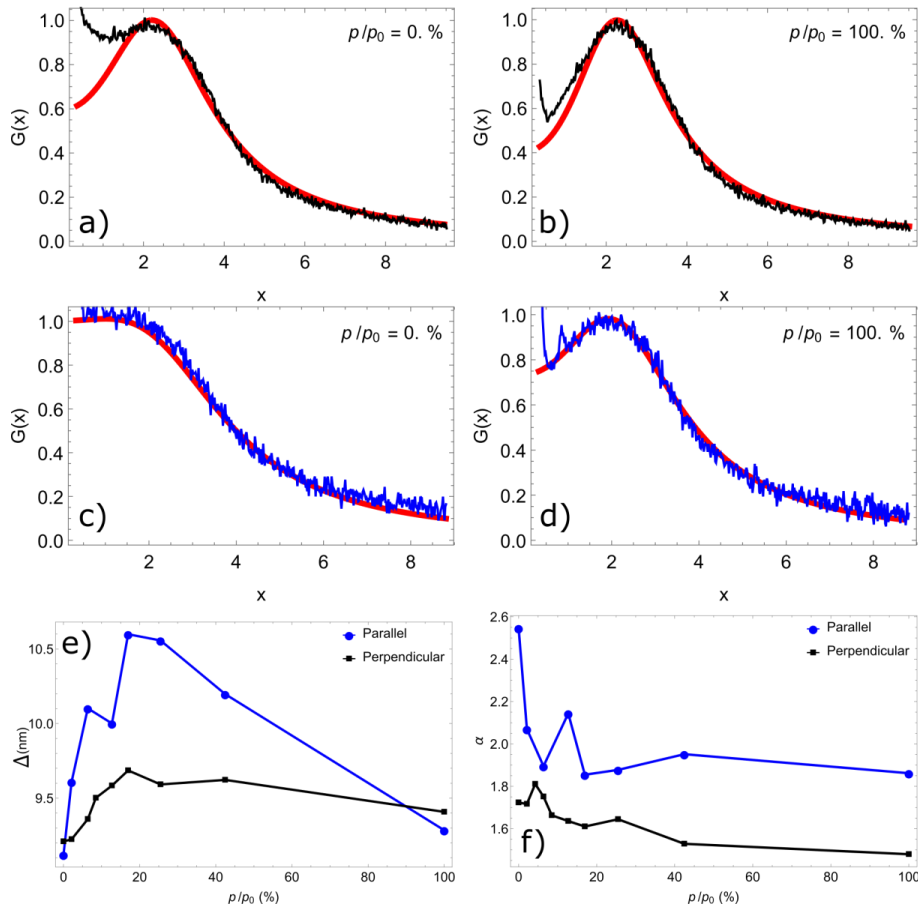


Figure 61: In sub-figures a), b) and c), d) the data transformed to $G(x)$ and fitted $G(x)$ curves are shown for the perpendicular and parallel integration cakes respectively, where the full lines represent the measured patterns and the red, dashed lines are the fit. Resulting platelet distances and disorder parameters are shown in e) and f).

Results of this analysis are shown in **Figure 61** above, where in a), b) and c), d) the $G(x)$ data and their corresponding fits of the perpendicular and parallel collagen fibril orientation are depicted. In contrast to the perpendicular orientation, the parallel direction shows a clearly less defined peak-like feature, resulting in largely increased disorder parameter. With increasing relative pressure, α decreases quite dramatically, whereas the mean distance between successive platelets mirrors the behavior found for the T-parameter. Here, the evaluation parallel to the fibril long axis exhibits a large change in contrast to the perpendicular direction, which is unexpected. Still, at dry and wet sample states, the interplatelet distance is relatively similar, mirroring the relations found in the respective T-parameters. This further indicates that the changes in T-parameters found, are due to sequential filling of structures increasing in size. Hence, the results are

probably marred by contrast effects and swelling of structures outside the scope of this experiment, which makes the T-parameter unreliable for the present evaluation.

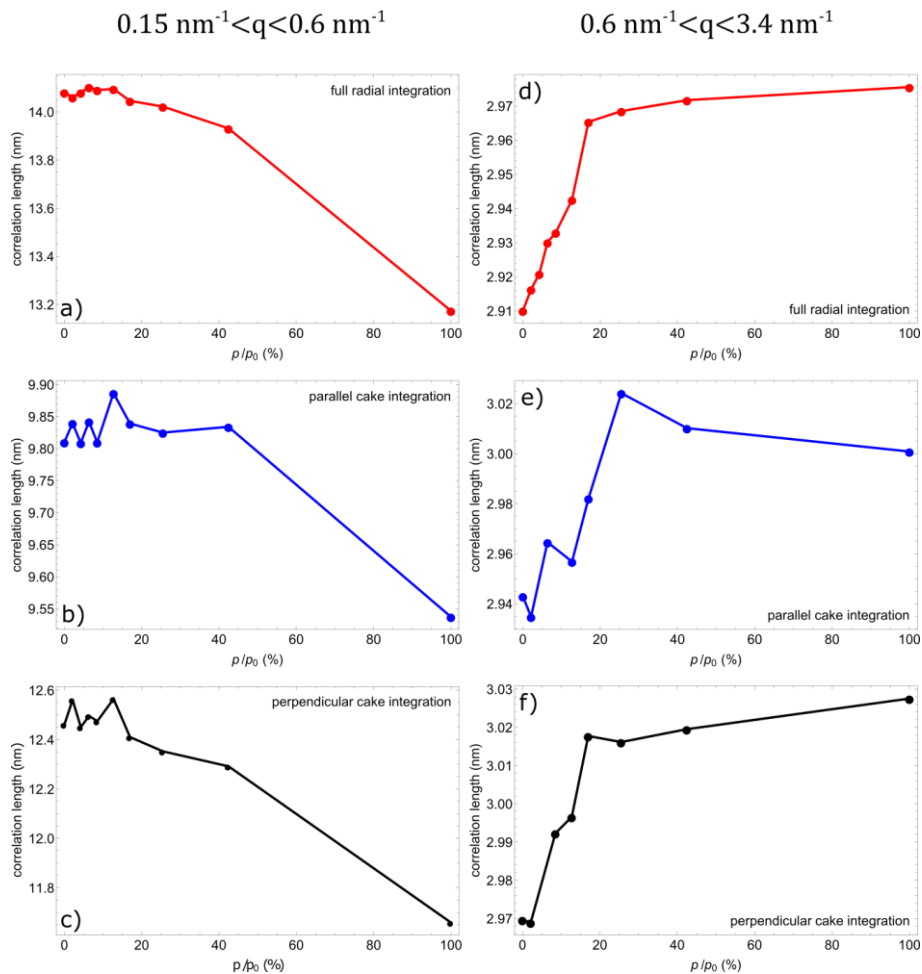


Figure 62: The correlation lengths of all three integration sectors determined from q -values ranging from 0.15-0.6 and 0.6-3.4 nm^{-1} are shown in the top and bottom three subfigures. In a) and d) the full radial integration and in b), e) and c), f) the parallel and perpendicular cake integrations are shown respectively.

Another measure of size applicable to non-diluted, non-particulate systems is the correlation length⁸⁰, which is proportional to the first moment of intensity. Even though the fits obtained from the Stack-of-Cards model do imply a relatively loosely ordered alignment, this parameter should represent the mean platelet size quite well. To distinguish scattering by smaller and larger structures, the patterns were evaluated in q ranges from 0.15 – 0.6 (corresponding to structures of $> 5 \text{ nm}$) and 0.6 – 3.4 nm^{-1} (corresponding to structures $< 5 \text{ nm}$), for the full radial and the perpendicular and parallel cake integrations, with the results displayed in **Figure 62**.

In **Figure 62** a), b) and c) the correlation lengths of q values, ranging from 0.15 – 0.6 nm^{-1} , for all three areas of integration of 2-D SAXS patterns are shown, where all exhibit highly similar behavior outside their magnitude. At low relative pressures, the lengths obtained remain largely constant until they decrease significantly at the filled sample state. The largest overall values are found for the full radial integrations, with the cake integration aligned along the collagen fibrils exhibits the smallest values. Additionally, both, the fully radial and the perpendicular cake integration, show a relative drop in length at about 7%, whereas along the fibril axis only 2.9 % relative drop are

observed. For q values ranging from $0.6 - 3.4 \text{ nm}^{-1}$, all integration areas show remarkably similar behavior, where a steep increase in correlation length can be observed with increasing relative pressure, until 20% p/p_0 are reached and only relatively minor changes in values are apparent, until the wet sample state is reached. All three integration areas show very similar values (within 3-5%), where a relative difference between the wet and dry sample state of about 1.95-2.1% is observed for all.

If one compares the change in platelet-distance of the sectoral integration perpendicular to the axis of main alignment of the collagen fibrils (black line in **Figure 61 e**), the mean distance grows from $\Delta(p/p_0 = 0) \sim 9.2 \text{ nm}$ to $\Delta(p/p_0 = 0.95) \sim 9.4 \text{ nm}$. This corresponds to a swelling of 2.2%, which matches the results from the correlation length analysis at large q and can be consistently found for all three positions of measurement. In contrast, the evolution of the parameter Δ with relative pressure of the sectoral integration parallel to the main alignment of collagen fibrils is similar to the behavior of the T -parameter as a function of relative pressure in **Figure 57 c**) (red line). With the values for the correlation length and the interplatelet distance Δ at $p/p_0 = 0$ the mineral platelet thickness can be calculated with equation 3.12. Naively plugging the values of the dry sample state, $\Delta (= 9.2 \text{ nm})$ and the correlation length ($= 2.97 \text{ nm}$) of the perpendicular sectoral integration into 3.12, the platelet thickness comes out to be $\sim 4.38 \text{ nm}$ which is in fair agreement with literature values⁷⁴. To determine the change in measured chord length from the dry to the wet sample, either by the T -parameter or the correlation length, the mean chord length can be calculated with equation 3.12 by applying the thickness of the mineral platelets ($\sim 4.38 \text{ nm}$) and the mean platelet distance $\Delta(p/p_0 = 0.95) \sim 9.4 \text{ nm}$ to it. The chord length for this case comes out at $\sim 3.01 \text{ nm}$ which corresponds to a swelling of $\sim 1.4 \%$. This is quite close to the change in correlation length found for large q and serves as a consistency check. If the swelling predicted by this approach would be significantly smaller or larger than according values from the correlation length, either the platelet distance Δ or the correlation length would be erroneous. Here, the values for the mean chord length obtained from calculation and measurement are consistent, which gives further confidence in the approach taken with the sectoral evaluation and the results obtained from it and the correlation length.

SAXS experiments resolving larger Structures: To elucidate changes observed in scattering patterns and derived integral parameters, subsequent in-situ water absorption SAXS measurements, at a distance favoring larger structures (sample-detector distance $\sim 113 \text{ cm}$) with high resolution using a $300 \mu\text{m}$ Scatex pinhole, with a resulting q interval reaching from $0.07 - 2 \text{ nm}^{-1}$, were conducted. The evaluation presented here is purely based on corrected scattering patterns, omitting further evaluations in this thesis. Resulting 1D SAXS patterns obtained from integration cakes parallel and perpendicular the main collagen fibril (for reference see **Figure 59**) orientation are presented in **Figure 63 a**) and **b**) in a Kratky representation to highlight features.

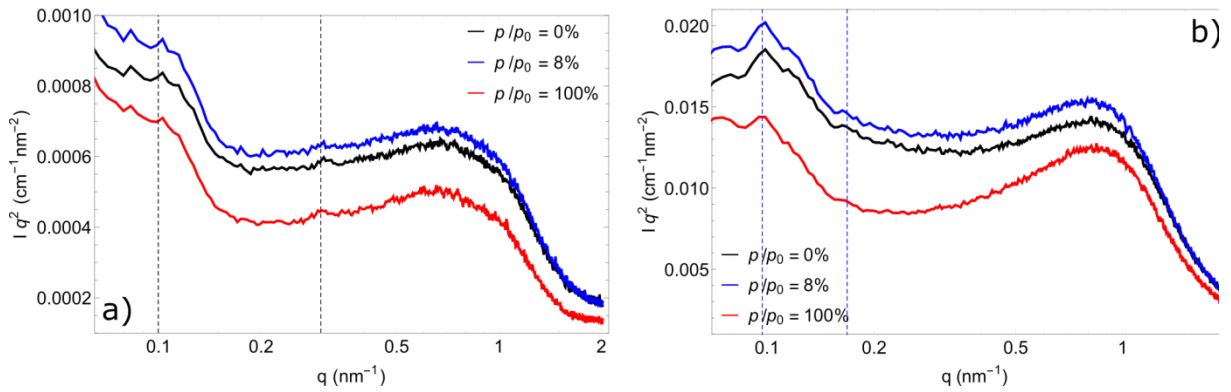


Figure 63: In sub-figures a) and b) the cake integration parallel and perpendicular to the general fibril orientation are shown for several relative pressures. The black, dashed lines in a) highlight the first and third order of the collagen stagger, whereas in b) the lines denote the positions of a proposed 2-D close packed order of the collagen fibrils.

The results presented are the same for all positions investigated. As expected from the fact that sectors of the 2-D SAXS patterns corresponding to structures perpendicular to the collagen fibrils main alignment, no third order of the collagen stagger is observable. For the integration in meridional direction, meaning parallel to the collagen fibril alignment, the first and third order of collagen peaks are resolvable (**Figure 63 a**). Due to limited resolution of the detector for very small q , which originates from the small number of pixel counting photons, the first peak appears as a collection of jagged features. For the sectoral integration perpendicular to the collagen fibrils alignment two peaks are distinguishable in **Figure 63 b**), whose positions are in a strict $\sqrt{3}$ ratio¹⁵⁸. Unfortunately the resolution is quite limited at small q , hence it is not clear whether the peak at $\sim 0.09 \text{ nm}^{-1}$ in **Figure 63 b**) originates from the packing of microfibrils (for reference see Chapter 2.3) or results from the stagger of collagen. As no higher order of collagen is resolvable in **Figure 63 b**) where significantly higher counting statistics are observed (**Figure 63 a**) and **Figure 63 b**), it is questionable if the feature originates from the collagen stagger. Although these observations indicate 2D hexagonal order such as expected from collagen fibrils¹⁵⁸, more orders of the 2-D hexagonal arrangement of microfibrils are necessary to proof this proposition.

Comparing the evolution of scattering patterns between both angular sectors integrated allows to further understand the effects observed. At q values inbetween $0.15 - 0.7 \text{ nm}^{-1}$ it is evident that the direction along the collagen fibers seems to only shift in intensity without clear change in slope at increasing relative pressures, whereas the perpendicular integration cake shows a large change in slope upon filling of the sample. This a definite change to steeper slopes mirrored in the shapes of the associated $G(x)$ curves shown in **Figure 61**. Changes for $q > 0.7 \text{ nm}^{-1}$ are more subtle and can be related to filling and deformation of small structures. Further evidence for length change of different structures can be found if one considers the correlation length in **Figure 62 d) - f)**, whereas changes in larger structures seem to happen at higher relative pressures. This sequential change of scattering intensity leads to the pronounced change in the parameters $\Delta(p/p_0)$ and $\alpha(p/p_0)$ in **Figure 58 a)** and **b)**. Still, if all structures are filled with water once the highest relative pressure is reached, the original contrast relation between different hierarchical levels should be restored and patterns at $p/p_0 = 0\%$ and $p/p_0 = 100\%$ should be parallel. The fact that the contrast relations between different hierarchical levels should be the same for $p/p_0 = 0$ and 0.95 , the T - parameter and correlation length should reliably reflect the change in size of these respective parameters

between these relative pressures. Looking at **Figure 63** a) and b), it is evident from data of sectoral integration parallel to the collagen fibers that filling of the sample mostly leads to a parallel shift in intensity with more subtle differences in scattering at small and large scattering vectors. For perpendicular directions, changes in structure or contrast upon absorption seem to occur as evident by the strong change in slope for intermediate $0.15 \text{ nm}^{-1} < q < 0.7 \text{ nm}^{-1}$ values. Both sectoral integrations share that between $p/p_0 = 0\%$ and 8% most changes seem to occur at large $q > 0.7 \text{ nm}^{-1}$, whereas the rest of the pattern shifts to higher intensities.

7.2 Discussion

The main question arising from the data presented on in-situ water absorption SAXS measurements on human root dentin is whether the change of correlation length or interplatelet spacing Δ observed (see respective figures **Figure 62** and **Figure 61** e) originate from structural or contrast changes.

Analysis of SAXS patterns was performed by full radial integration and cake integration of sectors of the 2-D SAXS patterns parallel and perpendicular to the long axis of the collagen fibrils. From the 1-D patterns, obtained from azimuthally integrating the full 2-D SAXS patterns, integral parameters \tilde{I} and P were determined as a function of relative pressure. By taking their relation (\tilde{I}/P) the T –parameter was determined, which should be indicative of the mean thickness of the mineral platelets within mineralized collagen fibers. A large hysteresis was found for the T –parameter, where in absorption a maximum increase of 13% in platelet thickness was observed at $p/p_0 \sim 0.2$ which then decreased until the original T –parameter at $p/p_0 = 0$ was approximately retained (see **Figure 57** c). As the mineral is very stiff and strains in the range of $\sim 2\%$ ¹⁵⁹ were found using synchrotron radiation, associating this maximum in T with strains on the mineral phase is highly questionable.

Indications on the origin of this behavior can be found if the integrated intensity \tilde{I} and the P –parameter are compared (see respective **Figure 57** a) and b). P exhibits a sharp drop off at low relative pressures and reaches a constant minimum value at $p/p_0 \sim 0.2$, whereas \tilde{I} exhibits a monotoneous decline from the dry to the wet sample state. Under the assumption that water and biological materials in the region between neighboring mineral platelets form a homogeneous phase and that the surface between biological matter and mineral remains constant, the parameter P was pointed out as being correspondent to the amount of water absorbed in the collagen matrix wherein the mineral platelets are embedded. Consequently, absorption and changes of changes in structure, for instance expansion of the collagen matrix between mineral platelets, should be completed at $p/p_0 \sim 0.2$ and \tilde{I} should remain constant for higher relative pressure. As this is clearly not the case (check **Figure 57** a) for reference), different structures than the parallel mineral platelets and the surrounding collagen in the human root dentin sample absorb water and/or deform for relative pressures $p/p_0 > 0.2$. Application of the stack-of-cards model to the 1-D SAXS scattering patterns showed that q – values associated with larger scale structures seem to change in contrast or structure at relative pressure $p/p_0 > 0.2$, as highlighted by the change in slope of the $G(x)$ curve for $x < 2$ (corresponding to $q < 0.7$) in **Figure 58** c) for $p/p_0 > 0.2$.

By performing sectoral azimuthal integration of the 2D SAXS patterns to 1D SAXS patterns, the anisotropic scattering of the human root dentin sample can be analyzed in more detail. For sectors parallel to the alignment of the collagen fibrils, information on

the collagen stagger and the mineral platelets can be extracted, whereas for sectors perpendicular to the collagen fibrils information on the fibrils dense packing and the mineral platelets can be obtained¹⁵⁸. The T –parameter for both sectoral integrations yield different numerical values (**Figure 60 e**) but qualitatively similar behavior as a function of relative pressure. Applying the stack-of-cards model to both directions, once for sectors parallel and once perpendicular to the collagen fibrils main orientation, the scattering data transformation to $G(x)$ curves and their fit reveal that both directions exhibit different behavior. Sectors of the 2D-scattering pattern aligned in parallel to the collagen fibrils exhibit large values of the disorder parameter α (**Figure 61 f**), which changes significantly with relative pressure (decrease of $\sim 26\%$), and show behavior of the platelet distance Δ as a function of relative pressure similar to the T –parameters behavior (compare **Figure 61 e**) to **Figure 60 e**). For scattering patterns associated with sectors in perpendicular alignment to the collagen fibrils on the other hand show decidedly smaller values of the disorder parameter α (with a drop of $\sim 11\%$ between the dry and wet state), reflected in the defined peak-like features in the associated $G(x)$ patterns in **Figure 61 a**) and b), and the interplatelet distance Δ seems to reach somewhat constant values for $p/p_0 \gtrsim 0.2$. This behavior of Δ as a function of relative pressure is indirectly proportional to the P –value of the patterns obtained from azimuthal integration of sectors in perpendicular alignment to the collagen fibrils (see **Figure 60 d**), which points to the fact that the swelling of the interplatelet spaces is directly associated with filling of the collagen with water. The increase in interplatelet distance (black curve in **Figure 61 e**) of about 2.2% from $p/p_0 = 0$ to 0.95 is in satisfactory agreement to the increase in collagen fibril diameter of 2.5 % found by Masic et al⁴⁶.

Applying a different measure of length, the so-called correlation length, to different intervals in q one can in principle separate the deformation of larger and smaller structures as a function of relative pressure. Because no clear separation of structures in size is known to the author, this discrimination in smaller and larger size structures is only qualitative and not definitive. For $q > 0.6 \text{ nm}^{-1}$ the deformation of smaller scale structures is evaluated. For the fully azimuthal, the parallelly and perpendicularly aligned the correlation lengths found are highly similar (see **Figure 62 d**), e) and f) and show practically the same behavior as a function of relative pressure with a relative difference in correlation length between the dry and wet sample state of about 1.95-2.1%. This extension is in good accordance with the value of 2.5% found by Masic et al⁴⁶ and Forien et al¹⁵⁹ and in excellent agreement with the swelling of the collagen matrix between mineral platelets found by the stack-of-cards model mentioned in the previous passage. A simple analysis where the swelling of the collagen found by the stack-of-cards model is expressed through the change in correlation length at $p/p_0 = 0$ and $p/p_0 = 0.95$ with equation 3.12 finds a mineral platelet thickness of 4.38 nm and a relative change of Δ with water absorption of 1.4%. This simple and crude calculation still agrees relatively well with the change in $\Delta \sim 2.2\%$ and points out that the change in correlation length is directly related to the change in interplatelet distance with water absorption. Evaluation of the correlation length for $q < 0.6 \text{ nm}^{-1}$ in **Figure 62 a**), b) and c) shows that swelling of larger scale structures, whatever they may be, occurs for relative pressures $p/p_0 > 0.4$.

These evaluations lead to the interpretation of the T-parameters behavior as a function of relative pressure. The gaps in the staggered arrangement of collagen molecules are also filled with highly polar Glycosaminoglycans, which attract water also at lower relative pressures. These gap regions are then filled at low relative pressures which leads to an increase in spacing between mineral platelets which is reflected in the change in correlation length. Because gap regions fill at low relative pressures compared to larger

structures present, the Porod scattering decreases before these larger structures have filled with water. A direct consequence of this behavior is that the integrated intensity, which is dependent on all structural elements across different hierarchical levels in contrast to the Porod scattering, decreases only at slightly higher relative pressures. This leads to the increase in T-parameter observed, which is consequently not uniquely a measure of mineral platelets spacing in in-situ water absorption SAXS measurements. Once the equilibrium pressure of water is reached, large structures have finally filled and the original contrast relations between different hierarchical levels should be restored. Consequently, different measures of size, meaning the T –parameter, the correlation length and Δ , should yield reliable results when comparing their values at $p/p_0 = 0$ and 0.95. Indeed, the relative expansion of approximately between all three approaches of $\sim 2\%$ is in good agreement with measurements by Masic et al⁴⁶. The only difference between all three approaches is the measure of extension between the dry and wet state, where the chord length seems to provide the most accurate results as it's behavior closely mirrors the evolution of the P – parameter which can be assumed to be proportional to the filling of the collagen between mineral platelets and therefore to physical changes in dimension with water content.

8 Summary & Outlook

This thesis deals with concepts surrounding adsorption and adsorption induced deformation in synthetic hierarchically nanoporous silica and carbon materials, as well as absorption in human root dentin. Due to the breadth in topics, results pertaining to every single material are summarized separately.

Silica: For monolithic, hierarchically nanoporous silica existing theoretical concepts, which allow the determination of adsorption induced stress and deformation purely on the basis of associated sorption isotherms³², were applied to water sorption. Because the mechanical parameters, those being the Young's modulus of the mesopore wall and the aspect ratio of the struts building up the monolith, are not a-priori known, these theoretical concepts can be used to characterize hierarchical, nanoporous materials. For two silica samples with different thermal history, the S-C and S-S sample, the results obtained from in-situ 0-SLD water adsorption SANS and dilatometry were fitted with the theoretical thermodynamic stress model^{32,33} described in chapter 3.3. Good agreement between previous findings using nitrogen sorption pertaining to the Young's modulus was achieved for both samples investigated, yet the aspect ratio of the struts did not reflect previous values obtained from SEM. A possible origin of this discrepancy discussed between experiment and model could be the insufficient description of water adsorption in nanoporous silica materials.

Further, contrast effects responsible for apparent strains in in-situ adsorption SAXS measurements are evaluated. By comparing water adsorption strain isotherms for the S-C sample obtained from SAXS and SANS using 0-SLD water, apparent strains for the entire range of relative pressures from 0 to 0.95 were determined. To model the apparent strain two models were considered in simulations of the samples SAXS patterns as a function of relative pressure by application of the Debye scattering equation⁹⁴. The first model dealt with apparent strains due to adsorption in mesopores alone, whereas the second model considered all hierarchical levels by application of a hierarchical model for SBA-15⁸⁹. By tracking the apparent change of the (10) peak position due to adsorption as a function of relative pressure allows for the determination of apparent strain isotherms. Consequently, the applicability of the model describing sorption in the hierarchically nanoporous material is crucial to accurately model apparent deformations. Model 1 failed in describing apparent strains found for the S-C sample. In contrast, model 2 was able to capture the essentials of the experimental apparent strain isotherms.

However, both studies pointed out general discrepancies in the description of water adsorption in silica. As has been discussed in this work, the macroscopic thermodynamic theory of adsorption is able to describe adsorption of non-polar fluids sufficiently well in well defined, highly symmetric materials. But once a certain amount of disorder or any interaction outside of classical London forces is present, clear conclusions based on these classical descriptions are not viable anymore. This is evident in the description of the adsorption isotherm of the calcined hierarchically nanoporous silica sample, where discrepancies regarding the filling mechanism of the cylindrical mesopores arise. In the classical picture, a multimolecular liquid film covers the mesopore walls which grows with increasing pressure until capillary condensation sets in. Form factor fits of in-situ SAXS patterns show that only the corona of the mesopore fills with water upon adsorption, which is substantiated by the behavior of the apparent strain found. Here,

multilayered films on a mesopore wall would only lead to negative apparent strains, whereas positive apparent strains were found in measurements. The reason for this behavior should be found in the polar character of the adsorbing water molecules which interact with possibly polar surface groups on the silica mesopore wall. This kind of interaction isn't even well described by state-of-the-art methods such as NLDFT or QSDFT, which points out the limits of current methods. In as far irregular surface structure plays a role is not entirely clear, but earlier works¹⁰⁵ have shown that these also have strong influence on the perceived sorption behavior. Hence, further experimental work is necessary to not only develop sufficient descriptions of non-polar interactions between adsorbate and adsorbent, but also quantify the influence of disorder of pore surfaces and shapes. The impact could be far reaching, as this could open new, more precise engineering possibilities in catalysis, actuation or medical applications.

Carbon: In-situ n-pentane adsorption SANS and dilatometry measurements to determine adsorption induced deformation of monolithic, hierarchically nanoporous carbon materials were conducted. These carbon materials mesostructure is a negative replica of the silica materials investigated in this thesis and exhibit an open and concave mesostructure similar to conventional CMK-3. Three carbon materials at different degrees of activation, 0, 30 and 120 minutes respectively (according to samples CN, C30 and C120), were investigated using in-situ n-pentane adsorption SANS and dilatometry measurements. Because no theory describing adsorption of non-polar fluids, such as n-pentane or nitrogen, necessary to interpret recorded strain isotherms has been developed so far, a model from Dobbs et al¹¹³, based on the application of variational calculus to the grand potential of three distinct liquid phases, was adapted. The phases considered were a separated phase where a multilayered liquid film covers individual nanowires, a bridged phase where liquid bridges span the interstitial spaces between neighboring nanowires and a filled phase where the whole concave pore space is filled with liquid. Solutions of the non-linear, second order ordinary differential equations, obtained from applying the Euler-Lagrange equation to the grand potential, were obtained numerically for the separated and bridged phase. The profiles $l(\theta)$ describing the separated and bridged phase can be used to calculate the grand potential of the phases. By determining the phase which exhibits the minimal grand potential, the equilibrium phase at a given relative pressure and lattice parameter to nanowire radius ratio d/r defining the pore geometry can be deduced. By systematically varying the relative pressure and nanowire diameter, while keeping the lattice constant d determined from SAXS fixed, phase diagrams of d/r vs p/p_0 were calculated for nitrogen and n-pentane. These resulting equilibrium phase diagrams predicted a separated-to-bridged phase transition at lower relative pressures followed by a bridged-to-filled phase transition at higher relative pressures. These transitions result in two step like features for both phase transitions, which were also visible in the associated sorption isotherms of nitrogen and n-pentane on the monolithic, hierarchically nanoporous carbon material C30. Application of the Kelvin-Cohan equation for pore sizes corresponding to the gap between nanowires (similar to the separated-to-bridged transition) and the interstitial between three adjacent nanowires (similar to the bridged-to-filled transition) qualitatively confirm the positions of the phase lines in equilibrium in the phase diagram for nitrogen (for reference compare **Figure 42** and **Figure 39**). The geometry, defined by the nanowire radius r and lattice constant d , describing relative pressures of condensation in nitrogen and n-pentane adsorption experiments coincides satisfactorily with the mean nanowire distance and radius obtained from SAS experiments. The fact that equilibrium transitions were able to accurately describe phase transitions implies a disordered network of interconnections

and corrugations between the carbon nanowires, where local constrictions due to the disordered structure serve as nucleation sites for stable phases at equilibrium pressures (see **Figure 44**).

SANS n-pentane strain isotherms for three carbon materials CN, C30 and C120 were also analyzed, where all showed qualitatively identical behavior in adsorption induced deformation as a function of relative pressure. The overall magnitude of strain decreases with increasing physical activation time and therefore increasing microporosity, contrasting the findings on hierarchically nanoporous silica^{58,59}, where higher microporosity led to higher adsorption induced strains. Three distinct regions with differing behavior were identified in all three strain isotherms, which align satisfactorily with the pressure intervals of the three phases proposed above. By using a concept similar to the pore load modulus²⁷, an effective system modulus was determined for the filled phase by application of the Kelvin-Laplace equation (equation 3.101) for filled cylinders. In the pressure interval, derived from numerical calculations (see **Figure 40**), where the bridged phase is expected to be stable, the Laplace pressure due to the mean curvature of the associated liquid vapor profiles¹²⁷ of the bridged phase was calculated and also related to measured strains via an effective modulus. For both, the proposed bridged and filled phase, the strain isotherms are described well by the same pore load modulus, implying that the same structures, meaning interconnections between nanowires, are responsible for the stiffness of the material. Further, as the pore load modulus increases with increasing activation time, an effective stiffening of the interconnections seems to occur. A similar analysis was conducted for the n-pentane dilatometry data exclusively for relative pressures associated with the filled phase, where also an increase in pore load modulus can be observed but at different values than observed in SANS. With the effective moduli determined from the filled phase in SANS and dilatometry, effective Young's moduli E_c of the nanowires were determined which scale proportionally to the microporosity of the carbon nanowires. Applying the pore-load modulus from SANS and the Young's moduli E_c , a simple model describing the deformation of the carbon samples due to film formation on individual nanowires could be constructed. Calculations based on this simple model found that film formation alone can lead to compressive strains in the samples. Qualitative agreement of the compressive strains for the separated phase could be achieved with this simple model, where the main contribution to the deformation was due to the compliant structures between carbon nanowires and swelling of nanowires due to micropore filling are omitted. Still, the simple model seems to cover key processes of adsorption induced deformation in the separated phase. These findings lead to the conclusion that strains observed in SANS are mainly determined by stresses in the concave mesoporespace and the interconnections between nanowires for all three phases. In dilatometry, measured strains are the result of the comparatively large compliance in radial deformations of the struts and expansion of micropores.

The principles applied¹¹³ to develop a model of adsorption in concave porespace as they are found in CMK-3 or the investigated hierarchically nanoporous carbon material. The concepts applied could be further developed to investigate adsorption induced deformation in other similarly materials exhibiting concave porespace such as CMK-1¹⁴⁹ and CMK-5¹⁶⁰. The question remains, why simulations of nitrogen adsorption on CMK-3¹⁵⁵ don't yield a bridged phase and replicate the results from a cylindrical kernel in QSDFT¹⁵⁰ and GCMC¹⁵³. To answer this question the phase transition between separated and bridged phase could be investigated by the second variation of the grand potential. First indications on this by evaluating the second variation by crude means points to an extended metastable relative pressure region of the separated phase close reaching into

the pressure interval where the filled phase is already stable, hence the bridged phase would be omitted entirely in this case. First indication of this have been found by Jain et al¹⁵⁴, where a considerable amount of interconnections was necessary to force the pressure of capillary condensation in CMK-3 to lower relative pressures found in experiment. Alternatively, the solid-liquid potentials used in these studies are highly idealized and sometimes even tuned to replicate results from earlier studies, whereas measured disjoining pressures were applied in this thesis. A different avenue to further investigate adsorption in concave pore structures would be a DBdB analysis of statistically representative real space structures¹⁰⁵ obtained from SAS data of the desired material and simple structural considerations¹⁴² as these have been shown to quite accurately represent characteristics from adsorption¹⁶¹. The results from these approaches could then serve to develop an accurate model of adsorption induced deformation in materials exhibiting concave pore spaces.

Human Root Dentin: In-situ water absorption SAXS measurements of human root dentin were performed to gain insight into processes on a nanometer level during hydration. To assess the swelling of the collagen sandwiched between parallel mineral platelets (for reference see **Figure 3**) the T –parameter, which is thought to be closely linked to the mean platelet thickness, was calculated as a function of relative pressure. Large changes in T –parameter values were observed as a function of relative pressure in absorption, with a defined maximum of approximately 23% at $p/p_0 \sim 0.2$, although the total difference between dry and wet sample states was only $\sim 2\%$. This overall value is close to the 2.5% found for the swelling of collagen fibrils in an earlier in-situ water absorption synchrotron SAXS study by Masic et al⁴⁶. The P – parameter, indicating the filling of the collagen surrounding the mineral platelets, drops of at low relative pressures and stays constant for $p/p_0 > 0.2$. This means that filling of the collagen and other biological structures sandwiched between mineral platelets has finished once $p/p_0 \sim 0.2$ has been reached in absorption. Sectoral cake integrations of the root dentin's anisotropic 2D SAXS pattern in directions corresponding to signals along and perpendicular to the main orientation of collagen fibrils were performed, where a large discrepancy in T –parameter values between both sectoral integrations was observed, although the overall qualitative evolution with as a function of relative pressure was similar. Evaluation of the stack-of-cards model⁸⁵ was performed for both sectoral integrations, which lead to distinctly different behavior, where the sectors perpendicular to the collagen fibrils main orientation showed a behavior similar to the P –parameter, indicating a clear link between absorption and deformation. Consequently, correlation lengths for different q ranges were calculated, where a clear difference in behavior as a function of relative pressure was observed. Still, qualitative and quantitative agreement over the whole range of relative pressures investigated between all sectoral cake integrations and full radial integration was found for q ranges corresponding to sizes of 5 nm and below. Overall relative change in correlation length observed was around 2% between wet and dry sample states, implying that this parameter is closely related not only to the general thickness of the platelets but also their arrangement relative to each other. Consequently, this change in size should reflect the swelling of the collagenous and non-collagenous matrix between mineral platelets in human root dentin, with the total relative change of 2% being mirrored by findings from Masic et al⁴⁶. Also, the subsequent filling of the hierarchical structure can be roughly differentiated by sectoral integration of the anisotropic SAXS patterns. Still, the study conducted here is a first indication, that a better understanding of the structural hierarchy in highly mineralized tissues should be achieved to more accurately determine parameters of interest.

The study on human root dentin in this work is far from giving a complete picture on the effect of dehydration and rehydration and delivers only some implications of the sorption behavior of water within the hierarchical structure of dentin. Because necessary sorption experiments to resolve true deformations using in-situ sorption with water tuned to zero scattering length density at neutron sources are practically impossible due to the extremely long equilibration time, it is questionable if such an experiment will ever be conducted. However, evaluation of the WAXS signal of the mineral platelets crystal structure in in-situ (synchrotron) SAXS experiments can give further in-sights on the strain induced by water absorption. Other approaches which could give some insight into the effect of water would be introducing well defined changes to the material. Heating of samples which would consequently result in denaturation of collagen, hence cooking it, and complete removal of collagen at even higher temperatures combined with in-situ water absorption SAXS could give better indications on the role of collagen and other organics present during water absorption and its structural implications.

9 References

- (1) Cao, S. C., Liu, J., Zhu, L., Li, L., Dao, M., Lu, J., Ritchie, R. O. Nature-Inspired Hierarchical Steels. *Sci. Rep.* **2018**, *8*, 5088.
- (2) Kaneko K., Rodríguez-Reinoso F. *Nanoporous Materials for Gas Storage*; Springer Singapore: Singapore, 2019.
- (3) Adebajo, M. O., Frost, R. L., Klopogge, J. T., Carmody, O., Kokot, S. Porous Materials for Oil Spill Cleanup: A Review of Synthesis and Absorbing Properties. *J. Porous Mater.* **2003**, *10*, 159–170.
- (4) Rashidi, S., Esfahani, J. A., Karimi, N. Porous materials in building energy technologies—A review of the applications, modelling and experiments. *Renew. Renew. Sust. Energ. Rev.* **2018**, *91*, 229–247.
- (5) Ulfa, M., Prasetyoko, D. Synthesis of Mesoporous Carbon CMK-3 and CMK-5 Materials and Their Application for Drug Loading-Release System. *KLS* **2019**, *4*, 1.
- (6) Ehlers, W. Porous Media in the Light of History. In *The History of Theoretical, Material and Computational Mechanics - Mathematics Meets Mechanics and Engineering*; Stein, E., Ed.; Springer Berlin Heidelberg: Berlin, Heidelberg, 2014; Vol. 1, pp. 211–227.
- (7) Gibbs J. W. *Thermodynamics*; Ox Bow Press: Woodbridge, Conn., 1993.
- (8) Langmuir, I. The Adsorption of Gases on plane Surfaces of Glass, Mica and Platinum. *J. Am. Chem. Soc.* **1918**, *40*, 1361–1403.
- (9) Brunauer, S., Emmett, P. H., Teller, E. Adsorption of Gases in Multimolecular Layers. *J. Am. Chem. Soc.* **1938**, *60*, 309–319.
- (10) Derjaguin, B. A theory of capillary condensation in the pores of sorbents and of other capillary phenomena taking into account the disjoining action of polymolecular liquid films. *Prog. Surf. Sci.* **1992**, *40*, 46–61.
- (11) Broekhoff, J., de Boer, J. H. Studies on pore systems in catalysts IX. Calculation of pore distributions from the adsorption branch of nitrogen sorption isotherms in the case of open cylindrical pores A. Fundamental equations. *J. Catal.* **1967**, *9*, 8–14.
- (12) Broekhoff, J., de Boer, J. H. Studies on pore systems in catalysts XII. Pore distributions from the desorption branch of a nitrogen sorption isotherm in the case of cylindrical pores A. An analysis of the capillary evaporation process. *J. Catal.* **1968**, *10*, 368–376.
- (13) Lastoskie, C., Gubbins, K. E., Quirke, N. Pore size heterogeneity and the carbon slit pore: a density functional theory model. *Langmuir* **1993**, *9*, 2693–2702.
- (14) Neimark, Ravikovitch, Grün, Schüth, Unger. Pore Size Analysis of MCM-41 Type Adsorbents by Means of Nitrogen and Argon Adsorption. *J. Colloid Interface Sci* **1998**, *207*, 159–169.
- (15) Kresge, C. T., Leonowicz, M. E., Roth, W. J., Vartuli, J. C., Beck, J. S. Ordered mesoporous molecular sieves synthesized by a liquid-crystal template mechanism. *Nature* **1992**, *359*, 710–712.
- (16) Ravikovitch, P. I., Neimark, A. V. Density functional theory model of adsorption on amorphous and microporous silica materials. *Langmuir* **2006**, *22*, 11171–11179.
- (17) McBain, J. W., Ferguson, J. On the Nature of the Influence of Humidity Changes upon the Composition of Building Materials. *J. Phys. Chem.* **1927**, *31*, 564–590.
- (18) Bangham, D. H., Fakhoury, N. The Expansion of Charcoal accompanying Sorption of Gases and Vapours. *Nature* **1928**, *122*, 681–682.
- (19) Haines, R. S., McIntosh, R. Length Changes of Activated Carbon Rods Caused by Adsorption of Vapors. *J. Am. Chem. Soc.* **1947**, *15*, 28–38.
- (20) Wiig, E. O., Juhola, A. J. The Adsorption of Water Vapor on Activated Charcoal. *J. Am. Chem. Soc.* **1949**, *71*, 561–568.

- (21) Lakhanpal, M. L., Flood, E. A. Stresses and Strains in Adsorbate Adsorbent Systems: I.V. Contraction of activated Carbon on Adsorption of Gases and Vapors at low initial Pressures. *Can. J. Chem.* **1957**, *35*, 887–899.
- (22) Amberg, C. H., McIntosh, R. A Study of Adsorption Hysteresis by means of length changes of a Rod of Porous Glass. *Can. J. Chem.* **1952**, *30*, 1012–1032.
- (23) Dolino, Bellet, Faivre. Adsorption strains in porous silicon. *Phys. Rev. B Condens. Matter* **1996**, *54*, 17919–17929.
- (24) Bellet, Dolino. X-ray observation of porous-silicon wetting. *Phys. Rev. B Condens. Matter* **1994**, *50*, 17162–17165.
- (25) Albouy, P.-A., Ayral, A. Coupling X-ray Scattering and Nitrogen Adsorption: An Interesting Approach for the Characterization of Ordered Mesoporous Materials. Application to Hexagonal Silica. *Chem. Mater.* **2002**, *14*, 3391–3397.
- (26) Zickler, G. A., Jähnert, S., Funari, S. S., Findenegg, G. H., Paris, O. Pore lattice deformation in ordered mesoporous silica studied by in situ small-angle X-ray diffraction. *J. Appl. Cryst.* **2007**, *40*, s522-s526.
- (27) Prass, J., Müter, D., Fratzl, P., Paris, O. Capillarity-driven deformation of ordered nanoporous silica. *Appl. Phys. Lett.* **2009**, *95*, 83121.
- (28) Gor, G. Y., Neimark, A. V. Adsorption-induced deformation of mesoporous solids. *Langmuir* **2010**, *26*, 13021–13027.
- (29) Gor, G. Y., Neimark, A. V. Adsorption-induced deformation of mesoporous solids: macroscopic approach and density functional theory. *Langmuir* **2011**, *27*, 6926–6931.
- (30) Gor, G. Y., Paris, O., Prass, J., Russo, P. A., Ribeiro Carrott, M. M. L., Neimark, A. V. Adsorption of n-pentane on mesoporous silica and adsorbent deformation. *Langmuir* **2013**, *29*, 8601–8608.
- (31) Schoen, M., Paris, O., Günther, G., Müter, D., Prass, J., Fratzl, P. Pore-lattice deformations in ordered mesoporous matrices: experimental studies and theoretical analysis. *Phys. Chem. Chem. Phys.* **2010**, *12*, 11267–11279.
- (32) Balzer, C., Waag, A. M., Gehret, S., Reichenauer, G., Putz, F., Hüsing, N., Paris, O., Bernstein, N., Gor, G. Y., Neimark, A. V. Adsorption-Induced Deformation of Hierarchically Structured Mesoporous Silica-Effect of Pore-Level Anisotropy. *Langmuir* **2017**, *33*, 5592–5602.
- (33) Balzer, C., Waag, A. M., Putz, F., Hüsing, N., Paris, O., Gor, G. Y., Neimark, A. V., Reichenauer, G. Mechanical Characterization of Hierarchical Structured Porous Silica by in Situ Dilatometry Measurements during Gas Adsorption. *Langmuir* **2019**, *35*, 2948–2956.
- (34) Brandhuber, D., Hüsing, N., Raab, C. K., Torma, V., Peterlik, H. Cellular mesoscopically organized silica monoliths with tailored surface chemistry by one-step drying/extraction/surface modification processes. *J. Mater. Chem* **2005**, *15*, 1801.
- (35) Putz, F., Waag, A., Balzer, C., Braxmeier, S., Elsaesser, M. S., Ludescher, L., Paris, O., Malfait, W. J., Reichenauer, G., Hüsing, N. The influence of drying and calcination on surface chemistry, pore structure and mechanical properties of hierarchically organized porous silica monoliths. *Microporous Mesoporous Mat.* **2019**, *288*, 109578.
- (36) Balzer, C., Morak, R., Erko, M., Triantafillidis, C., Hüsing, N., Reichenauer, G., Paris, O. Relationship Between Pore Structure and Sorption-Induced Deformation in Hierarchical Silica-Based Monoliths. *Z. Phys. Chem* **2015**, *229*, 526.
- (37) Morak, R., Braxmeier, S., Ludescher, L., Putz, F., Busch, S., Hüsing, N., Reichenauer, G., Paris, O. Quantifying adsorption-induced deformation of nanoporous materials on different length scales. *J. Appl. Cryst.* **2017**, *50*, 1404–1410.
- (38) Prass, J., Müter, D., Erko, M., Paris, O. Apparent lattice expansion in ordered nanoporous silica during capillary condensation of fluids. *J. Appl. Cryst.* **2012**, *45*, 798–806.

- (39) Koczwarra, C., Rumswinkel, S., Prehal, C., Jäckel, N., Elsässer, M. S., Amenitsch, H., Presser, V., Hüsing, N., Paris, O. In Situ Measurement of Electrosorption-Induced Deformation Reveals the Importance of Micropores in Hierarchical Carbons. *ACS Appl. Mater. Interfaces* **2017**, *9*, 23319–23324.
- (40) Hasegawa, G., Kanamori, K., Kiyomura, T., Kurata, H., Abe, T., Nakanishi, K. Hierarchically Porous Carbon Monoliths Comprising Ordered Mesoporous Nanorod Assemblies for High-Voltage Aqueous Supercapacitors. *Chem. Mater.* **2016**, *28*, 3944–3950.
- (41) Ganser, C., Fritz-Popovski, G., Morak, R., Sharifi, P., Marmiroli, B., Sartori, B., Amenitsch, H., Griesser, T., Teichert, C., Paris, O. Cantilever bending based on humidity-actuated mesoporous silica/silicon bilayers. *Beilstein J. Nanotechnol.* **2016**, *7*, 637–644.
- (42) Meyers, M. A., Chen, P.-Y., Lin, A. Y.-M., Seki, Y. Biological materials: Structure and mechanical properties. *Prog. Mater. Sci* **2008**, *53*, 1–206.
- (43) Hwang, J., Jeong, Y., Park, J. M., Lee, K. H., Hong, J. W., Choi, J. Biomimetics: forecasting the future of science, engineering, and medicine. *Int. J. Nanomedicine* **2015**, *10*, 5701–5713.
- (44) Martin R. B., Burr D. B., Sharkey N. A., Fyhrie D. P., Eds. *Skeletal Tissue Mechanics*; Springer New York: New York, NY, 2015.
- (45) Zaslansky, P. Dentin. In *Collagen*; Fratzl, P., Ed.; Springer US: Boston, MA, 2008; Vols. 27, pp. 421–446.
- (46) Masic, A., Bertinetti, L., Schuetz, R., Chang, S.-W., Metzger, T. H., Buehler, M. J., Fratzl, P. Osmotic pressure induced tensile forces in tendon collagen. *Nat. Commun.* **2015**, *6*, 5942.
- (47) Shemesh, H., Lindtner, T., Portoles, C. A., Zaslansky, P. Dehydration Induces Cracking in Root Dentin Irrespective of Instrumentation: A Two-dimensional and Three-dimensional Study. *J. Endod.* **2018**, *44*, 120–125.
- (48) Liu, P. S., Chen, G. F. Special Porous Metals. In *J. Porous Mater.*; Elsevier, 2014, pp. 189–220.
- (49) Perego, C., Millini, R. Porous materials in catalysis: challenges for mesoporous materials. *Chem. Soc. Rev* **2013**, *42*, 3956–3976.
- (50) Wang, L., Hu, X. Recent Advances in Porous Carbon Materials for Electrochemical Energy Storage. *Chem: Asian J.* **2018**, *13*, 1518–1529.
- (51) Santos H., Ed. *Porpus silicon for biomedical applications*; Elsevier/WP Woodhead Publishing: Amsterdam, Boston, Cambridge, 2014.
- (52) Thommes, M., Kaneko, K., Neimark, A. V., Olivier, J. P., Rodriguez-Reinoso, F., Rouquerol, J., Sing, K. S.W. Physisorption of gases, with special reference to the evaluation of surface area and pore size distribution (IUPAC Technical Report). *Pure Appl. Chem* **2015**, *87*, 1051–1069.
- (53) Di Renzo, F., Cambon, H., Dutartre, R. A 28-year-old synthesis of micelle-templated mesoporous silica. *Microporous Mesoporous Mat.* **1997**, *10*, 283–286.
- (54) Angloher, S., Bein, T. Organic functionalisation of mesoporous silica. In *Molecular Sieves: From Basic Research to Industrial Applications, Proceedings of the 3rd International Zeolite Symposium (3rd FEZA)*; Elsevier, 2005; Vols. 158, pp. 2017–2026.
- (55) Brandhuber, D., Torma, V., Raab, C., Peterlik, H., Kulak, A., Hüsing, N. Glycol-Modified Silanes in the Synthesis of Mesoscopically Organized Silica Monoliths with Hierarchical Porosity. *Chem. Mater.* **2005**, *17*, 4262–4271.
- (56) Nakanishi, K., Tanaka, N. Sol–Gel with Phase Separation. Hierarchically Porous Materials Optimized for High-Performance Liquid Chromatography Separations. *ChemInform* **2007**, *38*, 863.
- (57) Pollock, R. A., Walsh, B. R., Fry, J., Ghampson, I. T., Melnichenko, Y. B., Kaiser, H., Pynn, R., DeSisto, W. J., Wheeler, M. C., Frederick, B. G. Size and Spatial Distribution of Micropores in SBA-15 using CM-SANS. *Chem. Mater.* **2011**, *23*, 3828–3840.
- (58) Roland Morak. *Sorption induced deformation of hierarchical porous materials*, 2017.

- (59) Ludescher, L., Morak, R., Balzer, C., Waag, A. M., Braxmeier, S., Putz, F., Busch, S., Gor, G. Y., Neimark, A. V., Huesing, N., Reichenauer, G., Paris, O. In-situ small-angle neutron scattering investigation of adsorption-induced deformation in silica with hierarchical porosity. *Langmuir* **2019**.
- (60) API, Ed. (2017). Measurement of the Young's modulus of amorphous carbon nanowhisker by static and dynamic method; API.
- (61) Jun, S., Joo, S. H., Ryoo, R., Kruk, M., Jaroniec, M., Liu, Z., Ohsuna, T., Terasaki, O. Synthesis of New, Nanoporous Carbon with Hexagonally Ordered Mesostructure. *J. Am. Chem. Soc.* **2000**, *122*, 10712–10713.
- (62) Joo, S. H., Ryoo, R., Kruk, M., Jaroniec, M. Evidence for General Nature of Pore Interconnectivity in 2-Dimensional Hexagonal Mesoporous Silicas Prepared Using Block Copolymer Templates. *J. Phys. Chem. B* **2002**, *106*, 4640–4646.
- (63) Ryoo, R., Joo, S. H., Jun, S., Tsubakiyama, T., Terasaki, O. 07-O-01 - Ordered mesoporous carbon molecular sieves by templated synthesis: the structural varieties. In *Zeolites and Mesoporous Materials at the dawn of the 21st century, Proceedings of the 13th International Zeolite Conference*; Elsevier, 2001; Vols. 135, p. 150.
- (64) Freeman, J. J. Active carbon Edited by R. C. Bansal, J.-B. Donnet and F. Stoeckli. Marcel Dekker, New York, 1988, pp. xiv + 482, US\$150.00. ISBN 0-8247-7842-1. *J. Chem. Technol. Biotechnol.* **1990**, *48*, 240–241.
- (65) Koczwar, C., Rumswinkel, S., Hammerschmidt, L., Salihovic, M., Elsaesser, M. S., Amenitsch, H., Paris, O., Huesing, N. Nanofibers versus Nanopores: A Comparison of the Electrochemical Performance of Hierarchically Ordered Porous Carbons. *ACS Appl. Energy Mater.* **2019**, *2*, 5279–5291.
- (66) Fratzl, P., Gupta, H. S., Paschalis, E. P., Roschger, P. Structure and mechanical quality of the collagen–mineral nano-composite in bone. *J. Mater. Chem.* **2004**, *14*, 2115–2123.
- (67) Nanci A. *Ten Cate's oral histology: Development, structure, and function*, 9th ed.; Elsevier: St. Louis, Missouri, 2018.
- (68) Fratzl P., Ed. *Collagen*; Springer US: Boston, MA, 2008.
- (69) M. F. Ashby, Ed. *The CES EduPack Database of Natural and Man-Made Materials*, 2012nd ed.: Cambridge.
- (70) Djomehri, S. I., Candell, S., Case, T., Browning, A., Marshall, G. W., Yun, W., Lau, S. H., Webb, S., Ho, S. P. Mineral density volume gradients in normal and diseased human tissues. *PloS one* **2015**, *10*, e0121611.
- (71) Lara-Curzio E., Salem J., Eds. *Mechanical properties and performance of engineering ceramics and composites III: A collection of papers presented at the 31st International Conference on Advanced Ceramics and Composites, January 21 - 26, 2007, Daytona Beach, Florida ; [contains papers presented at the Symposium on Processing, Properties and Performance of Engineering Ceramics and Composites*; Wiley: Hoboken, NJ, 2008.
- (72) Wang, J., Chen, Y., Li, L., Sun, J., Gu, X., Xu, X., Pan, H., Tang, R. Remineralization of dentin collagen by meta-stabilized amorphous calcium phosphate. *CrystEngComm* **2013**, *15*, 6151.
- (73) Petruska, J. A., Hodge, A. J. A subunit Model for the Tropocollagen. *Proc. Natl. Acad. Sci. U. S. A.* **1964**, *51*, 871–876.
- (74) Goldberg, M., Kulkarni, A. B., Young, M., Boskey, A. Dentin: structure, composition and mineralization. *Front. Biosci. (Elite Ed.)* **2011**, *3*, 711–735.
- (75) Almer, J. D., Stock, S. R. High energy X-ray scattering quantification of in situ-loading-related strain gradients spanning the dentinoenamel junction (DEJ) in bovine tooth specimens. *J. Biomech.* **2010**, *43*, 2294–2300.

- (76) Voegel, J. C., Frank, R. M. Ultrastructural study of apatite crystal dissolution in human dentine and bone. *J. Bio. Buccale* **1977**, *5*, 181–194.
- (77) Tesch, W., Eidelman, N., Roschger, P., Goldenberg, F., Klaushofer, K., Fratzl, P. Graded Microstructure and Mechanical Properties of Human Crown Dentin. *Calcif. Tissue Int* **2001**, *69*, 147–157.
- (78) Delves P. J., Ed. *Encyclopedia of immunology*, 2nd ed.; Elsevier: Amsterdam, 2004.
- (79) Sears, V. F. Neutron scattering lengths and cross sections. *Neutron News* **1992**, *3*, 26–37.
- (80) Glatter O., Kratky O. *Small angle x-ray scattering: Edited by O. Glatter and O. Kratky*, 2nd ed.; Academic Press: London, New York, 1983.
- (81) Jensen, G. V., Barker, J. G. Effects of multiple scattering encountered for various small-angle scattering model functions. *J. Appl. Cryst.* **2018**, *51*, 1455–1466.
- (82) Basano, L., Bianchi, A. Rutherford's scattering formula via the Runge–Lenz vector. *Am. J. Phys.* **1980**, *48*, 400–401.
- (83) Hamilton M. L. *Effects of radiation on materials: 19th international symposium, [held in Seattle, Washington on 16 - 18 June 1998]*; ASTM: West Conshohocken, Pa., 2000.
- (84) Teixeira, J. Scattering by fractals. *Ferroelectrics* **1999**, *235*, 231–234.
- (85) Fratzl, P., Gupta, H. S., Paris, O., Valenta, A., Roschger, P., Klaushofer, K. Diffracting “stacks of cards” - some thoughts about small-angle scattering from bone. In *Scattering Methods and the Properties of Polymer Materials*; Springer Berlin Heidelberg: Berlin, Heidelberg, 2005, pp. 33–39.
- (86) Smarsly, B., Antonietti, M., Wolff, T. Evaluation of the small-angle x-ray scattering of carbons using parametrization methods. *J. Chem. Phys.* **2002**, *116*, 2618–2627.
- (87) Mazzolo, A., Roesslinger, B., Gille, W. Properties of chord length distributions of nonconvex bodies. *J. Math. Phys.* **2003**, *44*, 6195.
- (88) Märten, A., Fratzl, P., Paris, O., Zaslansky, P. On the mineral in collagen of human crown dentine. *Biomaterials* **2010**, *31*, 5479–5490.
- (89) Gommès, C. J., Prieto, G., Jongh, P. E. de. Small-Angle Scattering Analysis of Empty or Loaded Hierarchical Porous Materials. *J. Phys. Chem. C* **2016**, *120*, 1488–1506.
- (90) Zickler, G. A., Jähnert, S., Wagermaier, W., Funari, S. S., Findenegg, G. H., Paris, O. Physisorbed films in periodic mesoporous silica studied by in situ synchrotron small-angle diffraction. *Phys. Rev. B* **2006**, *73*, 17.
- (91) Impéror-Clerc, M. Three-dimensional periodic complex structures in soft matter: investigation using scattering methods. *Interface Focus* **2012**, *2*, 589–601.
- (92) Jähnert, S., Müter, D., Prass, J., Zickler, G. A., Paris, O., Findenegg, G. H. Pore Structure and Fluid Sorption in Ordered Mesoporous Silica. I. Experimental Study by in situ Small-Angle X-ray Scattering. *J. Phys. Chem. C* **2009**, *113*, 15201–15210.
- (93) Findenegg, G. H., Jähnert, S., Müter, D., Prass, J., Paris, O. Fluid adsorption in ordered mesoporous solids determined by in situ small-angle X-ray scattering. *Phys. Chem. Chem. Phys.* **2010**, *12*, 7211–7220.
- (94) Debye, P. Zerstreuung von Röntgenstrahlen. *Ann. Phys.* **1915**, *351*, 809–823.
- (95) Gor, G. Y., Huber, P., Bernstein, N. Adsorption-induced deformation of nanoporous materials—A review. *Appl. Phys. Rev* **2017**, *4*, 11303.
- (96) Calvert, J. G. Glossary of atmospheric chemistry terms (Recommendations 1990). *Pure Appl. Chem.* **1990**, *62*, 2167–2219.
- (97) Rouquerol F. *Adsorption by powders and porous solids: Principles, methodology and applications*; Elsevier/Academic Press: Amsterrdam, 2014.
- (98) McMurry J. *Fundamentals of organic chemistry*, 5th ed.; Brooks/Cole: Pacific Grove, Calif., London, 2003.

- (99) P., H. R. Kapillarchemie, Eine Darstellung der Chemie der Kolloide und verwandter Gebiete. *Nature* **1911**, *85*, 534–535.
- (100) Halsey, G. Physical Adsorption on Non-Uniform Surfaces. *J. Am. Chem. Soc.* **1948**, *16*, 931–937.
- (101) Hill, T. L. Theory of Physical Adsorption. In ; Elsevier, 1952; Vols. 4, pp. 211–258.
- (102) Derjaguin B. V., Churaev N. V., Muller V. M. *Surface Forces*; Springer: Boston, MA, 1987.
- (103) Churaev, Starke, Adolphs. Isotherms of Capillary Condensation Influenced by Formation of Adsorption Films. *J. Colloid Interface Sci* **2000**, *221*, 246–253.
- (104) Grosman, A., Ortega, C. Nature of capillary condensation and evaporation processes in ordered porous materials. *Langmuir* **2005**, *21*, 10515–10521.
- (105) Gommès, C. J., Roberts, A. P. Stochastic analysis of capillary condensation in disordered mesopores. *Phys. Chem. Chem. Phys.* **2018**, *20*, 13646–13659.
- (106) Ravikovitch, P. I., Haller, G. L., Neimark, A. V. Density functional theory model for calculating pore size distributions: pore structure of nanoporous catalysts. *Adv. Colloid Interface Sci* **1998**, *76-77*, 203–226.
- (107) Ravikovitch, P. I., Neimark, A. V. Calculations of pore size distributions in nanoporous materials from adsorption and desorption isotherms. In *Nanoporous Materials II, Proceedings of the 2nd Conference on Access in Nanoporous Materials*; Elsevier, 2000; Vols. 129, pp. 597–606.
- (108) Landers, J., Gor, G. Y., Neimark, A. V. Density functional theory methods for characterization of porous materials. *Colloids Surf. A* **2013**, *437*, 3–32.
- (109) Gor, G. Y., Huber, P., Weissmüller, J. Elastocapillarity in nanopores: Sorption strain from the actions of surface tension and surface stress. *Phys. Rev. Mater.* **2018**, *2*.
- (110) Cohan, L. H. Sorption Hysteresis and the Vapor Pressure of Concave Surfaces. *J. Am. Chem. Soc.* **1938**, *60*, 433–435.
- (111) Philip, J. R. Adsorption and geometry: the boundary layer approximation. *J. Chem. Phys.* **1977**, *67*, 1732–1741.
- (112) Saam, W. F., Cole, M. W. Excitations and thermodynamics for liquid-helium films. *Phys. Rev. B* **1975**, *11*, 1086–1105.
- (113) Dobbs, H. T., Yeomans, J. M. Capillary condensation within an array of cylinders. *Mol. Phys.* **1993**, *80*, 877–884.
- (114) Gelfand I. M. *Calculus of Variations*; Dover Publications, 2012.
- (115) Lanczos C. *The Variational Principles of Mechanics*; Dover Publications: Newburyport, 2012.
- (116) Nič M., Jiráť J., Košata B., Jenkins A., McNaught A. *IUPAC Compendium of Chemical Terminology*; IUPAC: Research Triangle Park, NC, 2009.
- (117) Evans, R. Fluids adsorbed in narrow pores: phase equilibria and structure. *J. Phys.: Condens. Matter* **1990**, *2*, 8989–9007.
- (118) Butt H.-J., Graf K., Kappl M. *Physics and chemistry of interfaces*, 1st ed.; Wiley-VCH: Weinheim, 2003.
- (119) Israelachvili, J. Solvation forces and liquid structure, as probed by direct force measurements. *Acc. Chem. Res.* **1987**, *20*, 415–421.
- (120) Israelachvili J. N. *Intermolecular and surface forces*, 3rd ed.; Academic Press: Burlington, MA, 2011.
- (121) Churaev, Setzer, Adolphs. Influence of Surface Wettability on Adsorption Isotherms of Water Vapor. *J. Colloid Interface Sci* **1998**, *197*, 327–333.
- (122) Gor, G. Y., Bernstein, N. Revisiting Bangham's law of adsorption-induced deformation: changes of surface energy and surface stress. *Phys. Chem. Chem. Phys.* **2016**, *18*, 9788–9798.
- (123) Scherer, G. W. Dilatation of Porous Glass. *J American Ceramic Society* **1986**, *69*, 473–480.
- (124) Ravikovitch, P. I., Neimark, A. V. Density functional theory model of adsorption deformation. *Langmuir* **2006**, *22*, 10864–10868.

- (125) Balzer C. *Adsorption-Induced Deformation of Nanoporous Materials — in-situ Dilatometry and Modeling*; Universität Würzburg: Würzburg, 2018.
- (126) Bangham, D. H., Razouk, R. I. The saturation and immersion expansions and the heat of wetting. *Proc. R. Soc. Lond. A* **1938**, *166*, 572–586.
- (127) Spivak M. *A comprehensive introduction to differential geometry*, 3rd ed.; Publish or Perish: Houston, Texas, 2005.
- (128) Timošenko S. P., Goodier J. N. *Theory of elasticity*, 3rd ed.; McGraw-Hill: New York, 1987.
- (129) Derjaguin, B. V., Churaev, N. V. Polymolecular adsorption and capillary condensation in narrow slit pores. *Prog. Surf. Sci.* **1992**, *40*, 173–191.
- (130) Iwamatsu, M., Horii, K. Capillary Condensation and Adhesion of Two Wetter Surfaces. *J. Colloid Interface Sci* **1996**, *182*, 400–406.
- (131) Kowalczyk, P., Ciach, A., Neimark, A. V. Adsorption-induced deformation of microporous carbons: pore size distribution effect. *Langmuir* **2008**, *24*, 6603–6608.
- (132) Godet, C., David, D. Derivation of Hamaker Dispersion Energy of Amorphous Carbon Surfaces in Contact with Liquids Using Photoelectron Energy-Loss Spectra. *Braz. J. Phys.* **2017**, *47*, 594–605.
- (133) Kruk, M., Jaroniec, M., Sayari, A. Application of Large Pore MCM-41 Molecular Sieves To Improve Pore Size Analysis Using Nitrogen Adsorption Measurements. *Langmuir* **1997**, *13*, 6267–6273.
- (134) Chen, M., Coasne, B., Guyer, R., Derome, D., Carmeliet, J. Molecular Simulation of Sorption-Induced Deformation in Atomistic Nanoporous Materials. *Langmuir* **2019**, *35*, 7751–7758.
- (135) Erko M. *Water properties in confined geometry*: Leoben, 2013.
- (136) Bohren C. F., Albrecht B. A. *Atmospheric thermodynamics*; Oxford Univ. Press: New York, 1998.
- (137) Orthaber, D., Bergmann, A., Glatter, O. SAXS experiments on absolute scale with Kratky systems using water as a secondary standard. *J. Appl. Cryst.* **2000**, *33*, 218–225.
- (138) Heinemann, A., Mühlbauer, S. SANS-1: Small angle neutron scattering. *JLSRF* **2015**, *1*.
- (139) National Institute of Standards and Technology. *Scattering Length Density Calculator*. <https://www.ncnr.nist.gov/resources/activation/>.
- (140) Keiderling, U. The new ‘BerSANS-PC’ software for reduction and treatment of small angle neutron scattering data. *Appl. Phys. A* **2002**, *74*, s1455-s1457.
- (141) Ludescher, L., Morak, R., Braxmeier, S., Putz, F., Hüsing, N., Reichenauer, G., Paris, O. Hierarchically organized materials with ordered mesopores: adsorption isotherm and adsorption-induced deformation from small-angle scattering. *Phys. Chem. Chem. Phys.* **2020**, *22*, 12713–12723.
- (142) Gommès, C. J., Pirard, J.-P. Morphological models of complex ordered materials based on inhomogeneously clipped Gaussian fields. *Phys. Rev. E* **2009**, *80*, 61401.
- (143) Gommès, C. J., Friedrich, H., Wolters, M., Jongh, P. E. de, Jong, K. P. d. Quantitative Characterization of Pore Corrugation in Ordered Mesoporous Materials Using Image Analysis of Electron Tomograms. *Chem. Mater.* **2009**, *21*, 1311–1317.
- (144) Debye, P. Interferenz von Röntgenstrahlen und Wärmebewegung. *Ann. Phys.* **1913**, *348*, 49–92.
- (145) Ludescher, L., Braxmeier, S., Balzer, C., Reichenauer, G., Putz, F., Hüsing, N., Gor, G. Y., Paris, O. Capillary bridge formation between hexagonally ordered carbon nanorods. *Adsorption* **2020**, *26*, 563–578.
- (146) Silvestre-Albero, A., Silvestre-Albero, J., Martínez-Escandell, M., Futamura, R., Itoh, T., Kaneko, K., Rodríguez-Reinoso, F. Non-porous reference carbon for N₂ (77.4 K) and Ar (87.3 K) adsorption. *Carbon* **2014**, *66*, 699–704.
- (147) Croucher, M. D., Hair, M. L. Hamaker constants and the principle of corresponding states. *J. Chem. Phys.* **1977**, *81*, 1631–1636.

- (148) Morishige, K., Nakahara, R. Capillary Condensation in the Void Space between Carbon Nanorods. *J. Phys. Chem. C* **2008**, *112*, 11881–11886.
- (149) Joo, S. H., Jun, S., Ryoo, R. Synthesis of ordered mesoporous carbon molecular sieves CMK-1. *Microporous Mesoporous Mater.* **2001**, *44-45*, 153–158.
- (150) Gor, G. Y., Thommes, M., Cychosz, K. A., Neimark, A. V. Quenched solid density functional theory method for characterization of mesoporous carbons by nitrogen adsorption. *Carbon* **2012**, *50*, 1583–1590.
- (151) Restagno, F., Bocquet, L., Crassous, J., Charlaix, E. Slow kinetics of capillary condensation in confined geometry: experiment and theory. *Colloids Surf. A* **2002**, *206*, 69–77.
- (152) Osborn, Yeomans. Wetting on lines and lattices of cylinders. *Phys. Rev. E* **1995**, *51*, 2053–2058.
- (153) Barrera, D., Dávila, M., Cornette, V., Oliveira, J. A. de, López, R. H., Sapag, K. Pore size distribution of ordered nanostructured carbon CMK-3 by means of experimental techniques and Monte Carlo simulations. *Microporous Mesoporous Mater.* **2013**, *180*, 71–78.
- (154) Jain, S. K., Pellenq, R. J.-M., Gubbins, K. E., Peng, X. Molecular Modeling and Adsorption Properties of Ordered Silica-Templated CMK Mesoporous Carbons. *Langmuir* **2017**, *33*, 2109–2121.
- (155) Yelpo, V., Cornette, V., Toso, J. P., López, R. H. Characterization of nanostructured carbon CMK-3 by means of Monte Carlo simulations. *Carbon* **2017**, *121*, 106–113.
- (156) Dunlop J. W. C., Fratzl P., Weinkamer R., Eds. *Materials design inspired by nature: Function through inner architecture*; The Royal Society of Chemistry: Cambridge, 2013.
- (157) Gourrier, A., Bunk, O., Müller, K., Reiche, I. Artificially Heated Bone at Low Temperatures: A quantitative Scanning-small-angle X-Ray Scattering Imaging Study of the Mineral Particle Size. *Archeosciences* **2011**, 191–199.
- (158) Suhonen, H., Fernández, M., Serimaa, R., Suortti, P. Simulation of small-angle x-ray scattering from collagen fibrils and comparison with experimental patterns. *Phys. Med. Biol.* **2005**, *50*, 5401–5416.
- (159) Forien, J.-B., Zizak, I., Fleck, C., Petersen, A., Fratzl, P., Zolotoyabko, E., Zaslansky, P. Water-Mediated Collagen and Mineral Nanoparticle Interactions Guide Functional Deformation of Human Tooth Dentin. *Chem. Mater.* **2016**, *28*, 3416–3427.
- (160) Darmstadt, H., Roy, C., Kaliaguine, S., Kim, T.-W., Ryoo, R. Surface and Pore Structures of CMK-5 Ordered Mesoporous Carbons by Adsorption and Surface Spectroscopy. *Chem. Mater.* **2003**, *15*, 3300–3307.
- (161) Prehal, C., Grätz, S., Krüner, B., Thommes, M., Borchardt, L., Presser, V., Paris, O. Comparing pore structure models of nanoporous carbons obtained from small angle X-ray scattering and gas adsorption. *Carbon* **2019**, *152*, 416–423.